Mathematical Modelling and Control of Renewable Energy Systems and Battery Storage Systems

A thesis submitted by

Singappuli M Wijewardana

in partial fulfilment of
the requirements of the degree of

Doctor of Philosophy

School of Engineering and Materials Science
Queen Mary, University of London
Mile End Road
London, E1 4NS, UK

October 2016

School of Engineering and Materials Science
Queen Mary, University of London

PhD THESIS

DECLARATION

this thesis entitled

Mathematical Modelling and Control of Renewable Energy Systems and Battery Storage Systems

presented herewith is my own work and this thesis has not been submitted for any other qualifications.

Signed

Name: SINGAPPULI M WIJEWARDANA

Date: 12 October 2016

Abstract

Intermittent nature of renewable energy sources like the wind and solar energy poses new challenges to harness and supply uninterrupted power for consumer usage. Though, converting energy from these sources to useful forms of energy like electricity seems to be promising, still, significant innovations are needed in design and construction of wind turbines and PV arrays with BS systems. The main focus of this research project is mathematical modelling and control of wind turbines, solar photovoltaic (PV) arrays and battery storage (BS) systems. After careful literature review on renewable energy systems, new developments and existing modelling and controlling methods have been analysed. Wind turbine (WT) generator speed control, turbine blade pitch angle control (pitching), harnessing maximum power from the wind turbines have been investigated and presented in detail. Mathematical modelling of PV arrays and how to extract maximum power from PV systems have been analysed in detail.

Application of model predictive control (MPC) to regulate the output power of the wind turbine and generator speed control with variable wind speeds have been proposed by formulating a linear model from a nonlinear mathematical model of a WT.

Battery chemistry and nonlinear behaviour of battery parameters have been analysed to present a new equivalent electrical circuit model. Converting the captured solar energy into useful forms, and storing it for future use when the Sun itself is obscured is implemented by using battery storage systems presenting a new simulation model.

Temperature effect on battery cells and dynamic battery pack modelling have been described with an accurate state of charge estimation method. The concise description on power converters is also addressed with special reference to state-space models. Bi-directional AC/DC converter, which could work in either rectifier or inverter modes is described with a cost effective proportional integral derivative (PID/State-feedback) controller.

Preface

This dissertation is original, prepared by Singappuli Wijewardana at the School of Engineering and Materials Science, Queen Mary, University of London, Mile End Road, London E1 4NS, UK in partial fulfilment of the degree of Doctor of Philosophy in Engineering. The research project has been supervised by Dr Hasan Shaheed.

This interdisciplinary research project has a potential for substantial impact on multiple renewable energy electricity generations from WT, PV combined with BS systems. With this compendium, I have attempted to bring everything in concise and conscientious manner.

With the mathematical modelling and simulation for every renewable energy subsystem under consideration, model predictive control (MPC) is applied to the wind turbine control and optimising power output. MATLAB/Simulink has been used as a tool for modelling and simulations.

Singappuli M Wijewardana

12 October 2016

Acknowledgement

I wish to express my profound thanks and deepest gratitude towards my supervisor Dr M Hasan Shaheed for his invaluable guidance and support during my research project. He guided me in every aspect during my studies and encouraged me at every stage when I had questions regarding my project. Also, I wish to thank Dr Ranjan Vepa for his valuable advice given to me during my research work.

I dedicate this thesis to Professor Sam Karunaratne, former Chairman and Chancellor, SLIIT and Vice Chancellor University of Moratuwa, Sri Lanka. Without his blessings and advice at the inception, I would not have embarked on this research endeavour.

I owe my sincere thanks to my wife Sujatha and I am indebted to her for her patience and encouragement. Ishan, Ishanga my son and daughter, have been always helpful to me in numerous ways during my research work. Finally, I would like to thank my mother for giving me the moral support that I needed to complete this task.

Singappuli M Wijewardana

12 October 2016

Table of Contents

List of Figures

List of Tables

Acronyms

AC	Alternating Current
ANN	Artificial Neural Network
BEM	Blade Element Momentum
BP	Battery Pack
BS	Battery Storage
BW	Bandwidth
CB	Capacitor Bank
CC/CV	Constant Current/Constant Voltage
CCF	Capacity Correction Factor
CSP	Concentrating Solar Power
DC	Direct Current
DFIG	Doubly Fed Induction Generator

EKF	Extended Kalman filter
EU	European Union
EV	Electric Vehicle
FC	Fuel Cell
FLC	Fuzzy logic control
GA	Genetic Algorithm
GS	Gain scheduling
GSC	Grid side converter
HAWT	Horizontal Axis Wind Turbine
HE	Hybrid Energy
HES	Hybrid Energy Systems
HEV	Hybrid Electric Vehicle
HRES	Hybrid Renewable Energy System
ICT	Information and Communication Technology
INC	Incremental conductance
LIDAR	Light detection and ranging
Li-ion	Lithium-Ion batteries
LPV	Linear parameter varying
MPC	Model Predictive Control
MPP	Maximum Power Point
MPPT	Maximum Power Point Tracking
NMPC	Nonlinear Model Predictive Control
OC	Open Circuit
P&O	Perturb and Observation
PEV	Plug in electric vehicle
PHEV	Plug in hybrid electric vehicle
PI	Proportional Integral (PI)
PID	Proportional Integral & Derivative
PLL	Phase Lock Loop
PMSG	Permanent Magnet Synchronous Generator
PV/SPV	Solar Photovoltaic
PWM	Pulse Width Modulation
RC	Resistor/Capacitor
RO	Renewable Obligation
RSC	Rotor side converter
SBC	Synchronous buck converter
SCADA	Supervisory control and data acquisition
SEI	Solid-Electrolyte Interphase
SG	Specific gravity (kg/m^3).
SOC	State of Charge
SOD	State of Discharge
SOFC	Solid Oxide Fuel Cell
SPV	Solar Photovoltaic
UAV	Unmanned aerial vehicle
UKF	Unscented Kalman Filter
VAWT	Vertical Axis Wind Turbine
VSC	Voltage Source Converter
WF	Wave form
WT/WTs	Wind Turbine/Wind Turbines

Symbols

x	State vector
x_{k-1}	Previous state
SOC_{init}	Initial state of charge
C_{usable}	Usable battery capacity (Ah or mAh)
T_{cell}	Electrolyte temperature in a battery cell in degree Celsius/or Kelvin
$\hat{x}$	Estimated state vector
T_{amb}	Ambient temperature in degree Celsius/ or in Kelvin
t	discharge/charge time (s)
k	Time step
Δt	Time step or sampling time (s)
i_{bat}	Battery current (A); $i(t)$ and i also denoted as battery current
C_p	Specific heat capacity (J/kgK)
C_p	In chapter-3 this coefficient is identified as the turbine power-coefficient.
C_{Che}	Empirical constant (numerical)
C_{Cha}	Empirical constant (numerical)
N_p	Length of the optimisation window (Prediction horizon)
N_c	Control horizon dictating the number of parameters used to capture the future control trajectory
k_i	Current time (sampling instant)
λ	Conductive heat coefficient (W/m^{2}K)
Φ	Current density A/cm^2
$\bar{u}(k)$	Input vector
$\Delta u(k)$	Input to the state-space model
$\bar{w}(k)$	White noise with zero mean and covariance R_w
q	Number of output states
$x(k_i + m \mid k_i)$	Is the predicted state variable at a time instant ($k_i + m$) and the current plant information $x(k_i)$ at time instant k_i.
$\bar{v}(k)$	Measurement Noise
ΔS	Combined entropy change J/K
ΔS_c	Entropy change in cathode material (J/K)
ΔS_a	Entropy change in anode material (J/K)
V_m	Mean wind speed (m/s)
v_t	Turbulent wind speed (m/s)
v_r	Relative wind speed (m/s)
P_w	Wind power in the absence of a rotor disc (W)
P_r	Power absorbed from the wind to rotor (driveshaft)(W)
P_e	Electrical power of generator from mechanical power (W)
A	State matrix

B	Input matrix
C	Output matrix
D	Feedthrough matrix
F	Faraday constant (1 Farad = 1coulomb/volt)
G	State matrix
H	Input matrix
I	Identity matrix
I	Current (A): this symbol is used to indicate the current from Simulink step input block.
k	Battery constant
K	Kalman gain
P	Covariance matrix
Q	Covariance matrix
Z_1	Impedance of cell1 (ohms)
V_{OC}	Battery open circuit voltage (V)
V_{bat}	Battery terminal voltage (V)
V_{c1}	Cell1 output voltage (V)
$R_{\text{int}S}$	Battery internal resistance (ohms)
R_{CYC}	Battery cyclic resistance (ohms)
R_{TS}	Short transient resistance due to polarization (ohms)
R_{TL}	Long transient resistance (ohms)
C_{TS}	Short transient capacitance of the RC network (F)
C_{TL}	Long transient capacitance of the second RC network (F)
V_1	Voltage across the capacitor C_{TS} measured in volts (V)
V_2	Voltage across the capacitor C_{TL} measured in volts (V)
ΔE	Change in voltage due to active material in the electrode (V)
ΔC_{Che}	Change in Voltage due to battery electrolyte (V)
$R_{self}(T, n, SOC)$	Self-discharge resistance (ohms)
$V_{OC}(SOC)$	Battery open circuit voltage as a function of SOC (V)
V_{OC_sim}	Battery open circuit voltage from simulation results (V)
V_{OC_Exp}	Battery open circuit voltage from experimental results (V)
x_t	Displacement of nacelle (horizontal) (m)
$\dot{m}$	Mass flow of air (kg/s)
N_g	Gear ratio
C_P	Aerodynamic power coefficient (numerical value)
C_T	Aerodynamic torque coefficient
J_r	Moment of inertia of rotor (kg.m^2)
J_g	Moment of inertia of generator (kg.m^2)
K_s	Driveshaft spring constant (Nm/rad)
D_s	Driveshaft damping constant (kgm^2/rad/s)

M_t	Mass of part of tower and nacelle (kg)
K_t	Tower spring constant (Nm/rad)
D_t	Tower damping constant (kgm^2/rad/s)
F_t	Thrust force on tower (N)
T_r	Aerodynamic torque from the wind to rotor (drive-shaft) (N.m)
T_g	Mechanical torque from generator to driveshaft (N.m)
N_g	Gear ratio
N	Number of cells
n	Cyclic number
P_{m}	Mechanical power from driveshaft to generator (W)
R	Rotor blade radius (m)
T	Temperature in degree Celsius or in Kelvin
v	Wind speed (m/s)
α	Heat transfer coefficient for forced cooling or convective heat exchange coefficient W/m^{2}K
β	Pitch angle (˚)
β	Empirical constant (numerical)
Ω	Resistance (ohms)
ε	Radiation coefficient (the emissivity coefficient)
η	Generator efficiency (expressed as a % numerical value)
η	Battery constant
σ	the Stefan- Boltzmann constant (W m^{-2} K^{-4}: generally taken as 5.6703x10^{-8})
ξ	Empirical constant
λ	Empirical number
θ	Collective pitch of rotor blades (◦)
λ	Tip speed ratio (TSR)
ω_r	Angular speed (velocity) of rotor (rad/s)
ω_g	Angular speed (velocity) of generator (rad/s)
ω_n	Natural frequency (of pitch actuator) (rad/s)
ϕ_r	Angular displacement of rotor (radians or written as rad)
ϕ_g	Angular displacement of generator (rad)
ϕ_Δ	Relative angular displacement or torsion of driveshaft (rad)
ς	Damping ratio
ψ_{qr}	Rotor oriented q-axis flux (Wb)
ψ_{ds}	Stator oriented flux (Wb and Flux density is measured in Wb/m^2) (Stator oriented d-axis flux)
ψ_{qs}	Stator oriented q axis flux (Wb)
ψ_{dr}	Rotor oriented d-axis flux
ρ	Mass density of air (kg/m^3)

Chapter 1

Introduction

1.1. Background

It is a well-known fact that fossil fuel resources are depleting very rapidly and renewable energy has been considered as a promising substitute for ever increasing energy demand (Amusat et al., 2016; Eltiganin and Masri, 2015). The conventional fossil fuel (oil, gas and coal) power plants not only emit harmful gasses to the environment but also increase the carbon dioxide level in the atmosphere leading to global warming (Shivarama and Kumar, 2015). Invariably, scientists are exploring effective methods to harness energy from the abundant wind and solar renewables as substitutes to replace fossil fuel driven power plants. The vision has not been for a short term solution but, for a viable sustainability (EU PARLIAMENT DIRECTIVE 2009/28/EC) in the long run to avoid fossil fuels completely before they run out. However, intermittent nature of this renewable energy (the wind and solar) poses several challenges to the engineers and scientists to establish uninterrupted, reliable and continuous power supply. One such problem is the Grid integration of these renewable energy electricity generation systems. Another critical problem is to design energy storage systems using these renewable energy conversion systems to supply reliable uninterrupted power for consumer usage. Amusat et al., (2016) state that energy storage integration is very critical if renewable energy power generation plants are to be incorporated into such systems. Maheshn and Sandhu, (2015) reported that there is always a mismatch between the generated energy and the load demand due to weather and climate changes when using the wind and solar renewables as energy conversion systems. This can either be resolved by using energy storage systems (e.g. battery storage systems) or by mixing the two systems as the wind and solar renewables are complementary in nature.

The other requirement for implementing these renewable energy systems is the application of modern technology and control systems to improve the plant efficiency and reliability. The manufacturing companies, researchers in this area are now concentrating on developing new control systems and advanced switching devices to improve the efficiency and reliability of these wind/solar power plants.

1.2. Modelling and control of WT, SPV arrays and BS systems.

Nowadays, mathematical modelling has become a common tool for dynamic system analysis, optimization, design and control. However, modelling and controlling of these renewable energy conversion systems like wind turbines, solar photovoltaic (SPV) arrays and battery storage (BS) systems poses challenges to the engineers as these systems have nonlinear parameters when presenting equivalent mathematical models.

One such good example is when modelling BS systems, it is necessary to consider the non-linear battery parameters related to electrolytes with the temperature effects. Battery parameters such as internal resistance, battery output voltage, battery capacity, cycle number and state of charge change with the battery electrolyte temperature (Bhide and Shim, 2009; Erdinc et al., 2009). Martinez (2007) states that wind energy conversion systems are very different in nature and, when modelling wind turbines, researchers' main problem is a lack of data and insufficient information on control-system structures due to the strong competition between wind turbine manufacturers. In this scenario many researchers model large capacity wind turbines in a relatively simple form, neglecting some of the essential parameters that could influence the reliability and the stability of the analytical results. Another obstacle that the researchers have to overcome is the different engineering specialisms related to subsystem modelling such as gear changing mechanisms and the gearboxes, wind turbine blades, aerofoil studies, blade element moment theory, doubly fed induction generators (DFIG), power converters, grid integration etc. Modelling SPV systems involves the study of chemistry and power electronics and power converters and their close-loop control strategies.

This thesis is aimed at contributing some engineering specialist knowledge in modelling and simulation of large capacity wind turbines (WTs), SPV arrays and BS systems. It is also aimed at presenting comparative simulation studies of the models with experimental data available in the research archives. Another focus of this thesis is to model each system independently for controller applications, harnessing maximum power while considering the stability. Without presenting any critical reviews at this stage, it is correct to mention with the existing knowledge BS systems play an important role in quality direct current (DC) power supply and in back up energy storage facilities. The investigation into current developments and literature search into battery cell modelling and BP development would further encompass the goal of accomplishing expected substantial contribution to the research community. Also, with the general knowledge gained by reading newspaper articles, industry websites and by reading new product

information published by the manufacturers (e.g. battery cars) it can be stated that lithium-ion (Li-ion) batteries are superior to other battery types. Li-ion battery cell modelling, equivalent electric circuit model concept, simulation and their applications are the other contextual points come under the purview of this research. Significant contributions in this area are expected with new mathematical formulations related to battery packs. The nonlinear behaviour of the battery cell chemistry and how to extend the developed models for similar applications will be explored after critical literature review. Temperature effect on nonlinear battery parameters, modelling and simulations with an equivalent electric circuit model are the other areas considered for specific investigations in this research.

Other important area considered in this research project is the application of model predictive control (MPC) which is an optimal control technique when many parameter constraints are involved with controlling and optimizations. Wind turbine pitch angle control which is famously known as pitching by WT manufacturers is considered for specialism in addition to the BS systems. Eventually, the extensive study will be focussed in harnessing maximum power at any desirable wind speed for WT designs and control techniques. Stall control of the WT and the application of MPC control with the blade pitch angle is the other area that will be explored for new findings and developments in this research. With the above pre-contextual broad guidelines and boundaries specified at the inception, the following sections describe the critical literature review related to BS systems, WT control, MPC control, PV arrays and Power converters.

1.3. Literature Review and recent developments

1.3.1. BS Systems

Numerous battery types and battery cell models have been reported in the literature. Research in new battery technologies has been increasing steadily as the demand for various applications differs from each other. This section presents a literature review on battery cell models, equivalent electrical circuit (EEC) models and BS systems.

Bao (2012) states that there are two types of battery models reported in literature and they are the modified Shepherd type mathematical model and the circuit-oriented battery model. Polarization effect and the use of Peukert's equation has been emphasized in Bao's approach for building an effective mathematical model. The model described in this reference was for

lead-acid batteries and has to be modified if the model is to be used as a generic battery model. In addition, it is further reported that the extracted battery model using regression technique had inconsistent results. Tremblay and Dessaint (2009) had presented a mathematical battery cell model which is ideally similar to the model presented by Bao (2012). In both presentations (where they used the modified Shepherd equation) they had assumed that battery cell temperature does not change due to discharging/charging current and the battery internal resistances have been assumed to be constant during charging/discharging. Tremblay and Dessaint (2009) further identifies that the exponential part of the battery output voltage versus battery capacity curve can be used to represent the lithium-ion battery discharge characteristics. However, it is noted that the portion of the curve is a small percentage of the battery voltage drop with respect to the battery capacity which can be insufficient for simulation studies. Gallo et al., (2013) used the same modified Shepherd equation for their experimental analysis in Pb-acid batteries. However, Gallo et al., (2013) used genetic algorithm (GA) Sequential Quadratic Programming (SQP) to find out an optimal solution for battery parameters. The "Global Optimisation Toolbox" in MATLAB was used to find the optimal solution. The battery model presented by MathWorks Inc., (2013) was based on the model developed by Tremblay and Dessaint (2009). In addition, there are some new features included recently in the MathWorks Inc. model (e.g. battery cell temperature effect, ambient temperature, electrolyte type etc.).

Zoroofi (2008) described that battery models can be classified into five main areas: (i) electrochemical (ii) equivalent electric-circuit (EEC) (iii) dynamic lumped parameters battery model (iv) hydrodynamic, finite element type (v) Tabulated battery data used models. He further states that among these model-types only the electrochemical and the EEC types are widely used for analysis and simulation studies. Electrochemical models extensively use the modified Peukert equation or modified Shepherd Model Equation.

Chen and Rincon-Mora (2006) stated that electrochemical models are mainly used by battery manufacturing companies to optimize the battery design parameters related to battery open-circuit voltage, current, microscopic concentration distribution of the electrolytes etc. They specified that the electrochemical models are complex and computationally time consuming as the models are formulated with coupled time-variant spatial partial differential equations. In addition, Chen and Rincon-Mora (2006) described that, mathematical models do not offer battery current and voltage variation characteristics which are important for circuit simulation and optimization studies. They (Chen and Rincon-Mora, 2016) further highlighted that the EEC

model has become a favorite candidate for modelling and simulation studies due to the intuitive nature and versatility to represent the battery chemistry when all circuit elements are assembled into one circuit. They are accurate enough to capture the non-linear behavior of the battery chemistry using active and passive circuit elements like voltage sources, capacitors and resistors. Finally, Chen and Rincon-Mora (2006) presented two RC networks in series with a resistor and a voltage source to represent the EEC. Two RC networks represent the slow transients and the fast transients of the electrolyte chemistry of the battery cell. Though, the battery self-discharge and the battery life were modelled by a separate RC network, and with a current source, Chen and Rincon-Mora (2006) neglected the slow transient effects and forwarded a reduced order model at a later stage. Zoroofi (2008) presented an RC network with a voltage source and a series resistor. However, Zoroofi's (2008) model used two diodes connected in reverse bias and forward bias method in the RC-loop for battery charging/discharging.

He et al., (2011) emphasized that among the many types of battery models, that the Li-ion EEC model had produced very accurate and repeatable dynamic simulation results. He et al., (2011) used experimental data and the Genetic Algorithm to identify the battery model parameters. Robust extended Kalman filter (REKF) has been used to testify the *SOC* values and for sensitivity analysis of the initial *SOC* values. The improved dual polarization (DP) circuit model which was presented by He et al., (2011) was a Thevenin's model with an extra RC network. Generally, a Thevenin's model has a single RC network in series with a resistor and a voltage source (He et al., 2011). The two capacitor RC model presented by He et al., (2011) was the same mathematical model used by Valerie et al., (2001) at the NREL (NREL/CP-540-28716, USA.) in 2001. Shamsi (2016) presented two RC networks with a series resistor and a voltage source to represent the EEC model. For parameter identification, Shamsi (2016) used a Panasonic NCR 18650B Li-ion battery cell, widely used by many researchers for their experimental studies. Pulse Current Discharge test and continuous discharge tests have been used by Shamsi to identify the battery cell parameters for the EEC model. Shamsi (2016) further described how the two resistors in the RC-network model can contribute to the Faradaic effect, including the charge transfer resistance. Two capacitors were used to model the surface effects at the battery electrodes and the internal chemical kinetics or charge transfer kinetics through the electrolyte of the cell.

Shamsi (2016) and Thanangasundram et al., (2012) used similar types of EEC models and they both used the hybrid pulse power characterization test (HPPC) which is sometimes identified as the pulse current discharge test to identify the battery cell parameters. Shamsi's (2016) battery parameter test results are similar to the test results forwarded by Chen and Rincon-Mora (2006). Erdinc et al., (2009) presented a two RC network battery EEC model which can model the cyclic effect and the capacity fading. The empirical formula presented by Erdinc et al., (2009) for the cyclic resistance varies with the squire root of the cycle number. The cyclic resistance in this model is connected in series with the battery internal resistor. In Erdinc et al., (2009) model, cyclic resistance variation with the temperature is also addressed by presenting an empirical formula.

Gao et al., (2002) presented Thevenin's EEC model for dynamic simulation studies of Li-ion battery cell. The main difference in this EEC model is the inclusion of an additional voltage source to represent the equilibrium potential due to temperature effect. In battery chemistry, the equilibrium potential is defined as a fractional increase of the battery open circuit voltage when charging or discharging process is completed. The amount of active material remained at the electrode-surface can increase the open circuit voltage after some time due to temperature effect or due to ongoing chemical reactions at the electrodes. Furthermore, Gao et al. had presented the thermal energy balance equation applicable to the battery cell and the battery open circuit voltage as a function of the battery current and the cell temperature. However, the detailed analytical approach was not presented there for state of discharge (*SOD*) and battery output voltage in terms of temperature and battery current which were reported as functions of simulation time.

The experimental analysis has shown that the lithium-ion (Li-ion) batteries have extended cycling ability (2000-5000 cycles) than other existing battery types (Wu, Y. 2015). They are lighter than other batteries for a given capacity (battery capacity is a measure of charge stored in a battery under certain conditions and is measured in ampere-hours (Ah)). Li-ion chemistry delivers high open circuit voltage and low self-discharge rate. Opitza et al., (2017) in their review article compared many commercially available battery types such as lead-acid (Pb-acid), Ni-Cd, Ni-MH and Li-ion. Their review further states that Pb-acid batteries are relatively less expensive among automobile battery systems but the manufacturers use toxic materials, as well as Pb-acid batteries, exhibit lowest energy density (energy density in a battery cell is expressed as mAh/g). The volumetric capacity of a battery is also another measure that can be

used to compare how good the battery is. It is a measure of energy stored per unit volume. (for battery cells volumetric capacity is measured in mAh/cm^3). Opitza et al., (2017) reported that Li-ion battery is a good candidate among battery types due to its highest energy density, safety, longer cycle life with no memory effects. Jaguemont et al., (2016) described that though, Li-ion batteries have become one of the best choices for electric vehicles and for many other applications, their performance at very low temperatures has been very poor (e.g. below -20^{0}C). Other major concern reported there was the performance loss and degradation due to cycling and ageing.

Li and Mazzola (2013) presented a battery pack (BP) modelling approach considering only the external measurements and the characteristics of a battery module (battery module is identified as more than two cells connected either in series or in parallel. BP comprises battery modules connected in series/parallel). Though, it is too early to analyse the literature regarding BP modelling, the method reported by Li and Mazzola (2013) is discussed here, as their model is a mixture of both BP and battery cell modelling. Their BP modelling technique is based on the bandwidth experimentation for the BPs. The BP is modelled into two RC networks connected in series with a series resistor and a voltage source similar to the battery cell model given by Chen and Rincon-Mora (2006). The two RC networks BP model parameters were estimated using sequential quadratic programming technique. Popular Panasonic CGR18650, 3.6V (nominal voltage) standard capacity of 2450 mAh Li-ion battery cells were used by Li and Mazzola (2016) also for the experimental analysis.

Makinejad et al., (2015) emphasised that battery internal resistance varies due to cycling, ambient temperature, *SOC* and ageing. A series resistor connected with a single RC network was presented as their EEC model. Mean square error minimization method was used to investigate the battery cell parameters after initial calculations were performed in off line mode. The experimental analysis shows that the battery internal resistance, open-circuit voltage changes due to cycling and *SOC*. The results conform to the previous literature presented by Erdinc et al., (2009) and Chen and Rincon-Mora (2006). Makinejad et al., (2015) concluded that in large format of Li-ion batteries the battery internal cell temperature varies locally. The temperature changes and the concentration gradients near the electrodes can change the battery internal resistance and the cyclic resistance. The temperature gradients can be in the range of 0.2-0.9^{0}C within the electrolyte. Though they have presented experimental data for cycling versus open circuit voltage, battery capacity etc. analytical presentations or empirical

formulations were not given for further analysis. In contrast, Li and Mazzola (2016) concluded that their BP model is an accurate model (with two RC networks) while ignoring cycling, temperature, ageing and lithium plating effects on individual cells. Hence the battery pack model presented by Li and Mazzola (2016) should be modified in order to use for repeatable cycling, aging, variable temperature and variable current.

Smith (2006) reported that computational fluid dynamics (CFD)-type model validates the low order battery models and estimation algorithms. He further states that CFD type model validation is useful, as it is not physically possible to measure concentration/potential distributions inside a battery and thus directly validate the estimates. Smith has not described any EEC models though he had presented an exhaustive mathematical analysis on model reduction techniques.

Xiong et al., (2011) presented a Li-ion battery model which is suitable for electric vehicles with 32V and battery capacity of 12Ah. They have combined a single *RC* network and a series resistor with an open circuit voltage source which is modelled by Nernst equation. The Nernst equation models the electrochemical characteristics and the polarization effects. According to Xiong et al., (2011) the model parameter values identified have been considered as constants, though they are functions of the temperature (measured in degree Kelvin) when actual Nernst equation is applied to battery chemistry.

Literature review in this section briefly covers the areas in the application of thermal energy balance equation, heat generation mechanism in the battery cell (application of Bernardhi equation).

Makinejad et al., (2015) presented the heat generation mechanism in a battery cell in two scenarios: irreversible Joule heating and the reversible heating. Irreversible Joule heating is the summation of heat dissipated by each resistor. Mathematical relationships for the reversible heating, application of thermal energy balance equation were presented in this article and the thermal model was studied using MATLAB and COMSOL. Battery internal cell temperature was observed by placing sensors. The generated heat in the battery cell is transferred by conduction, convection and radiation. In their research article, it was assumed that the amount of heat flow absorbed by conduction effect is taken as equivalent to the heat absorbed by convection.

Xiao and Choe (2013) presented the irreversible heat generation with two methods: one method assumes the voltage difference between the open circuit voltage and terminal voltage includes a sum of all voltage drops caused by electron and ion transport and chemical reactions; which is simply expressed by the product of battery current multiplied by the difference between the battery open circuit voltage and the battery output voltage. The battery open circuit voltage is taken as a function of *SOC*. The mathematical formulation derived there is based on two terms which are identified as heat dissipation by reaction kinetics and the ohmic heating. Both reaction kinetics and the ohmic heating expressions were derived using electrochemical formulations. In this research, they have taken that the reversible heat releases at discharging is absorbed in when charging. Cho et al., (2014) used modified Butler-Volmer equation to model the battery electrode current density in terms of electrode potential considering the cathodic and anodic reactions separately. The current density changes with time especially when the battery is discharging. This equation gives the detailed relationship of initial battery cell current density, dynamic current density, the electrode potential and the equilibrium potential at each electrode. Therefore, it is noted that the current density approach is an accurate method of modelling when lithium plating and cycling is considered.

Viswanthan et al., (2010) reported that $LiFePO_4$ based cells with either titanate or graphite anodes can be used for thermal energy management of BP with cycling. The cycling process according to battery chemistry, there is a cooling effect at the cathodes and while at discharge there is a heat generation. Hence, for battery management systems, this pro-activity can limit the charge-discharge currents to prevent the temperature effect increasing beyond predetermined value. Sarre et al., (2004) reported the stability phenomena caused due to passivation layer built at the electrode/electrolyte interface due to electrolyte reduction by lithium. The other issue considered here was the growth caused by electron tunnelling through the layer is irreversibly consuming lithium self- inhibiting due to thickness increase. This can cause the battery to collapse due to extensive cycling.

The application of Nernst equation for low temperature phenomena with battery cell charging and discharging is reported by Jaguemont et al., (2016). One dimensional energy balance equation, applied to battery cell models, and the cycle aging dynamics are covered in the review. Kroeze and Krein (2008) presented a three RC network EEC model that can be used in different applications. The model presented was capable of predicting the characteristics of battery current versus voltage and was ideally suitable for portable electronics and

recommended not accurate for the transient response to short-duration loads (less than 1 second). Conductive and convective heat transfer models were given by Tan et al., (2011) with the SIMULINK model. The experimental results had been obtained using with Panasonic CGR17500 and Panasonic 4.2V, CGR18650 batteries. Model equations presented were based on modified Tremblay and Dessaint (2009) model. Huria et al., (2012) described a multi-RC network model which was identified as a complex model with computationally time consuming. However, it was finally reduced to a single RC network, in series with a battery internal resistance with a voltage source. Modified thermal energy balance equation had been presented in the article, ignoring the Joule heating, reversible heating, conduction and convective, radiation energy components. Finally, he had concluded that in a battery pack, cells are generally combined into cell packs, whose thermal parameters are different from those of single isolated cells.

Saiju et al., (2008) had presented an EEC battery model for Pb-acid batteries. Their model comprised two RC networks, series resistor, a voltage source and a variable resistor connected in parallel with the battery output voltage. The model is a combination of the EEC model components with some SIMULINK blocks that represent the mathematical formulations of the electrolyte behaviour. The specific gravity of the battery electrolyte was monitored during charging/discharging process. During the charging and discharging the gas emitted by the electrodes were taken into account to formulate mathematical relationships with the battery current. However, battery open circuit voltage variation, battery output voltage variation versus time characteristic curves did not show conclusive results with the manufacturer's data. A simple but comprehensive lead-acid battery model for hybrid system simulation was reported by Ross (2011). Modified Shepherd equation, an empirical formula for battery open circuit voltage versus electrolyte specific gravity (SG) variation characteristic curves were presented. It was further noted that the experimental and simulation data presented by Ross was similar to the battery manufacturer's data.

During the recent past, many researchers have published various *SOC* estimation methods suitable for many applications. Chang (2013) describes that accurate estimation of battery state of charge (*SOC*) is a very complex and difficult process as there are many parametric uncertainties due to limited availability of accurate models. The *SOC* is defined as the ratio of current capacity to the nominal capacity. Mathematical methods of *SOC* estimation found in Chang's (2013) publication are: Open circuit voltage method, Terminal voltage method,

Impedance method, Impedance Spectroscopy method, Modified Coulomb Counting method, Neural network, Kalman Filter (KF), Coulomb counting, KF Combination method and the Support Vector Machine method. Chang, further reported that Qmax Adaptation Algorithm (which is a new computational algorithm) will substantially increase the *SOC* and the remaining run time estimation accuracy. When compared both Coulomb counting method and the modified Coulomb counting method, the only difference found there was the use of a quadratic discharging current equation which is a function of charging/discharging time. According to Chang (2013) the Support Vector Machine method (SVM) is an adaptive system similar to KF, Fuzzy neural network method. The SVM method is suitable for highly non-linear systems and is based on least-square estimation.

Pandey and Bansal (2012) presented two battery cell models (model one and model two) involving thermal effects. In model one, the *SOC* variation with the battery internal cell temperature, battery current, voltage gradient with cell temperature was reported. In model two, modified mathematical formulations were presented and these were based on the Arrhenius equation and Nernst equation.

An adaptive *SOC* estimation method based on unscented Kalman filter (UKF) algorithms for lithium-ion batteries was published by He et al., (2013). The state-space parameter vectors A and B had calculated off line by using the least-square method. Simulation results proved that the application of UKF was more accurate than the extended Kalman filter (EKF). Han et al., (2009) presented an adaptive EKF based *SOC* estimation method for Pb-acid batteries.

Zhang et al., (2009) reported a combined experimental and Extended Kalman Filter (EKF) recursive method to identify the battery parameters. Similar to the improved dual polarization battery model presented by He et al., (2011), Zhang's (2009) model comprised two RC-networks. In addition, Zhang's model had included the hysteresis effect and the equilibrium potential. Zhang (2009) has assumed that the equilibrium potential is equal to battery open-circuit voltage having given the battery to settle for one hour to observe final measurements during experimentation. Zhang (2009) has not included the equilibrium potential variation due to film, gas formation at the electrodes and the ambient temperature effects for more than one hour.

When using KF for the *SOC* estimation or any other measurement estimation of nonlinear parameters, the process covariance and measurement noise matrices are pre-determined

(guessed values). If the guessed values are incorrect, then there will be large divergent estimation errors. The other method of correcting large guessed-errors is to employ the adaptive Kalman filter which uses the covariance matching method (e.g. Han et al., 2011). Lee et al., (2007) presented a reduced order EKF method to estimate the *SOC*. They (Lee et al.) suggested that by reducing the order of the EKF (reducing the number of RC networks to one) could maximise the computational efficiency. Furthermore, it can reduce the calculation time which is very useful for the *SOC* estimation in hybrid electric vehicle application. Pérez et al., (2015) reported an enhanced closed-loop *SOC* estimator for lithium-ion batteries based on EKF. The speciality with this model is the inclusion of the hysteresis effect and the model had been validated by using several current profiles. Nonlinear observer was used for the *SOC* estimation by Xia et al., (2015). The function of the nonlinear observer is to verify the validity of the proposed parameter identification method in the *SOC* estimation. Second order RC network (two RC networks) had been used for the experimentation. The nonlinear least square algorithm was used to evaluate the model parameters from collected data with the discharge and rest processes.

BP model reported by Li and Mazzola (2013) was described briefly earlier in this review. Ganesan et al., (2016) presented a reconfigurable BP model. Ganesan et al., (2016) not only presented an electrochemical mathematical model but also presented an anode degradation and capacity fading equations relating current density and the effective electrolyte conductivity through the

formation of a solid-electrolyte interphase (SEI) layer. The definition of SEI layer can be described when capacity fade occurs when cycle number exceeds thousands of cycles, electrochemical processes are obstructed by the formation of a SEI in the negative electrode, which compete with reversible lithium intercalation. The thermal model presented there was based on the Bernardhi equation. Bruen and Marco (2016) presented a BP model in which cells are connected in parallel. The state-space model which was representing a single cell was taken as a building block to make the total state-space model according to the number of single cells.

Summary

Having analysed relevant literature, it can be concluded that the battery models with two RC networks (e.g. He et al., 2011; Zhang et al., 2009) are popular among researchers as they can offer sufficient accuracy with less computational burden. Among the battery types, it was noted

that Li-ion batteries are promising candidates for further developments. Though, there are several modelling methods available in literature, most models are application oriented but, EEC models offered sufficient accuracy (within 1-2% error) and the flexibility to combine into similar electric models for different analysis (Erdinc et al., 2009; Zhang et al., 2007 etc.)

It is further noted that the battery parameter variation due to ambient temperature and the Joule heating effect has been neglected by many researchers in battery modelling. Among the battery cell models in literature, only a few papers had addressed the temperature effect and the application of Bernardhi thermal energy balance equation with the use of EEC model approach. Application of the Bernardhi thermal energy balance equation for battery cell modelling will also be focussed in this thesis.

BP modelling and design is the other emerging area where many researchers are still trying to develop efficient, reliable energy storage systems. Having developed the battery cell model, an extension of the circuit into a BP model will also be considered in this thesis. Battery models presented by Saiju et al., (2008) and Ross (2013) will be revisited to analyse the validation as the simulation results with Saiju et al., (2008) model was not in consonance with the Manufacturer's data for Pb-acid batteries. The *SOC* estimation has become an important battery parameter for electric and hybrid electric vehicles as it is not possible to measure it directly. State-space battery model presentation and the application of the EKF based *SOC* estimation will also be examined and described in the thesis to add value to the research work.

1.3.2. Solar PV Arrays

Electricity generation using solar photovoltaic systems poses a unique challenge to improve the efficiency while minimising the manufacturing cost. Research and development in this area have been expanding as it is environmentally friendly and helping the planet to reduce the greenhouse gases by reducing the carbon footprint. Thus, PV electrical power generation systems have become more popular in sustainable energy research (Brever et al., 2015). A Large number of research papers have already been published related to PV systems spanning in the areas of solar power technology, economic aspects of solar power utilisation, dynamic modelling of PV systems, maximum power point tracking (MPPT) systems, Grid integration of PV systems, optimisation algorithms (Elmetennani et al., 2016). Research and development are wide open to many in these areas as they are linked together to improve the applications of renewable energy sources (Bhatnagar & Nema, 2013). However, within the boundaries of this study, articles published in the areas of PV technology, dynamic modelling in solar systems

related to MPPT and distributed grid integration with other renewables like wind, battery storage systems have been considered.

The PV technology for grid connection and off-grid PV power plants has been reported by Arsalan et al., (2016). In their publication, major emphasis was given to PV and concentrated solar power (CSP) technologies. CSP technologies use mirrors and lenses to concentrate solar power from a large catchment area and then it is projected in a form of a beam to convert the solar energy to heat energy and electrical energy. Advantages of CSP technology versus PV are also discussed by Arsalan et al., (2016). Recent advances in solar photovoltaic systems for emerging trends and their advanced applications have been presented by Pandey et al., (2016). Building integrated PV systems (Including outer brick walls), Concentrated PV plants, PV heat energy generating plants, and PV desalinization plants are some of the applications reported there.

Thin film solar cell manufacturing technology and how to minimise the manufacturing cost was presented by Breeze (2008). The materials used for solar photovoltaic cell manufacture and their efficiency have been reported in the articles published by Sankarganesh et al., (2012) and in Tsang et al. (2013). Various internet sources could be found regarding microelectronic manufacturing sector with the introduction of multi-junction PV cells and how these cells made an impact to increase the efficiency of the solar array from 20% to 43.5% (Solar cell efficiency, 2013). However, Heriche at al., (2016) reported that, as at today, copper-indium-gallium-diselenide (CIGS) cells offer maximum conversion efficiency of 25.9%. The chemistry behind the achievement is different doping techniques of certain chemicals and absorbing layers.

MPPT systems using perturb and observation (P&O), hill climbing, evolutionary algorithms were presented by Kamarzaman and Tan (2014). When environmental and shading conditions change, application of conventional MPPT methods using P&O and genetic algorithms fail due to rapid change of physical conditions and hence, neural network methods were proposed in their research.

Sankarganesh and Thangavel (2012) implemented P&O MPPT system and Fuzzy control mechanism to control the output power. Bhatnagar and Nema (2013) introduced a comparison of computational algorithms in tracking maximum power while evaluating the parameters. The parameters considered are the number of variables used in each algorithm, accuracy, the speed of tracking the maximum power point (MPP), hardware implementation, cost, tracking

efficiency. P&O algorithm, modified P&O algorithm, Incremental conductance (INC) method, Fuzzy logic control (FLC) based, artificial neural network (ANN) methods, Gradient descent methods were analysed in addition to a single diode equivalent electrical circuit used for modelling a PV cell.

In addition, Bhatnagar and Nema (2013) described that though, P&O and INC methods are widely used in the industry they have their advantages as well as disadvantages. The P&O technique has the problem of oscillation around the MPP due to the trial and error computational search method. Hence, a fair amount of absorbed power from the sunlight may be wasted by trying to achieve the best for a shorter time of the day due to variable sunlight. This problem can be reduced by using variable step size with the INC. The computational algorithms described above are generally applied to non-linear $I-V$ characteristic curves of the solar panel. When the search is based on the voltage versus-time curve then it is defined as the voltage based MPPT and when the algorithm is based on searching the MPP on the current versus time curve then it is defined as the current based MPPT. In both methods, they use DC/DC buck or boost converters to step down or step up the voltage. Other two methods used to track the MPP are: curve fitting based MPPT and the numerical calculation methods.

It was noted that altogether they have reported more than thirty online and offline computational algorithms used in practise for tracking the MPP with a PV array. Each method has its advantages and disadvantages depending on the applications. Bhatnagar & Nema (2013) finally concluded that the P&O and INC cannot calculate the MMP in one step as they are iterative based algorithms and therefore, they are slow. FLC, ANN and particle swarm optimization methods are good for when the inputs are not accurate and when the accurate mathematical models are not available. They further concluded that the MPPT based on load parameters method is better than the conventional methods.

Model-based rapid MPPT system for solar power extraction from a PV array was presented by Tsang and Chan (2013) and by Meenakshi et al., (2006). Orthogonal least squares estimation algorithm had been used with the experimental data to evaluate the parametric constants. MPPT system using MATLAB as a programming tool was presented by Qin and Lu (2012). An adaptive P&O algorithm was implemented for fast tracking by regulating the output voltage after measuring the changes of output power. The single diode equivalent electrical circuit PV cell model has been used in modelling the PV system. In order to improve the output efficiency of PV system, a novel variable step size P&O method was emphasized by Qin and Lu to track

the maximum power point of PV system. Grid connected PV system has been presented by Chouder et al., (2013). The single diode PV cell model is extended into an array and the system has been simulated using Lab-View. PV power generation system with a battery backup system was presented by Ding et al., (2012). Their PV array was connected to a common DC bus by a boost converter and the battery pack was then connected with a bi-directional DC/DC converter. Finally, the converter power was connected to the AC grid by a common DC/AC inverter. Hybrid Solar-WT system was presented by Meenakshi et al., (2006) to accommodate the varying wind velocities and solar intensities. A neuro controller has been presented to identify the MPP. A mathematical model for a single diode PV system has been presented by Pandiarajan et al., (2011). SIMULINK has been used as a tool to analyse the system. PV/FC/UC hybrid system was presented by Uzunoglu et al., (2009) with MPPT system for solar energy harvesting. Two diodes equivalent electrical circuit model was reported by Belhaouas et al., (2016) and Ishaque et al., (2011).

In literature for most applications and for modelling PV cell, current-voltage relationship derived for single diode has been used. In other publications found in literature, same current-voltage relationship derived for single diode has been used with minor modifications. Approximate empirical formulations were presented for the generated power estimation by Hocaoglu et al., (2009) and Mohammadi et al., (2012). PV arrays connected in series and parallel were modelled by Tsai et al., (2008). It was further emphasized that two diodes EEC model was not used in their research as there were some computing limitations to develop expressions for the voltage-current curve parameters due to implicit and nonlinear nature of the model.

Generally, the mathematical models for two diodes EECs are complex in nature and the programmes frequently get into loops due to decoupled exponential functions. Hence, many researchers have used the single diode equivalent electrical circuits for modelling PV systems where the accuracy is sufficient to be compared with two diode model. Therefore, in this thesis, a single diode model has been used to model PV systems.

1.3.3. Wind Turbines Control

The production of clean electricity from renewable energy sources (the wind, solar, geothermal etc.) has been promoted by many countries to tackle the current problem of green-house gases and to reduce the dependence on fossil fuels. Wind energy is now gradually becoming one of the most cost effective energy sources that can be converted into electricity. In the energy transformation process, wind turbines (WTs) are initially used to harness mechanical energy and then convert the mechanical energy, into electrical energy. Inherently, dynamics of the WTs are nonlinear in nature and complex control procedures are needed for maximising energy production while protecting the wind turbine (WT) components. In this section, a brief review of advanced control methods on wind turbines is presented.

Aho et al., (2012) emphasized that WT control can be categorised into four main areas according to wind regions (wind speeds). They are Region-1, Region-2, Region-3 and Region-4. The Region-1 spans from start-up of the WT to the 'cut-in' wind speed where the generator is turned on to produce electricity. Region-2 is defined as sub-region when the wind speed is between cut-in speed and just below the speed where the wind speed is still insufficient to produce maximum power. Region-3 is defined as the region where the wind speeds are high enough to generate its rated power. At this region, the generator is controlled to regulate speed and the power. The last region which is the Region-4, in which the turbine shuts down to prevent damage. In the transition, the main aim is to capture the maximum available power from the wind and it is harvested by controlling, blade pitch angle, turbine coefficient and the tip speed ratio (TSR).

The blade pitch control is generally achieved by using proportional integral (PI) control. The PI control system is designed to overcome the anti-wind up of saturation limits placed on the pitch angle (Leith and Leithead, 1998). For optimum control of the blades, gain scheduling (GS) is often used to adjust the PI gains with the pitch angle. Furthermore, GS will address the nonlinear sensitivity of the turbine coefficient (C_P) curve to blade pitch angle (Aho et al., 2012). According to Leith and Leithead (2000), gain-scheduling design is described as divide-and-conquer approach to nonlinear control systems to decompose into a number of linear sub-tasks. Further, they have applied Lyapunov stability condition for velocity based linearization.

Cut-in speed and Cut-out speed are two commonly used technical terms in wind turbine industry. The definition is as follows; 'Cut-in' speed: minimum wind speed necessary for the

wind turbine to generate power (generally between 3-4 metres per second. 'Cut-out' speed: maximum wind speed that the generator can operate safely. Beyond this speed, it is hazardous to operate the generator.

Wake power, frequency regulation, active power control (APC) are the other areas addressed by Aho et al., (2012). Hydraulic and DC motor actuators are used to control pitch angle and the generator torque at reference levels. They further concluded that the researchers are still investigating the strategies to balance aggressive power control demands against increased actuator usage and structural loads.

Njiri and Soffker (2016) emphasized that WT control system hierarchy has three distinct levels; namely, supervisory control, operational control, and subsystem control. They further reported that the supervisory control manages the starting-up and shutting-down procedures while operational control is concerned with the smooth functioning of the WT during its running. The subsystem control deals with the pitching, yawing, actuation mechanisms and power electronics. As pointed out by Njiri and Soffkor, (2016) though, $H_2$and H_∞controllers extensively used for WT control, they are more suitable for robust tracking systems such as disturbance rejection and noise suppression.

The review article presented by Wei et al., (2014) emphasized that GS can be applied to any control system from process engineering to aerospace engineering. Some of the examples reported there: gain-scheduled proportional-integral derivative (PID) control, H_2, H_∞ and mixed H_2/H_∞ gain-scheduling methods as well as fuzzy gain-scheduling techniques (Leigth et al., 2001).

Multi-objective and model predictive approach controllers were implemented by Kusiak et al., (2010). The method deploys an intelligent WT control system based on data mining, model predictive control, and evolutionary computation. To improve the quality of the controller, a multi-objective model was presented. Multi-objective model is nothing other than adjusting weights of objective control/operational parameters (in Kusiak et al., 2010) model five objective weights) in response to the variable wind conditions. In their design, three control factors, wind speed, turbulence intensity, and electricity demand had been considered in eight computational scenarios. Genetic algorithm was used to calculate the optimal weighing matrices of the LQG controller instead of using trial and error based Kalman filter gain and state feedback gain estimation. The speciality with this application is the use of supervisory

control and data acquisition (SCADA) to build the model whereas in the literature most dynamic models are derived from first principles.

Application of GS technique for Linear parameter varying (LPV) systems was presented by Bianchi et al., (2005). GS is particularly useful for WT control as the approach consists in designing linear controllers for several operating points and then applying an interpolation strategy to obtain the global control. Though, there were numerous applications for WT controllers in nineteen-nineties, the method did not give systematic design procedures. Though, the application of linear controllers by interpolating them to reach global control seems to be favourable to handle all four wind regions, the method was not given extra publicity and exposure by the manufacturers due to trade secrets. When applying the state-space method, a similar method is followed, but the linearization is performed using Taylor series expansion (see for example Larsen and Mogensen, 2006). The local controllers in the GS method use the H_∞ optimal control tools due to multi-input multi-output nature of the parameters. Hence, the predictive concept applied to model predictive controllers (MPC) can be considered as an evolution from GS techniques. In GS, the Jacobian Matrix with the Euler equation are used for linearization. In MPC Euler-Lagrange equations are used. In order to be able to perform control in the whole spectrum of wind speeds, gain scheduling and MPC methods were applied by Gosk (2010). In addition, the application of GS technique in frequency domain is a proven method offering successful results when the pitch and torque actuators are subject to frequent damping effects (Bianchi et al., 2005). GS can be applied to EKF to reduce the conceptual burden in calculating the Kalman gain in every iteration (Horkheimer, 2012).

Leith and Leithead (2002) reported a novel nonlinear gain-scheduling control technique for power regulation of a horizontal-axis grid-connected up-wind constant-speed pitch-regulated wind turbine. An interesting point to note here is that the plant dynamics has been considered adequately nonlinear and then transformed into linear systems while control objectives remaining nonlinear. Multivariable control strategy for variable speed, variable pitch wind turbine had been proposed by Boukhezzar et al., (2007). In this research, the nonlinear state feedback torque control strategy is combined with a linear controller to control the blade pitch angle. The proposed system has been identified as a better system than using a PID and LQG controllers.

Robust MPC controller for a wind turbine was reported by Mirzaei et al., (2012). The approach was defined as a minimax robust MPC approach. When the wind speed is below the rated value the WT is operating at MPPT mode and when the wind speed is above rated value then the WT is controlled by regulating the output power. Blade element momentum theory is used to model the power extracted from the WT blades and the EKF with Taylor series were used to estimate the operating points.

Controlling the generator side plays an important role for stable power supply and maximum power extraction from the WT at variable wind speeds. Most of the methods described so far belong to the rotor side control or control systems related to the turbine blades. With the blade side and the rotor side control (RSC) the power regulation, is achieved using State-feedback torque control, blade pitch control, and with the generator speed control methodology. MPPT with the wind speed, controlling the pitch, TSR, optimal torque extraction, output power control are some of the control problems encountered in this section. Controlling these parameters use the 'priori' knowledge of the optimum turbine coefficient. However, a perfect estimate cannot be achieved using analytical or experimental methods. In majority of MPPT algorithms, the pitch angle is kept constant and the $C_P$is slowly determined by TSR.

Indirect strategy for the active and reactive power control for the rotor side of the WT using a sliding mode controller was implemented by Cherfia et al., (2013). The dq-axis reference frame was used to model the DFIG. Control of the rotor side converter, which is used to regulate the active and reactive power exchange between the generator and the grid, is applied by indirect decoupled control without falling into a power loop. In contrast, modified direct power control (DPC) method to control active and reactive power was used by Jeong et al., (2008) without using any d-q axis transformation. Jeong, et al., (2008) used the voltage vectors from a look-up table to calculate the active and reactive power. Chen and Chen, P-H. (2014) used bidirectional AC/DC converter which could work in rectifier mode and inverter mode to control the active and reactive power of the DFIG.

Though, the performance improvement can be achieved by using fixed gain control methods, some of the control techniques utilized to improve the maximum power lead to other analytical and estimation problems. Some of them are: to calculate the TSR, wind speed is taken as an input, however, it is difficult to accurately calculate the wind speed from direct measurements. The P&O method does not need prior knowledge of the maximum power coefficient as it uses

the hill climbing method to locate the optimum point from the turbine characteristic curves. It was noted that P&O algorithm will also fail when there is a rapid variation of the wind speed. In contrast, sliding mode control and extremum seeking control techniques take considerably high computer iteration time to converge. Though, the system offered good reference tracking, chatter in the gearbox was inevitable. To overcome these problems to achieve the optimal control of torque and flux tracking, nonlinear sliding mode controller has been proposed at the expense of zero error tracking (Njiri et al., 2016). They further state that it is not possible to achieve both the efficiency and the reliability together for large WTs, as the two are conflicting in nature. The fatigue and stresses of large WTs are due to excessive up or down movement to adjust the reference of the pitch angle or demanded torque.

Schlipf et al., (2014) presented a comparison details of a linear and a commercial nonlinear MPC to a baseline controller. They further reported that the nonlinear model predictive controller achieved better results than the linear controller. Light detection and ranging (LIDAR) remote sensing technique was used to obtain accurate wind field data as input parameters ahead of time. Actually, LIDAR technology has been in existence since 1970s, but due to extensive cost of the equipment, the technology extension was hampered. This sensor measures the upwind speed before it interacts with the turbine, and hence turbine has sufficient time to self-control with the necessary actuators to face the incoming wind. LIDAR was used in advance to set the pitch angle and the generator torque. In contrast, Pao and Johnson (2009) emphasized that new LIDAR systems based on solid-state sources and off-the-shelf telecommunications equipment allow for inexpensive deployment, modularity, and improved reliability. Furthermore, they described that turbines are built for variable pitch angles at different radial positions along the blades relative to the standard blade twist angle.

Wind turbine model predictive speed controller based on identified piecewise affine discrete-time state space model was reported by Hure (2016). The main advantage over the other controllers has been emphasized as the predictive property and explicit integration of the constraints in the control problem. The performance had been compared with a baseline line controller through simulations for both below and above the nominal. Morari and Lee (1999) presented an MPC review article on: past, present and future. The main intention of the article was to present an overview of the origins of MPC and its glorious developments up to the year 1999.

The DFIG with slip-rings, whose stator windings are directly connected to the grid and its rotor winding are also connected to the grid through a bidirectional frequency converter using a back-to-back pulse width modulation technique is modelled by Martinez (2007). Okoro (2003) presented a complete dynamic model for induction machine which could be applicable for the WT modelling with the d-q axis transformation theory and Park transformation matrix. Though the model presented was for a motor, the same methodology could be used by changing the slip for negative values to apply for DFIG modelling. Ekanayake et al., (2003) presented state-space modelling of variable -speed wind turbine. Their systematic approach in state space modelling included 'current model', 'fluxes model' and 'rotor internal voltages and stator currents model'. In each method, the state vector is defined as the dq-axis current states, fluxes or fluxes with voltages. Ekanayake et al., (2009) used PI controllers to control the variable voltage/current changes and Okoro (2003) presented an algorithm to control the flux saturation effect.

Novak and Chalupa (2013) published a multiple MPC controller for WT control. The applied method was especially favourable since it was applicable for some of the states which were not measurable. The EKF was used to estimate the effective wind speed. The estimated states and active model parameters were then used within predictive control strategy for computation of control signals. A nonlinear model predictive control system was developed by Slegers et al. (2006), to control unmanned air vehicles (UAV). The system designed had six degrees of freedom. Unlike in the previous controllers in this system, the number of Taylor series expansion terms was used to indirectly penalize the control action.

Summary

Concluding the critical review in this section, it was noted that though, the development of GS started in 20 years ago, it did not spread into every possible system in engineering. Some of them might have confined into WT control and self-guided or autopilot control systems. On the other hand, manufacturing companies did not want to expose the detailed methodologies due to trade secrets or competition (e.g. guided missiles; Wu et al., 2002). Based on the number of research articles published recently, in the Journal of power sources, IEEE, and other reputed control journals, the GS method seems to be gradually picking up with some practical applications. However, not as fast as MPC control systems which at the moment are becoming very popular among the emerging researchers. An another reason that can be pointed out is the similarity of the linearization procedures at an equilibrium point and the MPC designs are

modelled by using favourite state-space methods (of course, this statement doesn't imply that MPC systems are confined only to state-space models, but, MPC controllers are well applicable to plants in frequency domain as well). With the state-space systems, there is a flexibility to expand the systems into many different state-space models to build a total linearized model if the subsystem dynamics are well modelled. In addition, the MPC Toolbox in Simulink allows one to program and manipulate MPC controllers as MATLAB objects (though, MATLAB is an another tool) through a variety of methods and functions for simulation, analysis, and tuning. The linear MPC controllers can be embedded arbitrarily in complex MATLAB programs, with maximum versatility (Bemporad, 2006). Rotondo (2016) reported the current advances in gain-scheduling and fault tolerant control techniques. Rotondo (2016) was mainly focussed in the area of gain-scheduling, and analysis of the connections between the linear parameter varying (LPV) and Takagi-Sugeno (TS) paradigms.

Considering the literature boundaries and the time limit for this research, though, GS is also a promising area, the application of MPC in WT control is mainly focussed in this research.

1.3.4. Hybrid Renewable Energy Systems

Literature review presented so far considered BS systems (or battery cell models), PV arrays and WT control separately. All of these systems together can play an important role in electricity generation as they are complementary in nature. Therefore, it is pertinent to describe such combined renewable energy systems which are normally identified as hybrid renewable energy systems (HRES). For hybrid system applications it is important to understand dynamic modelling and simulation characteristics of WT, PV and BS systems independently. A brief review on HRES is given in this section as most of the systems found in literature, elaborated on WT/PV/BS systems.

In future, the demand for stand-alone micro-grids using PV arrays combined with wind turbine generators/Fuel cells and BS systems will increase as they are sustainable and environmentally friendly (Wang et al., 2008). Intermittent nature of these renewables can be addressed with innovative control systems and switch power from wind energy to solar or solar to wind energy or by utilising BS systems. The micro-hybrid system designed by Wang et al. could provide adequate power for five households. They further emphasized that the output power was kept constant when the wind speed is higher than the rated wind velocity even though the wind turbine has the potential to produce more power. The pitch angle was controlled to protect the electrical system and to prevent over speeding of the rotor. When the wind speed was higher

than the ‘cut-out’ speed (25 m/s), the WT was shut down for operation due to safety reasons. Though, the wind energy and solar power are essentially discontinuous, harnessing and supply energy from them and marine current has become one of the most exciting emerging forms of renewable energy. Unlike many other forms of renewable energy, marine currents produce a consistent source of kinetic energy caused by regular tidal cycles influenced by the phases of the moon. However, energy harvest from tidal cycles is also not without problems as there are challenges due to the random power output variation. This can be alleviated through conditional outputs and phasing between different locations. The scarcity of proper geographical locations for tidal power generation (Commin et al., 2017) is another challenge that the designers have to overcome.

Grid integration and electricity supply from renewable energy sources have been facing a number of challenges. Especially, WT integration to the grid is a major challenge for power companies: in particular, to ensure the power balance, security of safe maintenance, computer-based remote control, automation systems development, smart metering, reactive power control, frequency control, voltage variation, harmonics and PLL control (Martinez and Aurelio, 2010). The unified state-space model (assembled for WT, BS, PV array and induction generator) presented by Martinez and Aurelio, can work both under transient and steady-state conditions. The model reported is presented with a complete schematic diagram of each subsystem of WT, PV arrays, BS system, inverters, and the Generator unit.

The application of proportional integral (PI) and proportional integral and derivative (PID) controllers has been reported in many research articles in hybrid renewable energy systems. Application of PI controller programmed with P&O optimisation algorithm was published by Kabalci (2013). In Kabalci’s research, the MPPT algorithm was used in the control step of the converter which was developed using P&O algorithm with an extended PI controller. In most of these hybrid systems, solar and the wind energy systems were widely used and they were modelled separately and assembled together to build a distributed generation system.

Dali (2010) presented a technical description of hybrid system devices and of the inverter energy management system. Dali’s experimental set up included a grid connected hybrid system, the wind and photovoltaic (PV) physical emulators, battery energy storage, load and a controlled interconnection to the Low Voltage (LV) grid. Wind turbine emulator with a permanent magnet synchronous generator (PMSG) has been used for experimental work. The PMSGs do not have the problem of cogging torque and robustness. DFIGs are generally used

for higher capacities of power generation in the Mega-Watt range. Unlike in Kabalci's (2013) research article, Dali's research paper had not included simulation results to compare with the experimental results.

Jitendra et al., (2012) proposed a hybrid Wind/PV system to provide electricity supply for a few household connections. The model designed by them was able to control the voltage, frequency fluctuations, and their power usage. Ciobotaru et al., (2006) presented a PV inverter control system and a single-phase PLL structure including grid voltage monitoring using dSPACE. Fuzzy controlled power management strategies for a grid connected hybrid energy system was presented by Kumar et al., (2014). The hybrid energy system presented included a PV array and a Solid Oxide fuel cell (SOFC). Simplified single diode solar cell model and the SOFC was modelled using Nernst's equation. Kumar et al, further emphasized that though there are many MPPT techniques available in the literature such as incremental conductance (INC), constant voltage (CV), and P&O, the P&O method has been widely used by many researchers because of its simple feedback structure and fewer measured parameters.

Fuzzy based P&O algorithm was used by Sankaganesh et al., (2012) for MPPT of the PV system. Standalone WT/PV hybrid system was presented by using HOMER software by Badawe et al., (2012). Fuzzy-PID controller to control a WT/PV hybrid power system was presented by Zhang et al., (2007). In this method, continuous power supply to the systems was achieved by using the fuzzy intelligence controller which monitors the *SOC* of the BS system.

Cost optimization, analysis, energy management and reliability studies for hybrid energy systems were reported in (Kaviani et al., 2009; Ahmed et al., 2011; Nandi and Ghosh, 2009). Research forte in most areas has been the application of fuzzy controllers and neural networks for system identifications. Fuzzy-PID controllers are also used to optimize the output power and to reduce the cost of the hybrid systems as stand-alone units. Though some researchers proposed the neural network models, sliding mode control and Lyapunov Functions with the Kalman Filters. They are suitable to apply for specific situations where the measurements are observable and for uncontrollable systems. For hybrid energy systems, they are still at the experimental stage and yet to be assessed with the economic viability. The PI and PID control systems are still very popular with WT control and DFIG control systems as they are cheaper to implement.

Summary

Application of MPC for hybrid energy systems can be found in many occasions emphasizing as a promising area for research and development during the recent past (Bemporad, 2006). Initially, the MPC systems have been widely adopted in the field of process control, and their application and that has now been extended to unmanned air vehicles (UAV), aerospace applications and hybrid energy systems (Khan et al., 2011; Slegers et al., 2006). The MPC also offers the versatility to combine, EKF or Fuzzy controllers to arrive optimal solution to numerical optimisation while manipulating future actions within the hard constraints.

Hence, in this research, more focus will be given to MPC design and application to WTs, DFIG modelling and electricity generation with constraints.

1.3.5. Power Converters

Power converters are generally used for DC-DC conversion or DC-AC conversion. Nowadays, high frequency switches working with the pulse width modulation (PWM) technique have become very popular and extensively used in power electronics. There are three main basic types of power converter used in electronic industry. They are Buck-converters, Boost converters and Buck-Boost converters. These converters, are also categorised as switched mode DC-DC power converters. In addition to the power converters, inverters also play an important role in WT power generation systems which are connected to the grid. Inverters convert DC power into AC supply. PWM technique is mainly used by the inverters. Dynamic behaviour of the Buck, Boost, Buck-Boost converter is highly nonlinear due to the function of the switch incorporated with.

Delimustafic et al., (2011) used a Buck-converter, AC-DC converter and a DC-AC converter for their HRES design. In addition to the above three basic categories of the converter, a Cuk-converter is sometimes used in WT industry for power conversion. Good description of AC-AC and Dual converters can also be found in Bose (2014). Large scale wind turbines (over 1-1.5 megawatt scale (MW)) are generally, coupled with doubly-fed induction generators (DFIG) for electricity generation. In these generators, rotor winding is connected to the grid with the back-to-back PWM voltage source converters (VSC) (Hess et al., 2000). Back-to-back converter which is a bidirectional power converter, consists of a controlled rectifier and a

controlled inverter. Schematic diagram for a stator-flux-oriented stator-side converter control is given by Hess et al., (2000).

Matrix converter which is another type of converter used in WT industry, has a unique topology of AC to AC converter does not require any intermediate DC conversion (Islam et al., 2013) to connect to the Grid. Islam et al, compared the Z-source converter and the Matrix converter with the Back-to-back converter. Islam et al., (2013) further reported that Cyclone converters are generally used by offshore wind farms. Matrix, Two-level and Multilevel converter topologies were presented with comparative control strategy and performance analysis by Melício et al., (2010) for wind energy conversion systems.

In addition to the back-to-back PWM-VSC, an innovative cost effective power converter was proposed by Hess et al., (2000) which differs from other converters as it has only one bridge, composed of active devices. It has half switching devices and the hardware components than a conventional converter. Kumar et al., (2013) proposed a converter which is proficient for energy diversification from renewable and storage energy sources individually or simultaneously. It has the capability to operate either in a buck, boost, or buck-boost mode and directionally. Kalanta et al., (2010) proposed a six-pulse inverter topology for their stand-alone hybrid power generation system. The six-pulse-full -controlled rectifier is used to convert the AC output of self-excited induction generator into DC voltage. Ciobotaru et al., (2006) proposed an inverter model and it was tested using dSPACE control board.

The preferred use of buck-boost converter than Cuk-converter has been proposed by Sankarganesh and Thangavel (2012). Limitations of Cuk-converter and how to improve it to accommodate high voltage conversion ratio is explained there and hence a hybrid boost mode Cuk-converter is proposed. Use of power converters in standalone hybrid energy systems has been well defined and hence, the power converter proposed by Sankarganesh and Thangavel (2012) and according to the reference of Babaei et al., (2014) is analysed in this thesis.

1.4. Motivation

The motivation for this study stemmed from (i) the passion for control systems, (ii) expected benefits of renewable energy and (iii) real-life renewable energy plants.

One of the main problems of this planet is the burning coal, oil and gas which increases the prevailing CO_2 concentration at an alarming rate. On the other hand, the monopoly of the oil

market and ever increasing oil prices creates the global poverty and scarcity of food, water and other essential needs to the human among many countries in the world. Whether it is a direct or indirect contribution to solving these issues, what matters is your own motivation and in what way you could contribute to solving these problems. This is where the intellectuals can contribute in a form of knowledge transfer or searching appropriate technology where the less affluent society can afford to improve their quality of life.

Current electricity supply systems in many countries originated from fossil fuel electricity generating plants, where the consumers are at the receiving end. Switching from fossil fuel to renewable energy is an ultimate priority by the year 2050 due to the depletion of fossil fuels.

High efficiency wind energy conversion systems, modelling and nonlinear optimal control of renewable energy conversion systems, energy storage control in renewable energy based micro grid, improving the efficiency of PV arrays are some of the control paradigms to be resolved with the renewable energy systems.

Supply of reliable and continuous electric power from modern renewable power systems to satisfy the consumer power demand in the absence of fossil fuel generating power has been the main motive to explore the utilization of advanced optimal control techniques.

The intention here is the improvement and advancement of available control methods and systems to achieve sustainability in the aforesaid scenario.

Having read sufficiently about the complexities of mathematical modelling, control and simulation of WTs, BS systems and PV arrays what inspired and motivated me most is to participate in the further advancement of knowledge in this field and make a significant contribution to be useful to the research community and society at large.

1.5. Aims and Objectives

The aim of this study is modelling and control of renewable energy systems, WT and PV systems, with a suitable BS system to increase the efficiency and reliability of these technologies.

The specific objectives of this study are as details below.
Battery cell models found in the literature are mostly application oriented and there are some modelling and simulation gaps related to generic accurate models.

- Hence, the objective here is to develop a new Li-ion battery cell model which could be extended into BS systems.

The application of the thermal energy balance equation and the thermal effect on the battery cell models using EEC model concept was not well defined in the literature.

- To study the application of thermal energy balance equation (Bernardi equation) with respect to cycling and lithium plating in Li-ion battery cells is the next objective.

Battery *SOC* estimation plays an important role in battery management systems as it cannot be measured directly.

- Hence, the study of Kalman filter estimation based *SOC* variation for the battery cell model is explored.
- To develop a new BP model based on the developed battery cell model for high voltage and high current applications is important for grid electricity storage applications.

Literature related to mathematical modelling and analysis of nonlinear HAWT, is not adequate to model a complete system but only sufficient for reduced order models.

- To develop a complete analytical nonlinear model for a HAWT is given prominent priority.

Current stall control braking systems applied to WTs are susceptible to hazardous situations mostly when the wind speed is in the high wind region ('cut-out') region. It was noted that while the turbine blades are rotating, shutting down the output power is favourable for the generator operation than applying brakes. MPC is currently an emerging area in control engineering due to its adaptive online optimization capability. MPC systems have been very widely used in many engineering disciplines starting from process control to aerospace applications and hybrid energy systems.

- To develop an MPC based pitch control mechanism to facilitate the control of stall flow control in high wind region.

To harvest maximum energy from sunlight using PV arrays is useful to meet the demanded power supply. Many different maximum power point tracking methods (MPPT) are reported in literature.

- To develop an efficient, MPPT method to harness maximum power from SPV arrays which is suitable to apply for a hybrid system is explored.

1.6. Contribution

Main contributions of this research include the following:

Accurate dynamic battery cell model is developed which is consistent not only with constant cell temperatures but also at varying ambient and internal cell temperatures. The new model developed comprises RC elements to model the electrochemical behaviour of the battery electrolyte and the anode/cathode reactions. A new mathematical formulation representing the SOC variation due to varying temperature is investigated. Building a new model contributes to the mathematical modelling methodology.

The new model developed is analysed with simulation results. The dynamic behaviour of the battery cell model was tested for repeatable results at varying SOC conditions, different discharge currents and at varying temperatures. The developed new Li-ion battery cell model was tested for accuracy and validity with the experimental data available in literature. This section contributes to the simulations.

A new BP model is presented which can accommodate the individual cell voltage changes due to physical conditions. The construction of the BP model is a new concept by using the battery EEC cell model as a building block. This section is a contribution to both modelling and simulations.

Analytically developed BP model is then investigated with manufacturers' experimental data and data published by researchers to validate the BP model for accuracy and repeatability. This section contributes to the simulations. The BP model developed is very useful for the electric vehicle designs and grid integration as an energy storage system. This contribution goes beyond the modelling and simulations in this field.

Non-linear mathematical model for a variable speed HAWT with six states input vector and a four states output vector for the state-space method has been presented. MPC versus PID-State-feedback controller was evaluated. This section contributes to both modelling and simulations.

An active and optimum controller is investigated to regulate the power output from a large (mega-watt scale) wind turbine rotor. A practical method of synthesising an active stall flow controller, where the feedback control law is derived by applying the concept of MPC has been

studied. The implemented method is analysed whether it is suitable to control the power output of the rotor to any desired value without applying the nonlinear stall model generally introduced by evaluating the blade profile coefficients of lift and drag. This section contributes to the modelling and simulation.

Dynamic EEC model for a single diode PV array is presented and its simulation results are analysed. An efficient and fast MPPT system has been investigated to absorb maximum power from the available solar radiation and at varying irradiances. Accurate dynamic simulation results with published data in literature with varying irradiances, varying ambient temperatures and their relevant power curves have been compared to validate the designed model. This section contributes to both modelling and simulations.

1.7. Outline of the thesis

Executive summary of each chapter is presented here:

Chapter 2 presents the analytical approach to battery cell models. Mathematical modelling and theoretical analysis of the existing battery cell models are described in this section. EEC concept for battery cell modelling which is ideally suitable for capturing nonlinear behaviour of the battery chemistry is used to develop a new battery cell model. Based on the battery cell model, BP equivalent electric circuit model is developed analytically to suit any voltage or current requirement. Battery cell model developed has been validated with the existing battery data published by researchers and by the battery manufacturers. The simulation results of the BP model will be tested with the experimental data to establish the validity, accuracy and repeatability. New mathematical formulations of *SOC* change with the temperature is also presented in this section. The *SOC* estimation of battery cell models and application of Kalman filter is described towards the end of this chapter.

Chapter 3 presents a complete mathematical description in modelling wind turbines (WT) and generators used in converting kinetic energy to electrical energy. With the mathematical models, six-state, state-space representations of the WT, turbine rotor power control, doubly fed induction generator (DFIG) are presented in this section. Pitch controls related to optimum power output delivery of the wind turbines have also been studied and presented.

Chapter 4 describes model predictive control (MPC) applied to WTs. MPC is an advanced control technique used mainly in process industry to control parameters which are not directly

measurable. The application of MPC for optimum power extraction from WTs subject to variable wind speed conditions with constraints have been presented in this Chapter.

Chapter 5 presents an equivalent electrical circuit model for Power Converters. The power converters play an important role in changing AC power to DC or vice versa. A state-space model for a synchronous buck converter closed loop control with Simulation results is presented in this section.

Chapter 6 describes mathematical modelling of PV Cells. The PV cells generate electricity by absorbing photons in the sunlight. Reliable, cost effective, supplemented power supply can be augmented when PV arrays are combined with wind turbines and the battery storage systems. Hybrid power generation systems in remote areas frequently use combined Wind-turbine/PV/BS systems to provide continuous power supply by exploiting the wind and solar energy as they are complementary to each other in time sequence. The Simulink model of the PV cell, light intensity, and extracted current/voltage characteristics are presented in this chapter. MPPT algorithms and a MATLAB source code have been presented.

Chapter 7 presents conclusions and suggestions for further work of the research project. Further work and future challenges in renewable energy power systems have been discussed in this section.

1.8. Journal Publications

- S. Wijewardana, R. Vepa, M. H. Shaheed, Dynamic battery cell model and state of charge estimation, Journal of Power Sources, Volume 308, 15 March 2016, Pages 109–120.
- S. Wijewardana, M. H. Shaheed and R. Vepa, Optimum Power Output Control of a Wind Turbine Rotor International Journal of Rotating Machinery, Volume 2016 (2016), Article ID 6935164, 8 pages, Open Access article: http://www.hindawi.com/journals/ijrm/2016/6935164/.
- S. Wijewardana, M. H. Shaheed, R. Vepa, Model predictive control and power regulation of a variable speed wind turbine, Submitted to IEEE Journal of Applied Energy, (Under reviews). Submitted on 15 April 2016.
- S. Wijewardana, M. H. Shaheed, R. Vepa, Generic dynamic modelling of Lithium-ion battery packs, Submitted to Energies ELSEVIER16 October 2016

Chapter 2: Battery Storage Systems

Outline

Battery storage systems play an important role in future smart grid implementation and in electric vehicle designs. They act as energy reserves or back up power sources and bring the balance of fluctuations. Analytical approach to battery cell modelling is presented with a new EEC cell model. The EEC is built using active and passive circuit elements of resistors, capacitors, voltage sources and current sources. The model presented captures the nonlinear behaviour of the battery cell chemistry. The description on short and long transients of the battery cell chemistry and the use of two *RC* networks for modelling is presented in this chapter. Dynamic modelling of battery cell and battery packs are described in this chapter. State space modelling, battery state of charge estimation using Kalman filter and the simulation results are presented towards the end of the chapter. Description of the symbols and the nomenclature used in this chapter is given on page 11-13.

2.0 Introduction

Modelling method

Randles-Warburg battery cell modelling method has been used as a tool to develop an EEC Li-ion battery cell model. As the Randles-Warburg (Nejad et al., 2016) circuit model is not sufficient to capture the nonlinear behaviour of the battery cell chemistry, modified non-linear Randle's model is applied to include the following: film/gas formation near the electrolyte/electrode surfaces, voltage stabilisation, reversible and irreversible heating effects. Battery packs (BP) have become indispensable for clean energy storage systems in smart grids. They not only improve the reliability of the power supply and reduce the cost of electricity but, also act as active energy sources to balance the fluctuations in power supply and demand (Barelli et al., 2016). In modern electric vehicles (EV) or in hybrid electric vehicles (HEV) advanced battery storage systems release uninterruptible power to the transmission for reliable long distance commuting when the gasoline power is turned off. Advanced battery management systems use an online accurate estimation of battery state of charge (*SOC*). The battery *SOC* is a numerical quantity which represents the ratio of available battery capacity to

its fully charged capacity (Erdinc et al., 2009). In EV high priority is given to the accurate estimation of *SOC* otherwise, the result can lead to an unexpected breakdown of the vehicle. Battery *SOC* cannot be measured directly as it is an internal state of the battery dealing with battery capacity or electrical charges. The *SOC* also gives an indication of how much longer that the battery can release power without undergoing recharging. The *SOC* behaviour is considerably complicated with the chemical reactions occurring within the cell and it changes with the thermal properties involved with the electrolytes and electrodes. The non-linear variations of these battery parameters, complex battery chemistry, corrosion dynamics and the cycling, have become major research challenges for the researchers to develop accurate dynamic battery cell models and BP models for experimentation and applications. One such demand is for efficient durable batteries to operate at -150ºC and the temperatures over 150ºC or even beyond these limits specially needed for space explorations.

When analysing it is found that the battery parameters like battery open circuit voltage, battery capacity, battery internal resistance etc. are polynomial functions of battery *SOC*. The non-linearity of these parameters occur mainly due to the electrochemical properties of the electrolytes and the reversible and irreversible chemical reactions when charging and discharging of batteries. The equivalent electrical circuit models for these battery cells and BPs play an important role when modelling and analysing those complex chemical reactions. Mathematical modelling and development of an accurate battery equivalent electrical circuit model are discussed in the next section.

2.1 Introduction to Dynamic Battery Cell Modelling

An accurate dynamic battery cell model is an essential subsystem in BP modelling as it can be used to model large energy storage systems from basic principles. At the inception, it is essential to investigate what is the best suitable equivalent electric circuit cell model which can be used to assemble into a battery pack model. In general, battery cell models can be divided into electrochemical models, analytical models, stochastic model, and equivalent electric circuit (EEC) models (Barelli et al., 2016; Yurkovich, 2010; He, 2011). The EEC models are again divided into the following types: Rint model, *RC* model, the Thevenin model or the PNGV model and the Randles-Warburg unit cell based or dual polarization models (He, 2011). PNGV circuit model and the Thevenin models are almost similar except to the additional capacitor found in series with the battery internal resistor which is in the PNGV equivalent

electric circuit model. In most improved PNGV models there is an additional *RC*-loop included capturing the slow transient characteristics of the electrolyte chemistries.

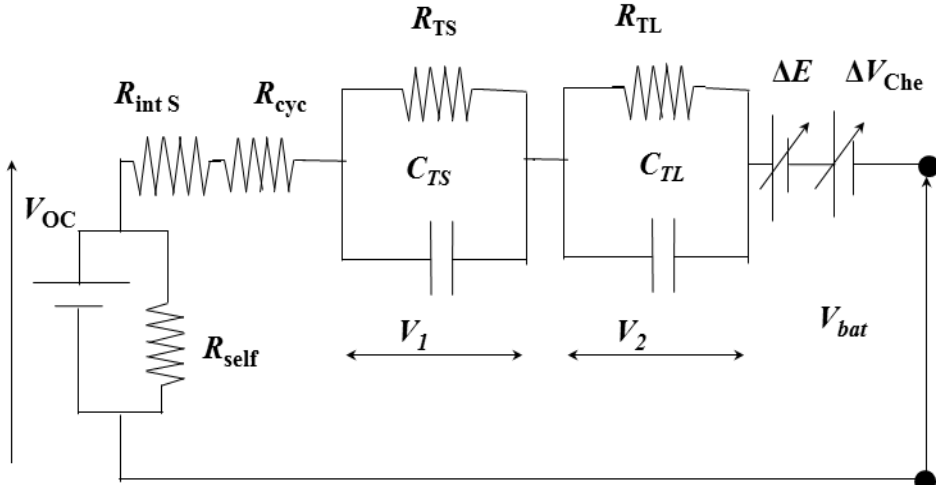

Figure.2.1. Equivalent electric circuit battery cell model

The EEC cell model presented here is a modified dual polarization (DP) model. Generally, a DP model consists of two RC networks which captures the slow transients and the fast transients of the electrolyte behaviour. Transient response of the battery is influenced by double layer and diffusion capacitance when the rates of reactions are high. The phenomenon of the electrolyte-electrode reactions which is defined as the double-layer formation at electrode/electrolyte solution interface where the capacitive effects build up when discharging/charging of the battery cell due to oxidation/reduction of the chemical reactions (Huria, 2012). This capacitance is defined as the electrical polarization capacitance or diffusion capacitance. Including more than two *RC*-loops in the equivalent electrical circuit can model the slow transients very accurately. However, literature review revealed that two *RC* loops sufficiently represent the model chemistry accurately without incurring much computational burden on the model. Introduction to the EEC model presented in Fig. 2.1 is given next:

a) The source voltage V_{OC}, is connected in parallel with the resistor R_{self} . The parameter $R_{self}(T, n, SOC)$ is symbolically shortened to R_{self} for convenience. The resistive component, R_{self} herein after represents the battery self-discharge feature due to storage effects. It is a function of temperature T , State of charge (SOC) and the cycle number n . The cycle number n is the number of cycles that the battery cell is charged or discharged. The ohmic value of

R_{self} is very high compared to the battery internal resistance $R_{\text{int}S}$ and therefore, in most modelling situations the current passing through the R_{self} is neglected.

b) Battery internal resistance which is modelled by two resistances in series $R_{\text{int}S}$ and R_{CYC} representing the electrolyte resistance and the resistance change due to the number of charging and discharging cycles the battery has undergone.

c) Two RC circuit loops with RC elements given by, R_{TS}, C_{TS} and R_{TL}, C_{TL} which represents the short and long transient effects of the battery. The transient effects arise due to double-layer formation at the electrode/solution interface. The capacitances C_{TS} and C_{TL} represent the electrical polarization capacitance and the diffusion capacitances. Transient response of the battery is influenced by double layer diffusion capacitance when the rates of reactions are high (Pandey and Bansel, 2013).

d) The parameters $R_{\text{int}S}$, R_{TS}, R_{TL}, C_{TS}, C_{TL} and *SOC/SOD* are all functions of the battery internal cell temperature.

e) Two variable voltage sources included in the circuit $\Delta E(T)$ and $\Delta V_{Che}(T)$ signify the battery cell voltage fluctuations due to temperature variations.

If the current passing through the capacitor C_{TS} is taken as i_1 and the current passing through R_{TS} is i_2 respectively then by using Kirchhoff's law, we can write:

$$i(t) = i_1(t) + i_2(t) \tag{2.1}$$

The current passing through the capacitor can be written as:

$$i_1(t) = C_{TS}\frac{dV_1}{dt} \tag{2.2}$$

Using Ohm's law, we can write:

$$i_2(t) = \frac{V_1}{R_{TS}} \tag{2.3}$$

Substituting equations (2.2), (2.3) into equation (2.1) we can write:

$$i(t) = i_1(t) + i_2(t) = C_{TS}\frac{dV_1}{dt} + \frac{V_1}{R_{TS}} \tag{2.4}$$

If the current $i(t)$ is taken as i for convenience, then we can write:

$$\frac{dV_1}{dt} = \frac{i}{C_{TS}} - \frac{V_1}{R_{TS}C_{TS}} \tag{2.5}$$

Similarly, we can derive:

$$\frac{dV_2}{dt} = \frac{i}{C_{TL}} - \frac{V_2}{R_{TL}C_{TL}} \tag{2.6}$$

The battery open circuit voltage V_{OC} is the voltage difference between two battery terminals when there is no external load is connected (Chen et al., 2006). The parameter V_{OC} is a function of SOC , ambient temperature and the battery electrolyte temperature. As given in Erdinc et al., 2009 the V_{OC} variation with SOC is given by equation (2.7).

$$V_{OC}(SOC) = -1.031 \times \exp(-35 \times SOC) + 3.685 + 0.2156 \times SOC$$
$$-0.1178 \times SOC^2 + 0.321 \times SOC^3 \tag{2.7}$$

The battery SOC at a given cell temperature, T_{cell} can be expressed as, (2.8) (Erdinc et al.).

$$SOC = SOC_{init} - \int \frac{i_{bat}}{C_{usable}} dt \tag{2.8}$$

The battery parameters $R_{\text{int}S}$, R_{TS} , R_{TL}, C_{TS} and C_{TL} are also functions of SOC and their characteristic curves are generally obtained by using experimental tests. Hybrid power pulse characterization (HPPC) tests have been carried out by Chen et al., (2006) and Erdinc et al., (2009) to establish the following relationships:

$$R_{\text{int}S}(SOC) = 0.1562\exp(-24.37 \times SOC) + 0.07446 \tag{2.9.a}$$

$$R_{TS}(SOC) = 0.3208\exp(-29.14 \times SOC) + 0.04669 \tag{2.10.a}$$

$$C_{TS}(SOC) = -752.9\exp(-13.51 \times SOC) + 703.6 \tag{2.11.a}$$

$$R_{TL}(SOC) = 6.603\exp(-155.2 \times SOC) + 0.04984 \tag{2.12.a}$$

$$C_{TL}(SOC) = -6056\exp(-27.12 \times SOC) + 4475 \tag{2.13.a}$$

The SOC relationships with $R_{\text{int}S}$, R_{TS} , R_{TL}, C_{TS} and C_{TL} can be obtained using MATLAB Curve Fitting Toolbox which uses the localized regression analysis. Within the MATLAB toolbox, there is an option to select either a first-order polynomial or second-order polynomial equation for accurate curve fitting. As it can be seen from equations (2.9.a) to (2.13.a) it

represents a single exponential term with a single constant for each equation which are normally less accurate than the second order polynomial equations. Hence, the equations (2.9.a) to (2.13.a) are further improved to obtain higher accuracy by incorporating additional exponential terms as shown in equations (2.9) to (2.13). Table 2.1 in this thesis presents improved new parametric constants. (C_{g1} ; g represents the row number; example: $C_{11} = 1.21$ in equation (2.9); $C_{22} = -24.37$ in equation (2.10))

Table 2.1: New constants in Eq. (2.9) to Eq. (2.13).

$R_{cg}(SOC)$	g	C_{g1}	C_{g2}	C_{g3}	C_{g4}
$R_{\text{int}S}(SOC)$	1	1.21	-52.1	0.0435	0.00941
$R_{TS}(SOC)$	2	0.1562	-24.37	0.04669	0.000
$C_{TS}(SOC)$	3	1100	.1500	-1200	-7.100
$R_{TL}(SOC)$	4	1.321	-34.72	0.0491	0.0071
$C_{TL}(SOC)$	5	5200	-0.2585	-8350	-19.4

$$R_{\text{int}S}(SOC) = 1.21\exp(-52.1 \times SOC) + 0.0435\exp(0.00941 \times SOC) \quad (2.9)$$

$$R_{TS}(SOC) = 1.562\exp(-24.37 \times SOC) + 0.04669\exp(0.0001 \times SOC) \quad (2.10)$$

$$C_{TS}(SOC) = 1100\exp(0.15 \times SOC) - 1200\exp(-7.1 \times SOC) \quad (2.11)$$

$$R_{TL}(SOC) = 1.321\exp(-34.72 \times SOC) + 0.0491\exp(0.0071 \times SOC) \quad (2.12)$$

$$C_{TL}(SOC) = 5200\exp(-.2585 \times SOC) - 8350\exp(-19.4 \times SOC) \quad (2.13)$$

Cyclic charging and discharging can reduce the battery life considerably. Generally, manufacturers specify the battery life up to 500 cycles for Li-ion batteries. However, the 500 cycle number does not imply that the Li-ion battery will be completely dead and inactive after 500 cycles. In reference (Hans et al., 2015) it is stated that a lithium-ion cell charged to 4.20V/cell typically has a cell life of 300–500 cycles. If the battery cells are charged up to only 4.10V/cell, the cell life can be prolonged to 600–1,000 cycles. At 4.0V/cell the cell life is 1,200–2,000 and at 3.90 V/cell it would be 2,400–4,000 cycles. It is also found that when the battery cell has reached 4000 cycles it can still be charged up to 58% of its original capacity. The typical simulation characteristics are shown by Fig.2.2.

Battery internal resistance change due to cyclic effect is assumed to be given by the empirical Equation (2.14), as in (Erdinc et al., 2009):

$$R_{cyc} = \xi \times n^{\lambda} \tag{2.14}$$

where, R_{cyc} is the cyclic resistance of the battery and ξ is an empirical constant. The parameter n signifies the cycle number and λ is also an empirical constant.

The battery terminal voltage V_{bat} can be expressed as the summation of all voltage drops in the equivalent electrical circuit given in Fig. 2.1:

$$V_{bat} = i(R_{\text{int}\,s} + R_{cyc}) + V_1 + V_2 + \Delta E(T) + \Delta V_{Che}(T)) \tag{2.15}$$

The variable parameter $\Delta E(T)$ represents the equilibrium potential correction of the battery open-circuit voltage which depends on the temperature and the amount of active ions available in the electrodes (Pandey and Bansal, 2013). The variable parameter $\Delta V_{Che}(T)$ represents the voltage change due to the temperature effect. The parameter $\Delta V_{Che}(T)$ changes due to film formation, non-uniform ion distribution near the electrodes, non-uniform heat generation rate, conductivity difference in the electrolyte due to hot regions and diffusion (Pandey and Bansel, 2013; Thanagasundram et al., 2012).

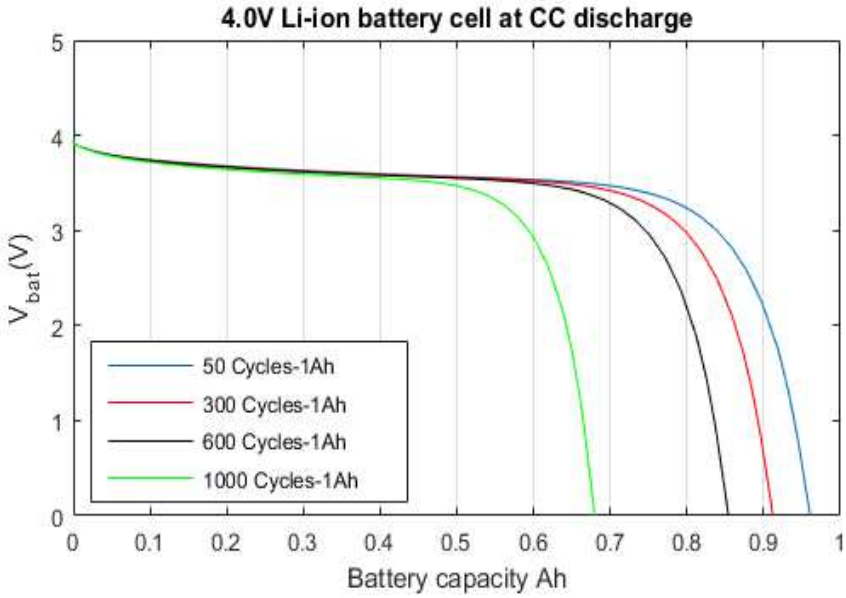

Figure.2.2. Li-ion 4.0V battery discharge due to cyclic effect. The battery cell capacity is taken as 1Ah; battery discharge at a constant current; 1000 cycles are considered as the cut off limit for charging or discharging and when the limit is passed then the maximum battery cell voltage achievable after charging is the 68% of the initial battery open circuit voltage.

When a fully charged battery is stored for a long time its capacity decreases over time due to automatic self-discharging. The self-discharging effect can be modelled with a resistive component added to the battery equivalent circuit in parallel with a voltage source, V_{OC} as presented previously. This resistance which is identified as $R_{self}(T, n, SOC)$ depends on the *SOC,* cycling, and the ambient temperature. As shown by Fig.2.1, the current passes through the resistor $R_{self}(T, n, SOC)$ can be taken as i_{S_D}. The current i_{S_D} comparable to the battery discharge current i, is very small and therefore $R_{self}(T, n, SOC)$ can be neglected in our battery equivalent circuit modelling.

2.2 Thermal Effect on the Battery Cell Modelling

Ambient temperature and the battery temperature variations can change the battery cell output voltage or battery open circuit voltage. Battery cell temperature can increase due to the current flow through the electrolyte. The heat in a battery cell is produced in three different ways: activation (interfacial kinetics), concentration (species transport), and ohmic (Joule heating from the movement of charged particles) losses. The model used for the simulation is the model presented in Fig. 2.1 presented earlier in this chapter. The presented model assumes the natural convection conditions and the heat generation and heat dissipation throughout the electrolyte as uniform. The heat energy released or absorbed due to chemical reactions with the anode and cathode is not considered separately but taken as average values (Viswanathan et al., 2009). Assuming the above conditions thermal energy balance equation can now be established for the heat generated by the battery cell which is equal to the heat dissipated (Bandhauer et al., 2011).

$$\Delta T = \left(T_{Cell} - T_{amb}\right) \tag{2.16}$$

$$\frac{dT_{Cell}}{dt} = \frac{1}{mC_p}\left[i\{V_{bat} - V_{OC}\} + \frac{T_{Cell}}{F}\Delta S\Phi - A\alpha\Delta T \right] - A\lambda\Delta T - A\sigma\varepsilon\left(T_{Cell}^4 - T_{amb}^4\right) \tag{2.17}$$

The term $(T_{Cell}/F)\Delta S\Phi$ is generally defined as the reversible heat generation rate by taking the number of electrons per reaction as 1. The battery cell temperature T_{Cell} is measured in degree Kelvin. The combined entropy change ΔS, can also be taken as zero as in Viswanathan et al., (2009). Generally, automated electrochemical thermodynamic measurement systems (ETMS) calculate the entropy change based on one Li-ion exchange during charge or discharge

from the equation $\Delta S = F\,\partial V_{OC}/\partial T$. The entropy change, ΔS typically corresponds to a reduction reaction, which is the discharge reaction for a cathode in a full cell (Entropy is heat added per unit of Kelvin or joule/K). Depending on convention, the sign for heat generation can be either positive or negative for an exothermic reaction (Viswanathan et al., 2009). If for an exothermic reaction the heat generation is taken as negative, then the discharge current is taken as positive. The entropy change in the cell is given by: $\Delta S = \Delta S_c + \Delta S_a$ (Viswanathan et al, 2009); where, ΔS_c is the entropy change in the cathode material for reduction reaction and ΔS_a is the entropy change of the anode material for an oxidation reaction. The irreversible heat generation rate is generally exothermic and is given by $Q_{irr} = -i^2(R_{\text{int}S})$. The parameter i represents the battery current and the $R_{\text{int}S}$ is the sum of ohmic, activation and diffusion polarization resistances (the combined effect has been taken into account as a variable total during the simulation time in the model presented). In the thermal energy balance equation (2.17), the term $i\{V_{bat} - V_{OC}\}$ represents irreversible heat generation component (Bandhauer et al., 2011). The equation (2.17) can now be simplified to give equation (2.18).

$$\frac{dT_{Cell}}{dt} = \frac{1}{mC_p}\left[i\{V_{bat} - V_{OC}\} - A\alpha\Delta T\right] \tag{2.18}$$

where:

m is the unit mass. The temperature effect on activation, diffusion polarization and due to different electrolyte chemistries is modelled by the parameter $\Delta V_{Che}(T)$ which is a function of the temperature.

The parameter $\Delta V_{Che}(T)$ is modelled by the polynomial equation (2.19) as given below:

$$\Delta V_{Che} = \beta w \exp^{(1/t)} \Delta T + \left.\frac{dV_{che}}{dT}\right|_{T=T_{Cell}} \left(C_{Che} + C_{Che1}\Delta T\right)(1+\beta)\Delta T \tag{2.19}$$

In equation $\left.\frac{dV_{che}}{dT}\right|_{T=T_{Cell}}$ represents the voltage gradient variation within the cell. It is introduced as a gradient variation since, the values of these voltage grid points can be different from one point to another point. The difference in these voltages (can be identified as grid points) can happen due to different concentration islands within the electrolyte. When electrons pass through these islands there can be different voltages and temperature zones within the cell.

Assuming the battery cell is cylindrical and the centre axis as the reference axis, this voltage gradient with respect to cell temperature is assumed as a constant and this figure could be evaluated by simulation results (see table 2.2 for details). This constant varies with different electrolytes. There is a similar voltage gradient parameter defined by $\left.\frac{dV_r}{dT}\right|_{T=T_{Cell}}$ which models the film formation and active ion formations near the electrodes and this parameter also varies in three dimensional form. But here also it is assumed as a constant and can be evaluated by simulation. T_{Cell} is the battery cell temperature and the T_{amb} is the operating temperature of the battery. The parameters β, w, C_{Che} and C_{Chd} are all numerical constants that depend on the properties of the electrolyte, the anode and the cathode materials. The first derivative dV_{che}/dT is defined as the effective voltage gradient. However, while considering those voltage/temperature gradients, the parameter $\Delta E(T)$ which is not a derivative like the former two, is positive or negative depending on charging or discharging. The variation due to the amount of active material available in the electrodes can be modelled by equation (2.20) given below:

Analytical and experimental proofs are required to establish the actual polynomial relations for $\left.\frac{dV_r}{dT}\right|_{T=T_{Cell}} = f(T, T_{Cell}, T_{wall}, x, y, z)$; $\left.\frac{dV_{che}}{dT}\right|_{T=T_{Cell}} = f(T, T_{Cell}, T_{wall}, x, y, z)$, and they are yet to be investigated and published. Where, T_{wall} is the battery casing temperature, T_{Cell} is the battery cell temperature at a reference point and x, y, z are the co-ordinates from a reference point in the battery cell. However, at this stage, taking both functionalities as numerical constants Equation (2.19) and (2.20) is presented:

$$\Delta E(T) = \left(1 + C_{E1}\Delta T\right)\left.\frac{dVr}{dT}\right|_{T=T_{Cell}} \Delta T \qquad (2.20)$$

Table 2.2 gives the parameters and constants derived from simulation results [indicated in the table as 'sim'] and directly from the literature or estimated from the literature [indicated in the table as 'Lit'].

TABLE: 2.2 Panasonic 17500 Li-ion Battery Parameters [21]

For Panasonic 17500 Li-ion, 3.7V discharge current of 830mAh, at 25^0C or at T_{amb} and $SOC = 1$	
dV_r/dT	0.00003 [sim]

dV_{che}/dT	0.0016 [sim]
C_{E1}	0.00011 [sim]
C_{Che}	0.07 [sim]
C_{Che1}	0.001 [sim]
β	0.0012 [sim]
w	0.012 [sim]
α ($Wm^{-2}K^{-1}$)	10.1-18.9 [Lit]
Surface area, A (m^2)	0.00459 [Lit]
C_p ($Jkg^{-1}K^{-1}$)	1350 [Lit]
Mass, m (kg)	.022 [Lit]
Nominal battery capacity (*amp sec*)	2988 [Lit]
C_{bat}(F)	1600 [Lit]
k	3.1 [Lit]
d	0.7 [Lit]

Literature: [Lit]; simulation: [sim]

The block diagram shown by Fig. 2.3 used model Equations (2.5), (2.6), (2,7), (2.8), (2.9), (2.10), (2.11), (2.12), (2.13), (2.14), (2.15), (2.18), (2.19) and (2.20) to construct the Simulink battery model.

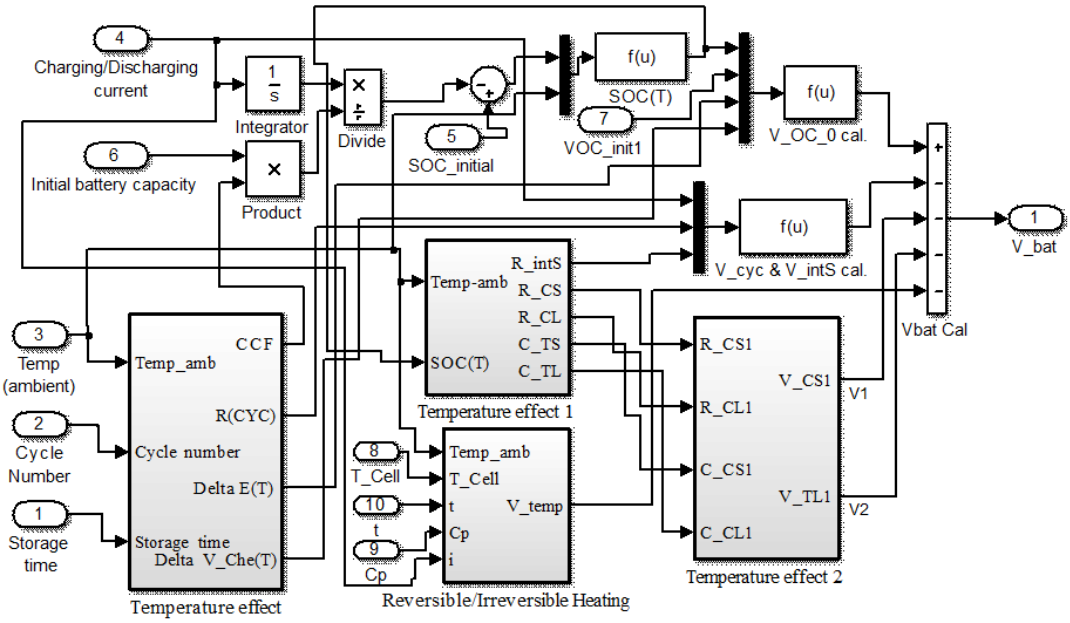

Figure.2.3. Simulink block diagram for the battery cell model

The experimental results published by Chen and Rincon-Mora (2006) and Thanagasundaram et al., (2012), have been used to test and validate the model. As described in the literature review, Panasonic Li-ion TCL PL-383562, battery cell which has the capacity of 850 mAh is used to validate the improved battery cell model. The other battery cell used to test the simulation results is the Panasonic 17500 (Li-ion-battery). The current pulse tests at discharging currents of 80, 160, 320 and 640 mA had been used. The nominal capacity (the average capacity) of the battery is 800 mAh ± 5% at a discharge rate of 0.2A in 0.2C (5 hours discharge) and it was discharging at a temperature of 25ºC with more than 300 cycles. The battery should be charged at a charge rate of 0.8A in 1C (1-hour charge). When discharging at 1.6A it will last 2-hours (0.5C). The manufacturers specify the charge cut off voltage as 4.2 V and the discharge cut off voltage as 2.75V [21].

Comparison of experimental data with the simulation results is shown in Fig. 2.4 to 2.5. These comparisons confirm the validity of the presented model. The model simulation results are accurate within 98.21% compared to the experimental measurements. From literature review it was noted that most researchers who performed HPPT and current pulse tests followed similar charging and discharging methodology for their experimentation: for example: CC/CV charge at 4.2V, 1C +25ºC and CC discharge at 0.2C to 2.75V; Nom. Volt.: 3.75, Nom. Capacity: 190mAh to 1800mAh, maximum current: 1C; maximum voltage: 4.2V (Chen and Rincon-Mora, 2006). Lithium Manganese Oxide Battery; nominal voltage 3.6CC: 750mA, nominal capacity 2200mAh (Thanagasundaram et al.). In Fig. 2.4 shows the comparison of experimental data and the

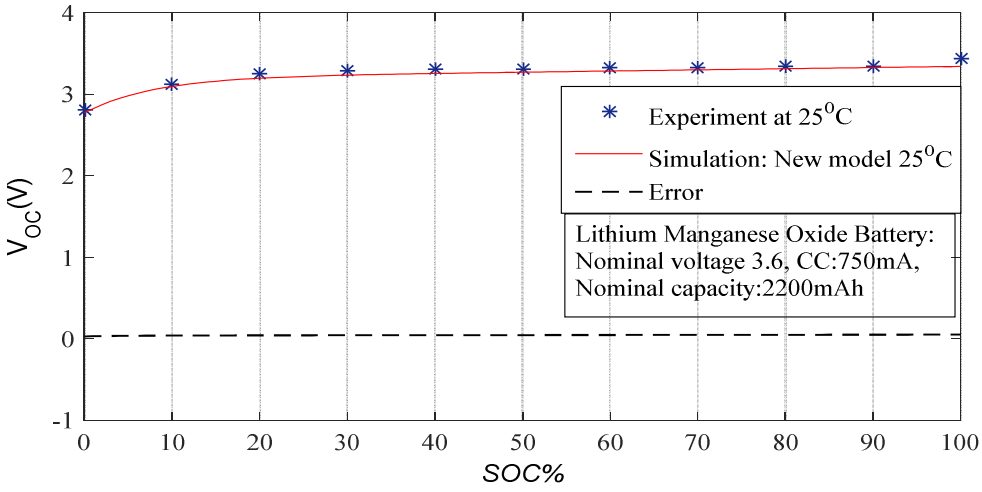

Figure.2.4. V_{OC} versus *SOC* Characteristics.

simulation data. As the error curve is hovering around zero axis and the experimental data points coincide with the simulation results it can be concluded that the model is quite accurate. The Fig. 2.5 shows the V_{OC} variation with *SOC* characteristics at 25˚C. The experimental data from Manufacturer's data manual published in 1999 and data from Chen and Rincon-Mora's published were used to compare the simulation results. As it can be seen from Fig. 2.3 and Fig. 2.4. experimental data as well as the manufacturer's data match with the model simulation results with a good accuracy.

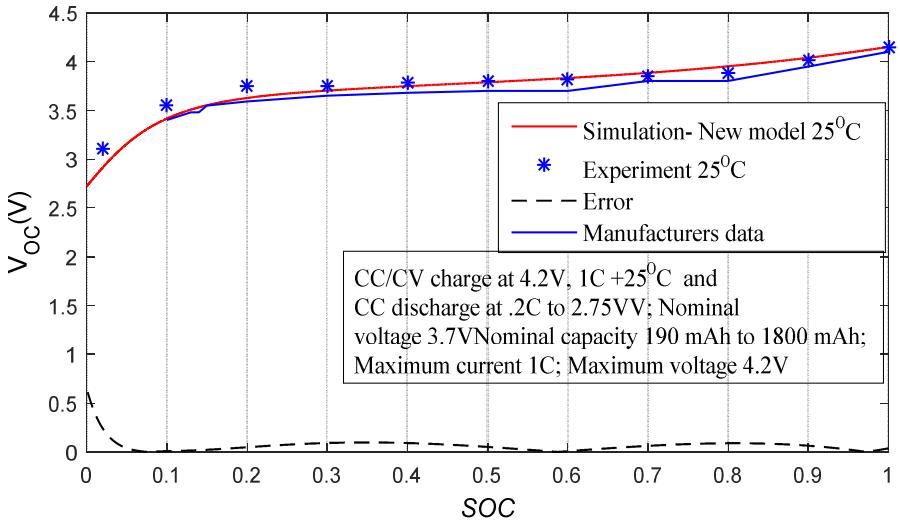

Figure.2.5. V_{OC} versus *SOC* Characteristics.

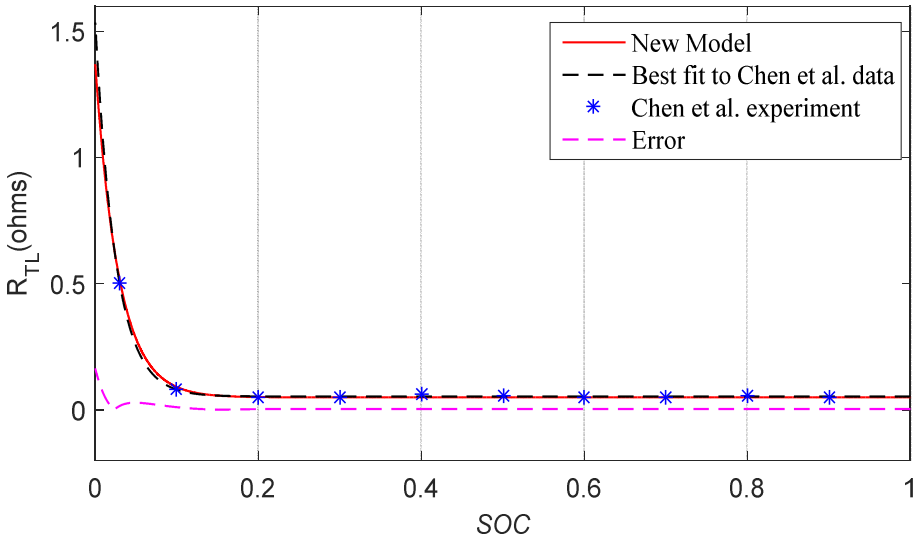

Figure.2.6. R_{TL} versus *SOC* Characteristics.

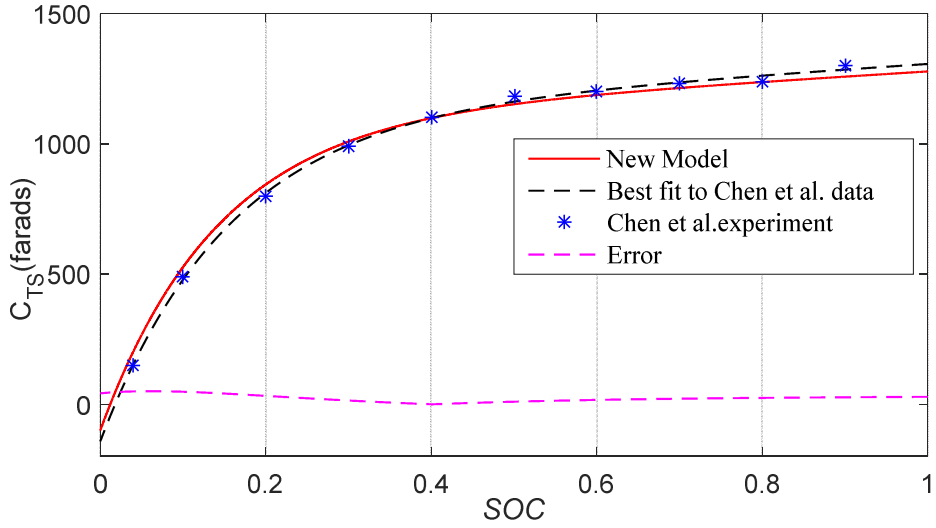

Figure.2.7. C_{TS} versus *SOC* Characteristics.

Fig. 2.4, 2.5, 2.6 and 2.7 illustrate the error variations of the battery parameters with the *SOC* at 750mA battery current. Percentage error was calculated for each graph by using the formula given by equation (2.21) which is embedded into MATLAB code and finally calculating the mean percentage error, which can be simply calculated by using MATLAB command.

$$Err(\%) = 100\frac{\left(1-(abs(V_{OC\_sim}-V_{OC\_Exp}\right)}{V_{OC\_sim}} \tag{2.21}$$

The *SOC* plot with many battery parameters shown in Fig. 2.4 to 2.7, the percentage error is within 0.5% to 1.5%. Therefore, the new battery model shown here which has a good accuracy can be used for other industrial applications.

Ambient temperature variation can change the battery capacity. It can be seen from Fig. 2.8 when the operating ambient temperature is below 0ºC then the battery capacity has reduced comparatively compared to 45ºC. With the simulation result it was noted that when the temperature increases more than 42ºC the battery capacity actually decreases. Fig. 2.9 shows the manufacturers' data and the Fig. 2.10 shows the characteristics of battery output voltage change with respect to battery capacity. As manufacturer's experimental tests were carried out at 23ºC (only for charging and discharging prior to experiments), the simulation tests were also carried out at the same temperature for accuracy. However, Thanagasundaram et al., (2012) and Chen and Rocorn-Mora's (2006) experiments were carried out at 25ºC, then the simulation results of the new model were also tested at 25ºC.

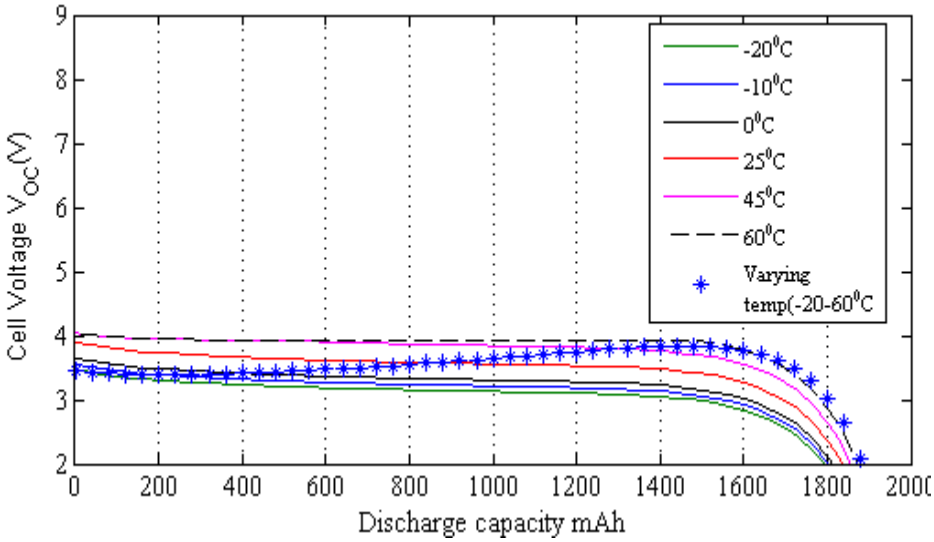

Figure.2.8. V_{OC} versus discharge capacity at different temperatures

From Fig. 2.9 it can be seen that battery cell open circuit voltage versus discharge capacity is shown at temperatures 45ºC, 23ºC, 0ºC, -10ºC, -20ºC. The temperatures in these curves are independent variables and the curves were generated exactly similar to the manufacturer's data. In Fig. 2.4 to 2.7 the ambient temperature is 25ºC, where Chen et al. and Thanagasundaram et al., (2012) carried out the experimentations. Hence, the simulation results were also taken at 25ºC for comparison. However, in Fig.2.9 the room temperature was taken as 23ºC by the manufacturers. Therefore, for simulation and actual data comparison, in Fig. 2.10, 23ºC is taken as the room temperature while other temperatures remain same except, 60ºC which was not found with the manufacturers data.

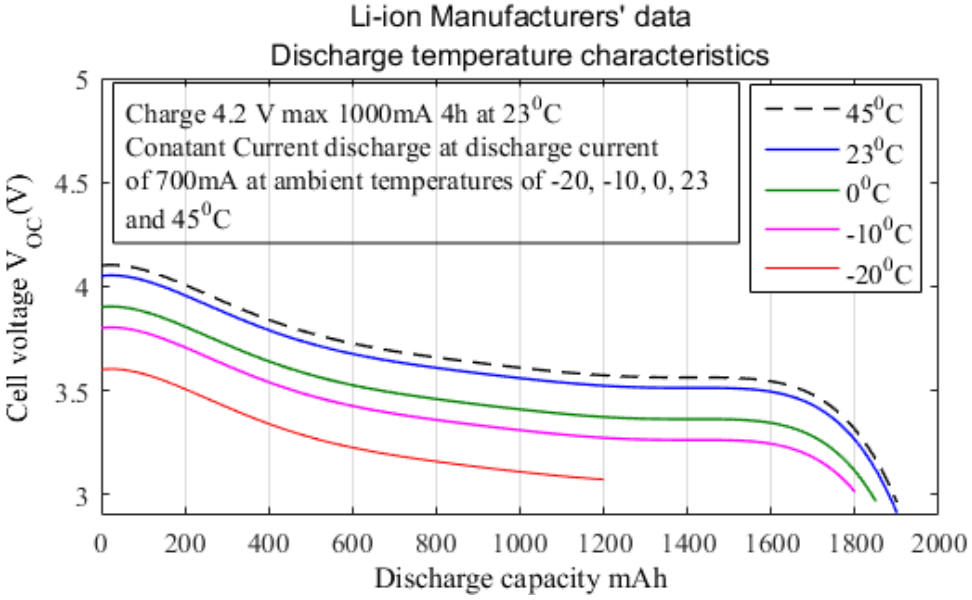

Figure.2.9. V_{OC} versus discharge capacity at different temperatures

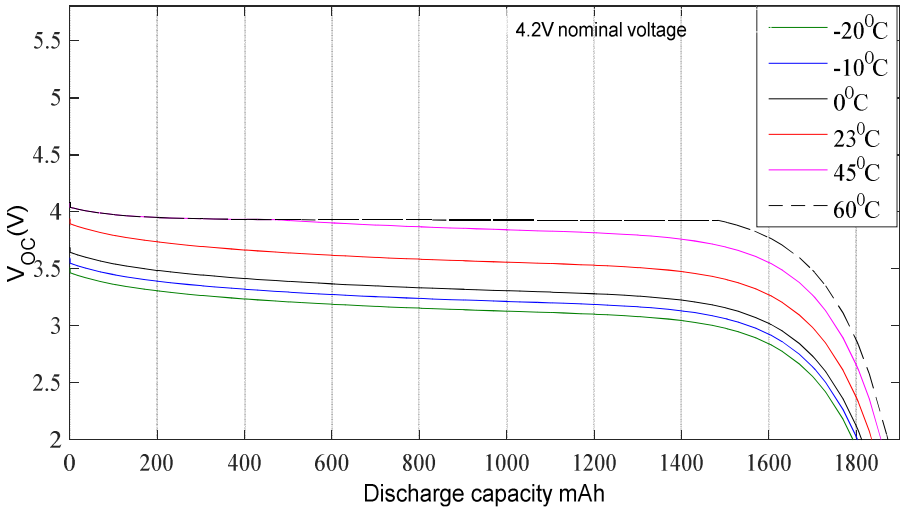

Figure.2.10. V_{OC} versus discharge capacity at different temperatures.

2.3. Battery Pack Modelling

Many methods have been found in literature for BP modelling. Manufacturers' common approach for modelling BPs is the identification of parameters with the extensive experimental analysis. When analysing, manufacturers' common approach they consider the BP as a single unit rather than theoretically combining a large number of cell models. The cell balancing is their main task as they consider the whole unit as one large battery. The other approach within the research community is to model BPs using equivalent electrical circuit model or by using mathematical algorithms. In this method, an equivalent electrical circuit cell model is either connected in series, parallel or series/parallel according to the hardware connections or voltage/current requirements for the end user. Single cell state-space method also used by other researchers to combine into a final state-space model where its subsystems are single cell state-space models.

Among the existing battery models available in the literature Saiju and Heier (2008) had proposed a lead acid battery model which could be extended for EV applications and for BP modelling. When mathematical formulations were examined carefully, the model did not offer correct output results and the reason was found to be with the incorrect Equation (2.22). According to the Equation (2.22), the maximum open circuit voltage it can reach is 2V considering the specific gravity of battery electrolyte (sulfuric acid) is equal to a numerical value 1.2. The Equation (2.22) should be modified either as $V_{OC} = 0.84 + f(SG)$ or the equation reported by Ross (2013) has to be used for correct simulation results. Using Equation

(2.23) (Ross, 2013), modified model was built based on Saiju et al., (2008). The simulation results from the improved model is given in Fig. 2.11.

$$V_{OC}=0.84+SG. \tag{2.22}$$

$$V_{OC} = -168.22968 + 174.1360 \times SG - 1.4836919 \exp(SG)$$

$$- 169.0027 \times SG^{1/2} \times \log(SG) - 0.00077765 / \log(SG) \tag{2.23}$$

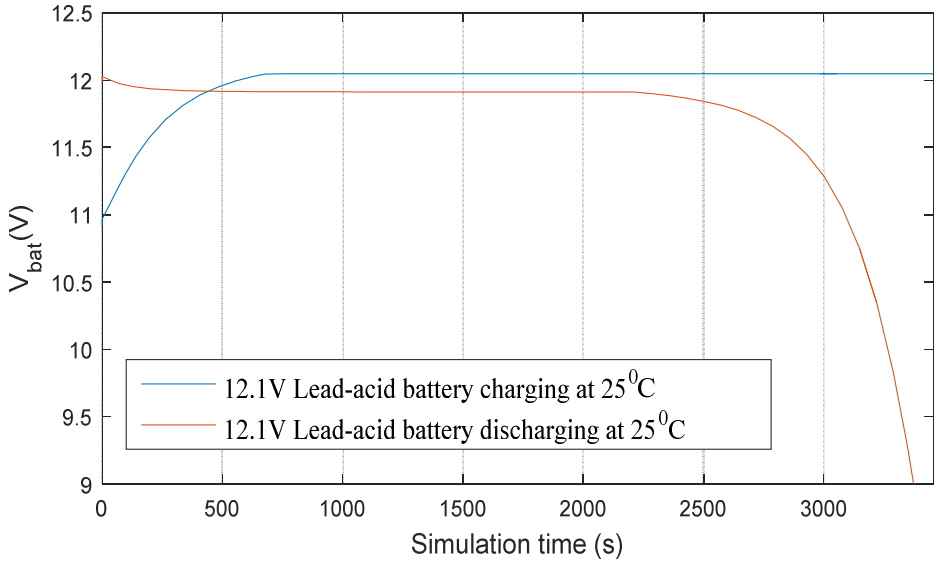

Figure.2.11. Improved model simulation results based on Saiju and Heier (2008).

The BP model presented in this thesis is based on the DP model which was developed in chapter 2. The simulation results of the BP model have been used to compare the experimental data from manufacturers to validate the model. Modelling difficulty reported by many researchers on how to split the battery discharge/charge current for each cell, when connected to an external current source in MATLAB/Simulink has also been resolved and the necessary mathematical formulations are presented in the next section to prove the method.

2.4. Mathematical Formulations for Battery Pack Modelling

When a large number of battery cells are connected in series (N = number of cells) to get a large voltage output, then the total battery terminal voltage is the summation of all cell voltages and can be written by the Equation (2.24).

$$V_{bat} = \sum_{i=1}^{N} V_{ci} \tag{2.24}$$

where, V_{ci} is the battery cell (for example N=5 for a single battery with five cells) output voltage and V_{bat} is the BP output voltage (Here the usage of a cell implies a single cell which is of 12V or 4V battery cell). The SIMULINK block diagram for two battery cells connected in series can be shown in Fig. 2.12.,

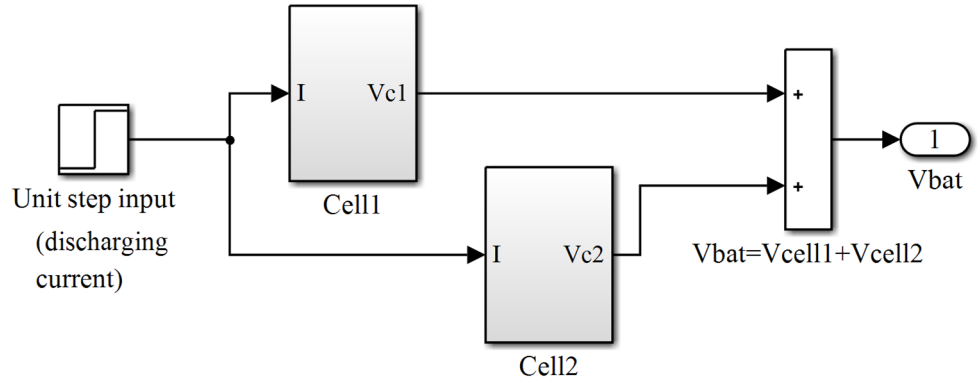

Figure. 2.12. The SIMULINK block diagram of two cells $N \times V_{CellMax}$,($N = 2$) connected in series.

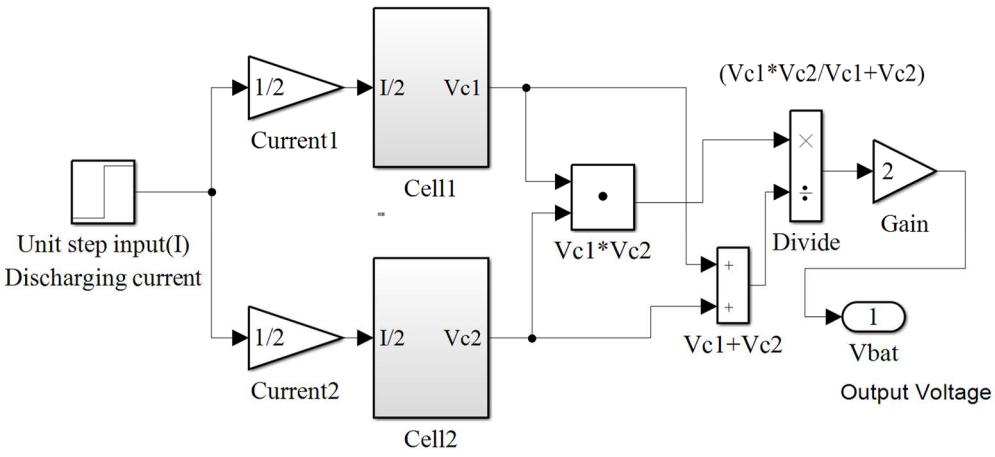

Figure. 2.13. SIMULINK block diagram of two cells in parallel.

When two batteries are connected in parallel, the SIMULINK block diagram for the same is shown in Fig. 2.13. Assuming the two battery cells are exactly similar, the current is split equally to each cell. Using the same notation as in, V_{c1} and V_{c2} are the output cell voltages of cell1 and cell2, and the current sent to each cell is equal to $I/2$. This configuration is shown in Fig. 2.13.

Using Ohm's law, the battery cell output voltage can be written in terms of the battery current and the lumped impedance of the battery cell.

$$V_{c1} = \frac{1}{2} I.Z_1,\ V_{c2} = \frac{1}{2} I.Z_2 \tag{2.25}$$

where, the parameters Z_1 and Z_2 represents the individual lumped impedances (electrolyte, cyclic, polarization, anode/cathode film formation etc.) of the first cell and the second cell. The Equation (2.25) can be used to formulate Equations (2.26) and (2.27)

$$V_{c1}V_{c2} = \frac{1}{4} I^2.Z_1Z_2 \tag{2.26}$$

$$V_{c1} + V_{c2} = \frac{1}{2} I(Z_1 + Z_2) \tag{2.27}$$

The BP output voltage can also be calculated by using the total impedance of the BP (which can be considered as a parallel connection of two impedances of Z_1 and Z_2) and the input current to the BP (which is equal to *I*). Hence, for two-cells the BP output voltage is given by Equation (2.28).

$$V_{bat} = I\left(\frac{1}{\frac{1}{Z_1} + \frac{1}{Z_2}}\right) \tag{2.28}$$

Equation (2.28) can also be deduced by the division of Equation (2.27) by Equations (2.26) and multiplying the result by the number of cells, as shown by Equation (2.29).

$$V_{bat} = 2 \times \frac{V_{c1}V_{c2}}{V_{c1} + V_{c2}} = \frac{2I^2(Z_1Z_2)}{4 \times \frac{1}{2} \times I(Z_1 + Z_2)} = \frac{I(Z_1Z_2)}{(Z_1 + Z_2)} \tag{2.29}$$

The Equation (2.29) is used to build the Simulink model given by Fig. 2.13.b to obtain the correct BP output voltage, V_{bat} for two cells. It may be observed that Equation (2.29) relating V_{c1} and V_{c2} is valid even when the current is not split equally between the two cells but in accordance with the relations given by Equation (2.30),

$$I_{c1} = \frac{I(Z_2)}{(Z_1 + Z_2)},\ I_{c2} = \frac{I(Z_1)}{(Z_1 + Z_2)} \tag{2.30}$$

Mathematical formulation of the output BP voltage for three cells connected in parallel can be derived similar to the two cells (Equation 2.29) that was derived earlier. Assuming the same terminology for three cells and taking V_{c3} as the third cell output voltage and Z_3 as the total impedance of the cell-3, the Equations (2.31) and (2.32) can be obtained as,

$$V_{c1}.V_{c2} + V_{c2}.V_{c3} + V_{c3}V_{c1} = \frac{1}{9} \times I^3 (Z_1 Z_2 + Z_2 Z_3 + Z_3 Z_1) \tag{2.31}$$

$$V_{c1}.V_{c2}.V_{c3} = \frac{1}{27} \times I^3 Z_1.Z_2.Z_3 \tag{2.32}$$

From Equation (2.31) and (2.32), the battery pack voltage V_{bat} can be written using individual cell voltages V_{ci} by (where i is an integer varying from 2 to N),

$$V_{bat} = 3 \times \frac{V_{c1} \times V_{c2} \times V_{c3}}{V_{c1}.V_{c2} + V_{c2}.V_{c3} + V_{c3}V_{c1}} \tag{2.33}$$

The Equation (2.33) can be generalised to *N* cells in parallel and is given by Equation (2.34),

$$V_{bat} = N \left(\prod_{i=1}^{N} V_{ci} \Big/ \sum_{i=1}^{N} \prod_{\substack{k=1 \\ k \neq i}}^{N} V_{ik} \right) \tag{2.34}$$

It is interesting to observe that although, the currents in each of the parallel lines were assumed to be equal, equation (2.33) ensures that correct overall relationship between the battery voltage and cell current is maintained. Moreover, the cells do not need to have identical characteristics and imbalances in the individual cell voltages due to variations in temperature or other properties are acceptable similar to the battery cell model developed earlier.

Three battery cells connected in series are shown in Fig. 2.14.a. and the simulation results are shown in Fig. 2.14.b respectively. The output of BP voltage V_{bat} is equal to the sum of the individual cell voltages. The Simulink block diagram for three 12V batteries connected in parallel (3 cells) is shown in Fig. 2.15.(a) and the simulation results of the same configuration is shown in Fig. 2.15.(b). Furthermore, the Simulink block diagram shown in Fig. 2.14.(a), the

step input is the input parameter and it represents the discharging current. The discharging current is assumed to be constant during the simulation time. Output voltages from each cell is added through the summing block to obtain the total output voltage for three cells in series (36V). The simulation results of this model is shown in Fig. 2.14.b. Though, the input discharging curret is taken as *I,* depending on the internal characteristic of the each cell, the output voltages can be different. However, the summing block adds all the voltages to offer the total BP output voltage shown by V_{bat}.

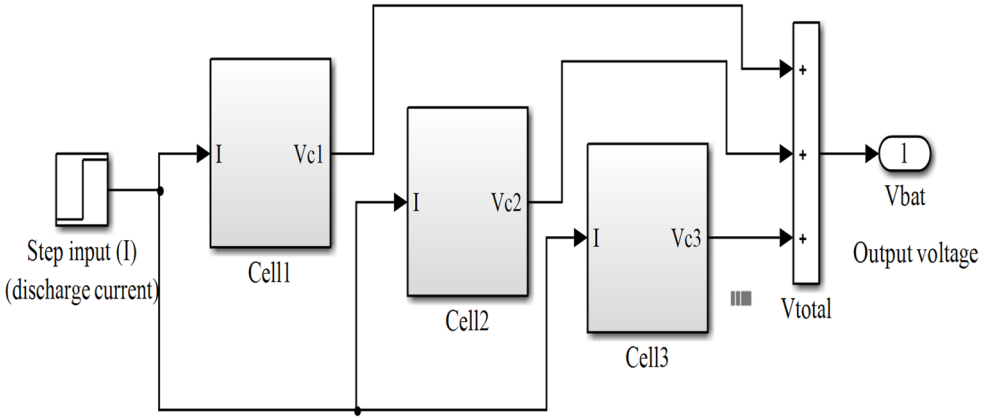

Figure. 2.14. (a) The SIMULINK block diagram of three 12V batteries ($N = 3$) connected in series.

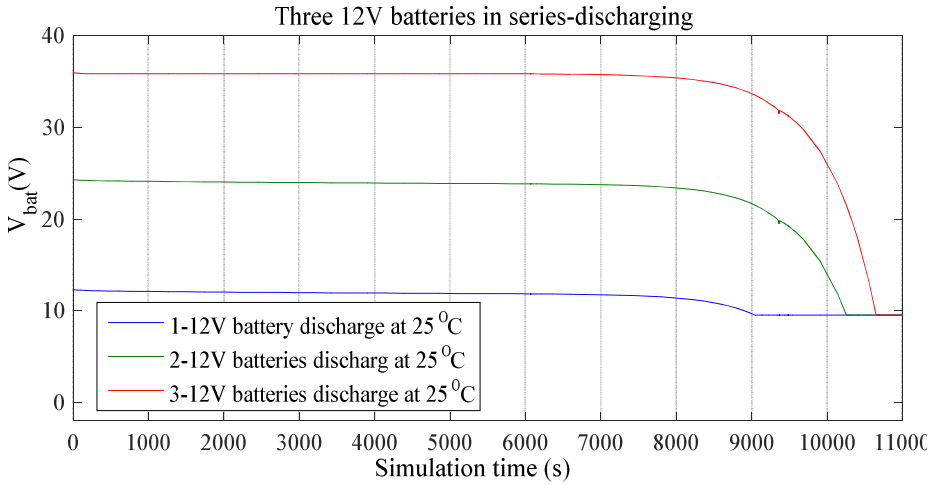

Figure. 2.14. (b) three 12 V batteries in series: the simulation characteristics of V_{bat} versus the simulation time at 1C, at 25ºC.

When the cells are connected in parallel the Simulink block diagram has to be changed according to the mathematical derivations given earlier for three cells. The reason for input current which is divided by three, is described by the Equation (2.31) itself, and then to obtain the correct voltage, the output has to be multiplied by the numerical value 3, which is why the

gain block is given there at the end to get the correct figure (see Equation (2.33)). In all these instances the modelling/simulation is considered only for the BP output voltages and not for the *SOC*.

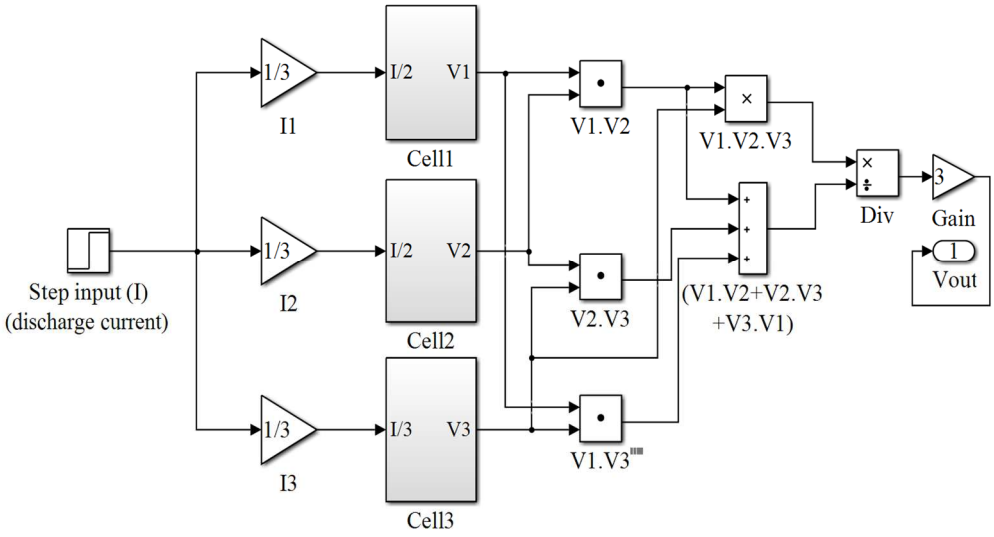

Figure. 2.15.a) The SIMULINK block diagram of three 12V batteries in parallel.

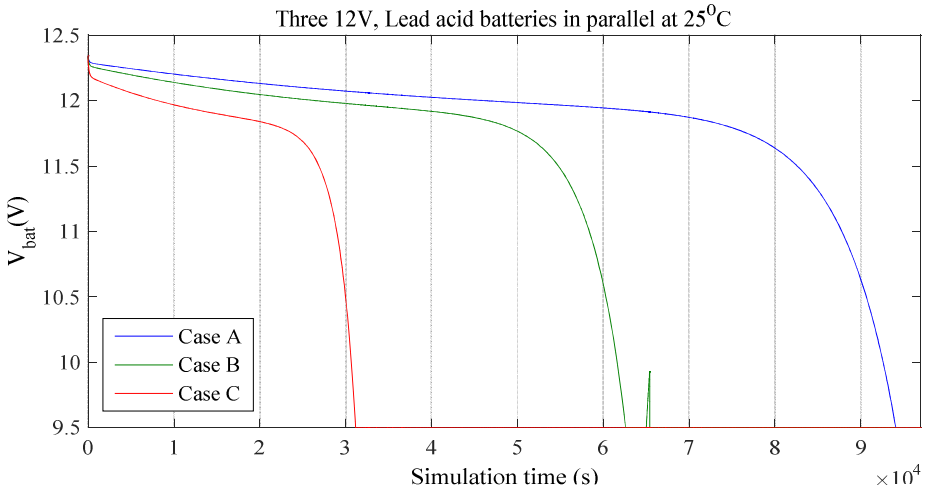

Figure. 2.15.b) the variation of V_{bat} versus the simulation time at 25ºC: Case A: three 12V batteries in parallel. Case B: two 12V batteries in parallel. Case C: single 12V battery simulation.

Fig. 2.16. presents the connection of three battery cells in parallel, two cells in parallel and a single cell. Starting from the top in Fig. 2.16, Cell4 can be either 12V Lead acid battery or 4V Li-ion battery. Output voltage is connected to a Simulink Mux block as shown there. The battery Cell1, Cell2 and Cell3 are connected in parallel similar to the circuit diagram previously shown in Fig. 2.15. The output voltage of these three cells also connected to the same Mux. The Cell5 and the Cell6 are connected in parallel and the output once again connected to the

same Mux block. As it can be seen from Fig. 2.15, the BP comprises with single (taking as 12V each) 12V battery, 3-12V batteries and 2-12 Batteries. Their separate simulation results could be viewed from the Scope block.

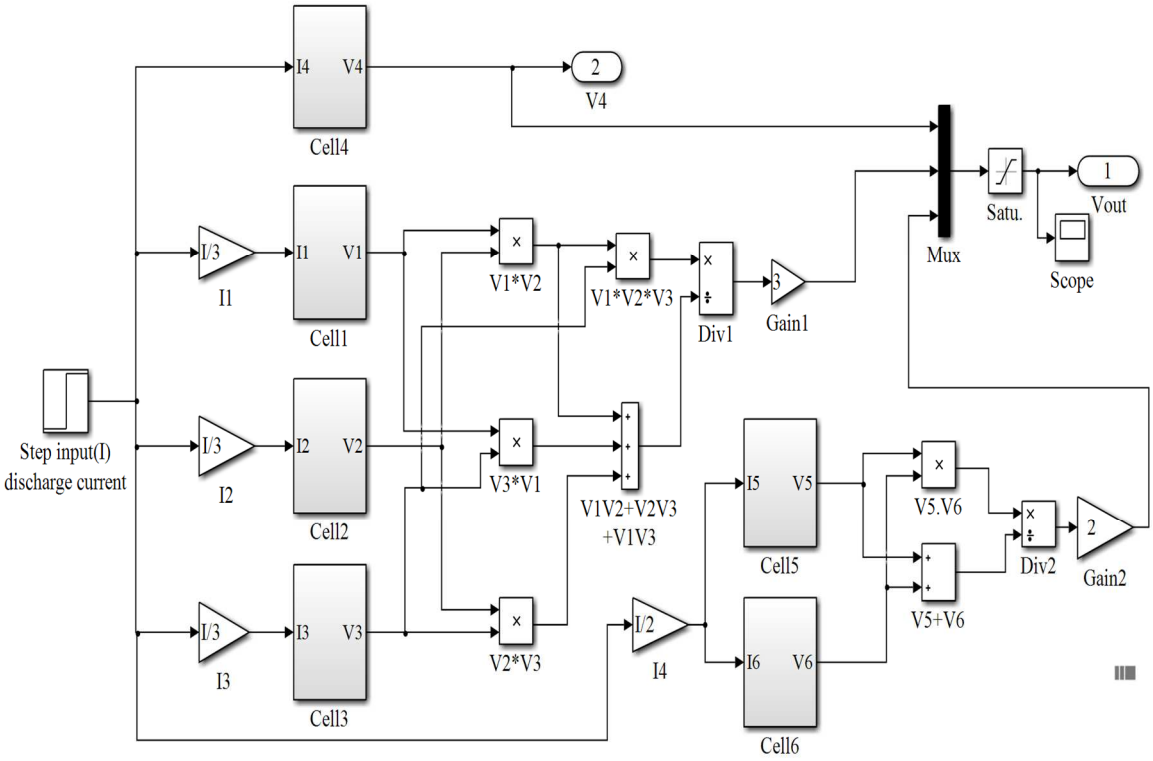

Figure.2.16. The Simulink block diagram for three Lead-acid batteries in parallel; two Lead-acid batteries in parallel; and a single Lead-acid battery are shown.

The Simulink block diagram given in Fig. 2.17.a presents a combination of series and parallel combinations and how to obtain the actual simulation results. Depending on the required BP capacity, the Fig. 2.17.(a) illustrates how the battery cells should be connected at different topologies to configure according to any design requirement. Fig. 2.17.(b) shows the simulation results. As it can be seen in Fig. 2.17.b., it has additional three battery cells of Cell7, Cell8 and Cell9, for the figure shown in Fig. 2.16. The output voltage of the parallel section (Vout1) of the cells: Cell1, Cell2, Cell3, Cell4, Cell5 and Cell6 is obtained from the Mux block in the right hand corner of Fig. 2.17.a. The output voltage of the series array of 3 cells: Cell7, Cell8 and |Cell9 is summed up with a Simulink summing junction (V7+V8+V9). One should note that this output is connected to the Mux1 block. For observation purposes, output from Cell7 and Cell8 also added through a Summing junction block and it is also connected to the Mux1. All these simulation results could be observed under one Scope block which is shown by Scope1. Such simulation results are shown in Fig. 2.17.b. In this simulation the main simulation

parameters are the BP voltage and the simulation time. The input current to the BP is kept constant and the ambient temperature is assumed to be constant during the time of simulation.

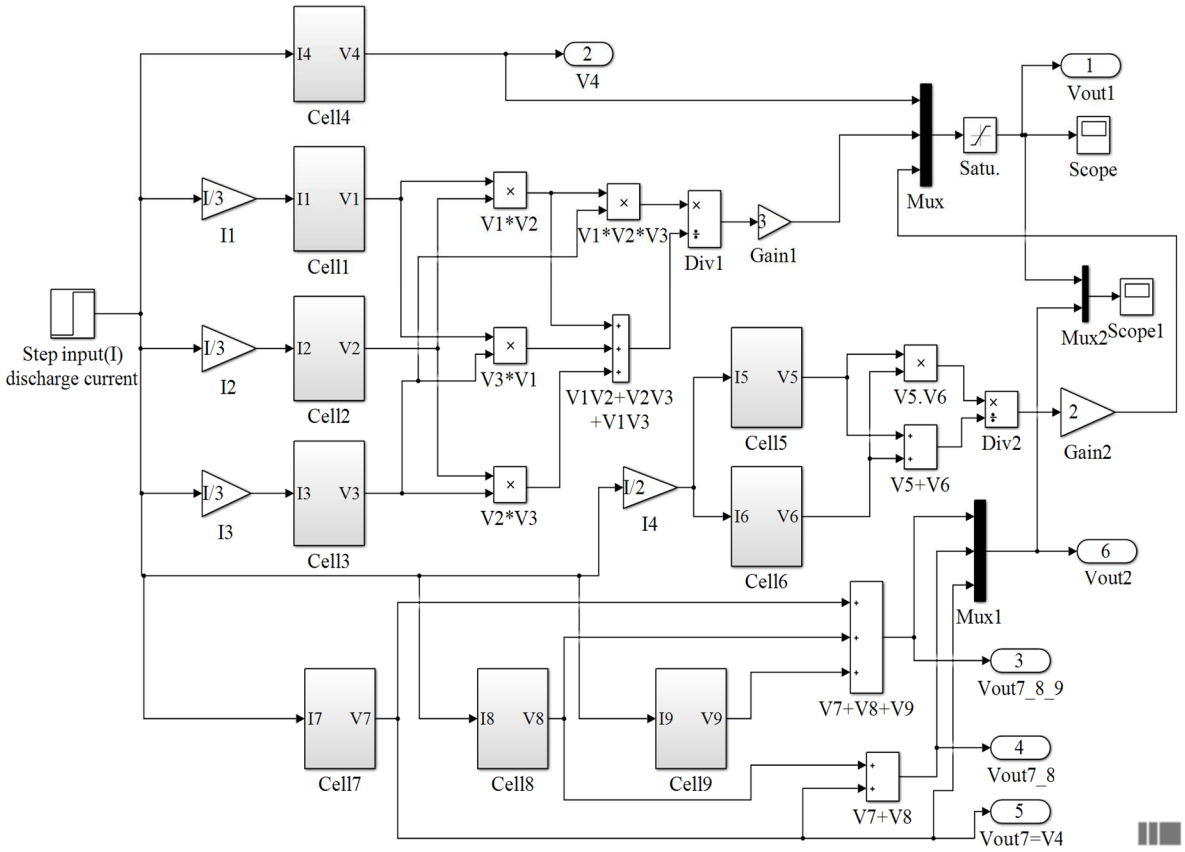

Figure.2.17.(a) The Simulink block diagram of nine 12V Lead-acid batteries connected in different topologies.

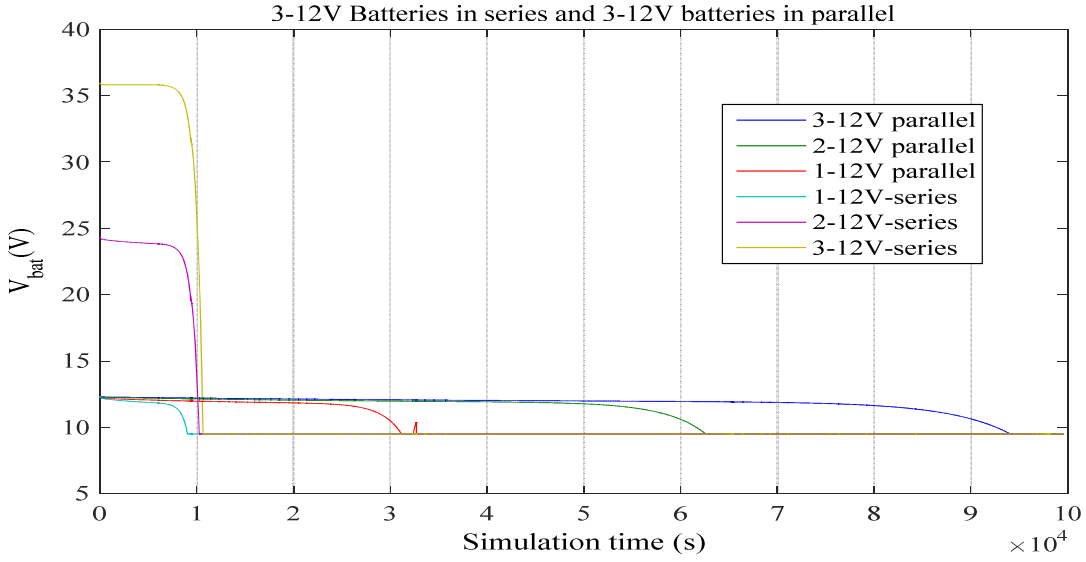

Figure.2.17.(b) Sectional simulations of battery output voltage versus simulation time in seconds at 25ºC.

2.5 Experimental Validation of the BP model

Experimental data published by Dubarry et al., (2009) and Ganesan et al., (2016) is used to validate the BP model presented in this thesis. From Fig. 2.18, it can be seen that the simulation curve is hovering around the experimental plot and the model results can be confirmed as accurate. The slight differences exist there due to electrode material differences and the developed model is a generic model which is not exactly similar with the experimental battery models. In Fig. 2.19, initial BP output voltage is 24.0V and the BP discharge voltage versus simulation time is shown there similar to the graph shown in Fig. 2.18. The data published by Ganesan et al., (2016) is used here to check the developed BP model again and the accuracy is very satisfactory.

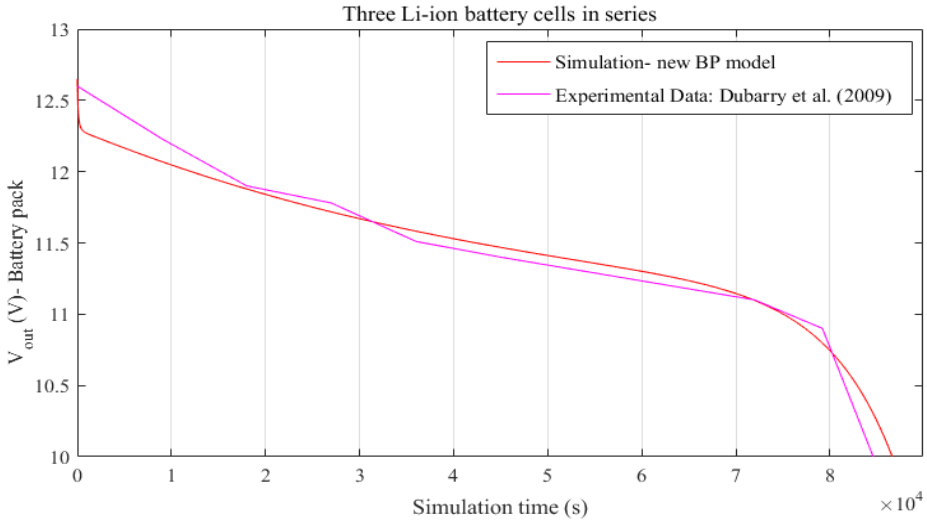

Figure.2.18. Battery pack model comparison with experimental data published by Dubarry et al., (2009)

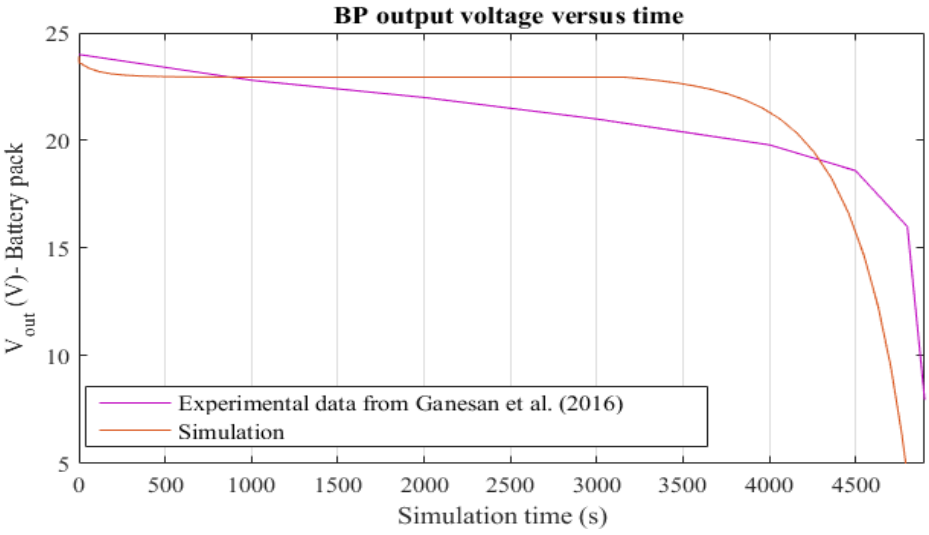

Figure.2.19. Battery pack model comparison with experimental data published by Ganesan et al., (2016)

2.6. State Space Model

The two RC network EEC model shown in Fig. 2.20 is used in this thesis to model the state-space representation. This is the same model that was described earlier in section 2.1 but now, without the temperature effects to reduce the complexity in linearization and computational burden. In literature it is found that even a single RC network model represents the battery chemistry accurately for applications in plug-in hybrid electric vehicles (PHEV) and plug-in electric vehicles (PEV) (Rahimi-Eichi and Chow, 2012; Dubarry et al, 2009). However, two RC networks model has been used by Chen and Chris, (2013); He et al., (2011); Yu et al., (2015); Zhang et al., (2009) and many other researchers to model battery cell model to obtain very accurate results. Hence, in this thesis too the two RC network model is used for the *SOC* analysis and Kalman filter applications.

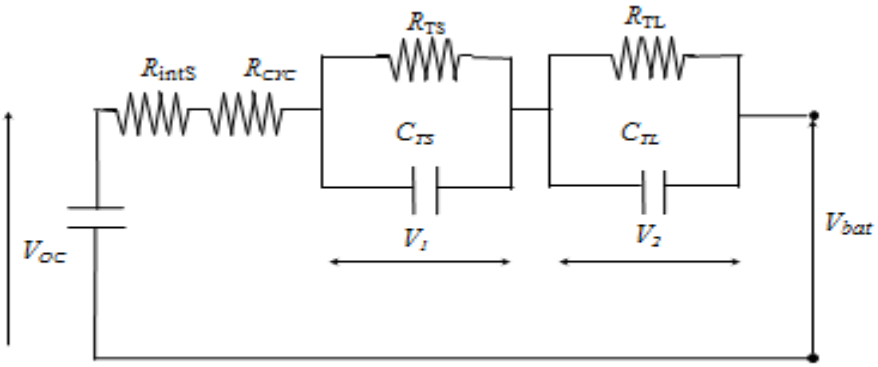

Figure.2.20. Modified equivalent battery circuit model for State-space applications

The current $i(t)$ which passes through the circuit is denoted as i_{bat} or i which is same at this instance. The previous Equations (2.5), (2.6), (2.7) and (2.8) which were used earlier in this chapter is used again in this section for linearization of the nonlinear battery model. The final objective is to use the discretized battery cell model for the Kalman filter applications.

It was noted earlier that the relationship of battery terminal voltage V_{bat} versus *SOC* is not linear and can be written as:

$$V_{bat} = V_{oc} + V_1 + V_2 + i_{bat}(R_{\text{int}\,S} + R_{cyc}), \tag{2.35}$$

But, we use a locally linear model to represent the V_{bat}-SOC behaviour (Yu et al., 2015) as an initial step to linearize the nonlinear behaviour. If the battery terminal voltage can be assumed to be related to the SOC by a locally linear relation,

$$V_{bat} = k \times SOC + d \tag{2.35.a}$$

we obtain the model equation in differential form,

$$\dot{V}_{bat} = k \times \dot{SOC} \tag{2.35.b}$$

Equation (2.35.b) is therefore, assumed to be valid. The value of k in Equation (2.35.b) is obtained from the measured battery characteristic curves. One should note that Equation (2.35.a) then follows by integrating equation (2.35.b).

By defining a new parameter, R_0 where, $R_0 = (R_{\text{int}\,S} + R_{cyc})$ (2.36)

There are two main methods of state-space modelling, relevant to the equivalent electrical circuit model found in literature. The first method is with the input matrix generally symbolises as B which is included in the State equation. The second method is to ignore the input matrix and instead to include it into the output equation. Chang (2013) reported that both of these methods have produced successful results when applied to Kalman filters.

As shown in the Fig. 2.20, let us choose the voltage drop across the two RC networks (capacitors) as V_1, V_2. Also, we choose V_1, V_2 and SOC as state variables for our state-space system (Chen et al., 2013)

The state space equation is given next (Equation 2.37):

$$\dot{x} = \begin{bmatrix} -\frac{1}{R_{TS}C_{TS}} & 0 & 0 \\ 0 & -\frac{1}{R_{TL}C_{TL}} & 0 \\ 0 & 0 & 0 \end{bmatrix} . x + \begin{bmatrix} \frac{1}{C_{TS}} \\ \frac{1}{C_{TL}} \\ -\eta \end{bmatrix} . i \tag{2.37}$$

Where, $x = \begin{bmatrix} V_1 & V_2 & SOC \end{bmatrix}^T$, $A = \begin{bmatrix} -\frac{1}{R_{TS}C_{TS}} & 0 & 0 \\ 0 & -\frac{1}{R_{TL}C_{TL}} & 0 \\ 0 & 0 & 0 \end{bmatrix}$, $B = \begin{bmatrix} \frac{1}{C_{TS}} \\ \frac{1}{C_{TL}} \\ \eta \end{bmatrix}$

Where, $\eta = \frac{1}{(3600C)}$ and C is the battery capacity (in Ampere.hours).

Equation (2.37) is discretized to obtain Equation (2.38) as given next:

$$x_k = \begin{bmatrix} -\frac{1}{R_{TS}C_{TS}}.\Delta t + 1 & 0 & 0 \\ 0 & -\frac{1}{R_{TL}C_{TL}}.\Delta t + 1 & 0 \\ 0 & 0 & 1 \end{bmatrix} . x_{k-1} + \begin{bmatrix} \frac{\Delta t}{C_{TS}} \\ \frac{\Delta t}{C_{TL}} \\ -\eta.\Delta t \end{bmatrix} . i \qquad (2.38)$$

$$y_k = C_d x_{k-1} + D_d i \qquad (2.39)$$

The output from Equation (2.39) can be obtained by defining the C_d matrix which has to be modified according to the requirement: if C_d is defined as [0 0 1] then the output is the *SOC*.

Where x_k and x_{k-1} represents the state variables at time step k and $(k-1)$ respectively. The parameter Δt signifies the sampling time. From equation (2.38) the state variable at time step k can be estimated from the previous step $k-1$. It should be noted that if the initial *SOC* is known for a time step k-1, then the current *SOC* can be calculated using equation (2.38).

2.7. Kalman Filter Application to Battery Cell Model

The Kalman filter is a set of mathematical equations represented in matrix form which provides an efficient recursive means to estimate the state of a process to minimize the mean of the squared error (He et al., 2011). The extended Kalman filter (EKF) represents the linearized version of the Kalman filter for nonlinear systems. It is also explained that an EKF is a quadratic state estimator for a nonlinear system. The purpose of implementing an EKF is to reach the estimated values, $\hat{x}(k)$ close to the true states, $x(k)$. Hence, EKF uses the entire observed data $u(k)$ and $y(k)$ to compute the mean squared error. The Unscented Kalman Filter (UKF) is a

novel development of the EKF. Implementation method is by exploiting several sampling points (Sigma points) around the current state estimate based on its covariance (Yu et al., 2015). This will permit propagating these points through the nonlinear map to get more accurate estimation of the mean and covariance of the mapping results. In this way, it avoids the need to calculate the Jacobian, and reduce the computation time and memory use. In this section Discrete Kalman Filter application to the battery cell model is explained. Implementation method used here is similar to the one presented by Cao (2014). Though, there were many publications found in the literature implementing the Kalman filter, Cao's (2014) method is used as it is simple and computationally faster than the other filters. Other advantage of this method is that it is possible to track any errors in simulation visually by this method. Battery state-space model applied to Kalman filter, Discrete Kalman filter and EKF is well described in references He et al., (2013); Tian et al., (2014); and in Plett (2006). In practical applications, battery management system (BMS) requires an accurate online estimation of the *SOC* in a BP. When the BP is used for a long time the *SOC* estimation is difficult and can leads to inaccuracies. Fuzzy system with EKF is used in reference Long et al., (2012) to improve the accuracy of *SOC* estimations. This approach is still at an experimental stage in its applications for the identification of *SOC* estimation for each single cell in the BP.

2.8. Kalman Filter in Simulink

The Model and the Kalman filter equations used by Cao (2014) are as follows:

Model:

$$\left.\begin{aligned} &\bar{x}(k+1) = G\bar{x}(k) + H\bar{u}(k) + \bar{w}(k), \qquad where, \qquad \bar{w}(k) = N(0, R_w) \\ &\bar{y}(k) = C\bar{x}(k) + \bar{v}(k), \qquad where, \bar{v}(k) \approx N(0, R_v) \end{aligned}\right\} \text{Process} \tag{2.40}$$

Initial conditions:

$$\hat{x}(0|0) = \hat{x}_0 \qquad and \qquad P(0|0) = P_0 \tag{2.41}$$

Gain:

$$K(k+1) = P(k+1|k)C^T\left[R_v + CP(k+1|k)C^T\right]^{-1} \tag{2.42}$$

Measurement Update:

$$\hat{x}(k+1|k+1) = \hat{x}(k+1|k) + K(k+1)\left[\bar{y}(k+1) - C\hat{x}(k+1|k\right] \tag{2.43}$$

$$P(k+1|k+1) = P(k+1|k - K(k+1)C.P(k+1|k) \tag{2.44}$$

There are two covariance matrices in this set of equations: one matrix is with the measurement update and the other is with the propagation (or Time update).

Propagation or Time Update is:

$$\hat{x}(k+1|k) = G\hat{x}(k|k) + H\bar{u}(k) \quad state\ update \tag{2.45}$$

$$P(k+1|k) = G.P(k|k)G^T + R_w \quad covariance\ update \tag{2.46}$$

Where, $\bar{u}(k)$ is the control input, $\bar{w}(k)$ is the process noise which is assumed to be continuous-time Gaussian zero-mean white noise with covariance, Q; $\bar{v}(k)$ represents measurement noise which is assumed to be discrete-time Gaussian white noise with zero mean and a covariance R_v (R_v is taken as 1000 in this case). The parameter, K is the Kalman gain and the matrix C is the partial derivative of $H_k(\hat{x}_k, \hat{v}_k)$ with respect to $\hat{x}_k$. One should note that these Kalman filter parameters are standard definitions and the details could be found in many papers published in the literature.

In the mathematical representation given above, our model (plant/process) is the battery cell model and the input parameter $\bar{u}(k)$ is the battery open circuit voltage.

Initial Kalman filter model is constructed in Simulink using equations (2.42) to (2.46). The following data matrices *A, B, Q, P* which were used in reference Yu et al., (2015) have been used here to test the Kalman filter simulations. One should note that EEC model parameter identification tests (HPPT, Voltage pulse discharge and current pulse discharge) were not done in this research due to some reasons, however, the data published by Yu et al., (2015) and Chen et al., (2013) is used to estimate the *SOC*.

TABLE 2.3. Parameter values for the equivalent circuit model shown by Fig. 2.18.

Parameter	Value (Chen, et al, 2012)	Value (Yu, et al. 2015)
R_0	0.0013Ω	0.0178 Ω
R_{TS}	0.0042 Ω	0.2336 Ω
R_{TL}	0.0024Ω	0.5667 Ω
C_{TS}	17111F	0.1764 F
C_{TL}	440.57F	127.35 F

The discrete-time state space model is obtained using Equation (2.38) and the average parameter values given in Table 2.3: sampling time is taken as 0.1s.

$$A=\begin{bmatrix}-0.014 & 0 & 0\\ 0 & -1.135 & 0\\ 0 & 0 & 0\end{bmatrix},\ B=\begin{bmatrix}5.8442\times10^{-5} & 2.2698\times10^{-3} & -1.3889\times10^{-5}\end{bmatrix}^{T}$$

(10^{-5} is frequently denoted as e-5).

R is taken as 1000 and $Q=\begin{bmatrix}0.1 & 0 & 0\\ 0 & 0.1 & 0\\ 0 & 0 & 0.01\end{bmatrix}$, Error covariance, $P=\begin{bmatrix}0.1 & 0 & 0\\ 0 & 0.1 & 0\\ 0 & 0 & 0.01\end{bmatrix}$

In literature it is reported that the battery parameters vary with the simulation time (Yu, et al., 2015). This statement confirms that the *SOC* and temperature also change during the simulation time.

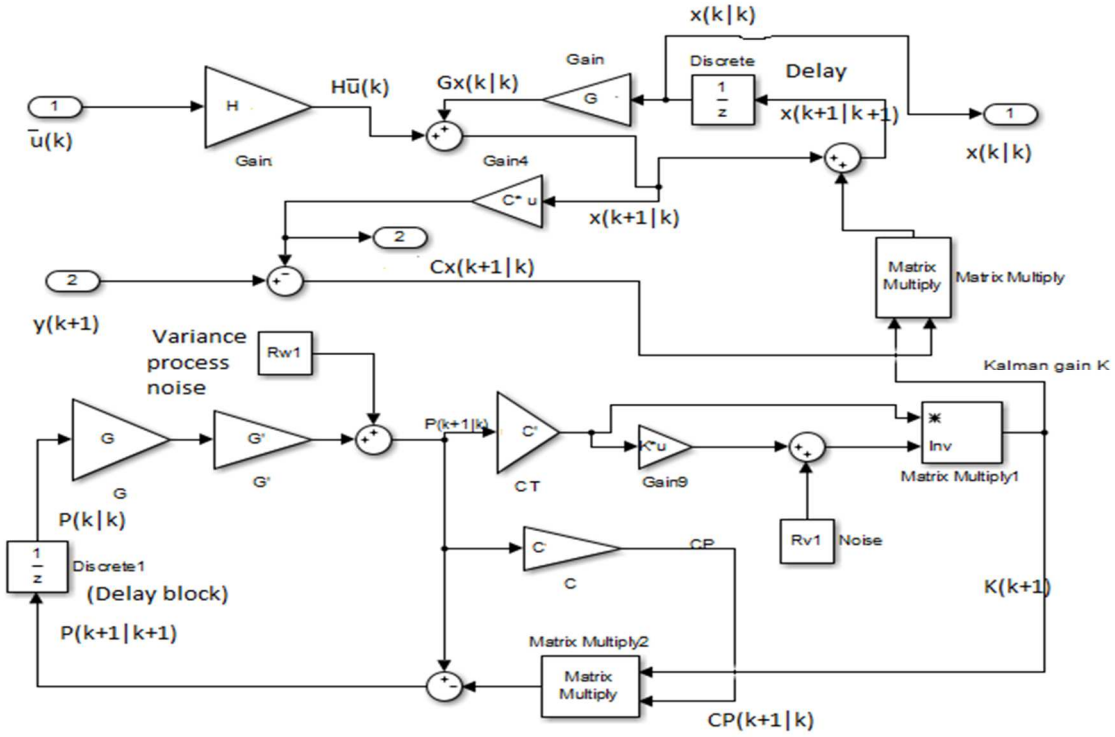

Figure.2.21. Extended Kalman Filter for battery output voltage estimation: Equations (2.42) to (2.46) is modelled in Simulink: battery cell model considered as a plant in state-space.

The battery cell model shown in Fig. 2.20. is constructed using Simulink in this sub-section. The Simulink block diagrams shown in Fig. 2.21 and Fig. 2.22 are the subsystems of the total system including Kalman filter. The total system with two subsystem blocks are shown in Fig.

2.23. It should be noted that without the total system shown in Fig. 2.23 it is impossible to obtain the simulation results.

Describing what is shown in Fig. 2.21, the plant (Simulink block diagram) represents the state-space equation given earlier by Equation 2.40. In Equation 2.40, R_w and R_v are related to the process noise and the measurement noise as described earlier: the random number generator block in the Simulink generates the Gaussian distributed noise, and generates zero mean noise with certain variance. To suit the variance R_w which is a matrix of σ^2, and the gain block R_w is actually the made $\sqrt{R_w}$ inside the gain block. The same procedure applies to the random number block to generate R_v which is contaminated with measurement noise and in the gain block shown in Fig. 2.22 (output from Random noise generator2) it is taken as the $\sqrt{R_v}$. It should be noted that the system states are $x=[V_1, V_2, SOC]^T$ and the matrix C [0 0 1]is generated to obtain *SOC* as the output.

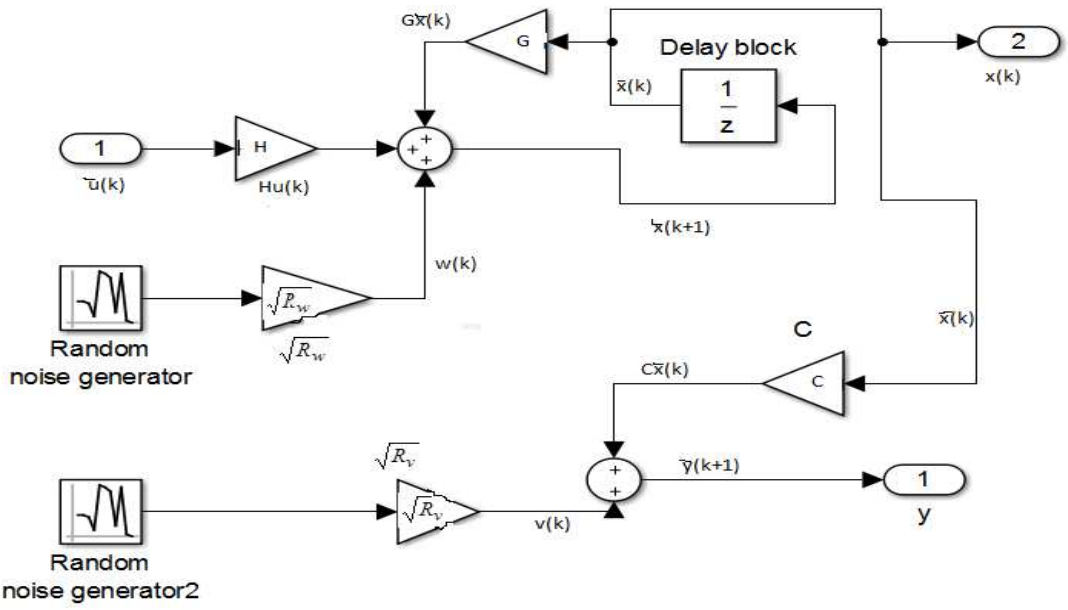

Figure.2.22. Battery cell model in state-space form with plant noise and measurement noise (Equations 2.40 which is given as the plant or process model)

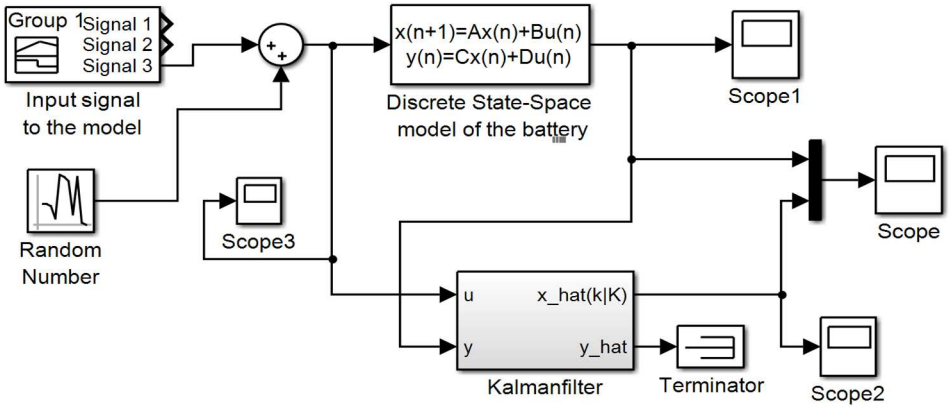

Figure 2.23. Total subsystems model combined with battery cell model and the Kalman filter

Simulation results were obtained from the total system which is shown in Fig. 2.23. Initially Battery open circuit voltage, V_{OC} versus the time steps were plotted and is shown by Fig. 2.24. The battery open circuit voltage is taken as 4.2V and it is assumed that the temperature does not change during the simulation time. The operating temperature is taken as 25ºC. Initially the plant output due to noise and measurement noise and errors it was moving up and down randomly. However, Kalman filter filters the noise and tracks the output correctly after about 80 time steps and follows the output correctly.

In this application the Discrete Kalman filter (DKF) was chosen as it is suitable for non-linear applications. DKF linearizes about an estimate of the current mean and covariance (Yu et al., 2015). Simulation results shown in Fig. 2.24 and Fig. 2.25 illustrate the battery open circuit voltage variation versus sampling steps and the *SOC* variation with the simulation time.

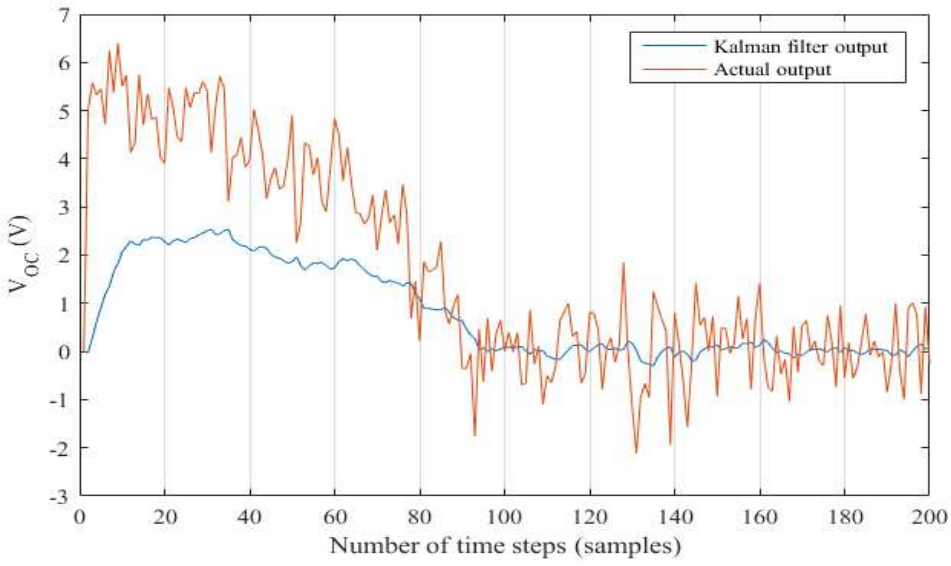

Figure.2.24. Battery open circuit voltage variation with time using DKF

The *SOC* versus simulation time characteristics are shown in Fig. 2.25. As shown by the legend, the output *SOC* signal is contaminated with noise and the Kalman filter eliminated the noise and tracks the *SOC* correct signal shown by blue line. The red line shows the actual simulated *SOC* with charge counting method. The simulation time is taken as 3000 seconds and the operating temperature is at 25^0C. It is assumed that the operating temperature is constant during the simulation time.

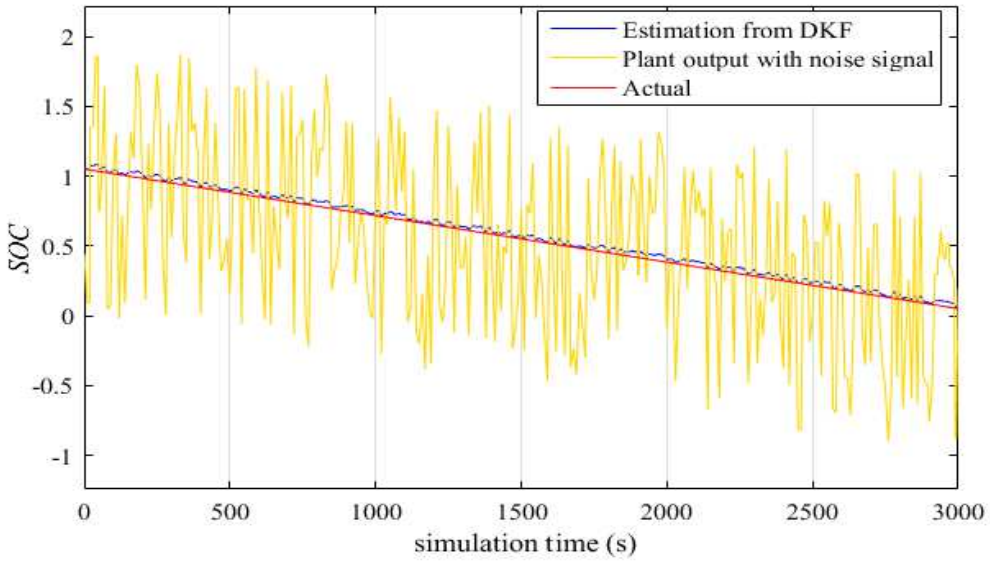

Figure.2.25. Battery *SOC* estimation versus time using EKF.

2.9. Summary

The BP model presented here is a new Simulink model which could be applied to model hybrid energy systems and study the simulation results. The building block used, is a single cell EEC model which is also a new cell model developed in this thesis. It was validated by simulating several multi-cell BP configurations in Simulink and also by comparing with experimental data available from literature. The battery cell model presented was also validated using manufacturers data and the data published by previous researchers. The cell model is suitable for a range of series-parallel combinations of dissimilar individual cells with differing voltage outputs, due to a variety of physical reasons (Temperature, internal impedances, initial state of charge of battery cells etc.). Mathematical formulations required to build the Simulink BP model was also described in this chapter. New improved parametric constants (Table 2.1) was

presented for Li-ion battery cell modelling and the table can be used to improve simulation results. Table 2.2 presented in this chapter is another contribution to the battery cell modelling and the parametric constants derived here are necessary for modelling thermal effects of the battery cell modelling.

New improved battery cell model simulations and the correct mathematical formulations were presented based on Saiju et al., (2009) Lead-acid battery model. Application of Bernardi thermal energy balance equation to Li-ion battery cell model was described and its application to Simulink had also been described with simulation results. Many new mathematical formulations were presented relevant to the battery cell chemistry.

Kalman Filters can accurately (minimum variance) estimate the states affected by broadband noise contained within the system bandwidth which cannot be filtered out generally using classical techniques, and therefore it is an empirical trade-off between modelling errors and the influence of noise. While KF can be applied to linear systems, DKF can estimate measurements related to nonlinear systems very accurately. In this chapter, state-space battery cell model was described and its Simulink model was applied to estimate the *SOC* values with the DKF. The simulation results had shown that the DKF estimated the correct *SOC* and the output voltage accurately when contaminated with noise. Finally, in summarising it can be stated that battery cell model and the BP model have been validated with experimental data and both models have been deemed quite suitable for EV or HEV applications.

Chapter 3: Nonlinear Modelling and Feedback Control of Variable Speed Wind Turbines

Outline

Feedback control of variable speed wind turbines is presented in this chapter. At the inception, modelling wind energy to harvest kinetic energy through the turbine blades is described. Thereafter, converting the mechanical energy into other useful forms of electrical energy through the generator is considered and the relevant mathematical formulations are presented. The state-space models for the gear changing mechanism, a hydraulic actuator, non-linear model of wind speed, doubly fed induction generator (DFIG) are presented and the mathematical analysis is given thereby transforming into linearized state-space models where necessary.

3.0 Introduction

Wind turbines (WTs) exploit wind energy to generate electricity from generators which are coupled to the turbine hub through gear box shafts. Typical megawatt capacity large scale wind turbine components are shown in Fig. 3.1. It comprises the following parts and subsystems: the tower (generally 25 to 75 metres in height for large scale WTs), turbine rotor blades (mainly made out of fibreglass-reinforced polyester or wood-epoxy; the blades are usually between 30 - 80 metres in diameter), hub, turbine shaft, antenna, the yaw mechanism, cooling system, wind speed & direction monitor, the gear box, cables, brackets and the main box called nacelle which stands on top of the tower structure (Energy, US Department of Energy, 2017).

There are two main types of wind turbines available in the market. They are horizontal axis and vertical axis wind turbines. The horizontal axis wind turbine (HAWT) has its blades rotating in an axis parallel to the ground. The vertical axis wind turbine (VAWT) has its blades rotating in an axis perpendicular to the ground. Generally, HAWTs are commercially popular and they have been outnumbered with the VAWTs (Renewableenergyfocus.com, 2009). There are a number of available designs for both categories and each type has certain advantages and disadvantages. HAWTs have higher wind energy conversion efficiency as they can reach stronger wind by increasing the tower height. The VAWTs have lower wind energy conversion

efficiency and the higher torque fluctuations where they can also be subjected to mechanical vibrations.

As at today, the largest HAWT has the electricity generating capacity of 7.6 MW (with the advancement of new control techniques these capacity values have been increasing). The HAWT installed in Estinnes, Belgium (model, E-126) has the tower height of 126 meters. However, limitations are there for the capacity increase as there are structural constraints related to installation in the sea or in the land (Blaabjerg and Ma, 2013).

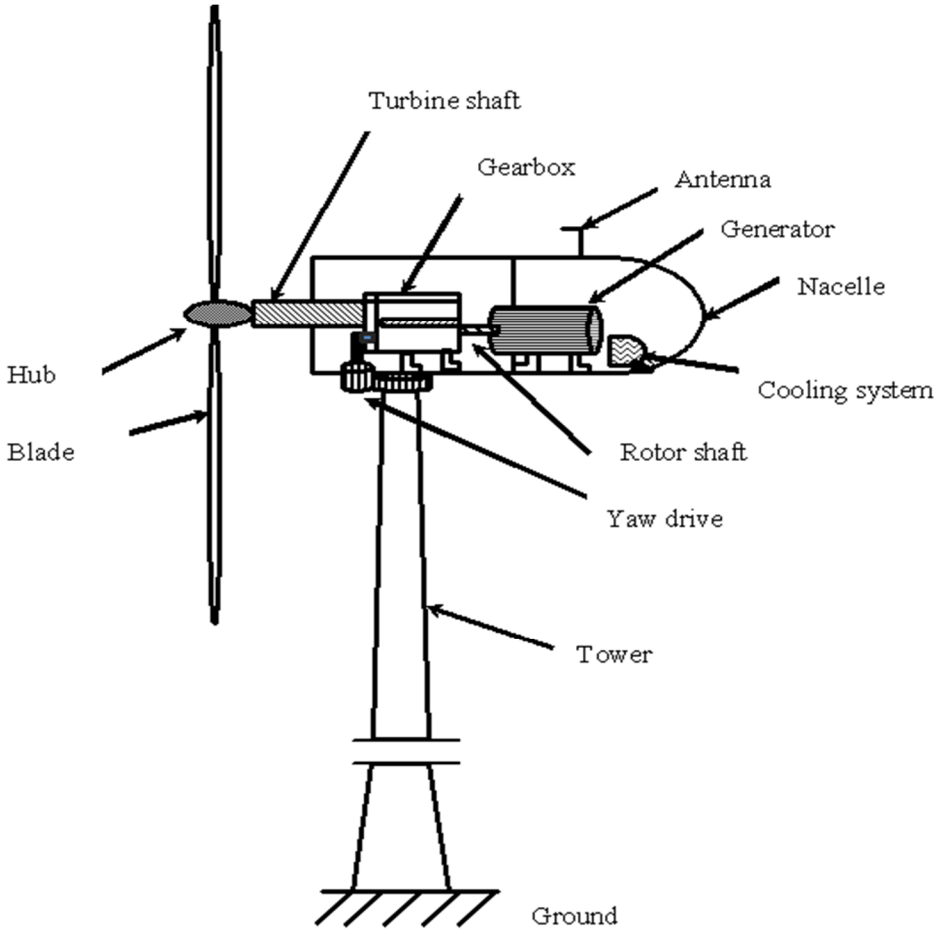

Figure 3.1. Cross-sectional view of a large horizontal axis wind turbine second (Larsen and Mogensen, 2006).

3.1. Mathematical Modelling and Simulations

The WTs operate in two positions depending on the nature of the tower height. In the upwind rotor configuration (with the upwind WTs, the turbine blades face the wind: where the wind catching elevation is at a higher level from the ground), the rotor axis is placed in front of the

tower and in the downwind type the rotor is placed behind the tower relative to the wind direction.

Energy in the wind can be modelled by considering a flow of wind stream passing through the turbine blades. The parameters can be defined as: V_1= upstream wind speed, V_2= downstream wind speed, ρ = density of air, S = air stream cross sectional area, S_1 = upstream cross sectional area, S_2= downstream cross sectional area.

Assuming the stream of air passing through the turbine blades as incompressible, the conservation of mass or continuity Equation can be written as,

$$\dot{m} = \rho S_1 V_1 = \rho S V = \rho S_2 V_2 = \text{Constant;} \tag{3.1}$$

Considering the mass flow rate as constant along the wind stream, the power exerted can be written by (Dolan, 2010): $P=FV$, where, F is the force. The power P as the rate of change in kinetic energy from upstream to downstream is given by,

$$P = \frac{1}{2}\dot{m}\left(V_1^2 - V_2^2\right), \tag{3.2}$$

where, $\dot{m}$ is the mass of the air stream passes through the turbine blades per second (Larsen and Mogensen, 2006).

Using the continuity equation with the application of Fluid mechanics,

$$P = \rho S V\left(V_1^2 - V_2^2\right), \tag{3.3}$$

where, V is the wind speed passing through the turbine rotor blades.

Equating the two expressions we can get,

$$P = \frac{1}{2}\rho S V\left(V_1^2 - V_2^2\right) = \rho S V^2 (V_1 - V_2) \tag{3.4}$$

$$\therefore \frac{1}{2}\left(V_1^2 - V_2^2\right) = \frac{1}{2}(V_1 - V_2)(V_1 + V_2) \tag{3.5}$$

Assuming the average wind speed at the turbine, $V = \frac{1}{2}(V_1 + V_2)$; since, $Force = \frac{Power}{Velocity}$, from Equation (3.3) we can write,

$$F = \rho S V (V_1 - V_2) = \frac{1}{2}\rho S\left(V_1^2 - V_2^2\right) \tag{3.6}$$

Power, P can also be written with V_1 and V_2 excluding V,

$$P = \rho S V^2 (V_1 - V_2) = \frac{1}{4}\rho S (V_1 + V_2)^2 (V_1 - V_2)) = \frac{1}{4}\rho S \left(V_1^2 - V_2^2\right)(V_1 + V_2) \tag{3.7}$$

By introducing a downstream velocity factor, b, as given in Ragheb (2015), we can write,

$$b = \frac{V_2}{V_1}. \tag{3.8}$$

Hence, the extractable power, P can be written as,

$$P = \frac{1}{4}\rho S V_1^3 (1 - b^2)(1 + b) \tag{3.9}$$

The kinetic power content of the undisturbed upstream wind stream with $V=V_1$ and over a cross-sectional area S becomes,

$$W = \frac{1}{2}\rho S V_1^3 \tag{3.10}$$

The performance coefficient or efficiency is a dimensionless ratio of the extractable power P to the kinetic power W available in the undisturbed stream, which is given by Equation (3.11),

$$C_p = \frac{P}{W} = \frac{\frac{1}{4}\rho S V_1^3 (1 - b^2)(1 + b)}{\frac{1}{2}\rho S V_1^3} \tag{3.11}$$

$$= \frac{1}{2}(1 - b^2)(1 + b) \tag{3.12}$$

Variation of C_P which is also identified as the power coefficient versus b is shown in Fig. 3.2: Maximum C_P value and the relevant b value can also be obtained analytically by differentiating Equation (3.12) with respect to b which is given next,

$$\frac{dC_p}{db} = \frac{1}{2}\left[\left(1 - b^2\right) - 2b(1 + b)\right] = 0 \tag{3.13}$$

The solution to the Equation (3.13) gives you either b=1/3 or b= -1. Neglecting b= -1 and taking b= 1/3= 0.33 confirms the graphical value. The corresponding C_P can be obtained as the maximum value: $C_{P_{Max}} = \frac{1}{2}\left(1 - b^2\right)(1 + b)) = \frac{1}{2}\left(1 - \left(\frac{1}{3}\right)^2\right)\left(1 + \frac{1}{3}\right) = 0.59259$ (3.14)

The $C_{P\_\max}$ value, 0.59259 is defined as the Betz coefficient or Betz limit and the theoretical limit is the value derived above. MATLAB script for the Fig. 3.2. is given in Appendix: A.

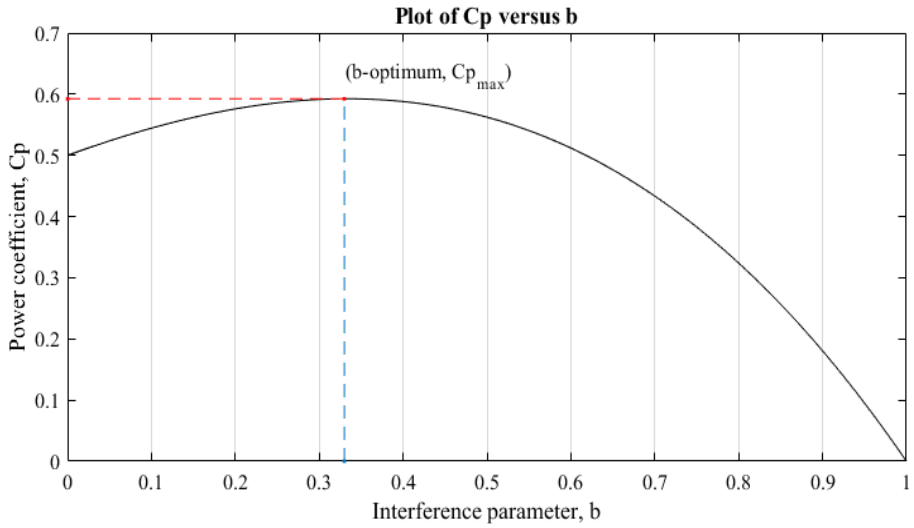

Figure 3.2: Plot of C_P versus *b*: $C_{P_{\max}}$ = 0.5926 and *b-optimum*= 0.3300.

Experimentally, it is found that the C_P value is a function of the pitch angle θ and the tip speed ratio λ (the tip speed ratio is also a function of wind speed *V*). The tip speed ratio (TSR) is defined as the ratio between the velocity of the tip of the blade to the actual velocity of the wind,

$$\lambda = \frac{\omega_r R}{V} \tag{3.15}$$

where, ω_r is the rotor's rotational speed, R is the radius of the blade and V is the wind speed at the rotor (In some references TSR is defined as $\lambda = \frac{V}{\omega_r R}$ then the λ values should be taken as the reciprocal of the previous λ defined by Equation (3.15). The aerodynamic torque, T_r extracted by the wind turbine: $T_r = \frac{P_r}{\omega_r}$ is related to the total power, P_r absorbed by the turbine from the wind is given by (Thomsen, 2006; Anderson, 2009),

$$P_r = \frac{1}{2}\rho\left(\pi R^2\right)V^3 C_p(V,\lambda,\theta) \tag{3.16}$$

For convenience by taking: $C_P(V,\lambda,\theta) = C_P$,

$$P_r = \frac{1}{2}\rho\left(\pi R^2\right)V^3 C_p \tag{3.17}$$

$$\text{or, } P_r = \frac{1}{2}\rho\pi R^2\left(\frac{{\omega_r}^3 R^3}{\lambda^3}\right)C_P \tag{3.18}$$

Using Equation (3.16) we can write,

$$\begin{aligned} T_r &= \frac{1}{2}\rho\pi\left(\frac{{\omega_r}^2 R^2}{\lambda^2}\right)R^3\frac{C_P}{\lambda} \\ T_r &= \frac{1}{2}\rho\pi V^2 R^3 C_T \end{aligned} \tag{3.19}$$

where, C_T which is equal to $\frac{C_P}{\lambda}$ is defined as the thrust force coefficient or torque coefficient. The power coefficient $C_p(V,\lambda,\theta)$ can be given as empirical formulations as shown in Equations (3.20) and (3.21), (Nasiri et al., 2014),

$$C_p(V,\lambda,\theta) = \underbrace{C_1\left(\frac{C_2}{\lambda_i} - C_3\theta - C_4\right)}_{f_1}\underbrace{e^{-C_5/\lambda_i}}_{f_2} + \underbrace{C_6\lambda}_{f_3} \tag{3.20}$$

$$\frac{1}{\lambda_i} = \underbrace{\frac{1}{\lambda+0.08\theta} - \frac{0.035}{1+\theta^3}}_{f_4} \tag{3.21}$$

It can be seen from Fig. 3.2 the maximum value that C_p could reach is 0.56. The information from Fig. 3.4, reveals that for the pitch angle of 0º and with the maximum C_p value of 0.48, the λ is equal to a numerical value 8. When the pitch angle is 5º the maximum value of C_p is 0.35 (black line shown in the legend). Hence it is fair to assume that the pitch angle between 0º and 5º the C_p values are maximum when λ=8. Literature review indicated that the pitch angle actuators operate generally, between 2º to 3º for large wind turbines, which is correct according to Fig. 3.4 results to harvest maximum power.

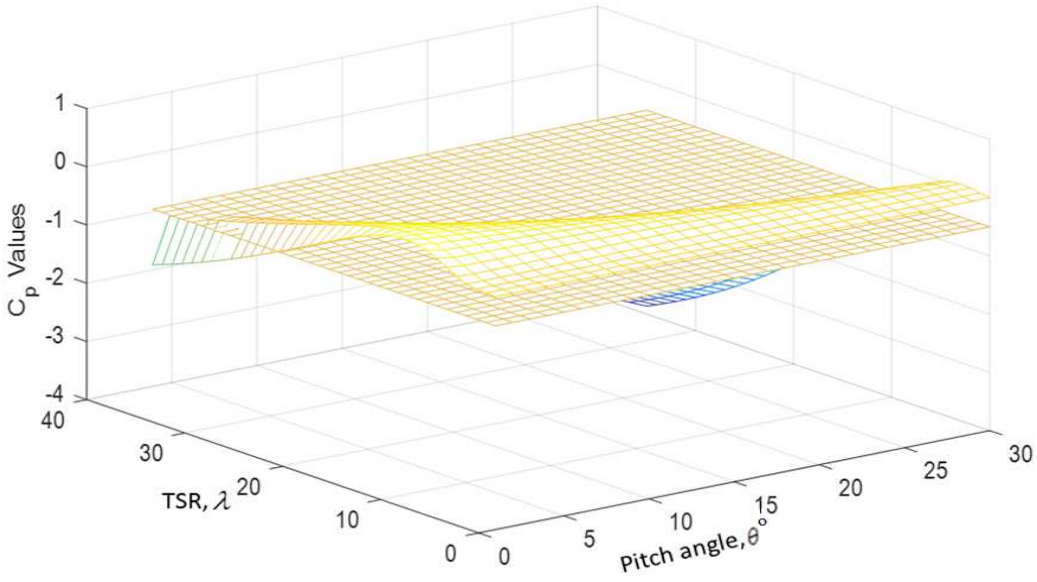

Figure 3.3: C_P plot with varying pitch angle, θ^o and TSR, λ.

While Fig. 3.3 shows the three dimensional view of all three parameters, C_P, λ and θ^o the variation of C_P values with λ against specific pitch angles is shown in Fig. 3.4. The variation of C_P values with λ and the variation of C_T values with λ for a constant pitch angle are shown in Fig. 3.5. The parameter θ^o is the pitch angle.

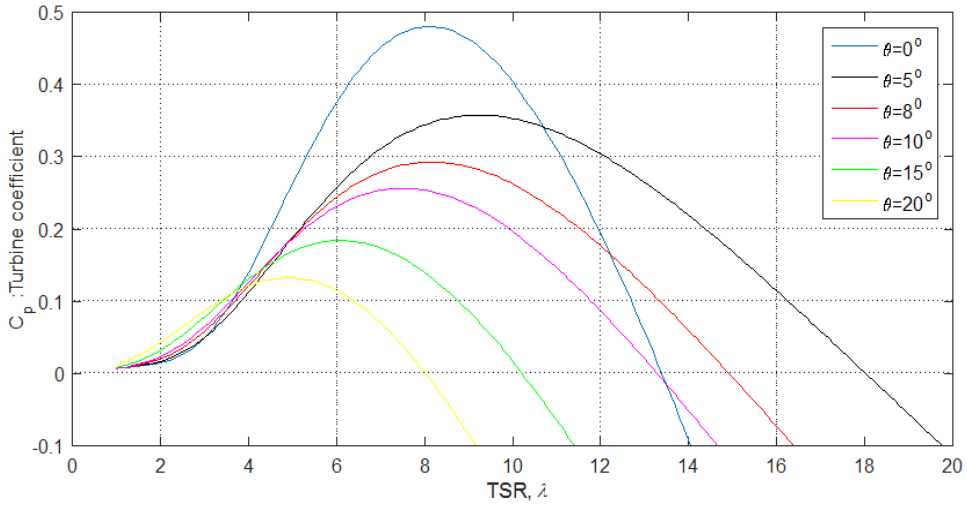

Figure 3.4: Characteristics of C_P versus λ at constant temperature and at varying pitch angles.

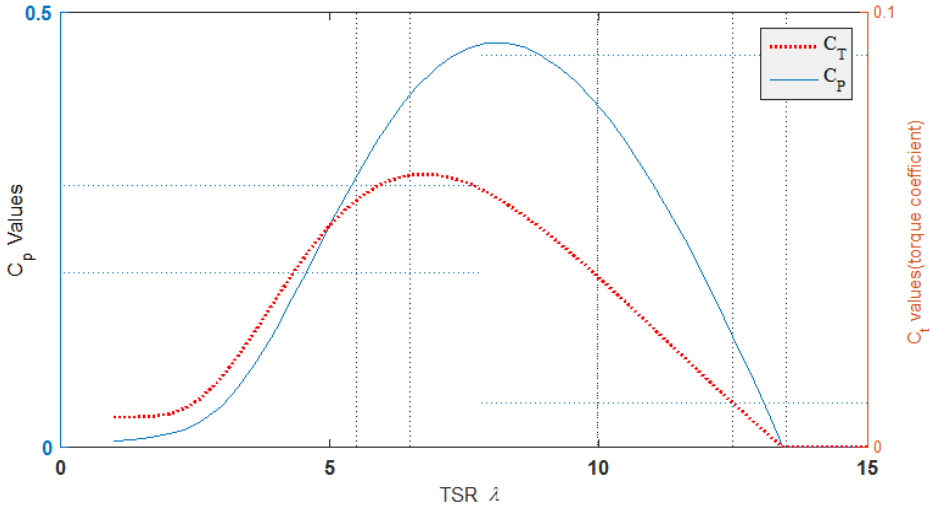

Figure 3.5: Typical characteristics of C_P and C_T versus λ at a constant pitch angle $\theta = 2^o$.

The C_P versus λ curves shown in Fig. 3.4. is generated using the Simulink subsystems models shown in Fig. 3.6 and in the Simulink model as shown in Fig. 3.7. In Fig. 3.6. under subsystem blocks, 'Subsystem with $B = 0$' implies that the pitch angle, θ^o which is equal to zero for that subsystem block. Inside each subsystem block, detailed Simulink block diagram is shown in Fig. 3.7.

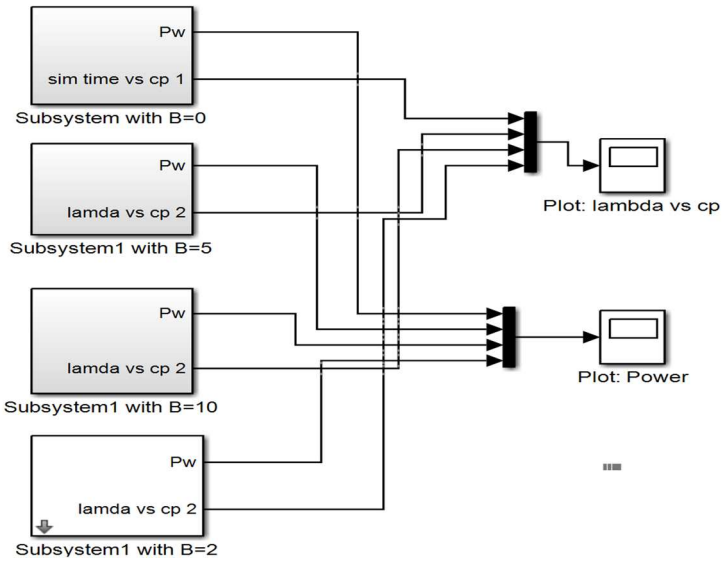

Figure 3.6: Simulink (Subsystems model) model for C_P calculations.

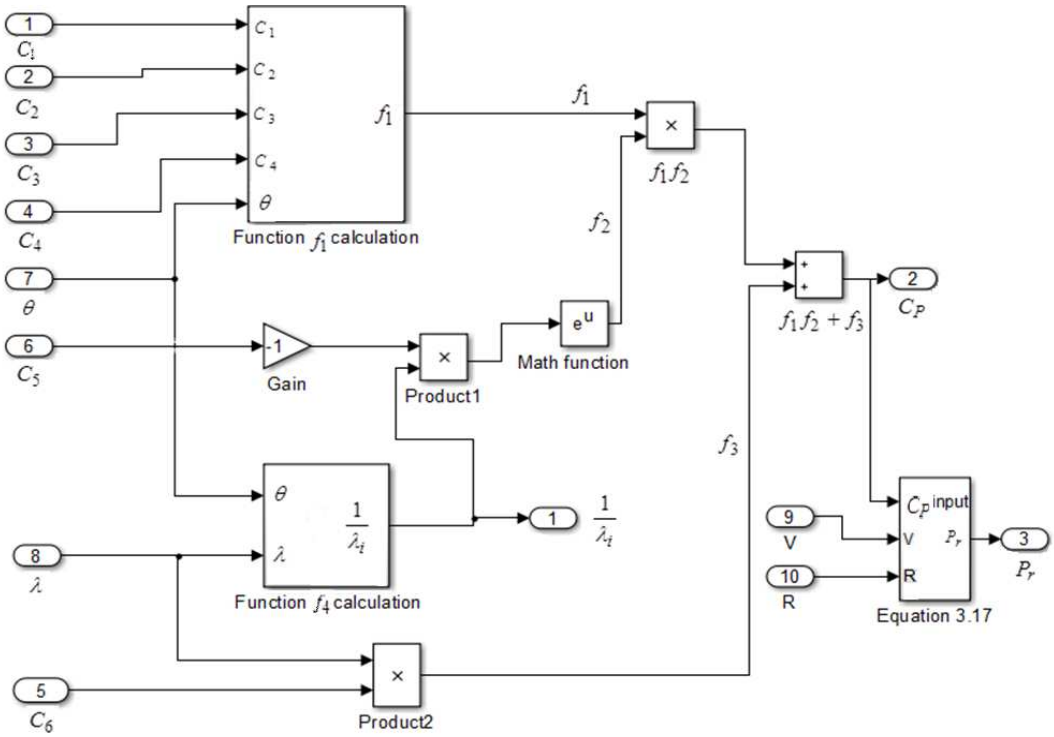

Figure 3.7: Simulink model which calculates the C_P versus TSR, λ with varying pitch angle θ° at constant temperature.

Simulink input blocks designated from 1-10 in the left half of the Fig. 3.7. represent the input variables to the system. All output parameters are shown in the right hand side of the Fig. 3.7. The Equations (3.20) and (3.21) have been designated several functional parts: namely, f_1, f_2, f_3 and f_4 for convenience to describe what calculations are performed inside each Math-function blocks shown in Fig. 3.7. Finally, the output power is calculated using C_p, wind speed, *v* and the turbine blade radius, *R*.

3.2. Wind model

State-space wind model:

There have been numerous publications and experimental work published by researchers regarding variable wind speed and real time modelling. Reasonably accurate modelling of the wind speed is important for pitch control and grid side voltage control. Fluctuating wind is the difference between combination of the real wind speed and the average wind speed. From literature it is understood that the wind is very close to the Gaussian distribution. While not focussing too much details on wind speed modelling and variation, favourite wind speed model

used by Dolan (2010) and Gosk (2011) and Henriksen (2007) is used in this thesis for illustration. The main intention is to incorporate MATLAB/Simulink model to combine with the other subsystems. Most researchers used the second order wind model system for their studies. The average wind speed of 8m/s is taken for illustration and modelling in this thesis as it is between 'cut in' speed and 'cut out' speed of the turbine. Other main reason is that wind turbine actual data will be tested in this region where the nonlinear data matrices will be linearized at this wind speed. Variable wind speed is modelled as given in (Gosk, 2011),

$$v = v_m + v_t \tag{3.22}$$

where,

$$v_t = \frac{k(v_m)}{(p_1(v_m)s+1)(p_2(v_m)s+1)}e; \qquad e \in N(0,1) \tag{3.23}$$

The symbol v_t is the turbulent wind speed and v_m is the mean wind speed and v is the wind speed. The parameters in $e \in N(0,1)$ are the shortened way of presenting white noise with zero mean and the variance 1 which implies the white noise normal distribution. The parameter k varies with the mean wind speed v_m. The parameters $p_1(v_m)$ and $p_2(v_m)$ vary with the mean wind speed v_m. Wind model in Simulink can be constructed by using the Band-Limited White Noise block (using default values given) and Equation (3.23). Taking the mean wind speed as 8m/s and typical values for $p_1(v_m)$, $p_2(v_m)$ and k as 5, 80, 8 respectively the Simulink model constructed is shown in Fig. 3.8. The values given were selected after running the simulation several times with different substitution of these constants. The other method to select these parameters is by using the curve fitting tool box in MATLAB. It is reasonable to assume the given wind speed variation as there is no 100% accurate wind speed model described in literature. The simulation results from the model are shown in Fig. 3.9.

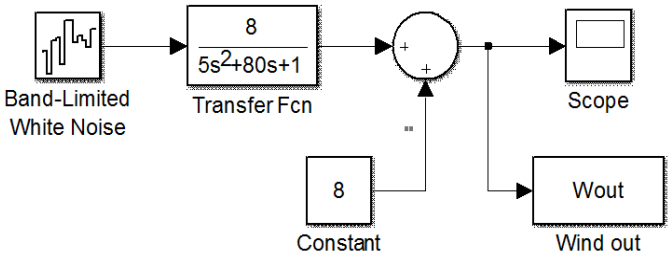

Figure 3.8: Simulink wind model.

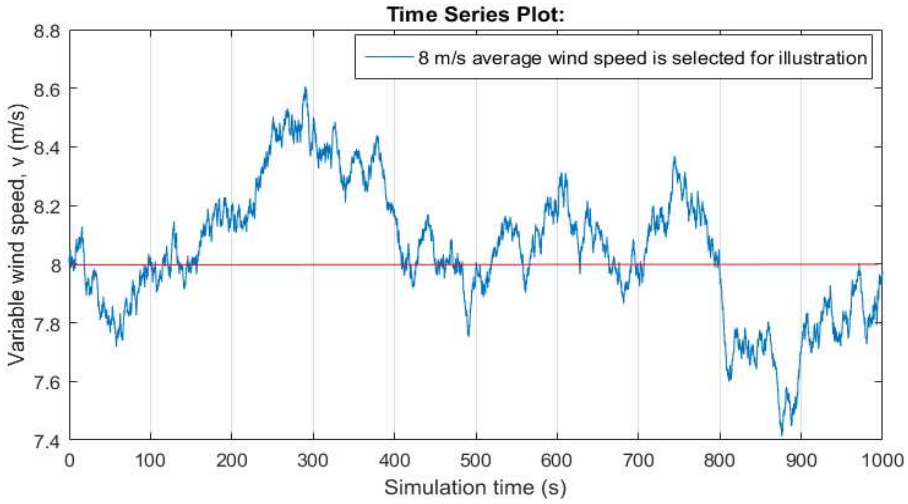

Figure 3.9: Wind speed variation with time: mean wind speed = 8m/s.

Equation (3.22) and (3.23) could be used to represent the fast varying turbulent wind speed v_t in state-space form as given in Equation (3.24),

$$\begin{pmatrix} \dot{v}_t \\ \ddot{v}_t \end{pmatrix} = \begin{bmatrix} 0 & 1 \\ -\dfrac{1}{p_1(v_m)p_2(v_m)} & -\dfrac{p_1(v_m)+p_2(v_m)}{p_1(v_m)p_2(v_m)} \end{bmatrix} \begin{pmatrix} v_t \\ \dot{v}_t \end{pmatrix} + \begin{bmatrix} 0 \\ \dfrac{k(v_m)}{p_1(v_m)p_2(v_m)} \end{bmatrix} e \qquad (3.24)$$

Wind speed generally changes from ground to the tower height, due to terrain effect and this effect has been neglected here.

3.3. Maximum Power Point Tracking (MPPT) from the Wind Turbines

Nedler-Mead simplex algorithm as described in Lagarias et al., (1998) is used to track the maximum point of turbine coefficient versus pitch angle curve which offers the maximum power for the variable wind speed at any instant. Pseudo code for the algorithm is found in reference Lagarias et al., (1998) The MATLAB inbuilt functions of fminsearch(@(x), initial guess) and function [beta]= fzero(fun, beta) deploys the same principle to obtain the solutions to the equations. The function fzero uses a combination of bisection, secant, and inverse quadratic interpolation methods. From Fig. 3.4 it can be seen that the C_P versus λ curve is a bell-shaped curve which has a maximum point for the coefficient C_P for a particular pitch angle. The power extracted from the wind is given in Equation (3.18). The maximum power occurs at the top of the curve when the C_p is at its highest numerical value. To harvest maximum power from the wind, it is necessary to operate TSR at this point of the curve. The

mechanism used to get the maximum power from the WT is to track this particular C_P at a particular TSR by varying the pitch angle θ . In Equation (3.20) the parameters C_1 to C_6 depend on the turbine design method, materials, and the shape of the nacelle. The parameter values as given in reference (Nasiri et al., 2014), (C_1=0.5176, C_2=116, C_3=0.4, C_4=5, C_5=21, C_6 =0.0068) have been used for the simulations in this thesis. The Equations (3.18, 3.20) and (3.21) which were introduced earlier have been used again for the following analysis,

Differentiating variable g in Equation (3.21) w.r.t. θ we can get,

$$\frac{\partial g}{\partial \theta} = -\frac{0.08}{(\lambda + 0.08\theta)^2} + \frac{0.035 \times 3\theta^2}{\left(1+\theta^3\right)^2} \tag{3.25}$$

From Equation (3.20) taking the derivative of C_P w.r.t. θ we can write,

$$\frac{\partial C_P}{\partial \theta} = C_1 e^{-C_5 \cdot g}\left\{C_2 \frac{\partial g}{\partial \theta} - C_3\right\} + \left(C_1\{C_2 g - C_3\theta - C_4\}\right) \times (-C_5).(e^{-C_5 g}).\frac{\partial g}{\partial \theta} \tag{3.26}$$

The maximum and minimum points for the C_P from Equation (3.26) can be resolved by making it equal to zero. Newton-Rapson numerical method can be used to get the accurate value of θ however, as the equation involves the second derivative the approach is tedious to find a solution using MATLAB as the program does not offer repeatable accurate answer. The solution for this type of equation can be found by using Secant method or by applying Direct Iteration method. But, one should understand that the wind speed is also related to TSR (λ).

The other empirical formula used in this project for C_P calculation and the MPPT is the formula presented by Abbas and Abdulsada (2010). The formula published for C_P calculation is given by the Equation (3.27) and is offered a realistic solution.

$$C_P = (0.44 - 0.0167)\sin\left(\frac{\pi(\lambda - 3)}{15 - 0.3\theta}\right) - 0.00184(\lambda - 3)\theta \tag{3.27}$$

The programme code (MATLAB) which can be used to track optimum θ is given in Appendix D.

Analysis of pitch angle θ variation with C_P when TSR is constant

Pitch angle variation can affect the C_P values which can finally lead to low power harvest from the wind turbine if not controlled. While TSR is keeping constant the variation of C_P versus pitch angle θ has been investigated to understand why the previous MATLAB functions offer improper results. The Fig. 3.10 shows the characteristics. The green line, in the legend, indicates the TSR, λ when it is equal to 5. For this curve the maximum occurs at 2.2º and at C_P value is equal to 0.3. It can be seen from Fig. 3.10 that the maximum C_P occurs for each constant λ curve when θ is equal to 2.3° degrees. The results of the Fig. 3.10 could lead to a conclusion that pitching could be used at high wind speeds when the pitch angle is greater than 17° as the C_P values are approaching towards zero. When C_P value is zero, from Equation (3.18) the output power will be zero. Hence, when the pitch angle is more than this particular angle the turbine coefficient leads to zero with no power output for large wind turbines. Therefore, other than the complete shutdown of the turbine, mathematically, at high wind speeds, pitching can control the power which is safe for the turbine blades at emergencies than applying brakes. Applying brakes at high wind speeds especially at 'cut out' wind speed region could be hazardous if disk braking systems are incorporated where the rubbing surface temperatures can be unduly increased. In Fig. 3.10, λ=10 curve has a maximum value for C_P which is at 0.456 and at a pitch angle of 2° which confirms the results from the Fig. 3.4. as shown earlier.

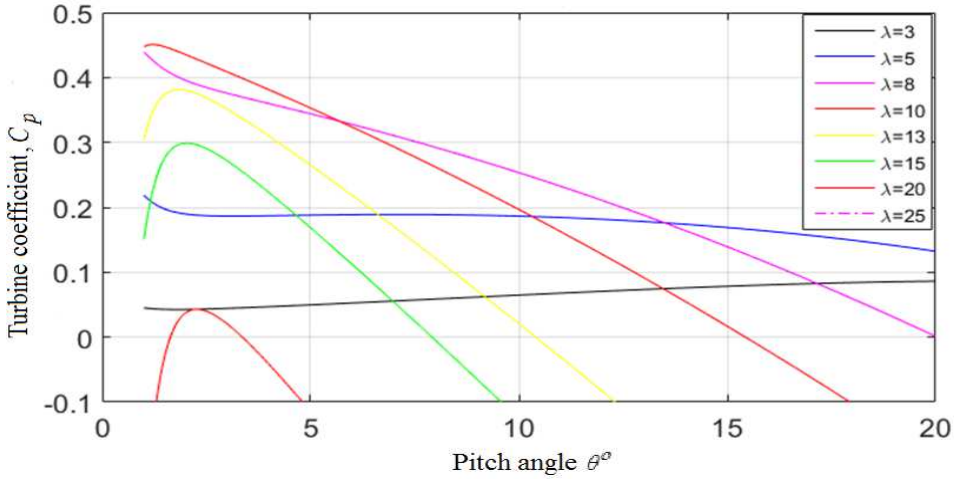

Figure 3.10: Turbine coefficient C_p versus pitch angle θ^o (measured in degrees)

Maximum power point tracking based from C_p versus λ curves

The other method of obtaining the MPP is by exploiting the C_p versus λ curves with the principle of searching maximum points. Similar to the previous approach, maximum points can be located by taking the derivative of C_p w.r.t. λ.

Taking the derivatives w.r.t variable λ (from Equation (3.20) & (3.21)) assuming the pitch angle θ is constant,

$$\frac{\partial g}{\partial \lambda} = -\frac{1}{(\lambda + 0.08\theta)^2} \tag{3.28}$$

$$\frac{\partial C_p}{\partial \lambda} = c_1 . e^{-c_5 . g} \left\{ c_2 . \frac{\partial g}{\partial \lambda} \right\} + \{c_2 g - c_3 \theta - c_4\} c_1 . e^{-c_5 . g} . (-c_5) . \frac{\partial g}{\partial \lambda} + c_6 \tag{3.29}$$

Using c_6=0.0068 from reference Nasiri et al., (2014) when c_6 is assumed to be zero then the Equation (3.29) could be simplified to get,

$$\frac{\partial C_p}{\partial \lambda} = \{c_2\} - c_5 \{c_2 g - c_3 \theta - c_4\} \tag{3.30}$$

For maximum points on the curve, $\frac{\partial C_p}{\partial \lambda} = 0$;

$$\therefore c_2 - c_5 (c_2 g - c_3 \theta - c_4) = 0 \tag{3.31}$$

Equation (3.31) is solved using an iterative method. Reference input value for the turbine rotor is calculated by using formula; $\omega_{ref} = v_w \times \lambda / R$; for a wind speed of 10 m/s. λ = 9.53, C_p = 0.4072; turbine rotor power = 3.1341e+05 kW; ω_{ref} = 4.76 rad/s. which are correct results for 10 m/s wind speed. Complete MATLAB programme code is given in appendix D. The program offers the flexibility to set the reference rotor speed to track the optimum power at that wind speed. MATLAB/Simulink block diagram with the implementation of a generic PID controller is presented in Fig. 3.11, 3.12 and in Fig. 3.13. The model presented here is a basic approach into the WT control paradigm and the detailed modelling is described after presenting the PID controller results. In this instance, ω_t is the turbine shaft angular speed. Parameter J_t is the total

moment of inertia of the turbine and rotor, T_r is the mechanical torque necessary to turn the generator, other shafts and it is assumed as a constant value which is commanded by the generator. Applying the Newton's 2nd law of motion for angular acceleration,

$$J_t \dot{\omega}_r = T_r - T_g \tag{3.32}$$

Where, T_g is the torque necessary to run the generator which is also assumed to be a constant and when the Equation (3.32) is linearized it is considered as a constant. In this particular WT, the total inertia is taken as 1270 kg·m^2 (micro-WT). Hence, we can write the Equation (3.33) as given here,

$$J_t \Delta\dot{\omega}_r = \gamma\Delta\omega_r + \xi\Delta v_r + \delta\Delta\theta \tag{3.33}$$

Where, γ, ξ *and* δ are linearization coefficients. The parameters $\Delta\omega_r, \Delta v_r$ *and* $\Delta\theta$ represent deviations from the chosen operating points of: ω_{ro}, v_{ro} *and* θ_o. Using Taylor series expansion, we can write,

$$T_r = T_{r0} + \left.\frac{\partial T_r}{\partial \omega}\right|_{\omega_{r0}} .\Delta\omega_r + \left.\frac{\partial T_r}{\partial v_r}\right|_{v_{r0}} .\Delta v_r + \left.\frac{\partial T_r}{\partial \theta}\right|_{\theta_0} .\Delta\theta \tag{3.34}$$

hence,
$$\Delta T_r = J_t \Delta\dot{\omega}_r = \gamma\Delta\omega_r + \xi\Delta v_r + \delta\Delta\theta \tag{3.35}$$

(where, $\gamma = \left.\frac{\partial T_r}{\partial \omega}\right|_{\omega=\omega_{r0}}$ etc.) Laplace transformation of the Equation (3.35) is given by Equation (3.36),

$$J_t s\Delta\omega_r = \gamma\Delta\omega_r(s) + \xi\Delta v_r(s) + \delta\Delta\theta(s) \tag{3.36}$$

$$\begin{aligned} \Delta\omega_r(s - \frac{\gamma}{J_t}) &= \frac{\xi}{J_t}\Delta v_r(s) + \frac{\delta}{J_t}\Delta\theta(s) \\ \therefore \Delta\omega_r &= \left[\frac{\xi}{J_t}\Delta v_r(s) + \frac{\delta}{J_t}\Delta\theta(s)\right]\frac{1}{\left(s - \frac{\gamma}{J_t}\right)} \end{aligned} \tag{3.37}$$

The Equation (3.37) can be shown by a block diagram as shown in Fig. 3.11.,

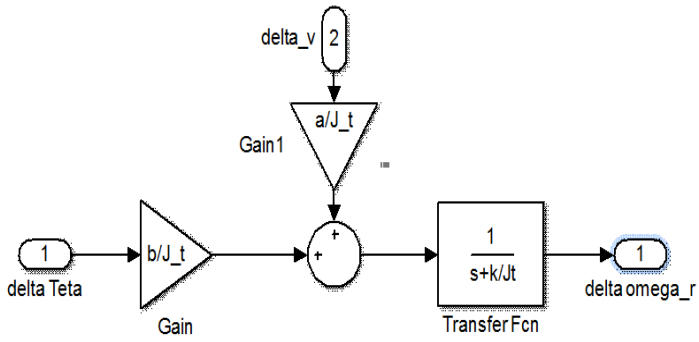

Figure 3.11: Block diagram for the Equation (3.37) (a, b, k are numerical constants).

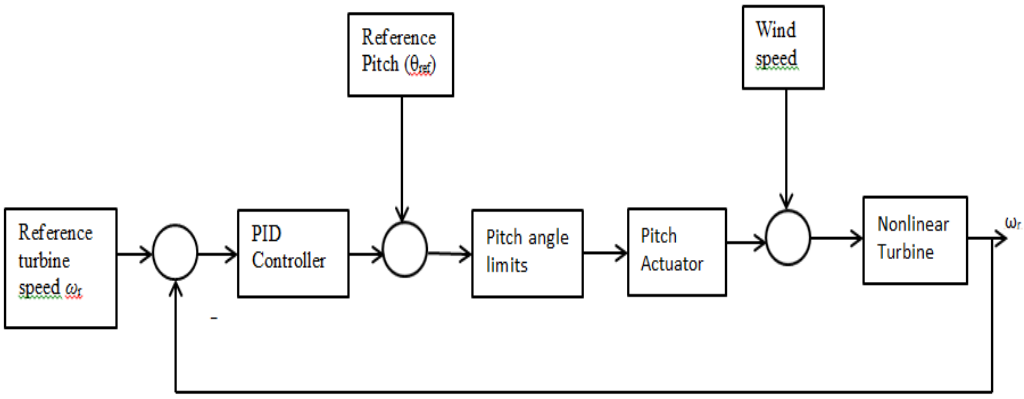

Figure 3.12: Turbine rotor speed control block diagram: closed loop (Abbas and Abdulsada, 2010).

The Equation (3.37) indicates that both pitch angle and the wind speed could be taken as inputs to the system. Generally, the pitch angle is implemented in a form of pitch actuator which includes a hydraulic actuator or DC motor. Pitch actuator can be modelled as a first order transfer function in control systems. The wind speed variation is modelled as described previously by a second order transfer function. The extended modified block diagram including all these features is shown in Fig. 3.13. The output turbine speed is fed back and compared with the reference ω_r to augment a closed loop control system. The error signal is then equal to $\Delta\omega_r$ (the measurement noise has been neglected but, a Kalman filter could be implemented if necessary when the noise measurements are high). The rotor speed error signal is then fed into the controller which controls the output and sends the signal to change blade-pitch-angle, $\Delta\theta$, based on $\Delta\omega_r$. The new pitch angle requested is then $\theta = \Delta\theta + \theta_{ref}$. In practice, this is limited to the angles between 2° and 17° for this type of small domestic wind turbines. The

actuator operates on a commanded angle. The pitch angle is determined from the difference between the commanded pitch angle and the measured blade-pitch-angle.

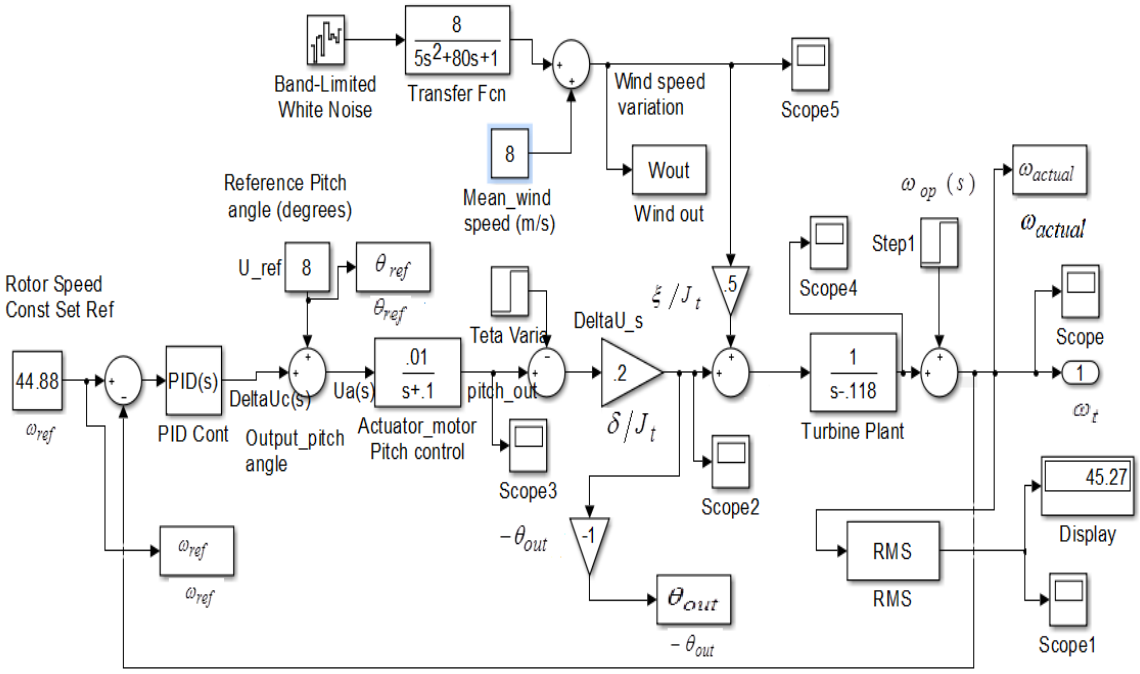

Figure 3.13: Modified pitch control and generator speed control with a modified wind model.

Analysis of the modified pitch control and generator speed control model is tested for small wind turbine data available from literature (npower, 2017; Wang, 2007; Cuesta et al., 2013). Most small WT manufacturers specify the rated WT speed, power coefficient and other necessary data (e.g. typical domestic WT with 1.75 m diameter at rated wind speed 12.5 m/s can generate 2870 W, (npower, 2017)). The shutdown speed recommended for domestic WT is 14-17 m/s and the minimum wind speed recommended is 4.7 m/s. As described previously, ω_{ref} (constant block shown in the Simulink block diagram in Fig. 3.13) is set for operation using ω_{opt} calculated from the MPPT program. The computed value is 44.88 rad/s, which is converted into RPM is equivalent to 428.40 rev/m is set as the reference speed to the wind turbine. With the PID controller, the output turbine speed is 44.87 rad/s and hence the percentage error is found to be 0.02% which is extremely good. However, overshoot of the ω_{out} and the pitch angle are high at this instance. Improvement to this design will be considered towards the latter part of this chapter using PID/State-feedback controller.

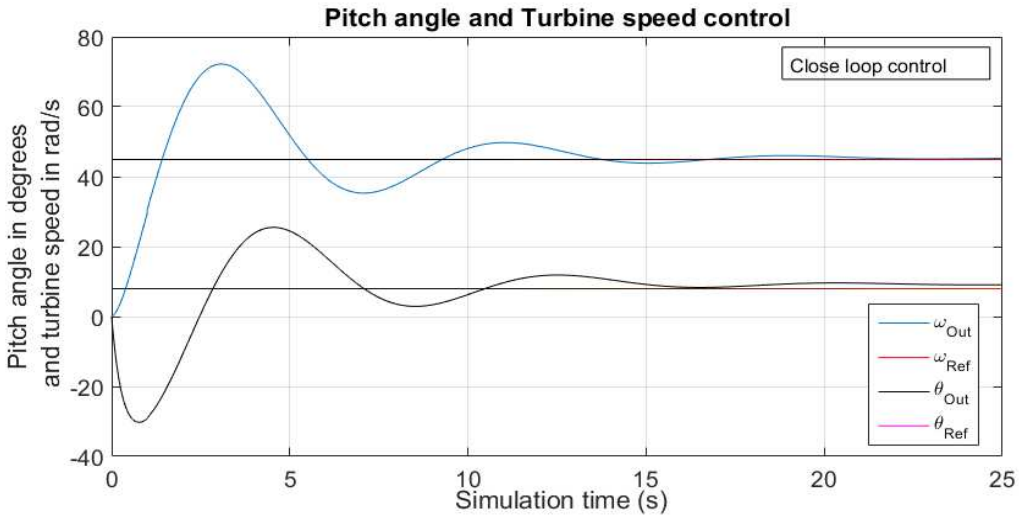

Figure 3.14: Modified pitch controller characteristics.

Modified turbine and pitch controller characteristics are shown in Fig. 3.14. and the PID (proportional, integral and derivative) controller parameters are *P= 312.258; I= 11.884; D=240.563;* PID controller parameters have been obtained from the simulation results.

Several methods are available in literature regarding PID controller designs and tuning. Best controller parameters can be achieved after good tuning of the system either on line or off line. Very good description on PID controller designs, tuning and Ziegler–Nichols Tuning Formula, could be found in reference Xue et al., (2007) than describing here. Transfer function for a PID controller in Laplace domain, $\frac{U(s)}{E(s)} = P + Ds + \frac{I}{s}$ which in numerator and denominator form is $\frac{U(s)}{E(s)} = \frac{Ps + Ds^2 + I}{s}$. Generally, when *P* is at a high value, the system can become unstable. When *P* and *I* are both large values the overshoot can be high. When the derivative constant is low then the setting time decrease and when the constant *D* is high the settling time will be quite high. The tuning method used here is the online method: first set *I* and *D* values to zero and increase *P* until loop output oscillates; then increase *I* until oscillation stops, and then increase the value of *D* gradually, until the close loop response is acceptably quick in reaching its reference value. The Ziegler–Nichols Tuning method is adopted by Simulink tool box given there in the library. When the PID Simulink block is double clicked, PID controller tuning window appears. When the tune button is pressed the plant linearization is automatically augmented by Simulink and PID tuner Step plot is displayed. By changing the two cursor buttons on the tool bar, Response time or Transient behaviour can be adjusted as necessary.

When you update the PID tuner the controller parameters will appear at the bottom and the complete description of the controller Parameters could be obtained by pressing the Show Parameters button on the tool bar. As described previously, the improvements of the settling time, overshoot and the stability aspects will be discussed towards the latter part of this chapter.

3.4. Modelling Wind Turbine Subsystems

Aerodynamic thrust on the tower:

The force exerted by the wind on the tower is modelled by considering the lateral deflections of the tower (Jain et al., 2015). The parameter F_t represents the thrust force due to the wind on the tower. We have considered only the back and forth movements of the nacelle. The displacement of the nacelle from the vertical upright position is taken as x_t. If the tower is modelled as a spring-mass-damper system not influenced by gravity,

$$F_t = M_t\ddot{x}_t + D_t\dot{x}_t + K_t x_t \tag{3.37}$$

At steady state of the nacelle movement, $\ddot{x}_t = 0$ and $\dot{x}_t$=0 and from Equation (3.37) we can derive: $x_{t0} = \frac{F_t}{K_t}$. The swaying movement is important to model as it can affect the wind speed. If the nacelle moves forward, then the actual wind speed should be: $v_r = v - \dot{x}_t$.

Equation (3.37) in state-space form is given by Equation (3.38),

$$\begin{pmatrix} \dot{x}_t \\ \ddot{x}_t \end{pmatrix} = \begin{bmatrix} 0 & 1 \\ -\frac{K_t}{M_t} & -\frac{D_t}{M_t} \end{bmatrix} \begin{pmatrix} x_t \\ \dot{x}_t \end{pmatrix} + \begin{bmatrix} 0 \\ \frac{1}{M_t} \end{bmatrix} F_t \tag{3.38}$$

Pitch actuator motor:

Wind turbines need a dynamic pitch control mechanism for reference pitch angles to harvest optimum power. This could be done by using an electric motor or by using a hydraulic system as described previously. When a DC motor is used to control the reference pitch angle then it is called an actuator motor and in control systems, it can be modelled as a second order transfer function. Pitch actuator model used in this thesis is the same model used by Henriksen, (2007). However, generic DC motor model presented in reference 'DC motor model', (2016) is given here to appreciate and compare the modelling differences.

Motor torque Q is proportional to the armature current,

$$Q = K_t i \tag{3.39}$$

Where, K_t is defined as the torque constant.

The back e.m.f, e , is proportional to the angular velocity of the shaft by a constant factor K_e

$$e = K_e \dot{\theta} \tag{3.40}$$

where, K_e is defined as the back e.m.f constant.

Dynamic Equations of motion and from Kirchhoff's voltage law,

$$I\ddot{\theta} + b\dot{\theta} = Ki \tag{3.41}$$

K_t and K_e can be taken as equivalent to K in SI units.

$$L\frac{di}{dt} + Ri = v - K_e\dot{\theta} \tag{3.42}$$

Equations (3.41) and (3.42) in Laplace domain,

$$s(Is + b)\theta(s) = KI(s) \tag{3.43}$$

$$(Ls + R)I(s) = V(s) - Ks\,\theta(s) \tag{3.44}$$

From which we can establish the transfer function for the DC motor,

$$\frac{\theta(s)}{V(s)} = \frac{K}{(Is+b)(Ls+R) + K^2} \tag{3.45}$$

In state-space form (angular velocity and the armature currents are the states),

$$\dot{i} = -\frac{R}{L}i + \frac{v}{L} - \frac{K}{L}\dot{\theta} \tag{3.46}$$

$$\ddot{\theta} = \frac{K}{I}i - \frac{b}{I}\dot{\theta} \tag{3.47}$$

$$\begin{bmatrix} \ddot{\theta} \\ \dot{i} \end{bmatrix} = \begin{bmatrix} -\frac{b}{I} & \frac{K}{I} \\ -\frac{K}{L} & -\frac{R}{L} \end{bmatrix} \begin{bmatrix} \dot{\theta} \\ i \end{bmatrix} + \begin{bmatrix} 0 \\ \frac{1}{L} \end{bmatrix} v \tag{3.48}$$

$$y = \begin{bmatrix} 1 & 0 \end{bmatrix} \begin{bmatrix} \dot{\theta} \\ i \end{bmatrix} \tag{3.49}$$

(Typical values for the parameters could be: I= 0.01, b=0.1, K=0.01, R=1, L=0.5)

The collective pitch actuator model presented by Henriksen (2007), Dolan (2010) and many other researchers used a second order system with constraints to model the pitch actuator. Hence, in this thesis also a second order system is used to model the pitch actuator. The parameter θ_{ref} is the desired pitch angle,

$$\ddot{\theta} + 2\varsigma\omega_n\dot{\theta} + \omega_n^2\theta = \omega_n^2\theta_{ref} \tag{3.50}$$

In state-space form, the final *pitch actuator* (Equation (3.51)),

$$\underbrace{\begin{bmatrix} \dot{\theta} \\ \ddot{\theta} \end{bmatrix}}_{\dot{x}_\theta} = \underbrace{\begin{bmatrix} 0 & 1 \\ -\omega_n^2 & -2\varsigma\omega_n \end{bmatrix}}_{A_\theta} \underbrace{\begin{bmatrix} \theta \\ \dot{\theta} \end{bmatrix}}_{x_\theta} + \underbrace{\begin{bmatrix} 0 \\ \omega_n^2 \end{bmatrix}}_{B_\theta} \theta_{ref} \tag{3.51}$$

State-space matrices for the pitch actuator can also be written as,

$$A_\theta = \begin{bmatrix} 0 & 1 \\ -\omega^2{}_n & -2\varsigma\omega_n \end{bmatrix};\ B = \begin{bmatrix} 0 \\ 1 \end{bmatrix};\ C = \begin{bmatrix} \omega_n^2 & 0 \end{bmatrix};\ \bar{x} = \begin{bmatrix} \hat{\theta} \\ \dot{\hat{\theta}} \end{bmatrix};\ \bar{u} = \begin{bmatrix} \theta_{ref} \end{bmatrix};\ \bar{y} = \begin{bmatrix} \theta \end{bmatrix};$$

Where, ω_n represents the natural frequency of the subsystem. The parameter, zeta ς is the damping constant. The Equation (3.51) is an approximated linear system subject to the following constraints as given in reference Thomsen (2006),

$$\theta_{\min} \le \theta \le \theta_{\max} \tag{3.52}$$

$$\dot{\theta}_{\min} \le \dot{\theta} \le \dot{\theta}_{\max} \tag{3.53}$$

$$\ddot{\theta}_{\min} \le \ddot{\theta} \le \ddot{\theta}_{\max} \tag{3.54}$$

First order model of the pitch actuator presented by Thomson (2016) is given by Equation (3.55),

$$\dot{\theta} = -\frac{1}{\tau_\theta}\theta + \frac{1}{\tau_\theta}\theta_{ref} \tag{3.55}$$

Where, θ_r is the reference pitch angle and τ_θ is a time constant. Hydraulic actuators response faster than DC motor actuators and there is no overshoot and high settling time.

When the second order Equation (3.50) is considered, it is necessary to design the actuator to response quickly for the pitch angle variations and to stabilise the system. Stable values for ς is .9 and ω_n = 0.88 rad/s taken from reference Jain (2015). MATLAB/Simulink block diagram for the Equation (3.50) and the actuator responses are shown in Fig. 3.15 and in Fig. 3.16. respectively,

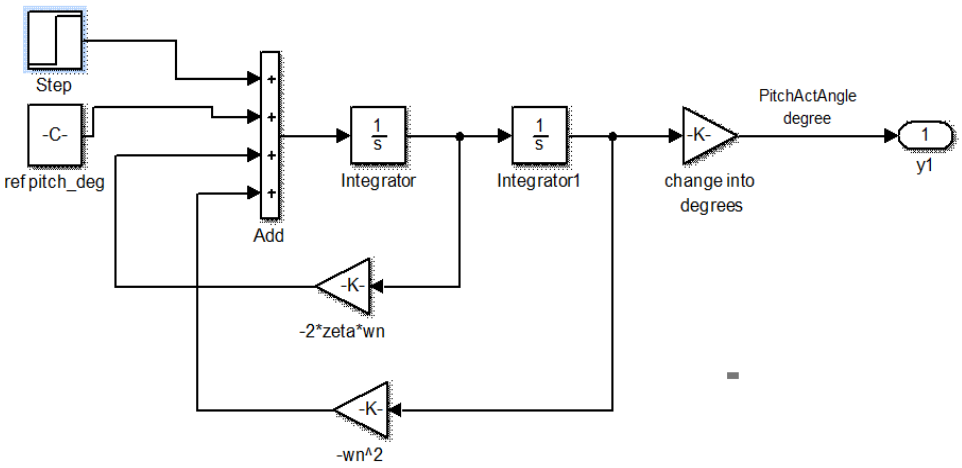

Figure 3.15: Hydraulic actuator model.

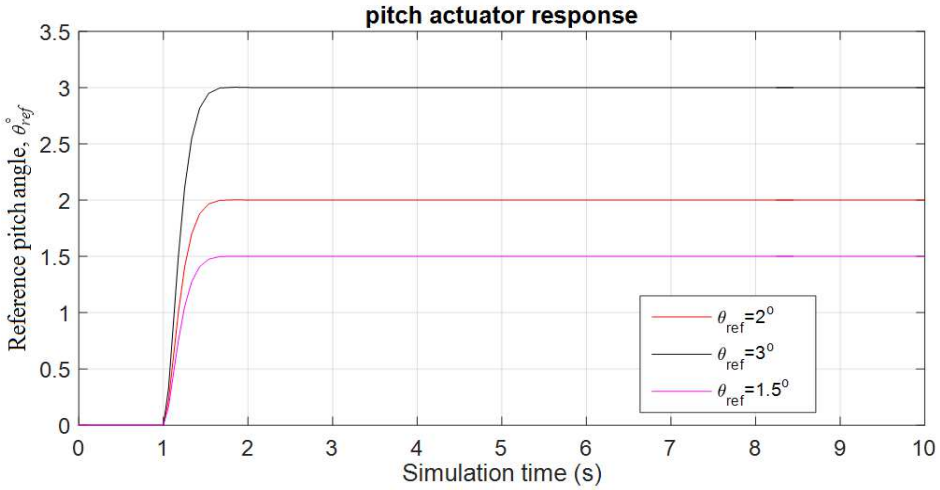

Figure 3.16: Pitch actuator response to the reference pitch angle with time.

Generator torque actuator:

The kinetic energy harvested from wind energy is transformed into electrical energy through the generator. Inside the generator due to electromagnetic induction a current is generated in the stator coils. The electrical power transformed from wind energy can be formulated as given by Equation (3.56),

$$P_e = T_g \omega_g \tag{3.56}$$

where, T_g is the generator torque and ω_g is the generator angular speed. The parameter P_e is the electrical power. It should be noted that the electrical power and the power harvested from wind energy are related with the efficiency factor and could be written as $P_r = \eta P_e$ (η is the efficiency of energy conversion).

The generator torque T_g is a variable output parameter which can be controlled. However, the generator torque is fed back into the system to harvest optimum power from the wind turbine to maximise the output power. The general strategy is to feedback the generator torque as a reference torque into the turbine rotor control system. The reference torque is fed back into the system by using a hydraulic actuator, though, hydraulic actuators are generally slower to response to instantaneous feedback changes. Dynamic response of a generator torque actuator can be modelled by a first order system (Equation (3.57)),

$$\dot{T}_g = -\frac{T_g}{\tau_T} + \frac{T_{g,ref}}{\tau_T} = \frac{T_{g,ref} - T_g}{\tau_T} \tag{3.57}$$

In Laplace domain transfer function is given by Equation (3.58) and its Simulink block diagram is given in Fig. 3.17.,

$$\frac{T_g}{T_{gref}} = \frac{\frac{1}{\tau_T}}{s + \frac{1}{\tau_T}} \tag{3.58}$$

where, $1/\tau_T$ is a constant and τ_T is the time constant and can be taken as 0.1 s which gives $1/\tau_T$ =10 (Henriksen, 2007).

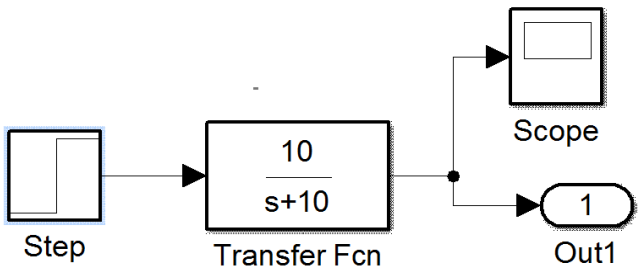

Figure 3.17: Generator torque actuator Simulink block diagram.

The response of the generator actuator model is presented in Fig. 3.18. Reference torque can be represented by a step input and the output torque T_g is the output of the model.

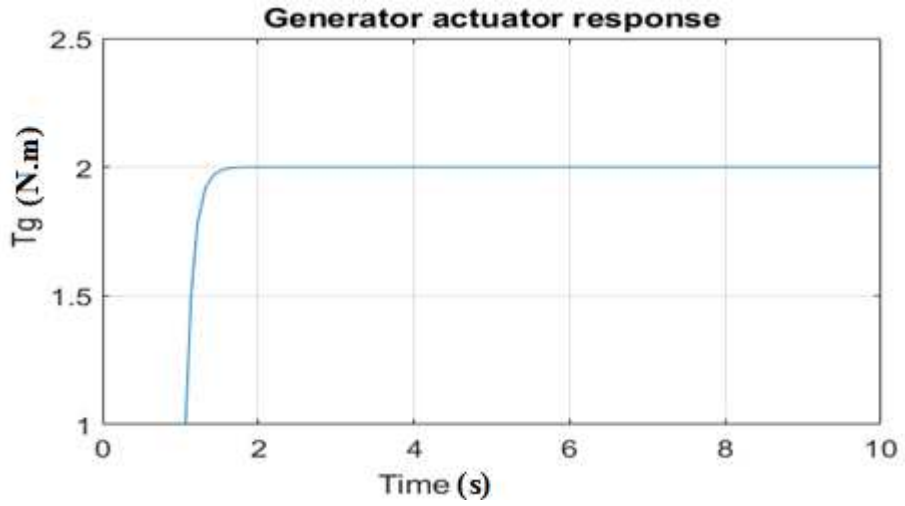

Figure 3.18: Generator torque actuator characteristics (generator torque, T_g versus time).

In state-space form the generator actuator is modelled as follows,

$$A_{T_g} = \underbrace{\left[-\frac{1}{\tau_T}\right]}_{A_{T_g}};\ B_{T_g} = [1];\ C_{T_g} = \frac{1}{\tau_T} \tag{3.59}$$

$$\text{where, } \bar{x} = \left[\hat{T}_g\right];\ \bar{u} = \left[T_{gref}\right];\ \bar{y} = \left[T_g\right] \tag{3.60}$$

Constraints for the subsystem are defined as,

$$T_{g\min} \le T_g \le T_{g\max} \tag{3.61}$$

$$\dot{T}_{g\min} \le \dot{T}_g \le \dot{T}_{g\max} \tag{3.62}$$

The parameter $T_{g,ref}$ is defined as the reference value for the torque-actuator's output and τ_T is the time constant.

Modelling Gear-train mechanism & linear aerodynamic torque:

The power that could be harvested from the WT has been derived earlier in the chapter and is given by,

$$T_r = \frac{P_r}{\omega_r} = \frac{\frac{1}{2}\rho\left(\pi R^2\right)V^3 C_p(V,\lambda,\theta)}{\omega_r} \tag{3.63}$$

Where, T_r is the harvested turbine torque and ω_r is the angular speed of the turbine rotor. The rotor torque is linearized around a linearization point denoted by the subscript 0, to implement the linear control techniques for the HAWT (Detailed description on linearization via Taylor series is given in appendix D; Equation (D.6) $e.g: \Delta\omega_r = \omega_r - \omega_{r0}$):

At the linearization point, we can write,

$$T_{r0} = \frac{P_{r0}}{\omega_{r0}} = \frac{\frac{1}{2}\rho\pi R^2 v_{r0}^3 C_P\left(\frac{\omega_{r0}R}{v_{r0}}, \theta_0\right)}{\omega_{r0}} \tag{3.64}$$

Using Taylor series expansion, we can write,

$$T_r = T_{r0} + \left.\frac{\partial T_r}{\partial \omega}\right|_{\omega_{r0}} .\Delta\omega_r + \left.\frac{\partial T_r}{\partial \theta}\right|_{\theta_0} .\Delta\theta + \left.\frac{\partial T_r}{\partial v_r}\right|_{v_{r0}} .\Delta v_r \tag{3.65}$$

Linearized state-space form of Equation (3.65) is given by Equation (3.66),

$$\Delta\dot{T}_r = \begin{bmatrix} \left.\frac{\partial T_r}{\partial \omega_r}\right|_{\omega_{r0}}, & \left.\frac{\partial T_r}{\partial \theta}\right|_{\theta_0}, & \left.\frac{\partial T_r}{\partial v_r}\right|_{v_{r0}} \end{bmatrix} \begin{pmatrix} \Delta\omega_r \\ \Delta\theta \\ \Delta v \end{pmatrix} \tag{3.66}$$

The partial derivatives given in Equation (3.66) can be written as given below,

$$\left.\frac{\partial T_r}{\partial \omega}\right|_{\omega_{r0}} = \frac{1}{\omega_{r0}} . \left.\frac{\partial P_r}{\partial \omega_r}\right|_{\omega r_0} - \frac{P_{r0}}{\omega_{r0}^2} \tag{3.67}$$

$$\left.\frac{\partial T_r}{\partial \theta}\right|_{\theta_0} = \frac{1}{\omega_{r0}} . \left.\frac{\partial P_r}{\partial \theta}\right|_{\theta_0} \tag{3.68}$$

$$\left.\frac{\partial T_r}{\partial v_r}\right|_{v_{r0}} = \frac{1}{\omega_{r0}} . \left.\frac{\partial P_r}{\partial v_r}\right|_{v_{r0}} \tag{3.69}$$

Using Equation (3.16) presented earlier in the chapter, partial derivatives of P_r can be established as given next,

$$\left.\frac{\partial P_r}{\partial \omega_r}\right|_{\omega_{r0}} = \frac{1}{2}\rho\pi R^2 v_{r0}^3 \left.\frac{\partial C_p}{\partial \lambda}\right|_{\lambda_0} . \left.\frac{\partial \lambda}{\partial \omega_r}\right|_{\omega_{r0}} \tag{3.70}$$

$$\left.\frac{\partial P_r}{\partial \theta}\right|_{\theta_0} = \frac{1}{2}\rho\pi R^2 v_{r0}^3 \left.\frac{\partial C_P}{\partial \theta}\right|_{\theta_0} \tag{3.71}$$

$$\left.\frac{\partial P_r}{\partial v_r}\right|_{v_{r0}} = \frac{1}{2}\rho\pi R^2 3v_{r0}^2 C_{P0} + \frac{1}{2}\rho\pi R^2 v_{r0}^3 \left.\frac{\partial C_P}{\partial \lambda}\right|_{\lambda_0} . \left.\frac{\partial \lambda}{\partial v_r}\right|_{v_{r0}} \tag{3.72}$$

Where,

$$\left.\frac{\partial \lambda}{\partial \omega_r}\right|_{\omega_{r0}} = \frac{R}{v_{r0}} \tag{3.73}$$

$$\left.\frac{\partial \lambda}{\partial v_r}\right|_{v_{r0}} = -\frac{R\omega_{r0}}{v_{r0}^2} \tag{3.74}$$

(note in some references: $\lambda = \frac{v_r}{R\omega}$ then $\left.\frac{\partial \lambda}{\partial \omega_r}\right|_{\omega_{r0}} = -\frac{v_r}{\omega_{r0}^2 R}$)

Derivatives related to C_P has been already derived previously at $\left.\frac{\partial C_P}{\partial \theta}\right|_{\theta=\theta_0}$ and at $\left.\frac{\partial C_P}{\partial \lambda}\right|_{\lambda=\lambda_0}$

which must be obtained using Equations (3.27), (3.26), (3.29) and (3.30),

$$\left.\frac{\partial C_P}{\partial \theta}\right|_{\theta=\theta_0} = c_1\ e^{-c_5 \cdot g}\left\{c_2 \frac{\partial g}{\partial \theta} - c_3\right\} + \left(c_1\{c_2 g - c_3\theta - c_4\}\right)\times(-c_5).(e^{-c_5 g}).\frac{\partial g}{\partial \theta} \tag{3.27}$$

$$\left.\frac{\partial g}{\partial \theta}\right|_{\theta=\theta_0} = -\frac{0.08}{(\lambda + 0.08\theta)^2} + \frac{0.035\times 3\theta^2}{\left(1+\theta^3\right)^2} \tag{3.26}$$

$$\left.\frac{\partial g}{\partial \lambda}\right|_{\lambda=\lambda_0} = -\frac{1}{(\lambda + 0.08\theta)^2} \tag{3.29}$$

$$\left.\frac{\partial C_p}{\partial \lambda}\right|_{\lambda=\lambda_0} = c_1.e^{-c_5 \cdot g}\left\{c_2 . \frac{\partial g}{\partial \lambda}\right\} + \{c_2 g - c_3\theta - c_4\}c_1.e^{-c_5 \cdot g}.(-c_5).\frac{\partial g}{\partial \lambda} + c_6 \tag{3.30}$$

One must note that the Linearization procedure is exhaustive and complex, however, the correct mathematical approach has been presented here without reservations.

Aerodynamics and turbine shafts modelling:

The modelling method adopted here is the state space method which is being adopted by many researchers (e.g. Jain, 2015; Henriksen, 2007; Larsen and Mogensen, 2006; Dolan, 2010, etc.) These researchers used the state-space method for modelling the subsystems and finally assembled them into a single state-space model which represents the total model of the WT system comprising with the pitch actuator, generator torque actuator, tower dynamics, generator, gearbox mechanism and wind speed variation. The advantage of this method offers the freedom to analyse the total system characteristics with one state-space model or individual subsystems independently for stability. Therefore, in this thesis also the same approach is followed for modelling and analysis of the complete WT system.

Two-mass model:

Two-mass model representation of the gear train mechanism is shown in Fig. 3.19.

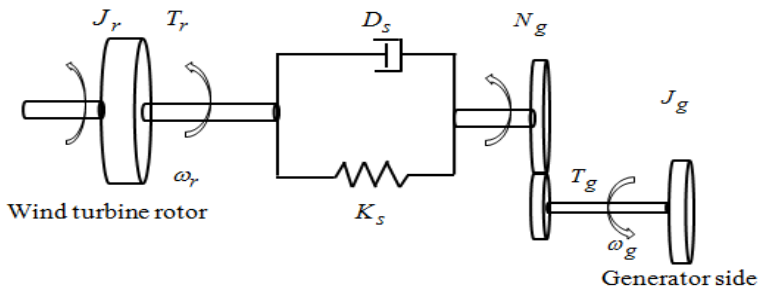

Figure 3.19: Wind turbine gearbox and the generator.

The turbine angular velocity ω_r and the generator angular velocity ω_g are related by the gear ratio N_g ,

$$\omega_r - \frac{\omega_g}{N_g} = 0 \tag{3.75}$$

Equation (4.75) can be written in terms of the angular positions as given next,

$$\phi_r - \frac{\phi_g}{N_g} = 0 \tag{3.76}$$

where, ϕ_r is the angular displacement of turbine rotor shaft and ϕ_g is the angular displacement of generator shaft under real conditions when the turbine is at transient state, Equation (3.75) and (3.76) can lead to the following equations,

$$\omega_r - \frac{\omega_g}{N_g} = \omega_\Delta \text{ and } \phi_r - \frac{\phi_g}{N_g} = \phi_\Delta \tag{3.77}$$

where, $\omega_\Delta \neq 0;\ \phi_\Delta \neq 0$ and $\omega_\Delta = \dot{\phi}_\Delta$.

$$\frac{d\phi_r}{dt} = \omega_r \text{ and } \frac{d\phi_g}{dt} = \omega_g \tag{3.78}$$

The generator torque and the turbine torque are related by the gear ratio N_g,

$$T_g = \frac{T_r}{N_g} \tag{3.79}$$

According to the construction of the turbine blades and the drive shaft, the rotor side is assumed to be flexible but, the drive shaft on the generator side is assumed to be rigid. This assumption can lead to a fractional dynamic angular displacement, between the angle of the rotor shaft ϕ_r and the angle of the generator shaft ϕ_g under operating conditions (Thomsen, 2006). Since the angular velocities are the derivatives of the angular displacements, we can introduce following variables to simplify the notation.

$$\omega_r \equiv \dot{\phi}_r;\ \ \omega_g \equiv \dot{\phi}_g \text{ and hence, if we take } \phi_\Delta \equiv \phi_r - \frac{\phi_g}{N_g}$$

$$\dot{\phi}_\Delta \equiv \omega_r - \frac{\omega_g}{N_g}. \tag{3.80}$$

Applying Newton's law of motion considering the total inertia of the system as J_{tot},

$$J_{tot}\,\dot{\omega}_r = T_r - T_g N_g \tag{3.81}$$

Turbine torque from wind energy, $$T_r = \frac{P_r}{\omega_r} \tag{3.82}$$

Total power harvested, $$P_r = \frac{1}{2}\pi\rho R^2 v^3 C_p(\lambda,\theta) \tag{3.83}$$

From Equations (3.81), (3.82) and (3.83) it is possible to get the Equation (3.84),

$$\dot{\omega}_r = \frac{\frac{1}{2}\pi\rho R^2 v^3 C_p(\lambda,\theta)}{J_{tot}\omega_r} - \frac{T_g N_g}{J_{tot}} \tag{3.84}$$

As ω_g and ω_r are related by Equation (3.75): it can be seen from Equation (3.84), ω_g is a function of wind speed, v , TSR, λ and the pitch angle θ . The Equations (3.81) to (3.84) can be linearized by transforming them into the state-space representation as given below,

$$\begin{aligned} \dot{\bar{x}} &= A\bar{x} + B\bar{u} \\ \bar{y} &= C\bar{x} + D\bar{u} \end{aligned} \tag{3.85}$$

where,

$$\bar{x} = [\omega_r],\ \bar{u} = \begin{bmatrix} v \\ \theta \\ T_g \end{bmatrix} \quad \text{and the output } \bar{y} = \underbrace{\begin{bmatrix} 1 \\ N_g \\ N_g T_g \end{bmatrix}}_{C} [\omega_r] = \begin{bmatrix} \omega_r \\ N_g\omega_r \\ N_g T_g \omega_r \end{bmatrix} = \begin{bmatrix} \omega_r \\ \omega_g \\ P_r \end{bmatrix}. \tag{3.86}$$

The output matrix D can be taken as zero as there is no forward coupling whatsoever with the nonlinear functions defined by the equations. The matrix C can also be defined as,

$$C = \begin{bmatrix} 1 \\ N_g \\ N_g T_g \end{bmatrix} \tag{3.87}$$

For linearization, the system matrix A is obtained by differentiating at an equilibrium point with respect to ω_r.

$$A = \left[\frac{\partial \dot{\omega}_r}{\partial \omega_r}\right] \tag{3.88}$$

$$B = \begin{bmatrix} \frac{\partial \dot{\omega}_r}{\partial v} & \frac{\partial \dot{\omega}_r}{\partial \theta} & \frac{\partial \dot{\omega}_r}{\partial T_g} \end{bmatrix} \tag{3.89}$$

Using Equation (3.84) the matrix A could be derived as,

$$A = \left[\partial \left(\frac{\frac{1}{2}\pi\rho R^2 v^3 C_p(\lambda,\theta)}{J_{tot}\omega_r} - \frac{T_g N_g}{J_{tot}} \right) . \frac{1}{\partial \omega_r} \right] \tag{3.90}$$

hence,
$$A = \left[-\frac{\frac{1}{2}\pi\rho R^2 v^3 C_p(\lambda,\theta)}{J_{tot}\omega^2{}_r} + \frac{\frac{1}{2}\rho\pi R^2 v^3}{J_{tot}\omega_r} . \frac{\partial C_p(\lambda,\theta)}{\partial \omega_r} \right] \tag{3.91}$$

T_g is assumed to be a constant value at the equilibrium point.

Since, C_p is a function of ω_r,

$$\frac{\partial C_p(\lambda,\theta)}{\partial \omega_r} = \frac{\partial C_p(\lambda,\theta)}{\partial \lambda} . \frac{\partial \lambda}{\partial \omega_r} \tag{3.92}$$

Using the chain rule of derivatives, it is now possible to determine the matrix *A,*

$$A = \left[-\frac{\frac{1}{2}\pi\rho R^2 v^3 C_p(\lambda,\theta)}{J_{tot}\omega^2{}_r} + \frac{\frac{1}{2}\rho\pi R^2 v^3}{J_{tot}\omega_r} . \frac{\partial C_p(\lambda,\theta)}{\partial \lambda} . \left(-\frac{v}{\omega_r^2 R} \right) \right] \tag{3.93}$$

The derivative $\frac{\partial C_p(\lambda,\theta)}{\partial \lambda}$ is a numerical value for a particular value of demanded pitch angle or for a particular TSR and it could be calculated from the equations that we have derived earlier namely,

$$\left. \frac{\partial C_p}{\partial \lambda} \right|_{\lambda=\lambda_0} = c_1 . e^{-c_5 . g} \left\{ c_2 . \frac{\partial g}{\partial \lambda} \right\} + \left\{ c_2 g - c_3 \theta - c_4 \right\} c_1 . e^{-c_5 . g} . (-c_5) . \frac{\partial g}{\partial \lambda} + c_6$$

where,
$$\left. \frac{\partial g}{\partial \lambda} \right|_{\lambda=\lambda_0} = -\frac{1}{(\lambda + 0.08\theta)^2}$$

The same method of chain rule differentiation can be applied to evaluate the numerical constants in matrix *B,*

$$B^T = \begin{bmatrix} \partial\left(\frac{\frac{1}{2}\pi\rho R^2 v^3 C_p(\lambda,\theta,v)}{J_{tot}\omega_r} - \frac{T_g N_g}{J_{tot}}\right)\frac{1}{\partial v} \\ \partial\left(\frac{\frac{1}{2}\pi\rho R^2 v^3 C_p(\lambda,\theta,v)}{J_{tot}\omega_r} - \frac{T_g N_g}{J_{tot}}\right)\frac{1}{\partial \theta} \\ \partial\left(\frac{\frac{1}{2}\pi\rho R^2 v^3 C_p(\lambda,\theta,v)}{J_{tot}\omega_r} - \frac{T_g N_g}{J_{tot}}\right)\frac{1}{\partial T_g} \end{bmatrix} \tag{3.94}$$

$$B^T = \begin{bmatrix} \frac{\frac{3}{2}\pi\rho R^2 v^2 C_p(\lambda,\theta)}{J_{tot}\omega_r} + \frac{\frac{1}{2}\pi\rho R^2 v^3 \frac{\partial C_p}{\partial \lambda}.\frac{\partial \lambda}{\partial v}}{J_{tot}\omega_r} \\ \frac{\frac{1}{2}\rho\pi R^2 v^3}{J_{tot}\omega_r}.\frac{\partial C_P(\lambda,\theta)}{\partial \theta} \\ -\frac{N_g}{J_{tot}} \end{bmatrix} = \begin{bmatrix} \frac{\frac{3}{2}\pi\rho R^2 v^2 C_p(\lambda,\theta)}{J_{tot}\omega_r} + \frac{\frac{1}{2}\pi\rho R^2 v^3 \frac{\partial C_p}{\partial \lambda}.}{J_{tot} R\omega^2{}_r} \\ \frac{\frac{1}{2}\rho\pi R^2 v^3}{J_{tot}\omega_r}.\frac{\partial C_P(\lambda,\theta)}{\partial \theta} \\ -\frac{N_g}{J_{tot}} \end{bmatrix} \tag{3.95}$$

We have now established a linearized state-space model for the wind turbine. The wind turbine is susceptible to operate at four different wind regions; they are described as low, mid, high and top wind regions as given in the literature review. The linearization has to be performed separately for all these regions to model correct wind turbine performance. It is clear that though, the mathematical formulations are interconnected and exhaustive, the elements within matrices lead to numerical constants when linearized at four regions. When all numerical values have been found for all regions it is convenient to model/simulate the total system.

Drive shafts modelling

The drive shaft mechanism shown in Fig. 3.20. has been analysed once again in this section for mathematical formulations and modelling. It is assumed that the drive shaft which is the main turbine rotor shaft has elastic properties that could be modelled with a second order differential equation with a spring constant and with a damping coefficient. The other main shaft in the gear train is the generator shaft which is driven by the turbine rotor shaft which is assumed to be rigid. The torque is transmitted from the turbine shaft to the generator shaft with a gear reduction wheels as shown in Fig. 3.20. (the gear reduction ratio is N_g). Energy loss through

the gear system is ignored. Taking $\omega_r = \dot{\phi}_r$ and $\omega_g = \dot{\phi}_g$ we can apply Newton's law of motion to obtain the differential equation for the net torque. Applying Newton's second law of motion:

$$T_r - T_g N_g = J_r \ddot{\phi}_r - J_g N_g \ddot{\phi}_g + \left(\dot{\phi}_r - \frac{\dot{\phi}_g}{N_g} \right) D_s + \left(\phi_r - \frac{\phi_g}{N_g} \right) K_s \tag{3.96}$$

Using Equation (3.77) and (3.96) it is possible to derive the following equation for,

$$\ddot{\phi}_r = \frac{T_r - T_g N_g + J_g N_g \ddot{\phi}_g - (\Delta\dot{\phi}) D_s - (\Delta\phi) K_s}{J_r} \tag{3.97}$$

From Equation (3.96) using algebra $\ddot{\phi}_g$ can be derived,

$$\ddot{\phi}_g = \frac{T_r - T_g N_g - J_r \ddot{\phi}_r + \Delta\dot{\phi} D_s + \Delta\phi K_s}{J_g N_g} \tag{3.98}$$

By using the relationships: $T_g N_g = J_g N_g \ddot{\phi}_g$ and $T_r = J_r \ddot{\phi}_r$ the Equations (3.97) and (3.98) presented can further be simplified to Equations (3.99) and (3.100),

$$\ddot{\phi}_r = \frac{T_r - \Delta\dot{\phi} D_s - \Delta\phi K_s}{J_r} \tag{3.99}$$

$\ddot{\phi}_g = \dfrac{-T_g N_g + \Delta\dot{\phi} D_s + \Delta\phi K_s}{J_g N_g}$ The two coupled equations can be represented by a Simulink model as given in Fig. 3.20. and their state-space representation is shown below,

$$\left.\begin{aligned} \ddot{\phi}_r &= \frac{T_r}{J_r} - \left(\omega_r - \frac{\omega_g}{N_g} \right) \frac{D_s}{J_r} - \frac{\Delta\phi K_s}{J_r} \\ \ddot{\phi}_g &= -\frac{T_g}{J_g} + \left(\omega_r - \frac{\omega_g}{N_g} \right) \frac{D_s}{J_g N_g} + \frac{\Delta\phi K_s}{J_g N_g} \\ \Delta\dot{\phi} &= \omega_r - \frac{\omega_g}{N_g} \end{aligned}\right\} \tag{3.100}$$

where, $A_a = \begin{bmatrix} -\frac{D_s}{J_r} & \frac{D_s}{J_r N_g} & -\frac{K_s}{J_r} \\ \frac{D_s}{J_g N_g} & -\frac{D_s}{J_g N^2 g} & \frac{K_s}{J_g N_g} \\ 1 & -\frac{1}{N_g} & 0 \end{bmatrix}$; $B_a = \begin{bmatrix} \frac{1}{J_r} & 0 \\ 0 & -\frac{1}{J_g} \\ 0 & 0 \end{bmatrix}$; $C_a = \begin{bmatrix} 1 & 0 & 0 \\ 0 & 1 & 0 \\ 0 & T_g & 0 \\ 0 & 0 & 1 \end{bmatrix}$ (3.101)

and the State and input vectors are, $\bar{x} = \begin{bmatrix} \omega_r \\ \omega_g \\ \Delta\phi \end{bmatrix}$; $\bar{u} = \begin{bmatrix} T_r \\ T_g \end{bmatrix}$ (3.102)

The output vector: $\bar{y} = \begin{bmatrix} \omega_r \\ \omega_g \\ P_{out} \\ \Delta\phi \end{bmatrix}$. (3.103)

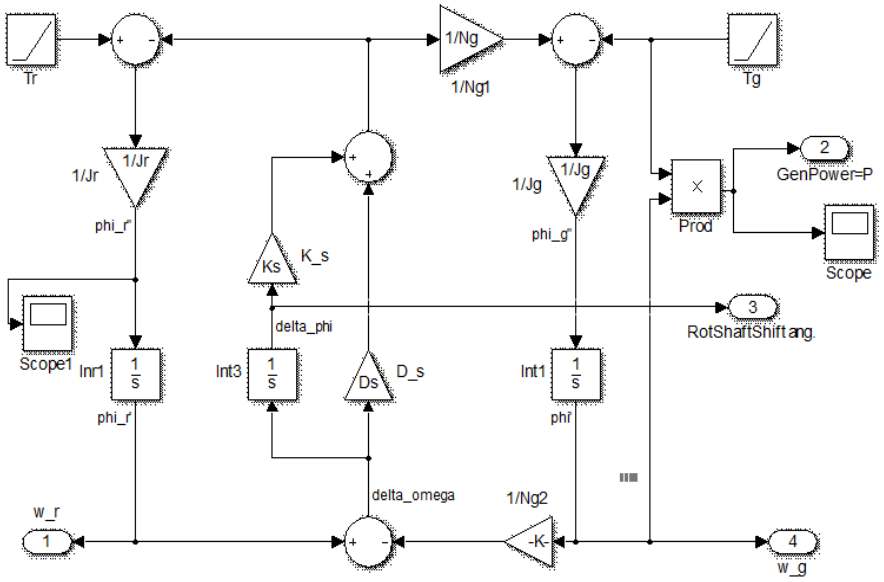

Figure 3.20: Simulink block diagram for the turbine shaft and the generator shaft with applied turbine torque.

Damping constant and the stiffness constant can be determined from simulations and by evaluating the shaft resonance frequency (Dolan, 2010),

$$K_s = (2\pi f_s)^2 . J_r \tag{3.104}$$

$$D_s = \frac{K_s}{100} \tag{3.105}$$

Evaluation of K_s and D_s parameters is carried out by a method similar to that used by reference Larsen and Mogensen (2006). Rule of thumb is that D_s is taken one tenth to one hundredth of K_s. It is assumed that the resonance frequency is equal to 0.55 Hz and therefore, the parameters K_s =1.039x10^8 N/m and D_s =1.039x10^6 s^{-1}.

Total model:

When designing a control system for wind turbines, depending on the capacity of the wind turbine and the model accuracy, the complexity of the controllers also changes. Wind turbine modelling can be categorised into three main types: a) the first type of the model is an uncomplicated simple mathematical model where the subsystems are in the first order and the tower dynamics is ignored by considering the tower as rigid, which has no effect with the wind speed. b) the second stage of the modelling includes two mass-model and the drive shaft where the actuators are modelled as second order transfer functions; c) the third stage of the modelling is a complex modelling that can include all subsystems in higher order transfer functions with three-mass turbine model including lateral tower deflections. Model equations and the combined state-space model considered here belong to the second stage of modelling that is extended to the third stage gradually at a later stage.

Starting from the gear train the following equations represent the second stage of modelling. The equations presented by (3.100) can be written again for convenience as,

$$\dot{\omega}_r = \frac{T_r}{J_r} - \frac{K_s}{J_r}\Delta\phi - \frac{D_s}{J_r}\omega_r + \frac{D_s}{J_r N_g}\omega_g \tag{3.106}$$

$$\dot{\omega}_g = -\frac{T_g}{J_g} + \frac{K_s}{J_g N_g}\Delta\phi - \frac{D_s}{J_g N_g}\omega_r - \frac{D_s}{J_g N_g^2}\omega_g \tag{3.107}$$

$$\dot{\phi}_\Delta = \omega_r - \frac{\omega_g}{N_g} \tag{3.108}$$

The turbine rotor shaft torque which was derived earlier in the chapter is given by,

$$T_r = \frac{\frac{1}{2}\rho\left(\pi R^2\right)v^3 C_p(v,\lambda,\theta)}{\omega_r}$$

Using the same state space modelling approach given in reference Larsen and Mogensen, (2006) we can build our A_{a_1} ; B_{a_1} and C_{a_1} ,

$$\text{where, } A_{a_1} = \begin{bmatrix} A_{a_1(1,1)} & \frac{D_s}{J_r N_g} & -\frac{K_s}{J_r} \\ \frac{D_s}{J_g N_g} & -\frac{D_s}{J_g N_g^2} & \frac{K_s}{J_g N_g} \\ 1 & \frac{1}{N_g} & 0 \end{bmatrix} \tag{3.109}$$

(Using Equation (3.95); please see B^T),

$$\text{And, } B_{a_1} = \begin{bmatrix} \frac{\frac{3}{2}\pi\rho R^2 v^2 C_p(\lambda,\theta)}{J_{tot}\omega_r} + \frac{\frac{1}{2}\pi\rho R^2 v^3 \frac{\partial C_p}{\partial\lambda}.}{J_{tot} R\omega^2{}_r} & \frac{\frac{1}{2}\rho\pi R^2 v^3}{J_{tot}\omega_r}.\frac{\partial C_P(\lambda,\theta)}{\partial\theta} & 0 \\ 0 & 0 & -\frac{1}{J_g} \\ 0 & 0 & 0 \end{bmatrix} \tag{3.110}$$

$$\text{and} \qquad C_{a_1} = \begin{bmatrix} 1 & 0 & 0 \\ 0 & 1 & 0 \\ 0 & T_g & 0 \\ 0 & 0 & 1 \end{bmatrix} \tag{3.111}$$

$$\text{and} \qquad A_{a_1(1,1)} = \left[-\frac{\frac{1}{2}\pi\rho R^2 v^3 C_p(\lambda,\theta)}{J_r\omega^2{}_r} + \frac{\frac{1}{2}\rho\pi R^2 v^3}{J_r\omega_r}.\frac{\partial C_p(\lambda,\theta)}{\partial\lambda}.-\frac{v}{\omega_r^2 R} - \frac{D_s}{J_r} \right] \tag{3.112}$$

In the newly defined system, input vector is: $\bar{u} = \begin{bmatrix} v & \theta & T_g \end{bmatrix}$,

output vector $\bar{y} = \begin{bmatrix} \omega_r \\ \omega_g \\ P \\ \Delta\phi \end{bmatrix}$ and the states are, $\bar{x} = \begin{bmatrix} \omega_r \\ \omega_g \\ \Delta\phi \end{bmatrix}$

However, the mathematical model presented now has to be extended by including the two actuator dynamics for pitch angle actuator and for the generator torque actuator respectively. When these actuators (models) are included the new state vector should be changed to the one given below,

$$\bar{x} = \begin{bmatrix} \hat{\theta} \\ \dot{\hat{\theta}} \\ \hat{T}_g \\ \omega_r \\ \omega_g \\ \Delta\phi \end{bmatrix} \tag{3.113}$$

The input vector is the same vector as defined earlier, however, θ and T_g are defined as θ_{ref} and T_{gref} ; $\hat{\theta}$ is the actuator angular displacement; $\dot{\hat{\theta}}$ is the pitch actuator rotational speed. $\hat{T}_g$ is the generator actuator torque.

where, $\bar{u} = \begin{bmatrix} v \\ \theta_{ref} \\ T_{gref} \end{bmatrix}$ and the output vector $\bar{y}$ remains unchanged.

It is now possible to include additional two subsystems representing the pitch actuator and the generator torque actuator to build our main state-space system with Equations (3.114) to (3.119) as given here (tower dynamics are included in the wind speed),

$$\dot{\hat{\theta}} = \qquad \dot{\hat{\theta}} \tag{3.114}$$

$$\ddot{\hat{\theta}} = -\omega_n^2 \hat{\theta} - 2\varsigma\omega_n \dot{\hat{\theta}} + \theta_{ref} \tag{3.115}$$

$$\dot{\hat{T}}_g = \left[-\frac{1}{\tau_T}\right]\hat{T}_g + \left[\frac{1}{\tau_T}\right]T_{g,ref} \tag{3.116}$$

$$\dot{\omega}_r = \frac{\frac{1}{2}\pi\rho R^2 v^3 C_p(\lambda, \hat{\theta}\omega_n^2)}{\omega_r J_r} - \frac{K_s}{J_r}\Delta\phi - \frac{D_s}{J_r}\omega_r + \frac{D_s}{J_r N_g}\omega_g \tag{3.117}$$

$$\dot{\omega}_g = -\frac{\hat{T}_g}{J_g \tau_T} + \frac{K_s}{J_g N_g}\Delta\phi + \frac{D_s}{J_g N_g}\omega_r - \frac{D_s}{J_g N^2{}_g}\omega_g \tag{3.118}$$

$$\Delta\dot{\phi} = \omega_r - \frac{\omega_g}{N_g} \tag{3.119}$$

It should be noted that in Equation (3.117) that the pitch angle variation is now changed into $\hat{\theta}\omega_n^2$ in concurrence with Equation (3.115). This variable is indeed acceptable as the $\hat{\theta}$ instead of applying it alone, it is multiplied by a constant ω_n^2. Linearized matrices A_m, B_m and C_m can now be derived by differentiating with respect to state variables from the six states. Input matrix B_m is also obtained by differentiating the three input variables.

$$A_m = \overbrace{\begin{bmatrix} 0 & 1 & 0 & 0 & 0 & 0 \\ -\omega_n^2 & -2\varsigma\omega_n & 0 & 0 & 0 & 0 \\ 0 & 0 & -\frac{1}{\tau_T} & 0 & 0 & 0 \\ \omega_n^2 \frac{\frac{1}{2}\rho\pi R^2 v^3}{J_r \omega_r} \cdot \frac{\partial C_p\left(\lambda, \hat{\theta}\omega_n{}^2\right)}{\partial \hat{\theta}\omega_n^2} & 0 & 0 & A_{m(4,4)} & \frac{D_s}{J_r N_g} & -\frac{K_s}{J_r} \\ 0 & 0 & -\frac{1}{\tau_T J_g} & \frac{D_s}{J_g N_g} & -\frac{D_s}{J_g N_g^2} & \frac{K_s}{J_g N_g} \\ 0 & 0 & 0 & 1 & -\frac{1}{N_g} & 0 \end{bmatrix}}^{A_m} \overbrace{\begin{bmatrix} \hat{\theta} \\ \dot{\hat{\theta}} \\ \hat{T}_g \\ \omega_r \\ \omega_g \\ \Delta\phi \end{bmatrix}}^{\bar{x}}_{This\_will\_come\_later} \tag{3.120}$$

$$B_m = \overbrace{\begin{bmatrix} 0 & 0 & 0 \\ 0 & 1 & 0 \\ 0 & 0 & 1 \\ \frac{1.5\pi R^2 v^2 C_P\left(\lambda, \hat{\theta}\omega_n^2\right)}{J_r \omega_r} + \frac{0.5\rho\pi R^2 v^3 \frac{\partial C_P\left(\lambda, \hat{\theta}\omega_n^2\right)}{\partial\lambda}}{J_r R \omega_r^2} & 0 & 0 \\ 0 & 0 & 0 \\ 0 & 0 & 0 \end{bmatrix}}^{B_m} \underbrace{\begin{bmatrix} v \\ \theta_{ref} \\ T_{gref} \end{bmatrix}}_{This\_will\_come\_later} \tag{3.121}$$

$$C_m = \begin{bmatrix} 0 & 0 & 0 & 1 & 0 & 0 \\ 0 & 0 & 0 & 0 & 1 & 0 \\ 0 & 0 & 1 & 0 & 1 & 0 \\ 0 & 0 & 0 & 0 & 0 & 1 \end{bmatrix} \tag{3.122}$$

The following wind turbine data (table 3.1; from Larsen and Mogensen, 2006) is applied to the linear state space model that we have built.

Table 3.1: wind turbine data

P_{nom}	2	[MW]	Nominal electric power
ω_{gnom}	167.6	rad/s	Rated generator speed
$\omega_{g\,\min}$	50.27	rad/s	Minimum generator speed
ω_{rnom}	1.97	rad/s	Nominal rotor speed
$\omega_{r\,\min}$	0.59	rad/s	Minimum rotor speed
N_g	1:85		Gear ratio
H	80	m	Tower height
R	40	m	Blade radius
J_r	8.7e6	kgm^2	Turbine rotor inertia
J_g	150	kgm^2	Generator inertia
J_{tot}	9.78e6	kgm^2	Total moment of inertia
r_{top}	1.2	m	Tower top radius
r_{bottom}	2.15	m	Tower bottom radius

m_t	200	T	Equivalent mass of the tower
f_s	0.55	Hz	Resonance frequency of the shaft
K_s	1.039e8	N/m	Stiffness coefficient of drive shaft
D_s	1.039e6	N/m	Damping coefficient of shaft
f_t	0.3	Hz	Resonance frequency of the tower
K_t	6.948e5	N/m	Stiffness coefficient of tower
D_t	2.316e4	s^{-1}	Damping coefficient of tower
ω_n	8.88	Hz	Undamped natural frequency of the pitch actuator
ς	0.9		Damping coefficient of pitch actuator
τ_T	0.1	s	Time constant of the generator actuator
ρ	1.2	kg/m^3	Density of air

The state-space representation of the total wind turbine model given by the Equations (3.120) to (3.122) is modelled by Simulink block diagram given in Fig. 3.21 and the simulation results are shown in Fig. 3.22 to Fig. 3.24:

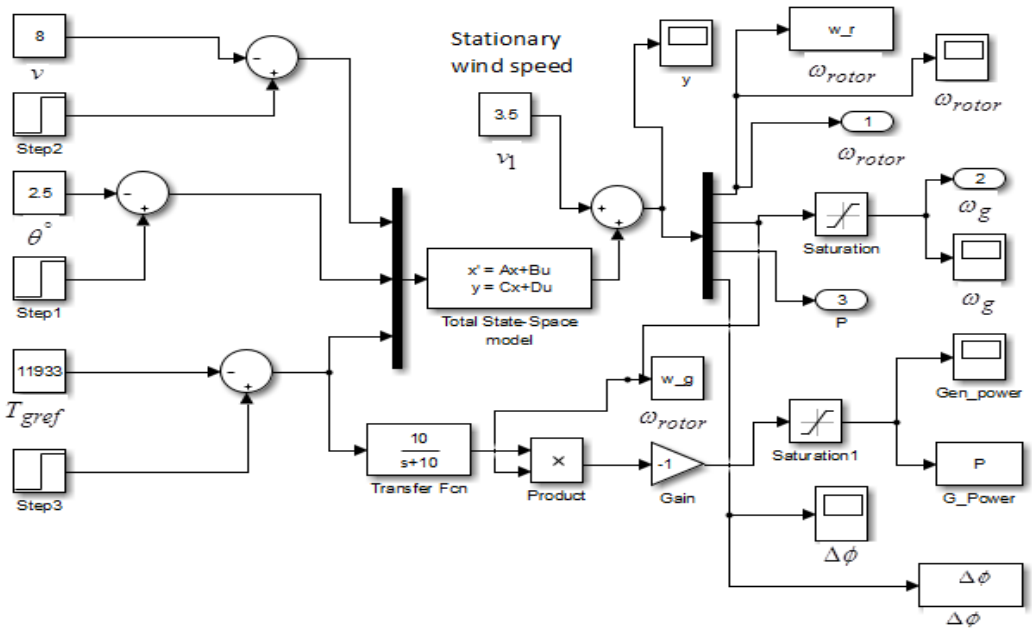

Figure 3.21: Simulink block diagram for the total state-space system of the WT.

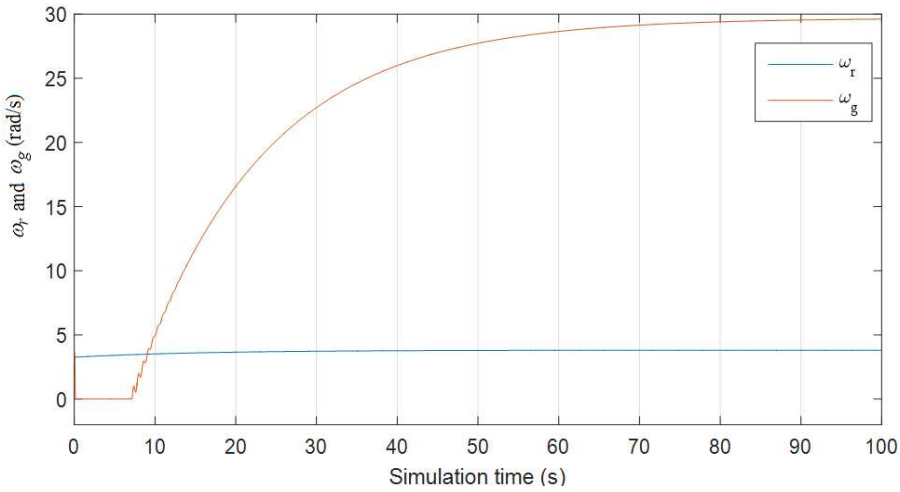

Figure 3.22: Simulation results of ω_r and ω_g versus time(s) for the total state-space system.

From the data table shown in table 3.1 assuming all data are correct, the WT nominal power is reported as 2 MW. Generator nominal speed is given as 167.6 rad/s. From these data and by using the formula $T_{\text{nominal}} = \dfrac{P_{\text{nominal}}}{\omega_{\text{g-nominal}}} = \dfrac{2\times10^6}{167.6} = 11933\,\text{Nm}$. This value is taken as the T_{g-ref} value for one of the input states of the system. Nominal rotor speed given in the table 3.1 is 1.97 rad/s. If the average wind speed is taken as 8 m/s and by assuming that the WT is

operating at maximum power for that wind speed, λ could be taken as 7.5 (numerical value). Using these values ω_{rotor} can be calculated using the formula $\frac{\lambda v}{R} = \frac{8 \times 7.5}{40} = 1.5$ rad/s which could be taken as a correct value by comparing the with the ω_{rnom} in table 3.1. From Fig. 3.23. it can be seen that the turbine rotor speed and the generator speed reach the stable positions with the initial conditions. It was noted that both turbine rotor speed and the generator speeds were unstable at the start without initial conditions. The constant block, v_1 which is shown in Fig. 3.21 is the stationary wind speed of the turbine. This is the minimum wind speed necessary to operate the generator (it is assumed to be 3.5 m/s for this WT). However, it is obvious that the settling time for ω_g is very high.

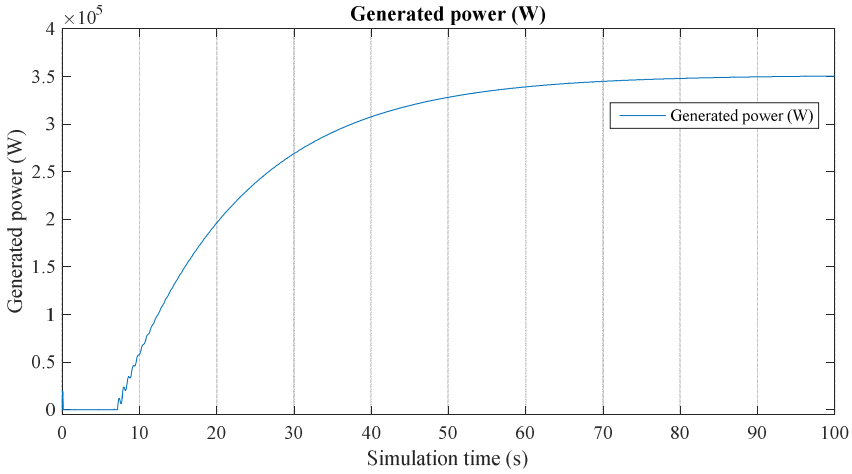

Figure 3.23: Generated power versus time (s) characteristics of the total state-space system.

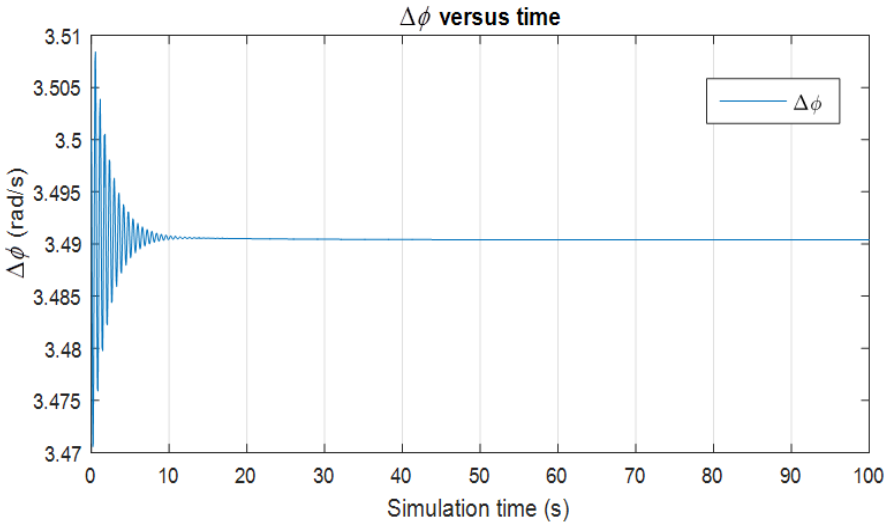

Figure 3.24: Characteristics of $\Delta\phi$ (rad/s) versus time (s).

The state matrix A_m from the simulation is given below,

$$A_m = \begin{bmatrix} 0 & 0.0010 & 0 & 0 & 0 & 0 \\ -3.1131 & -0.1004 & 0 & 0 & 0 & 0 \\ 0 & 0 & -0.0100 & 0 & 0 & 0 \\ 0.1440 & 0 & 0 & -0.0001 & 0.0000 & -0.0119 \\ 0 & 0 & -0.0001 & 0.0815 & -0.0010 & 8.1490 \\ 0 & 0 & 0 & 0.0010 & -0.0000 & 0 \end{bmatrix} *1.0e+03$$

The Eigenvalues are,

$$eig(A_m) = \begin{bmatrix} -50.2146 + 24.3227i \\ -50.2146 - 24.3227i \\ -0.0632 + 0.0000i \\ -0.4801 + 10.3725i \\ -0.4801 - 10.3725i \\ -10.0000 + 0.0000i \end{bmatrix}$$

When examined all Eigenvalues found to be negative and they are related to the poles of the system which lie in the left half of the Laplace plane. Though the system is stable the three poles closer to the origin; -0.0632 + 0.0000i; -0.4801 +10.3725i; -0.4801 -10.3725i are directly contributing to higher settling time for the system. According to control theory, the eigenvalues can be used to determine the system stability only for time-invariant systems and for systems which are time-variant, the methods using eigenvalues to determine system stability will fail. The controllability of the total system could be checked analytically or using an appropriate programming language. The rank is found to be equal to 6 which is the full rank of the system and therefore, the system is controllable.

Feedback Control of the Total Wind Turbine Model

Simulation response of the total wind turbine model has been very accurate and the results for a large scale wind turbine with a 40m diameter turbine blade, with $2x10^6$ W nominal capacity power output, is amazing. However, when the generator speed is observed, the settling time is more than 60 seconds and the generator output power also reaches to a steady state output after 60 seconds which needs to be considerate. This type of power output creates the problem of Grid power balancing and has to be controlled invariably. Initially, a PID/State-feedback

controller is implemented to control the generator speed. As the wind speed is one of the inputs, and the output that has to be controlled is the generator speed ω_g . Assuming the turbine is operating at optimum TSR, output turbine speed ω_r is fed back and compared with the calculated input turbine reference speed ω_{r-ref} as the wind speed is always available with the anemometer measurements or from the estimated measurements. Settling time for ω_g with the PID/State-feedback controller is still high and is more than 60 s. The simulation response of the system with a PID controller is shown in Fig. 3.25. and the Simulink block diagram with the PID/State-feedback controller is shown in Fig. 3.26.

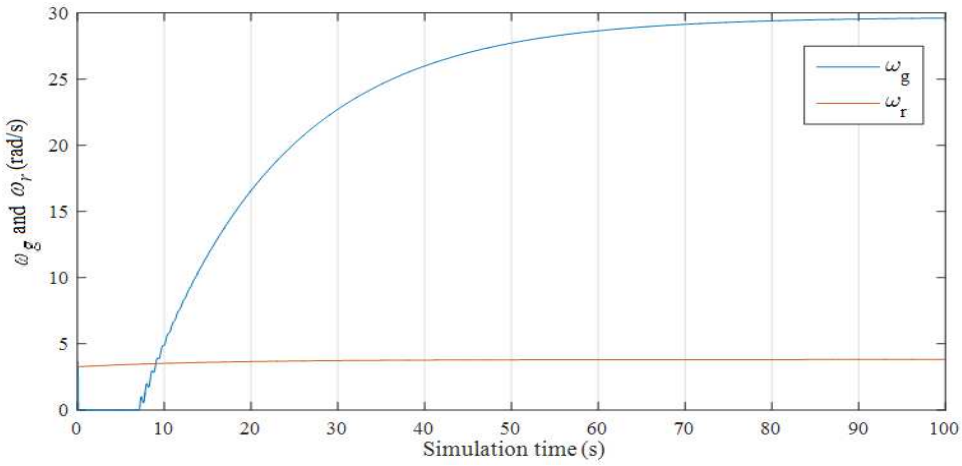

Figure 3.25: PID/State-feedback controller implementation results.

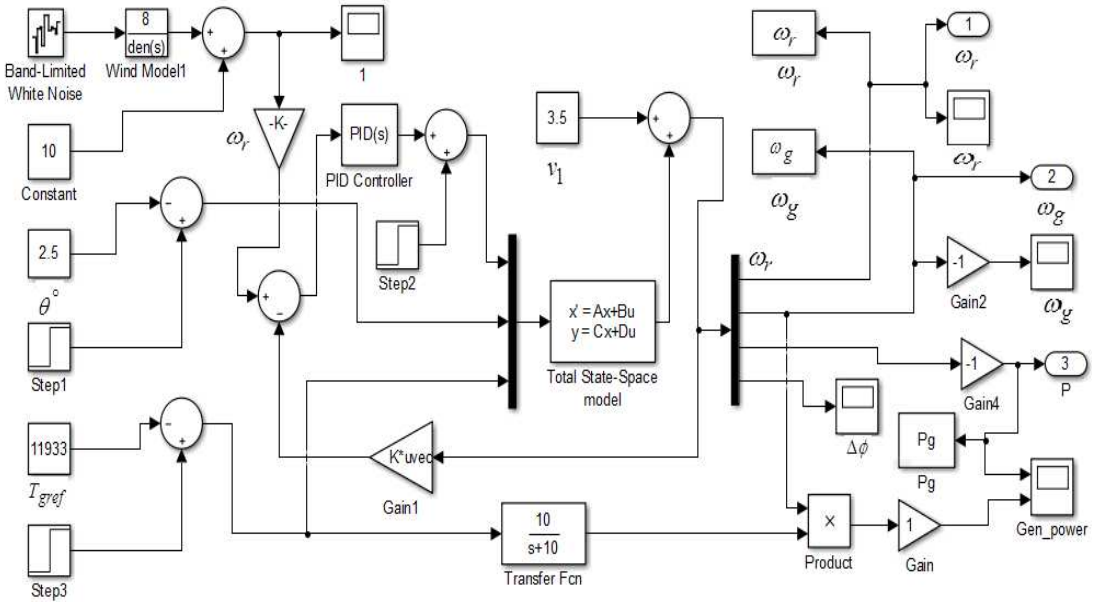

Figure 3.26: PID/State-feedback controller for the turbine speed and generator speed control.

The *PID* controller parameters obtained after tuning are: proportional (p)=3.7039, Integral (I)=1.1615, derivative (d)=-0.3170. and the State-feedback vector, k = [1.3, 0, 0 ,0]. The State feedback vector is to be in the form of a row vector with all other elements with zeros as it is necessary to tap only the ω_r from the four output states. It was noted that by increasing the State-feedback constant the settling time can be decreased but at the expense of overshoot.

3.5. Generator Side Modelling

Induction generator or asynchronous generator generates alternating current (AC). To generate electricity from a generator, the rotor has to rotate at a speed faster than synchronous speed. Synchronous speed means the speed of the rotating magnetic field. Induction generators are generally used in mini hydro plants, and also with large-scale wind turbines. In an electric motor, AC is supplied to the stator in a form of a rotating magnetic field. The rotor has magnets or magnetic field which have north and south poles as pairs. When the pole pairs in the stator are not in line with the pole pairs of the rotor (a north pole of a rotor is not facing with the south pole of the stator) then the tendency is there to catch these opposite poles resulting the rotor being made to rotate. Applying the principle of flushing these magnetic flux lines, the rotor is accelerated or made to rotate at a speed higher than the synchronous speed of the flux lines of the stator then the slip becomes negative. The slip is defined as a percentage difference between the synchronous speed of the magnetic field and the rotor shaft speed (Bose, 2014),

$$s = \left(\frac{\omega_s - \omega_g}{\omega_s} \right) 100 \quad \% \tag{3.123}$$

where, ω_s is the synchronous speed and ω_g is the generator rotor speed. The asynchronous generator is not a self-excited machine and it needs an excitation to start with. With the help of capacitors connected to the stator coils, these two magnetic fields are made to rotate continuously. This results in active power being supplied to the stator coils. Generally, induction generators take reactive power from AC power lines and supply active power back to the grid. The power exerted due to capacitive and the inductive components are identified as the reactive power and the power exerted due to resistive components are defined as the active power. In practice it is necessary to control the effects of reactive power in order to control the active power demand, though, a slight variation is allowable according to quality control discussions found in literature. In grid-connected power systems the generator voltage and frequency are locked to the grid system according to the grid code requirement. Changing the

energy output from the WT rotor, does not affect the frequency and voltage but will cause the output current to increase resulting in an equivalent change in the generator output power.

3.6. Doubly Fed Induction Generator (DFIG)

DFIG has been very widely used in wind turbine applications due to many reasons. They are capable of operating at speeds slightly above or below the synchronous speed than other types of generators. This feature is exploited for the benefit of variable gusts of wind speeds. When this happens turbine blades try to accelerate the rotational speed by creating a large force at the hub and gearbox resulting in an increase of generated power output. This effect is undesirable for WT operation. One such control mechanism is to accept the variation and convert it to DC and then reconvert it to AC at the desired output frequency using an inverter. As the inverters are very expensive for large-scale WTs, the other option is to connect both the wound rotor and the stator to the grid, hence the term 'doubly-fed' is appropriately defined. In this method, one winding is directly connected to the GRID and produces 3-phase AC power at the desired grid frequency. The other winding (traditionally called the field, but here both windings can be outputs) is connected to 3-phase AC power at variable frequency (Chen et al., 2014). This input power is adjusted in frequency and phase to compensate for changes in speed of the turbine. As we are discussing the advantages of DFIG, the inverter cost is comparatively lower for DFIG applications. For DFIG power factor control can be implemented at a lower cost. Adjusting the frequency and phase requires an AC to DC to AC converter. This is usually constructed from very large IGBT (insulated-gate bipolar transistor: high-efficiency electronic switching device) semiconductors. The converter is bi-directional, and can pass power in either direction. Power can flow from both windings to the Grid (Chen et al., 2014).

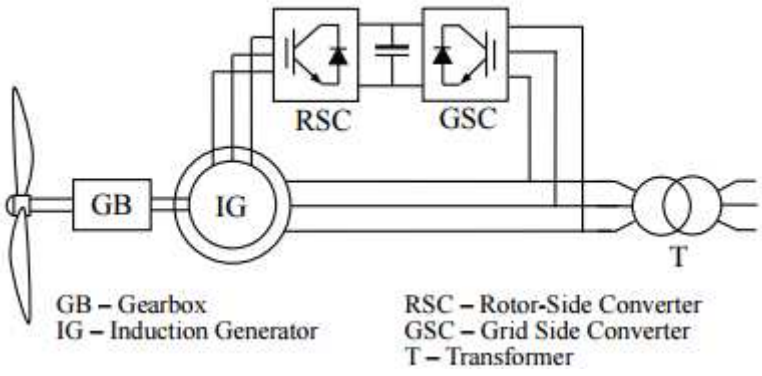

Figure 3.27: Schematic diagram of a DFIG (Chen et al., 2014).

DFIG is chosen for modelling in this thesis due to the advantages mentioned above. The following assumptions are made for this modelling (Fig. 3.27):

a) The stator and rotor windings are symmetrical.

b) The capacitance of all the windings can be neglected.

c) The active (real) and reactive power are positive when fed into the grid (sign convention).

Full detail of assumptions could be found in reference 'Electrical Machines', (2016) and in Fletcher and Yang (2016). For modelling purposes, the synchronously rotating reference frame can be linked to the stator or rotor flux of the machine. As it is a generator in this instance it is convenient to refer the frame with respect to stator flux. The 0dq frame is rotating at synchronous speed and the currents going out of the machine is taken as positive. The d -axis is oriented along the stator flux vector position. The relationship between the three-phase quantities and the dq components is defined by Park's transformation. The positive q-axis is ahead in the direction of rotation or lead the positive d-axis by $\pi/2$. The symbols ds and qs correspond to stator direct and quadrature axes; dr and qr correspond to rotor direct and quadrature axes ('Electrical Machines', 2016; Fletcher and Yang, 2016). For convenience in calculations and to avoid using $\sqrt{3}$ in three-phase calculations per-unit system is used.

$$\text{Per unit value} = \frac{\text{Actual value in any units}}{\text{Base or reference value in the same unit.}} \tag{3.124}$$

Active and Reactive Power

The basics of active and reactive power can be described as given next. In AC power systems, the current and the voltage signals are alternating in nature. The description given below is extracted from Ackermann (2005).

They can be represented as,

$$u(t) = U_M Cos(\omega t) \tag{3.125}$$

$$i(t) = I_M Cos(\omega t - \varphi) \tag{3.126}$$

where,

$u(t)$ = voltage as a function of time

$i(t)$ = alternating current

I_M = maximum current amplitude

φ = defined as the phase shift between voltage and current.

U_M = maximum voltage amplitude

$\omega = 2\pi f$

f = frequency (50 or 60 Hz)

Power is equal to the product of voltage and current:

$$p(t) = u(t)i(t) = U_M I_M \cos(\omega t)\cos(\omega t - \varphi)$$
$$= P[1+\cos(2\omega t)] + Q\sin(2\omega t)$$

where,

$$P = \frac{U_M}{\sqrt{2}}\frac{I_M}{\sqrt{2}}\cos\varphi \text{ =active power.} \quad (3.127)$$

$$Q = \frac{U_M}{\sqrt{2}}\frac{I_M}{\sqrt{2}}\sin\varphi \text{ = reactive power.} \quad (3.128)$$

cos (φ) is defined as the *power factor;*

$|U| = \frac{U_M}{\sqrt{2}}$ =root mean square(RMS) phase voltage, *U= complex current*

The complex power $S = |S|e^{j\arg(S)} = P + jQ = UI = |U||I|e^{j\varphi}$.

The line to line voltage: $U_{ab} = U_a - U_b = |U_a|(1-e^{-j120^0}) = \sqrt{3}\left|U_a e^{j30^0}\right|$;which implies that line to line voltage is $\sqrt{3}$ times larger than the phase voltage; Please note that phase voltages are normally defined as *V or U* and with a,b,c subscripts which indicate the phases a,b,c.

(Example: $V_a = |V|e^{j0^0}$; $V_b = |V|e^{-j120^0}$; $V_c = |V|e^{+j120^0}$.).

The reactive power depends on the phase shift φ and is related to active power as given next,

$$Q = \frac{\sin\varphi}{\cos\varphi}P \quad (3.129)$$

3.7. Generator Modelling and Reference frames

In section 3.4, wind energy conversion system was described considering harvesting energy from WT blades and the analysis and the modelling was carried out considering the gearbox. Turbine generator reference torque actuator was there to control the generated power from the generator to keep at a constant level or to harvest optimum power from the wind turbine blades. This section will describe the modelling of the electrical generator and its electrical characteristics with reference to the stator and rotor coils. Dynamic mathematical model for a DFIG is described with a flux model and the current model. Modelling and control of the electrical generator is entirely different from the previous controllers described under WT control. The DFIG with slip-rings, whose stator windings are directly connected to the grid and its rotor winding connected to the grid through a bidirectional frequency converter using a back-to-back pulse width modulation technique is used in this thesis, as this method has been very popular and used by many researchers during the recent past. Okoro (2003), presented a complete dynamic model for induction machine (motor) which could be applicable for the WT modelling with the d-q axis transformation theory and Park transformation matrix.

As stated in the literature review, Ekanayake et al., (2003) presented state-space modelling of variable-speed wind turbine. The state space method presented included 'current model', 'fluxes model' and 'rotor internal voltages and stator currents model'. In each method the state vector is defined as the d-q-axis current states, fluxes or fluxes with voltages. Martinez (2007) used a fluxes model to model the DFIG. Martinez's mathematical model is modified into a state space model in this thesis and modelled in Simulink which is convenient for controller applications. The reference frame is taken as a *synchronously rotating reference frame* (dq-frame), where the d-axis is oriented along the stator- flux vector position. Park's transformation is used to relate the 3-phase quantities and the d-q components as described previously. The current leaving the machine is taken as positive. Applying the Kirchhoff's law, the following equations can be obtained,

$$V_{ds} = -R_s i_{ds} + \omega_s \psi_{qs} + \frac{d\psi_{ds}}{dt} \tag{3.130}$$

$$V_{qs} = -R_s i_{qs} - \omega_s \psi_{ds} + \frac{d\psi_{qs}}{dt} \tag{3.131}$$

$$V_{dr} = 0 = -R_r i_{dr} + s(\omega_{s\,r})\psi_{qr} - \frac{d\psi_{dr}}{dt} \tag{3.132}$$

$$V_{qr} == 0 = -R_r i_{qr} - s(\omega_s)\psi_{dr} - \frac{d\psi_{qr}}{dt} \tag{3.133}$$

We can take the rotor voltage V_{dr} and V_{qr} as equal to zero since the current is only fed into the stator. Where, V_{ds}, V_{qs}, V_{dr} and V_{qr} are the $d-$and $q-$axis stator and rotor voltages. $s = slip$; i_{ds}, i_{qs}, i_{dr} and i_{qr} are the $d-$and $q-$axis of the stator and rotor currents. If ψ_{ds}, ψ_{qs} , ψ_{dr} and ψ_{qr} are the $d-$and $q-$axis of the stator oriented and rotor oriented fluxes, the flux equations are,

$$\psi_{ds} = L_s i_{ds} + L_m i_{dr} \tag{3.134}$$

$$\psi_{qs} = L_s i_{qs} + L_m i_{qr} \tag{3.135}$$

$$\psi_{dr} = L_m i_{ds} + L_r i_{dr} \tag{3.136}$$

$$\psi_{qr} = L_m i_{qs} + L_r i_{qr} \tag{3.137}$$

Where L_s, L_r and L_m are stator, rotor and mutual inductances. ω_s is defined as the angular velocity of a synchronously rotating frame and ω_r is the rotor angular velocity. The parameter R_s is the stator resistance and R_r is the rotor resistance. The slip is defined as (Bose, 2014),

$$s = 1 - \frac{p\omega_m}{2\omega_s} \tag{3.138}$$

(the slip is also defined as $s = \frac{\omega_s - \omega_g}{\omega_s}$). From flux equations, the current equations can be written as (Krause et al., 1998),

$$I_{ds} = \frac{1}{\sigma L_s}\psi_{ds} - \frac{L_m}{\sigma L_s L_r}\psi_{dr} \tag{3.139}$$

$$I_{qs} = \frac{1}{\sigma L_s}\psi_{qs} - \frac{L_m}{\sigma L_s L_r}\psi_{qr} \tag{3.140}$$

$$I_{dr} = \frac{-L_m}{\sigma L_s L_r}\psi_{ds} + \frac{1}{\sigma L_r}\psi_{dr} \tag{3.141}$$

$$I_{qr} = \frac{-L_m}{\sigma L_s L_r}\psi_{qs} + \frac{1}{\sigma L_r}\psi_{qr} \tag{3.142}$$

where, $\sigma = 1 - \frac{-L^2{}_m}{L_s L_r}$ is the leakage coefficient. It is assumed that the power losses associated with the stator and rotor resistances are negligible. The active and reactive stator and rotor power can be calculated by the following equations (Krause et al., 1998),

$$T_e = \varphi_{qr}.I_{dr} - \varphi_{dr}.I_{qr} \tag{3.143}$$

$$P_{active} = V_{ds}.I_{ds} + V_{qs}.I_{qs} \tag{3.144}$$

$$P_{reactive} = V_{qs}.I_{ds} - V_{ds}.I_{qs} \tag{3.145}$$

Total power,

$$P_{total} = V_{ds}.I_{qs} + V_{qs}.I_{qs} + V_{qs}.I_{ds} - V_{ds}.I_{qs} \tag{3.146}$$

The dq-axis currents and voltages so far presented originated by transforming three-phase system to two-phase system via Parks transformation. By defining the phase currents i_{sa}, i_{sb} and i_{sc} the transformation into d-q frame could be written as (Okoro, 2003):

$$\begin{bmatrix} i_{as} \\ i_{bs} \\ i_{cs} \end{bmatrix} = [C]^{-1} \begin{bmatrix} i_{qs} \\ i_{ds} \\ i_o \end{bmatrix} \tag{3.147}$$

The equation (3.147) could be extended to phase voltages,

$$\begin{bmatrix} V_{as} \\ V_{bs} \\ V_{cs} \end{bmatrix} = [C]^{-1} \begin{bmatrix} V_{qs} \\ V_{ds} \\ V_o \end{bmatrix} \tag{3.148}$$

Where, $[C]^{-1} = \begin{bmatrix} \cos\theta & \sin\theta & 1 \\ \cos\left(\theta - \frac{2\pi}{3}\right) & \sin\left(\theta - \frac{2\pi}{3}\right) & 1 \\ \cos\left(\theta - \frac{4\pi}{3}\right) & \sin\left(\theta - \frac{4\pi}{3}\right) & 1 \end{bmatrix}$ and $V_{as} = \sqrt{2}V\cos\omega_b t$,

$V_{bs} = \sqrt{2}V\cos\left(\omega_b t - \frac{2\pi}{3}\right)$ and $V_{cs} = \sqrt{2}V\cos\left(\omega_b t + \frac{2\pi}{3}\right)$. The subscript as, bs and cs denotes the phases a, b, c stator voltages. The V_{as}, V_{bs} and V_{cs} are inputs to the generator in

real world. Neglecting V_0 component of the dq0 axis frame, using matrix transformations, the Equation (3.148) could be transformed into,

$$\begin{bmatrix} V_{sq} \\ V_{sd} \end{bmatrix} = \frac{2}{3}\begin{bmatrix} \cos\theta & \cos\left(\theta - \frac{2\pi}{3}\right) & \cos\left(\theta - \frac{4\pi}{3}\right) \\ \sin\theta & \sin\left(\theta - \frac{2\pi}{3}\right) & \sin\left(\theta - \frac{4\pi}{3}\right) \end{bmatrix}\begin{bmatrix} V_{sa} \\ Vsb \\ Vsc \end{bmatrix} \tag{3.149}$$

Using algebra and based on the above mathematical formulations, modified state space flux model can be formulated as given next (Equations (130)- (137)). Though, in Equation (3.150) the states are currents, by using derivatives of fluxes from Equations (139)- (142), the left hand side of Equation (3.150) could be transformed into actual state-space form. However, Equation (3.150) is still in perfect form to apply in matrices form in Simulink.

$$\begin{bmatrix} \dot{\psi}_{ds} \\ \dot{\psi}_{qs} \\ \dot{\psi}_{dr} \\ \dot{\psi}_{qr} \end{bmatrix} = \underbrace{\begin{bmatrix} -R_s & \omega_s X & \omega_s X_m & 0 \\ -\omega_s X_s & -R_s & 0 & -\omega_s X_m \\ 0 & s\omega_s X_m & s\omega_s X_r & -R_r \\ -s\omega_s X_m & 0 & -R_r & s\omega_s X_r \end{bmatrix}}_{A}\underbrace{\begin{bmatrix} I_{ds} \\ I_{qs} \\ I_{qr} \\ I_{dr} \end{bmatrix}}_{States} - \underbrace{\begin{bmatrix} 1 & 0 & 0 & 0 \\ 0 & 1 & 0 & 0 \\ 0 & 0 & 0 & 0 \\ 0 & 0 & 0 & 0 \end{bmatrix}}_{\substack{B \\ Input\_Matrix}}\underbrace{\begin{bmatrix} V_{ds} \\ V_{qs} \\ 0 \\ 0 \end{bmatrix}}_{Input} \tag{3.150}$$

The stator and the rotor parameters of the generator R_s, X_s, X_m, R_r and X_r denote the stator resistance and reactance, mutual reactance and rotor resistance and reactance, respectively.

For simulation studies, there are two methods to build the dynamic model of the generator section. One approach is the build the Simulink blocks from basic principles using all equations from (3.130) to (3.138). The other approach is to build the Simulink model from Equation (3.150). In the first method the Simulink model does not offer all information at a glance for the reader to understand while the second method is clear and transparent on model equations. In this thesis Equation (3.150) is being built for simulation studies. The Equation (3.150) is modified here to model the system to reach the state space representation. The fluxes after integration is fed back into the input in a form of current vectors to obtain the coupled scenario (see the Simulink block in Fig. 3.29) for correct modelling approach. The Simulink block diagram for the Equation (3.150) of the DFIG is shown in Fig. 3.29. The exerted torque versus simulation time is given in Fig. 3.30. Initially, the torque exerted happened to be fluctuating at a diminishing rate due to the turbine rotor speed variation and finally settles into a fixed value.

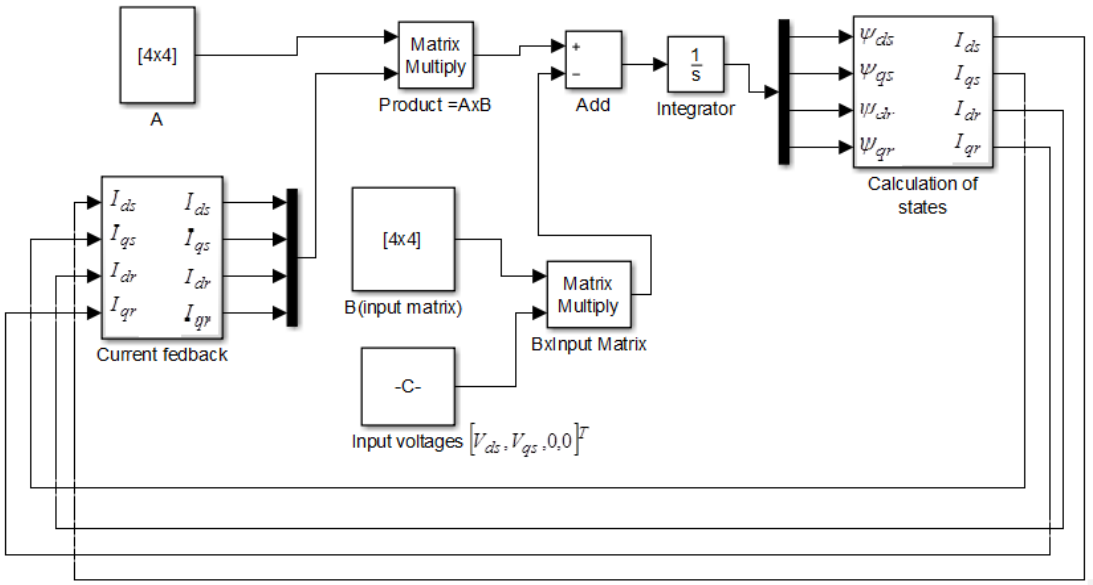

Figure 3.28: Simulink block diagram for DFIG.

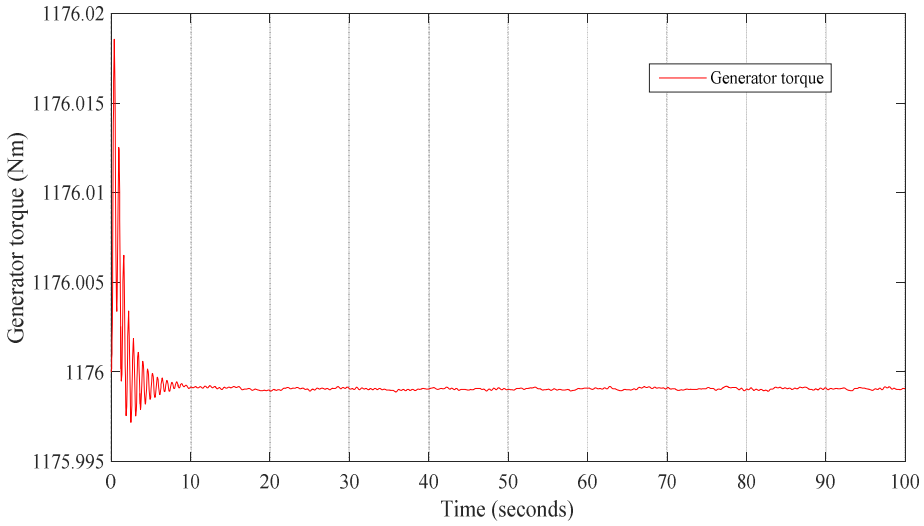

Figure 3.29: Torque versus time characteristics.

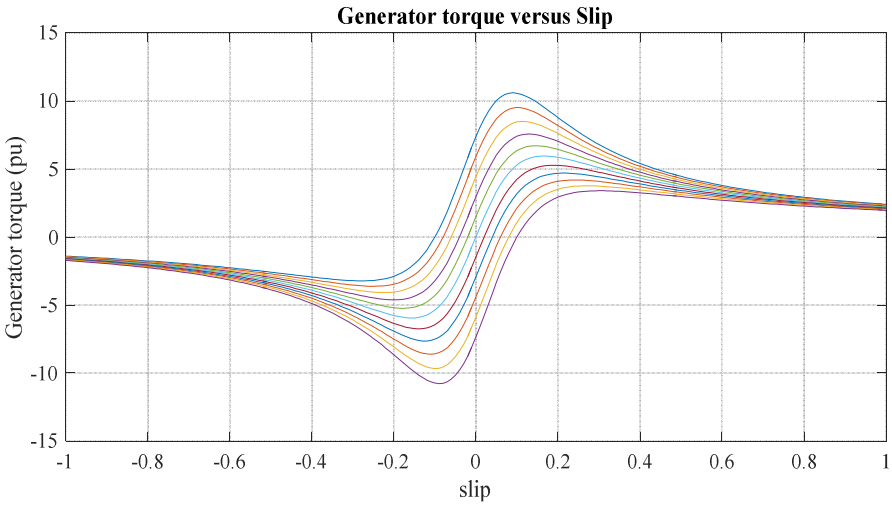

Figure 3.30: Generator torque characteristics versus slip: when rotor voltage increases the torque gradually increases (in motor mode) and then decreases.

Analytically, it can be proved (Krause et al., 1998 and Bose, 2014) that when the slip is low (closer to zero) then the torque is proportional to the slip, and when the slip is large s<1 (The maximum value for slip is equal to 1) then the torque is inversely proportional to the torque which shows the hyperbolic behaviour. Generator torque and the slip characteristics are shown in Fig. 3.32. For a high resistance of the stator, the torque decreases.

Summary

Nonlinear state space model for the WT was presented with mathematical formulations. Analytical presentations were given for each subsystem: wind model, turbine rotor, gearbox, generator, pitch actuator, generator torque actuator. Mathematical analysis was presented to harvest the maximum power from the wind turbine using the state space approach. Linearised state space model which is presented in this thesis has been a valuable contribution with the correct mathematical approach with the exploitation of partial derivatives of all nonlinear variables like turbine power coefficient, TSR, wind speed, time variant state matrix and the time variant input matrix of the total WT system.The author of this thesis believes that this contribution is especially important as many analytical approaches found in literature neglected some important parameters or had lapses with the mathematical approaches. MPPT programme and the Simulink models formulated there for all subsystems of the wind power generation system was the other contribution made in this thesis. The modified state space PID/State-feedback controller was implemented and the analysis was given there with the graphical presentations. The state-space model and its characteristic results were tested with 2 MW real

turbine data and the characteristic plots were presented with the application of initial conditions.

The complex part of the WT analysis involves in the modelling and control of the electric generator by transforming into a d-q axis coordinates system (reference frame). Convenient, modified matrix method presented here was the other contribution, which could be extended into a state space current or voltage model according to any control paradigm.

Chapter 4: Model Predictive Control

Outline

In this chapter application of a model predictive controller for electricity generation from wind WT is described. Introduction to the overview of MPC controllers is given in section 4.0. The advantages and disadvantages of PID, MPC and Gain Scheduling control techniques are briefly described in section 4.1. Analytical approach to the MPC method with special reference to state space modelling is presented in section 4.2. MPC application to WT control and the simulation results are presented in section 4.3. The Summary are given at the end of the chapter.

4.0 Introduction to MPC Controllers

Model predictive control (MPC) is a common name for optimal control of many variables using computer control algorithms. The MPC uses an explicit process model to predict the future plant response by manipulating the input variables of the plant (Wang, 2009). The application of Model-based predictive control initially started in 1980 within chemical industries. It is now being extensively developed into the other areas of engineering including robotics and aerospace engineering. When describing MPC, the prediction in the chosen period is generally known as the prediction horizon. If the current control interval is *k*, prediction horizon p is the number of future control intervals that the MPC is programmed to operate and optimise. The control horizon is defined as the chosen length of the input or in other words the control horizon, *m*, is the number of manipulated variables (MV) moves to be optimised at control interval *k*. The parameter *k* is the sampling instant. The reference trajectory is the desired output that we plan to achieve by implementing or manipulating the predicted control input based on the information available from past control input data with the present measured output variables. Measured output data is obtained from the plant up to the present instant. Prediction horizon and the sample time are decided initially. Generally, the prediction horizon is greater than the settling time.

The functionality of MPC is to optimise some variables subject to constraints in order to achieve the desired output (Maciejowski, 2002). An example of such optimisation could be to minimise the sum of the squares of the deviations between predicted future outputs and specific reference trajectory. Generally, when designing an MPC, all input variables are manipulated

variables or considered as all plant inputs as manipulated variables and all plant outputs as measured variables.

Recently, MPC control systems have been used to optimize the operation of gas turbines in aircrafts. In general, control and dynamics of aircrafts are analysed in two scenarios. Namely, the pitch dynamics which is the nose up/down movement and the lateral dynamics which is the wingtip up/down movement (roll motion) and nose left/right movement (yawing motion). The mathematics and the dynamics are similar to the rigid body motions and can be dealt with Newton's law of motion and state space modelling. However, the aerodynamic forces and moments are highly complex and nonlinear functions (involves with the application of computational fluid dynamics) which depend on a variety of parameters like aircraft's geometric properties and dynamic pressure, aircraft's attitude against the airflow, control surface deflections etc. (Simon, 2014).

One of the major objectives of a flight control system, is to limit the aircraft response to the pilot inputs such that it does not exceed any structural or aero dynamical limitations. The flight control system should be able to limit the response of the aircraft such that the states remain within a region where the aircraft is still flyable at steady state, the so called flight envelope. This capability is known as flight envelope protection or maneuver load limitations. Though, MPC systems have been tested in this area, they are still at the experimental stage.

The flight envelope protection and carefree manoeuvring is achieved by incorporating a well - designed control system which has limitations (or hard constraints) on the states and control (or the pilot commands). But, this results in a nonlinear control problem that in general is far more complicated to solve than the linear system. Therefore, in aircraft industry, popular Linear Quadratic Control (LQ) is used with a gain scheduled LQ controller for their primary stability. The MPC control technique though, very popular in many disciplines still, has some reservations in aeronautical (aircraft control) industry, due to poor test results. Therefore, they use anti-windup over-ride and ad-hoc engineering control systems (Simon, 2015). GS which was initially started in 1960, still popular in aircraft industry than MPC, where the application of MPC was initially originated in 1980s.

A generalised predictive controller (GPC) was presented by Călugăru and Dăniúor (2016) for pitch attitude hold control system that can be used for an auto pilot control system of an aircraft. It was noted that for a step response of the predictive controller the settling time was 4 seconds

while the generic PID controller results the settling time of 6 seconds. The GPC was also implemented in a single closed loop so as the PID controller. Linear model predictive control (LMPC) for the Encirclement of a target using a quadrotor aircraft was presented by Iskandarani et al., (2013). The nonlinear model of the quadrotor was replaced by a linear two state model for experimental analysis. The GPC based reliable oxygen control regulator was presented by Yuxin at al., (2015) for aiding high security, comfort breathing mask users in the aircraft. The simulation result suggested that, the GPC-based oxygen regulator was more effective in improving the response speed and lowering breathing resistance than PID controllers. A switching attitude MPC for an unmanned Tilt–Rotor, flying in a helicopter mode configuration was presented by Papachristos et al., (2011). The MPC Controller was designed for performing robust tracking control of the attitude.

4.1. Advantages, Disadvantages of PID Control, MPC and Gain Scheduling

Application of MPC extends to many complex control requirements as it gives the opportunity to implement closed loop optimal control strategy with constraints. On the other hand, the generic popular PID controllers cannot perform well for highly non-linear systems and many PID control loops are required when PID controllers are applied to multi-input multi-output (MIMO) systems. Moreover, the tuning of several PID controllers happened to be complicated and inflexible when many control constraints are involved with the state inputs and outputs but, tuning of MPCs are systematic and algorithm based. PID controllers do not perform well when applied to highly nonlinear systems. MPC can be applied to highly non-linear systems as well as they minimise the cost function at each time instant depending on the current situation and hence, the plant is closed loop optimally controlled at every moment. In linear systems optimization problem is a quadratic problem. However, MPC controllers can be sometimes very slow as it handles matrices for every iteration for manipulating variables.

Advantages and disadvantages of MPC Control

The MPC design technique is flexible to apply on any type of plant models such as: linear, nonlinear, multivariable, deterministic, stochastic or fuzzy. MPC controllers, have the facility to implement the constraints inputs and states (e.g. pitch actuator constraints for WT design, generator torque reference actuator: upper and lower boundaries could be specified; TSR can be specified with the lower and upper limits to harvest maximum energy from the WT; Lower

limit and the upper limit for the wind speed can be specified for the wind speed input for economic operation and the maximum limit could be specified for safety purposes).

The online parameter optimization technique offers the optimal operation of the plant at each computer iteration. However, the disadvantage is the large computational time and need for a large memory for online computation. In numerous occasions off-line calculation is proposed by many researchers to overcome this problem (e.g. Hypiusová and Vesely, 2015). Adding constraints to the infinite horizon linear quadratic optimal control problem makes it in general extremely difficult to solve explicitly (Simon, 2014). MPC design procedure does not always guarantee the stability and robustness of the closed-loop control (Hypiusová and Vesely, 2015).

Gain scheduling

Gain scheduling, is also one of the most commonly used control techniques which uses family of linear controllers to control nonlinear plants or systems. Many of the earlier articles reported in this area, were in the areas of flight control and in aerospace engineering. In this method the observable variables are defined as scheduling variables and they are used to determine the operating region (e.g. wind regions, in an aircraft flight control system, the altitude and Mach can be the scheduling variables, PID gain schedule specifies maximum values for the proportional, integral, and derivative gain parameters). Gradually, this approach has been used almost everywhere in control engineering (similar to MPC applications) which is greatly advanced with the introduction of linear parameter varying (LPV) systems (Ilka, 2015). As described in the literature review also, the gain-scheduled controllers use the principle of interpolating, in some manner, between the members of a family of linear time-invariant controllers (Leith and Leithead, 1997). The GS control system was proposed by Wu et al., (2008) to control vertical takes off and landing of an aircraft. The nonlinear aircraft dynamics were formulated as a LPV system with external parameter-dependent disturbances.

Advantages and disadvantages of GS

The GS approach enables the design of low computational effort controllers. Though, a family of linear time-invariant controllers are used in many designs, single type of linearization could be used for all controllers which is straightforward and conceptually appealing.

The non-equilibrium operating points in the plant could be incorporated directly and rigorously into the controller design. In literature, the robust GS technique is reported as more appealing

method to gain complete control over local behaviour of independent local controllers. The main drawback of fuzzy gain scheduling involves the lack of a relation between the dynamic characteristics of the original nonlinear model and the fuzzy model (Ilka, 2015).

Summarising the importance of MPC control and the GS control, it seems that both techniques are equally important and popular. However, according to the initial guidelines, advise at the inception and the research boundaries, MPC application to the WT modelling is addressed in this thesis.

4.2 Analytical Approach to MPC Designs

MPC toolbox in MATLAB does not offer extensive mathematical analysis for the reader in MPC designs. However, MATLAB/Simulink approach has become very popular among design engineers, as it is a graphical programming language and finally provides the C-programming codes which is necessary to apply for hardware designs. However, mathematical formulations are equally important to understand the, recursive iteration methods, optimisation and the cost function involved with the MPC designs. In addition, the mathematical formulations with the state space model clarifies the iterative steps for the designer to analyse and visualise the total system. This section describes the Mathematical formulations, the analysis required to understand and implement the MPC controller (Morari, 1999; Wang, 2009 and Maciejowski, 2002).

A general n^{th} order discrete-time linear state-space description takes the following form (Equations (4.1) and (4.2)),

$$x_m(k+1) = A_m x_m(k) + B_m u(k) \tag{4.1}$$

$$y(k) = C_m x_m(k) + D_m u(k) \tag{4.2}$$

Where, A_m, B_m and C_m are discrete state matrix, discrete input matrix and discrete output matrix respectively. If the system is time varying linear state-space model, then the matrices A_m B_m and C_m should be presented as $A_m(t)$, $B_m(t)$ and $C_m(t)$ which are functions of time. If the model is designed for variable wind speeds where the wind regions are described towards the later part of this chapter then the matrices A_m, B_m and C_m will vary for each linearization points. For controlling purposes then a Simulink switch has to be implemented when the wind

speed approaches each region. However, for each wind speed region when the matrices are established previously with respect to the linearized points the controlling is similar. The Subscript m represents the model and u is the manipulated or input variable. For better control purposes we normally design our system with an integrator included and also we assume that input variable has no forward coupling with the output vector $y(k)$. With these assumptions, we can decide that the matrix $D_m = [0]$. Hence, by taking the difference operation on both sides of the Equation (4.1) (Wang, 2009),

$$x_m(k+1) - x_m(k) = A_m(x_m(k) - x_m(k-1)) + B_m(u(k) - u(k-1)) \tag{4.3}$$

by taking,

$$\Delta x_m(k+1) = x_m(k+1) - x_m(k); \quad and \quad \Delta x_m(k) = x_m(k) - x_m(k-1)$$

And the difference of the control input variable also as: $\Delta u(k) = u(k) - u(k-1)$ we can write the new state-space equation as given next,

$$\Delta x_m(k+1) = A_m \Delta x_m(k) + B_m \Delta u(k) \tag{4.4}$$

In this iterative method, we purposely select the new state variable vector $x(k)$ with the output vector as given by,

$$x(k) = \begin{bmatrix} \Delta x_m(k) \\ y(k) \end{bmatrix} \tag{4.5}$$

From Equation (4.4) we can write,

$$\begin{aligned} y(k+1) - y(k) &= C_m\left(x_m(k+1) - x_m(k)\right) = C_m \Delta x_m(k+1) \\ &= C_m A_m \Delta x_m(k) + C_m B_m \Delta u(k) \end{aligned} \tag{4.6}$$

The Equations (4.4) to (4.6) can be combined to give the state-space model in matrix notation as given below (Wang, 2009),

$$\overbrace{\begin{bmatrix} \Delta x_m(k+1) \\ y(k+1) \end{bmatrix}}^{x(k+1)} = \overbrace{\begin{bmatrix} A_m & o_m{}^T \\ C_m A_m & 1 \end{bmatrix}}^{A} \overbrace{\begin{bmatrix} \Delta x_m(k) \\ y(k) \end{bmatrix}}^{x(k)} + \overbrace{\begin{bmatrix} B_m \\ C_m B_m \end{bmatrix}}^{B} \Delta u(k) \tag{4.7}$$

$$y(k) = \overbrace{\begin{bmatrix} o_m & 1 \end{bmatrix}}^{C} \overbrace{\begin{bmatrix} \Delta x_m(k) \\ y(k) \end{bmatrix}}^{x(k)} \tag{4.8}$$

Where, $o_m = \overbrace{[0 \quad 0 \cdots 0]}^{n_1}$ and the triplet (A, B, C) is identified as the augmented model which is generally used to design MPC controllers. The parameter n_1 represents the number of states or the dimension of the state vector. When the system is a second order system then $n_1 = 2$. then, $o_m = [0 \quad 0]$ and $o_m^T = \begin{bmatrix} 0 \\ 0 \end{bmatrix}$.

The key terms used in this section are: cost function, Hessian matrix, minimization of the cost function, future control signal, predicted plant output, control horizon etc. The following symbols are used for the mathematical formulation (list of symbol are given in the Nomenclature also; same symbol can appear in the nomenclature with different meaning):

k_i = current time (sampling instant)

N_p = length of the optimisation window (Prediction horizon)

N_C = control horizon dictating the number of parameters used to capture the future control trajectory

q = number of output states

$\Delta u(k)$ = input to the state-space model

$x(k_i + m | k_i)$ = is the predicted state variable at a time instant ($k_i + m$) where we have been given the current plant information $x(k_i)$ at time instant k_i.

Let us assume that the future control trajectory is defined by the following sequence of variables,

$$\Delta u(k_i), \Delta u(k_i + 1), \cdots, \Delta u(k_i + N_c - 1) \tag{4.9}$$

Future state variable can be defined as given below,

$$x(k_i + 1 | k_i), x(k_i + 2 | k_i), \ldots, x(k_i + m | k_i), \ldots x(k_i + N_p | k_i) \tag{4.10}$$

The control horizon N_C is chosen to be less than (or equal) the prediction horizon N_p.

Method developed here is based on the augmented state-space model (*A, B, C*) and the future state variables are calculated iteratively. The computing is facilitated by the future control parameters. Iteration sequence can be written as given next,

$$x(k_i + 1 | k_i) = Ax(k_i) + B\Delta u(k_i) \tag{4.11}$$

By substituting Equation (4.11) into the Equation (4.12) we can write,

$$x(k_i+2\,|\,k_i) = Ax(k_i+1\,|\,k_i) + B\Delta u(k_i+1) \tag{4.12}$$

$$x(k_i+2\,|\,k_i = A^2 x(k_i) + AB\Delta u(k_i) + B\Delta u(k_i+1)$$

$$\vdots$$

$$x(k_i+N_p\,|\,k_i) = A^{N_p}x(k_i) + A^{N_p-1}B\Delta u(k_i) + A^{N_p-2}B\Delta u(k_i+1) + \ldots$$

$$+ A^{N_p-N_c}B\Delta u(k_i+N_c-1). \tag{4.13}$$

Similar to the above method, from predicted state variables, the predicted output variables could also be derived as given next,

$$y(k_i+1\,|\,k_i) = CAx(k_i) + CB\Delta u(k_i) \tag{4.14}$$

$$y(k_i+2\,|\,k_i) = CA^2 x(k_i) + CB\Delta u(k_i) + CB\Delta u(k_i+1) \tag{4.15}$$

$$\vdots$$

$$y(k_i+N_p\,|\,k_i) = CA^{N_p}x(k_i) + CA^{N_p-1}B\Delta u(k_i) + CA^{N_p-2}B\Delta u(k_i+1) + \ldots$$

$$+ CA^{N_p-N_c}B\Delta u(k_i+N_c-1) \tag{4.16}$$

When carefully examined Equation (4.16), all predicted variables are formulated concatenating the current state variable information $x(k_i)$ and the future control manipulated movement $\Delta u(k_i+j)$; where, $j = 0,1,\ldots N_c-1$.

If we define: $Y = \left[y(k_i+1\,|\,k_i) \quad y(k_i+2\,|\,k_i) \quad y(k_i+3\,|\,k_i)\ldots y(k_i+N_p\,|\,k_i)\right]^T$ (4.17)

and $\Delta u = \left[\Delta u(k_i) \quad \Delta u(k_i+1) \quad \Delta u(k_i+2)\ldots\Delta u(k_i+N_c-1)\right]^T$ (4.18)

For a single input single output (SISO) case, the dimension of Y is equal to N_p and the dimension of $\Delta u = N_c$..

Collecting Equations (4.14) to (4.16) we can establish the following relationship,

$$Y = Fx(k_i) + \phi\Delta U \tag{4.19}$$

where,

$$F=\begin{bmatrix} CA \\ CA^2 \\ CA^3 \\ \vdots \\ CA^{N_p} \end{bmatrix}; and \quad \phi=\begin{bmatrix} CB & 0 & 0 & \cdots & 0 \\ CAB & CB & 0 & \cdots & 0 \\ CA^2B & CAB & CB & \cdots & 0 \\ \vdots & \vdots & & & \\ CA^{N_p-1}B & CA^{N_p-2}B & CA^{N_p-3}B & \cdots & CA^{N_p-N_c}B \end{bmatrix} \tag{4.20}$$

where, the matrix ϕ is defined as the *Toeplitz matrix.*

Optimization

The optimisation method is carried out similar to the technique used by Wang (2009). Assume the set point signal which is controllable and defined by $r(k_i)$ at a sample time k_i. The objective is to bring the predicted output as close as possible to the set point signal within a prediction horizon. The objective is achieved by manipulating the input variable ΔU such that the error between the set point signal and the predicted output is minimised.

Here, the set point signal is pre-set with data and is assumed to be equal to,

$R_s=\begin{bmatrix} 1 \\ 1 \\ 1 \\ \vdots \\ 1 \end{bmatrix}\times r(k_i)$ where the dimension of $R_s^T=\overbrace{\begin{bmatrix}1 & 1 & \cdots & 1\end{bmatrix}}^{N_p} r(k_i)$; hence we can define the cost function J to achieve the control objective as,

$$J=\left(R_s-Y\right)^T\left(R_s-Y\right)+\Delta U^T\overline{R}\Delta U \tag{4.21}$$

The first term minimises the errors between the predicted output and the set-point signal. The second term ΔU is the manipulated signal which considers the size of ΔU so that the objective function J diminishes to zero or set to reach as small as possible. The matrix $\overline{R}$ is a diagonal matrix and it is taken as $\overline{R}=r_w I_{N_c\times N_c}\,(r_w\geq 0)$. Where r_w is defined as a tuning parameter for a closed loop plant.

Details on how to minimise the cost function and how to obtain ΔU could be found in reference Wang (2009) than presenting in this thesis.

Hence, the optimal solution for the control signal is,

$$\Delta U=\left(\phi^T\phi+\overline{R}\right)^{-1}\phi^T\left(R_s-Fx(k_i)\right) \tag{4.22}$$

$$\therefore \Delta U = \left(\phi^T \phi + \overline{R}\right)^{-1} \phi^T \left(\overline{R}_s r(k_i) - Fx(k_i)\right) \tag{4.23}$$

The matrix $(\phi^T \phi + \overline{R})^{-1}$ is defined as the Hessian matrix in MPC literature. Here R_s matrix is the set point matrix and is fed into the iterative programming as given next:

$R_s = \begin{bmatrix} 1 & 1 & 1 & \dots & 1 \end{bmatrix}^T r(k_i) = \overline{R}_s r(k_i)$. where, $R_s = \begin{bmatrix} 1 & 1 & 1 & \dots & 1 \end{bmatrix}^T$ as defined earlier.

Theoretical, background necessary to form the Toeplitz matrix, Hessian matrix, set point matrix, cost function and discrete state space model of the plant was presented. Method of mathematical formulation of these matrices is helpful to generate the MATLAB script files when designing the MPC controllers.

4.3 Wind Regions

As described in the literature review, WT control can be categorised according to the wind speed regions. In practice the wind speed is divided into four main areas according to wind regions (wind speeds). They are Region 1, Region 2, Region 3 and Region 4. The Region 1 spans from start-up of the WT to the 'cut-in' wind speed where the generator is turned on to produce electricity. Region 2 is defined as sub-region when the wind speed is between cut-in speed and just below the speed where the wind speed is still insufficient to produce maximum power. Region 3 is defined as the region where, the wind speeds are high enough to generate its rated power. At this region generator is controlled to regulate speed and the power. The last region which is the Region 4, in which the turbine is shut down to prevent probable damage. In the transition region, which is normally defined as the region where the wind speed changes from sub-region (mid region) to Region 3. In the transition region the wind speed is at the high end of Region 2 and lower end of Region 3. In Region 2 and in the transition region, the main aim is to capture the maximum available power from the wind and it is harvested by controlling, blade pitch angle, turbine coefficient and the tip speed ratio (TSR). The blade pitch control is generally achieved by using proportional integral (PI) control and with a pitch angle actuator. In Region 2, as the wind speed is reasonably low compared to Cut-out speed, the control focus is to extract maximum possible power by controlling turbine pitch coefficient, pitch angle and TSR. However, when the wind speed is at Region 3, the wind speed is fairly high but the turbine rotation speed is controlled by controlling the pitch angle. At this region wind energy contains more than the rated extractable capacity of the WT and hence the turbine blades are set to operate at a controlled speed.

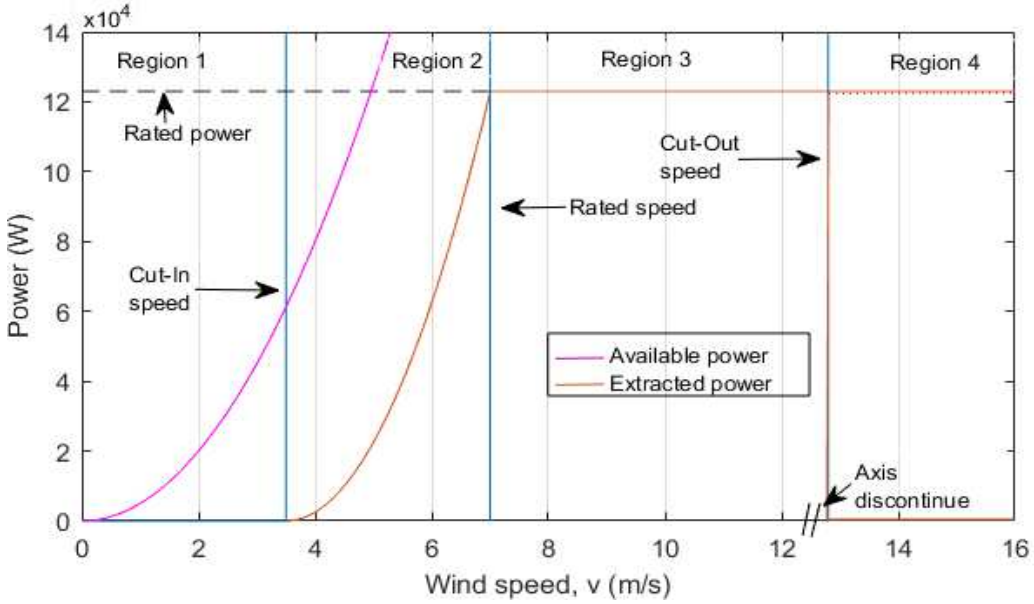

Figure 4.1. Wind turbine power versus wind speed and the illustration of wind regions

Theoretically, it is impossible to extract the all power available in the wind by the WT as this would require the wind to become stationary on the downwind side of the rotor. The Betz limit and the mathematical analysis was presented at the beginning of Chapter 3. This is the main reason that in Fig. 4.1, the available power curve is shown at a higher elevation (especially after wind speed of 3.5 m/s) while extracted power is at a lower level for the same wind speed. When the wind speed is more than 30 m/s (the wind speed is basically entering into the Region 4 beyond the Cut-out wind speed) the WT is shut down or Stall control procedure is implemented. The Stall control with an MPC design is described towards the latter part of this chapter. When the speed is less than 3.5 m/s the wind turbine is shut down as it is below the Cut-in wind speed and not profitable to operate. In this thesis, WT control, MPC design and application is addressed in Region 2 and in the transition region. When the wind speed is above the Cut-out wind speed (Region 4) the MPC stall control is applied using the pitching technique (stall control is described in section 4.8 under the topic of 'Power Output Regulation'.

4.4 Application of MPC for WT Control

MPC Controller Design.

As described in Chapter 3, the total wind turbine model, which was developed with the PID/ State-feedback controller produced very satisfactory results. However, the settling time for all output parameters with the variable Gaussian wind speed happened to be greater than five

seconds (approximately seven seconds). Though, these values have shown very good results, in this section, possibility of improving the output response to reduce the settling time within 5 seconds is investigated (Assuming that the control system requirements are: (i) the settling time is not larger than 5 seconds (ii) the rise time 10%-90% rise time is smaller than 0.5 seconds, (iii) the overshoot is smaller than 5% or at an appreciable satisfactory level for the last two requirements; these specifications are commonly used by control engineers when designing control systems). At the inception, it is necessary to load the state-space WT model (Equation (4.114) to Equation (4.119)) into the workspace by typing the matrices, A_m, B_m, C_m and C_m. The second step is to load the MPC controller into the MATLAB workspace by using the MPC Designer function: MPCobj=mpc(WT , T_S); Here, WT is the state-space model and T_S represents the sampling time (T_S is initially taken as 1 second). MPC controller used in Simulink is based on the following methodology.

Predicted future outputs = Function of current "state" (stored in memory) + feedforward measurement + feedback measurement correction + future input adjustments.

In the above relationship presented, the feedback/feedforward parts is there for the measurement correction. The method adopted in MPC designer function is a classical method. In a classical MPC, the control action at each time step is obtained by solving an online optimisation problem. In linear systems or linearized systems, more often the optimisation problem is a quadratic problem. The function of the MPC controller is to solve the optimisation according to the constraints provided.

When the MPC controller is applied to control the *WT*, the main objective is to maintain the output generator speed at its nominal set point (which is set at 3000 degrees/s; see Fig. 4.2. inports to MPC controller). In real time, the generator minimum speed is specified as 50.27 rad/s (see Table 3.1 for real WT data). One should note that when 3000 degree/s converted to radians is 52.3599 rad/s which is acceptable and similar to the minimum generator speed given in the Table 3.1. The minimum generator speed 52.3599 rad/s is a safe minimum speed to operate than at 50.27 rad/s specified by the table 3.1. The generator torque $T_{g,ref}$ is considered here as an unmeasured disturbance to the MPC controller. In real WT operation, the generator torque needed to kept constant because it this is fluctuated then the output phase voltage also changes as the DFIG is directly connected to the grid. The inputs to the plant are $T_{g,ref}$, θ^o and variable wind speed, v . Out of these three inputs to the real world WT control scenario, one

should decide, at this stage what would be the manipulated variable, measured disturbance and what would be the reference variable. As $T_{g,ref}$ has been already selected as the reference variable to keep it constant for grid connection, the choice lies between what is the measured disturbance variable and the unmeasured input variable. In this thesis the following method is adopted to isolate the measured disturbance variable and the unmeasured disturbance of pitch angle. When the generator turbine actuator torque is increased from 1500 Nm to 2000 Nm the variation of ω_{gen} (output) happened to be from 4700 degrees/s to 4800 degrees/s. However, the pitch angle variation and the wind speed variation offered greater changes in the output generator speed, ω_{gen}. In other words, the generator output speed is more sensitive to the changes of pitch angle and the wind speed.

For the pitch angle control in real life with large turbines, there is a limited controllability available as it is operated by the pitch actuator and the actuator is already defined to operate at maximum power point mode which lies between 2º and 5º (see the Fig. 3.4. in chapter 3; when the pitch angle is 8º then the C_P value is 0.28). The maximum flexibility offered by changing the wind speed from 3 m/s to 10 m/s which produced generator speed changes from 1400 degrees/s to 4200 degrees/s. It is very important to decide which parameter is preferred for the manipulated variable for the MPC controller not only to avoid uncontrollable outputs but also not to decide MPC controllers are ineffective. Hence, the wind speed is chosen as the measured disturbance and the MPC block outport mv is considered as the first input state to the plant.

The variable θ is considered as an unmeasured disturbance and the actuator torque, $T_{g,ref}$ which has the least impact on controlling generator speed. Power output is selected as an unmeasured disturbance to the system. All these WT data and the parameter boundaries were set according to the realistic WT data taken from Table 3.1. The Simulink block diagram of the plant with the MPC controller and the output simulation results are shown in Fig. 4.2. to 4.4. With the implementation of the MPC controller, wind speed variation from 3 m/s to 15 m/s and the pitch angle variation from 3º to 4º the MPC controller brings the generator speed into the steady state position within 5.5 seconds. Though, this is not perfect but the improvement is satisfactory.

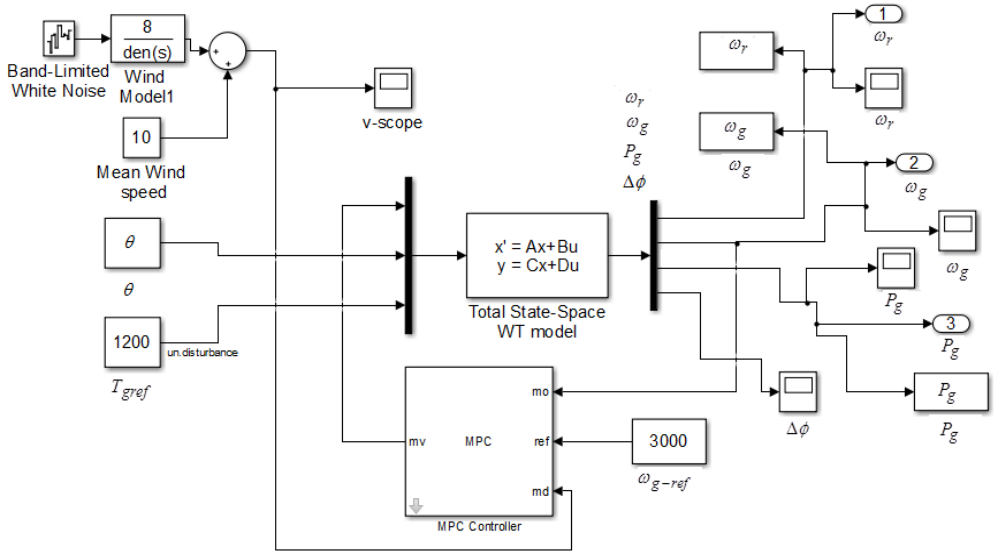

Figure 4.2: Implementation of the MPC controller using Simulink toolbox.

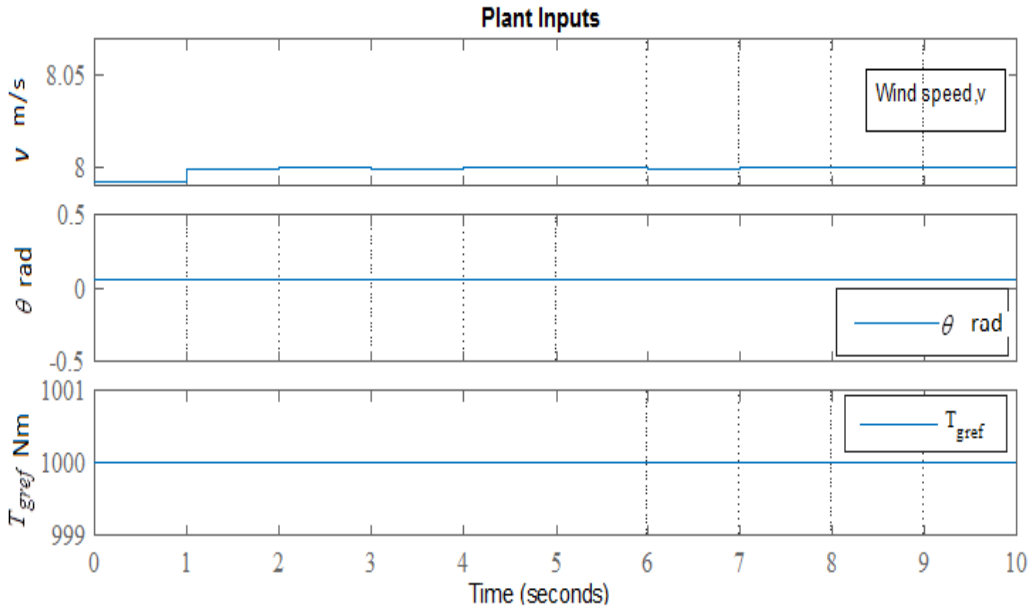

Figure 4.3: Input signals to the plant.

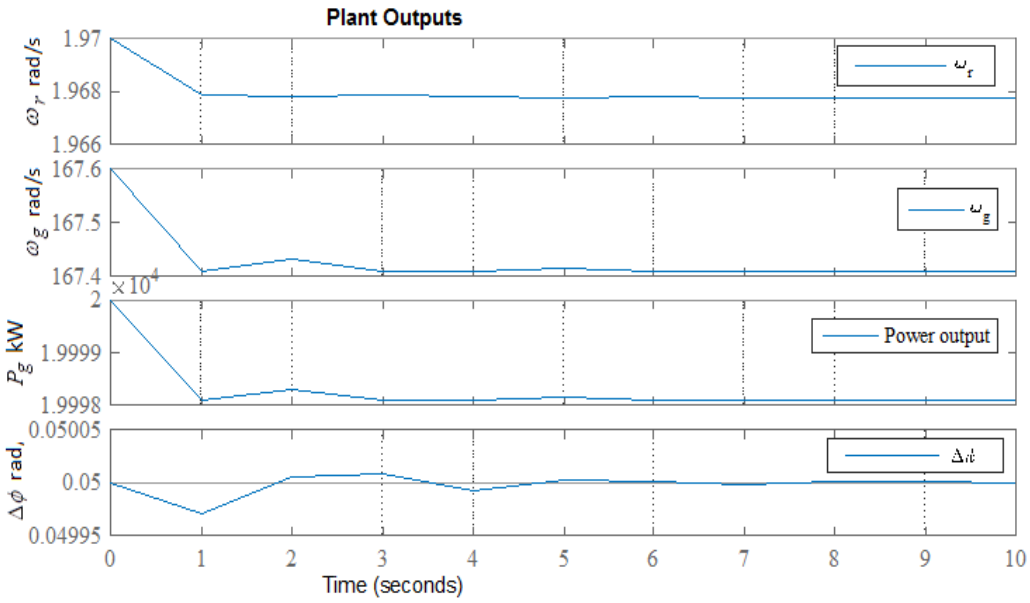

Figure 4.4: WT plant output characteristics with the MPC controller.

The generator speed, which is the most important aspect of control scenario reaches to steady state level less than 6 seconds (the plant output characteristics is shown in Fig. 4.4). The output speed also settles down to the steady state value of 167.52 rad/s within 5.5 seconds. The rotor speed which varies according to the wind speed also settles down into a steady state value within 5 seconds. The inputs to the plant is shown in Simulink Fig. 4.2. These values were selected considering the real operating conditions (e.g. if the pitch angle input is 4^o then the equivalent value in radians is 0.069, which the input to the plant as shown in Fig. 4.3) of the wind speed region from 3.5 m/s to 15 m/s where the linearization of the state matrix and the input matrix was performed. However, it is just indeed a matter of selecting the equilibrium point in any wind region and perform the linearization as described in Chapter 3 when the model is available for any wind region. Then the switching mechanism should be included according the wind speed to operate at correct region of the WT. With these plant output characteristic results the controller behaves exactly according to the design requirement in real scenario and the design proves to be successful.

Calculation of the linearized matrices which are contaminated with noise is given in Appendix A.

4.5. Optimum Power Output Control of a Wind Turbine Rotor

This section describes the *optimum power output control* of a wind turbine rotor using MPC technique.

An optimum controller is applied to regulate the power output from a wind turbine rotor. The controller is synthesised in two steps. The first step defines the equilibrium operation point and ensures that the desired equilibrium point is stable. The stability of the equilibrium point is guaranteed by a control law that is synthesised by applying the methodology of MPC. The method of controlling the turbine involves pitching the turbine blades. In the second step, the blade pitch angle demand, θ is defined. This involves minimising the mean square error between the *actual and desired power coefficient* C_P. The actual power coefficient, C_P of the wind turbine rotor is evaluated assuming that the blade is capable of stalling, using *blade element momentum theory*. This ensures that the power output of the rotor can be reduced to any desired value which is generally not possible unless a nonlinear stall model is introduced to evaluate the blade profile coefficients of lift and drag. The relatively simple and systematic non-linear modelling and MPC controller synthesis approach adopted here clearly highlights the main features of the controller that is capable of regulating the power output of the wind turbine rotor.

4.6. Blade Element Momentum Theory for Power Coefficient

The calculation of the power output must be done with some care using the blade element momentum (BEM) theory as outlined in literature. In Vepa (2013) based on BEM theory it is shown that, the power coefficient, may be expressed as,

$$C_P = \frac{P_w}{P_{wind}} = \frac{1}{\lambda_f}\int_{\bar{r}_h}^{1} \frac{\sigma'(1-a)^2}{\sin\phi}\left(\frac{C_l}{\tan\phi} + C_d\right)\bar{r}^2 d\bar{r} \tag{4.24}$$

Hence the axial induction factor a may be expressed as,

$$1 - a = \left\{1 + \frac{\sigma'}{8Q_{tip}\sin\phi}\left(\frac{C_l}{\tan\phi} + C_d\right)\right\}^{-1} \tag{4.25}$$

In the above equations for the power coefficient C_P and for the axial induction factor a, ϕ is the inflow angle defined by the in-plane and tangential velocity components as,

$$\phi = \tan^{-1}\left(u_P / u_T\right) = \tan^{-1}\left(\lambda_f\left(1-a\right)/\bar{r}\left(1+a'\right)\right) \tag{4.26}$$

Where, λ_f is the inflow ratio, $\lambda_f = 1/\lambda = V_w/\omega_m R$, Q_{tip} is Prandtl's tip-loss correction factor which will be evaluated from the expression in Vepa (2013), σ', is the local solidity ratio for an *N*-bladed rotor given in terms of the blade chord c and the local radial position r by, $\sigma' = Nc/\pi r$ and, a' is the angular velocity induction factor given by,

$$a' = \frac{\sigma'\left(1-a\right)}{8Q_{tip}\left(\sin^2\phi\right)}\lambda_f\left(-C_l\sin\phi + C_d\cos\phi\right). \tag{4.27}$$

The sectional angle of attack is, $\alpha = \phi - \theta$ where, θ is blade section pitch angle. Thus to evaluate the power coefficient C_P, the sectional lift and drag coefficients, C_l and C_d must be known. These two coefficients are evaluated both for the case of stalled blade and without stall as described in the next section.

4.7. Dynamic Stall Modelling

According to the BEM theory, aerodynamic loads on a section of an aerofoil are proportional to the dynamic pressure at only that section. Lift and drag coefficients are proportionality constants that enable the calculation of aerodynamic forces. Spera (2008) has provided several empirical methods for estimating the sectional lift and drag coefficients, C_l and C_d for several aerofoil sections, both for the case of stalled blade and without a stall. For the case without a stall, the corrections are made to the two-dimensional lift curve slope, mainly for the finite aspect ratio and the finite thickness to chord ratio. For aspect ratios that are very large, the aspect ratio corrections may be ignored. For the case of the post stall flows the models and corrections are based on the work of Viterna and Corrigan (1981), Tangler and Kocurek (2005) and Tangler and Ostowari (1984). In our work the blades have a very large aspect ratio and for this reason these corrections were ignored. However, for the post stall case aspect ratio corrections were deemed to be important in the post stall aerofoil characteristics and therefore we apply the corrections of Tangler and Ostowari (1984) which have also been presented by Tangler and Kocurek (2005). For BEM, the Viterna and Corrigan (1981) method provides a

convenient global approach to relate the post-stall C_l and C_d to the overall blade geometry rather than to the individual blade stations.

4.8. Application to Power Output Regulation

For purposes of power output regulation, we estimate the actual power output based on the BEM theory. Then the pitch angle command is adjusted so as to minimise the mean square error between the desired power output and the actual power output. The pitch angle command is updated and the simulation over the next time step is carried out.

Typical Simulations and Results

The parameters of a typical wind turbine and the blades are listed in Table 4.1. The time step for the computations is $\Delta t = 0.002\,\text{s}$. At each time step, the MPC law is obtained over a prediction window of 20 time steps.

Table 4.1: Typical parameter and initial state values for simulation
Extracted from Dolan (2010) and Henriksen (2007).

Parameter	Primary Value	State/ input	Initial Value
C_{p_nom}	0.38	V_w	8m/s
R	63m	N_{gr}	97
R_{root}	9.3564m	ω_{nb}	0.88
J_r	5.9154×10^7 kgm^2	ζ_b	0.9
J_g	500kgm^2	τ_{gen}	0.1
m_{tw}	4.2278×10^5 kg	ω_{g_nom}	121.91 rad/s
b_{tw}	2021.3 Nms/rad	ω_{r_nom}	1.26 rad/s
k_{tw}	1.6547×10^6 Nm/rad	N	3
B_{sh}	8.3478×10^7 Nms/rad	H	90m
K_{sh}	8.7354×10^8 Nm/rad	$n_{elements}$	17

In the first instance, we consider the wind turbine response speeds which is shown in Fig. 4.5. The generator speed for the open-loop and closed-loop modes are coinciding each other when

the time reaches 20 seconds. However, one should note that there is hardly any difference between the closed loop response and the open loop response for the generator output speeds. In Fig. 4.6. it is shown that the wind turbine response torque in both the open and closed loop cases. In the open loop (OL) mode, the generator torque over shoot is higher than the closed loop (CL) curve which can be expected as the CL system tries to establish the control law faster than the OL. The same scenario can be seen for the rotor twist rate as shown in Fig. 4.7.

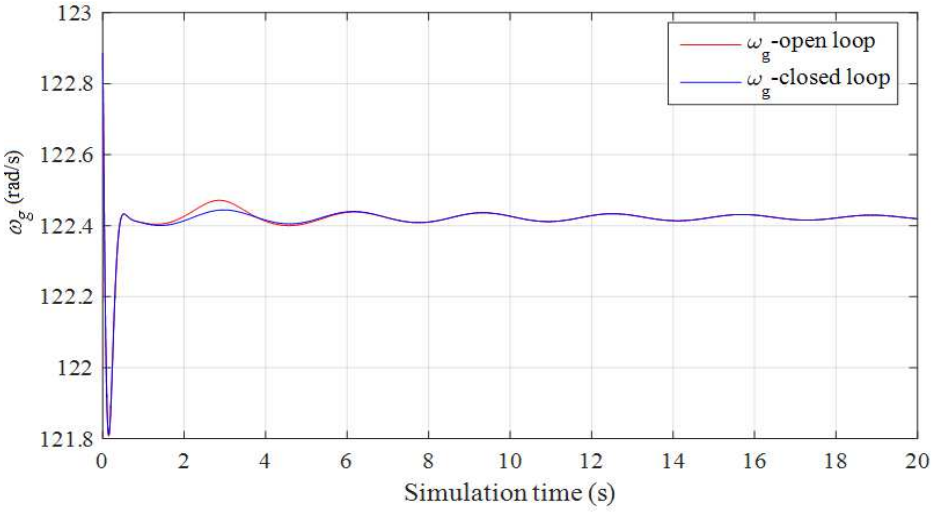

Figure 4.5: Horizontal axis wind turbine (HAWT) open and closed loop response speeds.

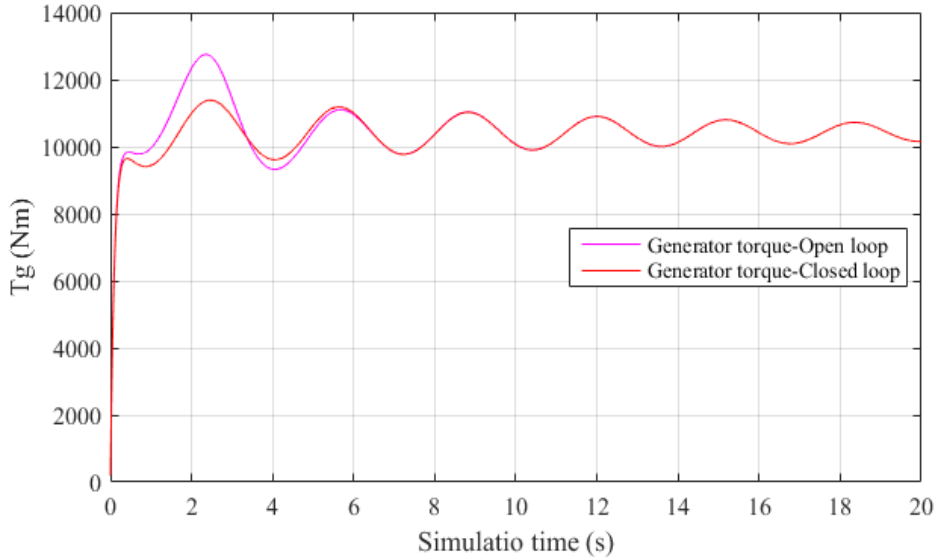

Figure 4.6: Horizontal axis wind turbine (HAWT) open and closed loop torque response.

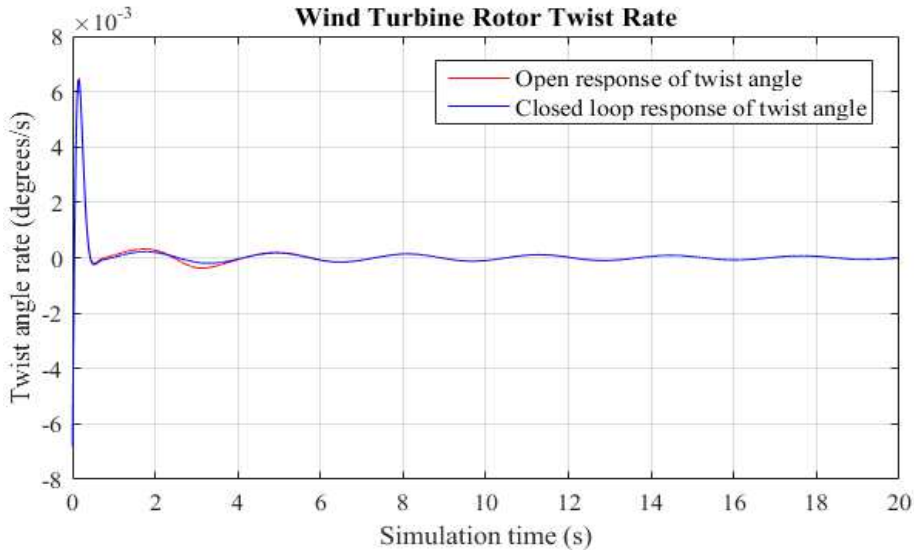

Figure 4.7: Horizontal axis wind turbine (HAWT) open and closed loop rotor twist rate response.

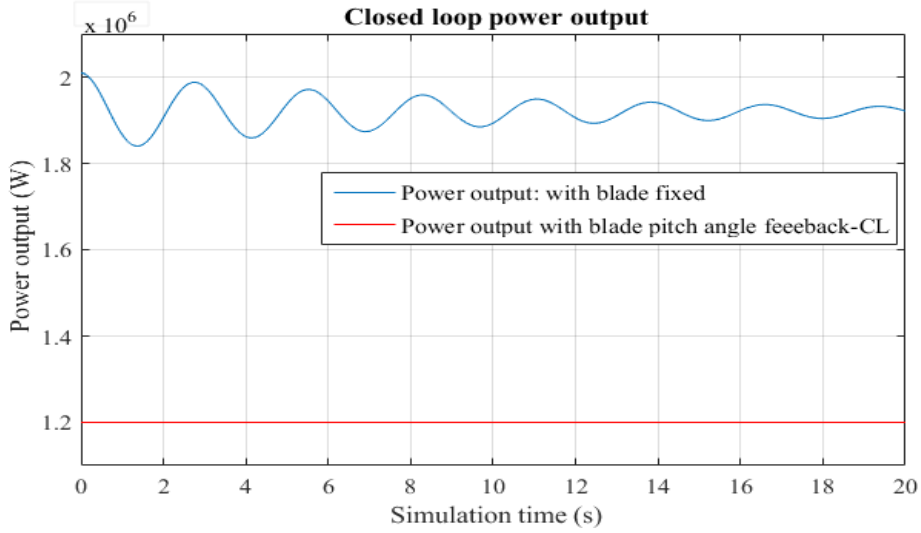

Figure 4.8: The Closed loop power output when the pitch angle is restricted to a prescribed limit.

When the blade is fixed at a pitch angle, then θ^{o} is fixed, and (see Fig. 3.4 also in Chapter 3 to visualise the situation) for a given TSR, the turbine coefficient, $C_P$also becomes a constant. However, when θ^{o} is varying as shown in Fig. 4.9. the relevant power output also varies as the power depends TSR and C_P. In this instance, the output power fluctuates for a considerable time as the pitch angle is varying, but trying to settle down according to control law. When the pitch angle variation is fed back into the system for controlling, then immediately, the power output becomes constant. In Fig. 4.8, this constant power line is shown by legend 'Power

output: pitch angle fed back'. One should question why the settling time for the output power takes a longer time than the previous design of the MPC with the use of MPC toolbox.

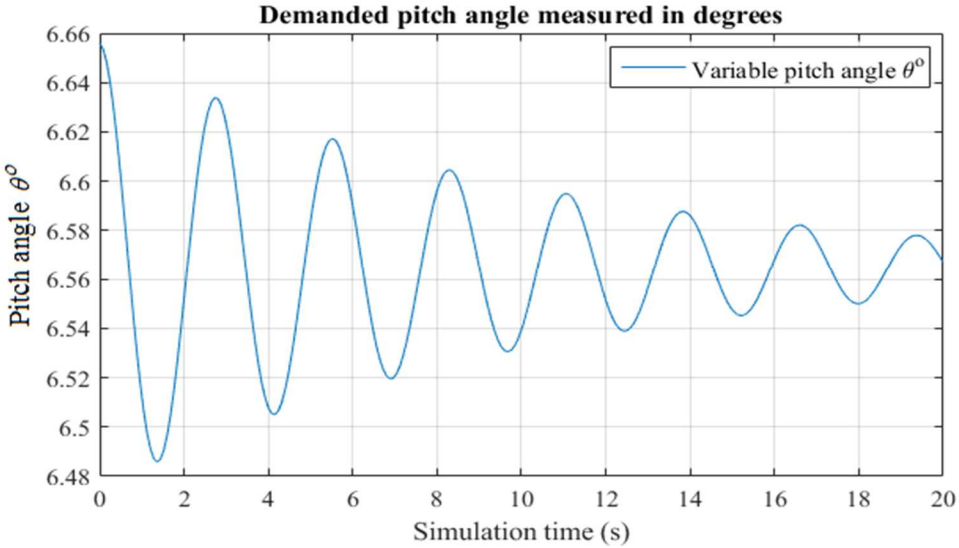

Figure 4.9: The open and closed loop demanded blade pitch angle corresponding to Figure 4.8.

One reason could be the large WT radius of 60 m for this design compared to the 40 m radius WT (20 meters longer than the previous WT), which, we used previously and the current inertia and the power output is very large compared to the previous case. For smooth controlling and reducing the settling time, the large inertia could be a hindrance. Furthermore, the pitch angle is also set to vary at each second can cause the fluctuation of the power output. However, our investigation objective is the stall control rather than controlling the output power every second due to change in pitch angle every second. In the second simulation trial as shown in Fig. 4.10, the mean pitch angle is increased to 9.09^o:

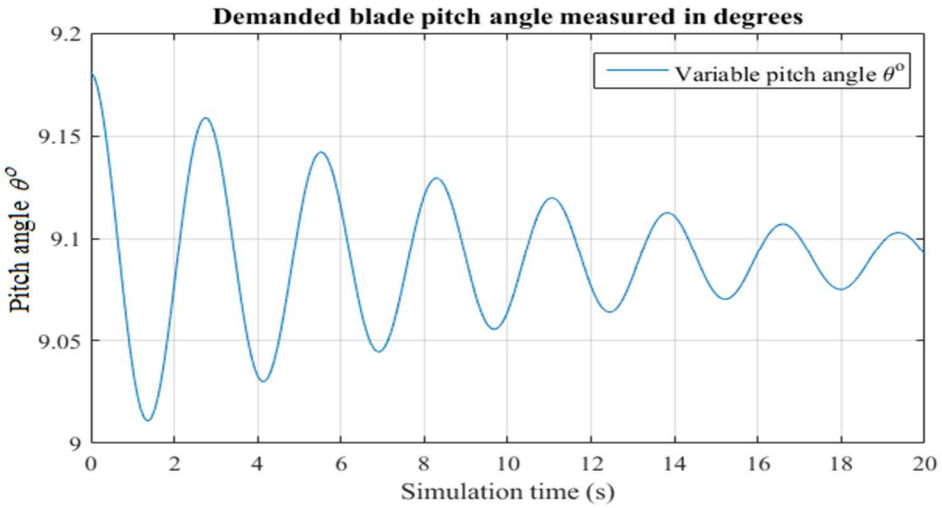

Figure 4.10: Demanded blade pitch angle corresponding to Figure 4.11.

The relevant power output variation is shown by Fig. 4.11. In this instance also the output power fluctuates for a considerable time and when the pitch angle is fed back according to MPC control law the output power becomes fixed at 700 kW.

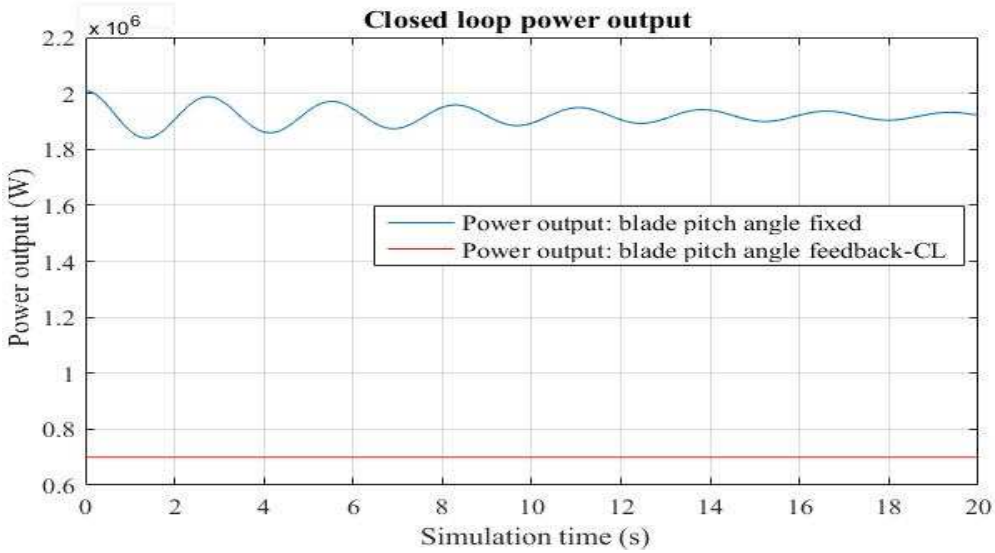

Figure 4.11: Response curves for the power output with the prescribed limit set at 700 kW.

It should be noted that when the prescribed limit of power was set at 1200 kW and then reduced to 700 kW the corresponding response curves for the power output and the demanded blade angle were shown in Fig. 4.8 and Fig. 4.11 respectively. The demanded blade angle in both cases is oscillatory about a mean value. The lower the limit set for the demanded power output the higher the mean value of the demanded blade pitch angle. It is indeed instructive to investigate the blade angle required to completely shut down the power output from the turbine. The power output response and the corresponding demanded blade angle are shown in Fig. 4.12. and in Fig. 4.13. respectively. The demanded blade angle is a constant and equal to $\theta_d = 11.6393°$. The blade angle will now be limited to a maximum of $\theta_d = 11°$. The corresponding power output response and the demanded blade angle are shown in Fig. 4.14. and in Fig. 4.15. respectively. While the blade angle is limited to $\theta_d = 11°$, it could be observed that there indeed a small residual power output of about 200 kW.

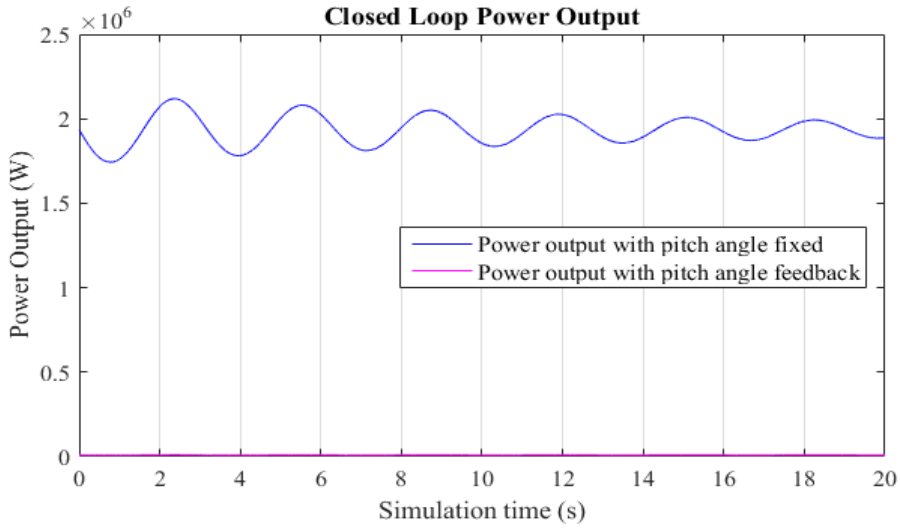

Figure 4.12: Response curves for the power output with the prescribed limit set at 0 kW.

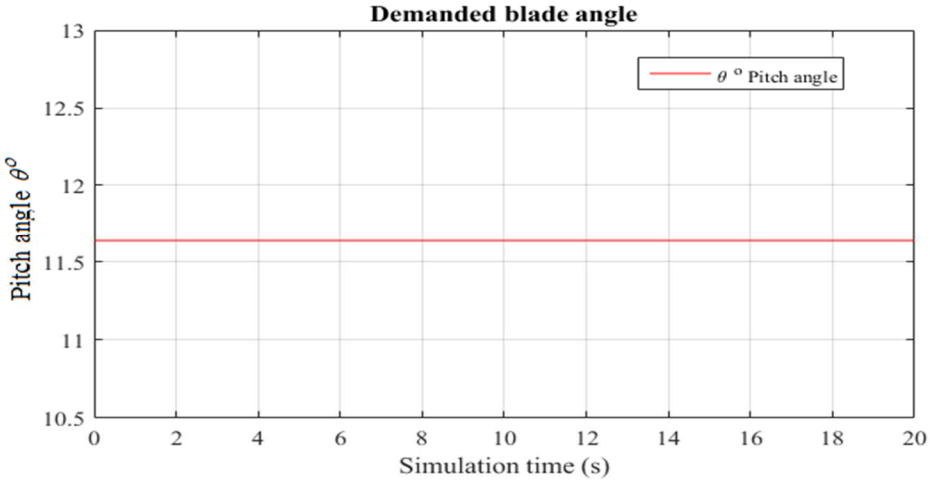

Figure 4.13: Demanded blade angle in degrees corresponding to Figure 4.12.

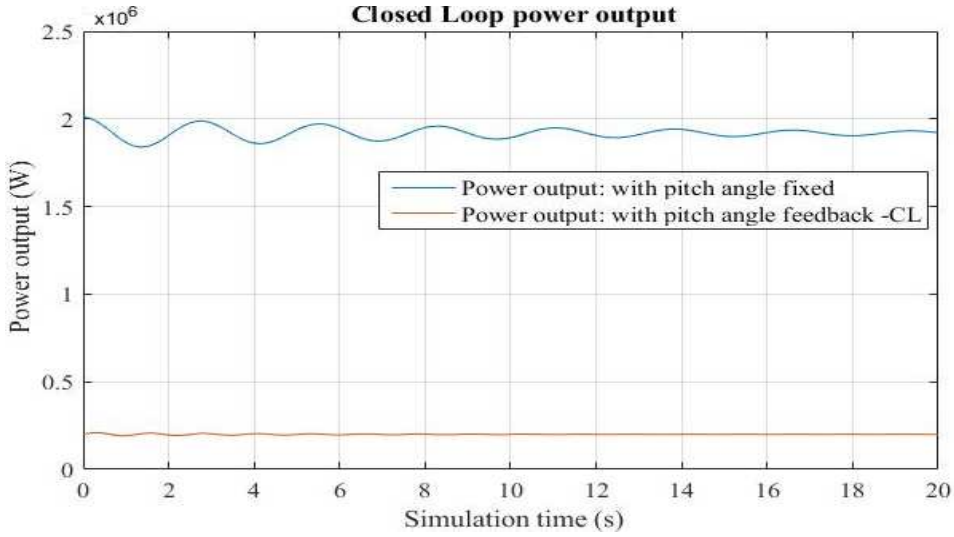

Figure 4.14: Power output with the prescribed limit set at 0 kW and the blade angle limited to $\theta_d = 11°$.

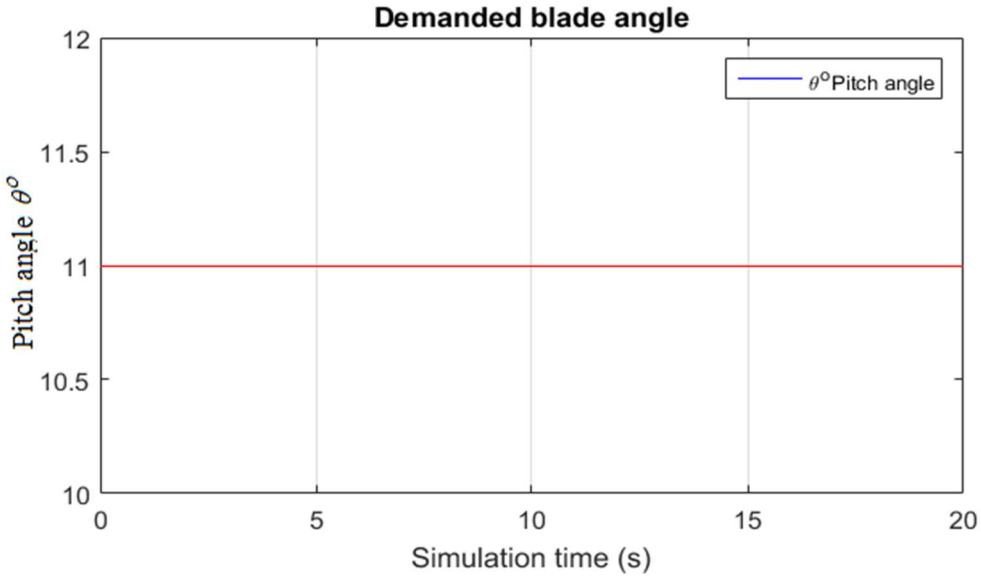

Figure 4.15: Demanded blade angle in degrees corresponding to Figure 4.14.

4.9 Analysis of the results

Although, the basic WT model is non-linear (addressed in Chapter 3), construction of a locally linear model is augmented for the MPC design. The MPC design methodology is to construct the control law over a prediction horizon window. In the second step, the blade pitch angle demand was defined. While there are two distinct approaches to regulate the power output of a variable speed turbine, by collectively controlling the pitch angle of the blades at the hub of the rotor, an alternate method based on operating the blade at an optimum angle, irrespective of the blade flow characteristics, can completely regulate the power output of the wind turbine rotor. The optimum blade pitch angle demand was found by minimising the mean square error between the actual and desired power output. Thus the optimum blade angle was defined irrespective of whether or not the blade flow had stalled or not. The methodology was applied to a typical wind turbine driving a DC generator, to test the efficacy of the active controller. The simulation results show that the controller is capable of regulating the actual power output within 2% of the desired power output.

It is observed from the above responses that the controller has all the characteristics of an active stall flow controller in the sense that the blade angle has to be increased beyond a critical value so the flow is stalled, to limit the power output at zero. Although we have not used the stall flow conditions explicitly, they have been implicitly employed. Whenever the blade section angle of attack at any blade section, which is given by, $\alpha = \phi - \theta$, where ϕ is the inflow angle

and θ is the blade section pitch angle. When α exceeds the local stall angle of attack, the turbine power coefficient C_P is calculated using stall flow conditions. These conditions depend on the blade section being considered in the evaluation of the C_P by integration of Equation (4.24). (In evaluating the C_P using Equation (4.24) we employed an appropriate distribution of the local blade chord and the blade twist or the aerofoil inlet angle along the blade length.). Hence our optimum demanded blade angle based controller, obtained by minimising the mean square error between the actual power output and the desired power output, resembles an active stall flow controller. The MPC law, used as a part of the controller, has the structure of a full State-feedback controller except that the feedbacks involving the blade angle and blade angle rate are interpreted as the feedbacks involving $e = \theta - \theta_d$ and $\dot{e}$. Thus we have provided a new and practical method of synthesising an active stall flow controller, where the feedback control law is derived by applying the concept of MPC.

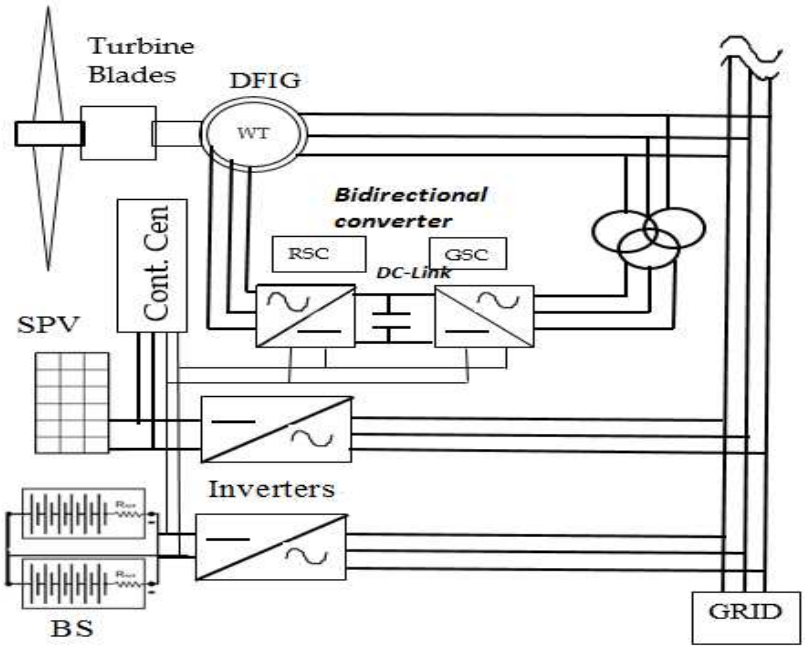

Figure 4.16: hybrid WT/SPV/BS system

Schematic diagram of a hybrid wind-solar-battery storage system is shown in Fig. 4.16. The 'Cont.Cen' block, in the block diagram depicts an application of a suitable controller to the hybrid electricity generation system. The main 'Cont.Cen' can include MPC, PID/State-feedback or any type of controller or a combination of many controllers.

Summary

The optimum output power regulation, stall control with the turbine blade pitching technique is one of the major contributions in this section. The other contribution made in this section is the design and implementation of the MPC controller using MATLAB as the programming language. With this concept, the optimum blade pitch angle demand was found by minimising the mean square error between the actual and desired power output. Thus the optimum blade angle was defined irrespective of whether or not the blade flow had stalled or not. One should note that the MPC design in first part of this Chapter was using the Simulink toolbox. The application of MPC controllers in flight control and aircraft industry is still under investigation and at experimental stage. Similar to this scenario, it seems that PID/State-feedback controllers are equally good (it could be even better with GS, though, not investigated here due to initial advice at the inception, for the research project) and cost effective for WT control compared to modern expensive MPC controllers. From the input variables, how to categorise the measured disturbance, unmeasured variables, manipulated variable and the measured output variable considering the sensitivity analysis of the MPC response was addressed in this chapter.

Chapter 5: Power Converters

Outline

This chapter mainly describes the energy conversion and control of high-efficiency switching mode power electronic converters widely used in wind turbine industry. The state-space modelling of power electronic converters, simulation with MATLAB/Simulink is elaborated within the section. Mathematical analysis is focussed with special reference to wind turbines. The importance of AC to DC and DC to AC conversion, power efficiency, control aspects of power converters is also enlightened. The description provides considerable specialism which is required for analysis and modelling power converters that is essential for converting wind/solar power into electrical energy.

5.0 Introduction

Electricity generation from WTs needs power electronic converters (PEC) to absorb maximum energy by exploiting the variable gust wind speeds. One of the advantages in using PEC is that they act like voltage stabilisers to guard against the uneven variable wind speeds causing turbine blades to rotate unevenly. AC-DC converter topology has been used very widely in the wind industry as a solution to this problem. Variable wind speeds not only create control difficulties but also results in unpredictable fluctuations in the output voltage. This variable voltage has to be controlled for grid connection and also for consumer usage. When converting the power (voltage from DFIG output), the source voltage is first transformed into a DC source and a DC-DC step up or step down transformation is used to achieve the power quality required before transforming back into AC output. With this technique no matter what speed the turbine blades are rotating, the output is controlled. Synchronous Buck (step down) converters with pulse width modulation (PWM) method using insulated gate bipolar junction transistors (IGBT) are favourable options for WTs. The sinusoidal pulse width modulation (SPWM) technique is used to control the harmonics as well as the output voltage. In addition, other converters used in WT industry are Boost (step-up) and Buck-Boost, Cuk, Matrix, Back-to-Back PWM, Z-source and Two level and Multilevel converters. Matrix converters do not use the principle of converting the power into AC-DC and instead they are directly connected to the grid (Islam et al. 2013).

Six-pulse-full-controlled rectifiers are used to convert the AC output of DFIG into DC voltage. Block diagram of a converter/inverter set up is shown in Fig. 5.1. It has six IGBTs and the process of converting AC into DC is defined as converting while DC to AC is defined as inverting. The conversion of AC to DC is also refers to as rectification.

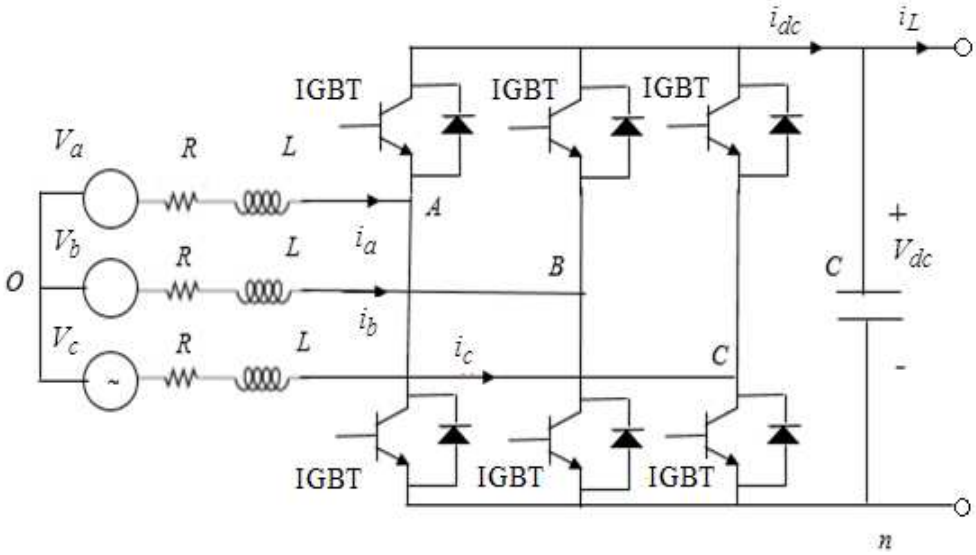

Figure 5.1: Grid-side converter arrangement.

Generally, the grid-side converter used in converting wind energy into electricity is a bi-directional AC/DC converter, which could work in rectifier state and inverter state.

This chapter from here onwards, it is divided into the following sections: Introduction to PWM is presented in Section 5.1. Mathematical modelling and the state space representation for the grid side back-to-back bidirectional converter is introduced in section 5.2. The Section 5.3 describes the mathematical formulations required to model the rotor side converter. Dynamic model for the MATLAB/Simulink Synchronous Buck converter (SBC) is presented in Section 5.4. Summary and the contributions are given at the end of the chapter.

Mathematical formulations and the rotor side converter modelling used in this thesis is the same mathematical approach given by Chen and Chen (2014) and it is used by many researchers. The simulation methodology used in this thesis is the technique used by Erickson and Maksimovic (2016). Erickson and Maksimovic (2016) used a dynamic SBC model in Simulink for simulation studies, which could be extended into any other converter type. However, good description on power converters can also be found in references: Erickson Byeon (2016), Vodovozov and Jansikene (2016), Rahmani (2015) and Byeon et al., (2010).

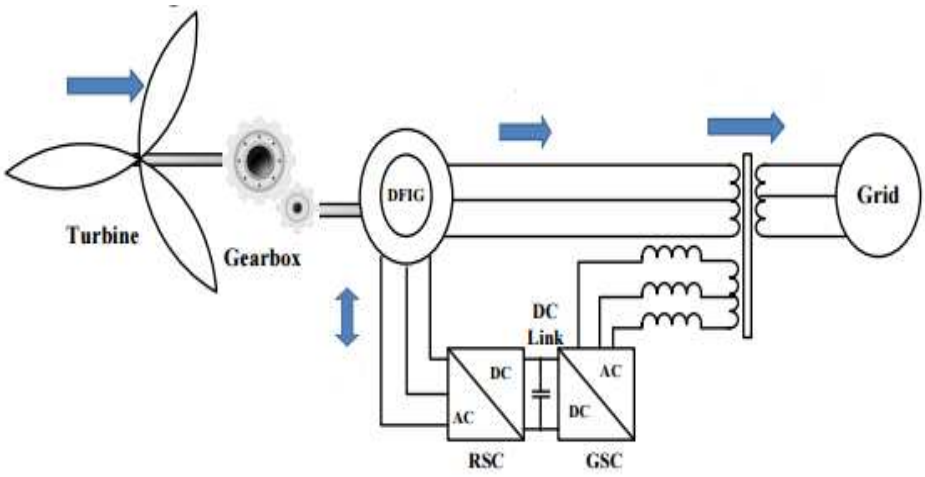

Figure 5.2: Grid side converter and the rotor side converter connections of DFIG.

Fig. 5.2. illustrates the circuit diagram of how the generator side converter (GSC) and the rotor side converter (RSC) topology which could be used to connect with the grid (Rahmani, 2015).

5.1. Pulse Width Modulation (PWM)

Pulse width modulation (PWM) waveforms are "on-off" digital wave form (WF) patterns which are generally, specified by two values: the period and the duty cycle. The duty cycle is the percent of time that the signal stays at high level. It is typically expressed as the percentage of the period. The PWM is based on generating constant amplitude pulses and then the pulse duration is modulated to get the specific WF required. When the value of the reference signal (the blue sine wave in Fig. 5.3) is more than the modulation WF (red), the PWM signal (black) is in the high state, otherwise it is in the low state.

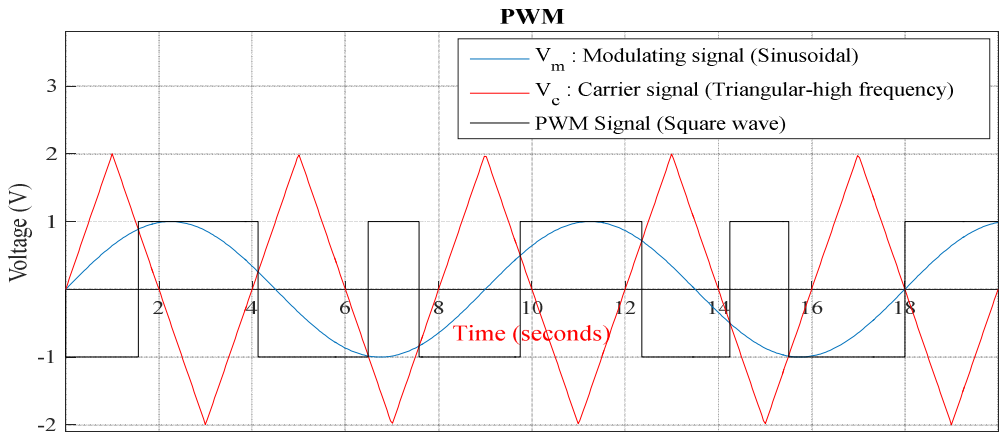

Figure 5.3: PWM technique and the input/output wave forms.

The Simulink block diagram shown in Fig. 5.4 is used to generate the input sinusoidal modulating wave V_m and the triangular wave V_c . The triangular WF which is the carrier wave, was generated using 'Repeating signal block' in Simulink.

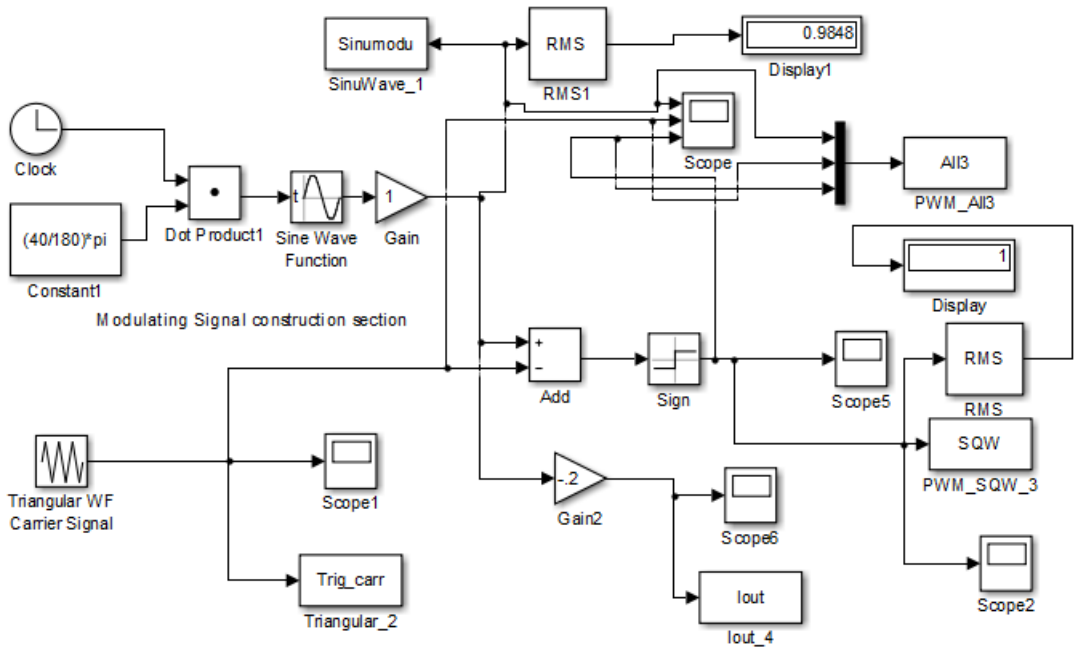

Figure 5.4: The Simulink block diagram for PWM technique: sinusoidal input signal and a triangular carrier wave which outputs the square wave pulse signal.

The carrier signal which is of higher frequency than the modulating signal, is generally synchronised with the supply voltage frequency. Modulated pulses' duration is determined by the intersection points of V_m and V_c points (Fig. 5.3). The pulse pattern is decided by the ratio of peak values of V_m to V_c . The frequency ratio which is defined as the carrier ratio is given by f_c / f_m and the modulation index is defined by the ratio of V_m / V_c .

These index values are important when deciding the number of carrier pulses and width of the pulses and RMS value of the inverter output voltage. The ratio f_c / f_m decides the number of pulses in each half cycle of the inverter output voltage and the ratio V_m / V_c decides the width of the pulses which is leading to RMS value of the inverter output voltage. Generally, the ratio V_m / V_c is taken as less than one in order to avoid harmonics. When the RMS value for the input sinusoidal signal is calculated using 'RMS' Simulink block the numerical value is 0.9848 and the PWM square wave RMS vale is equal to a numerical value 1 (See RMS blocks in Fig. 5.4). This is an appreciable situation to control the sudden changes in the demanded voltage

and frequency by deploying the PWM technique. But, literature states that the maximum frequency which could be controlled up to is 100 Hz where we can achieve 98% conversion efficiency (Bose, 2014). The Sinusoidal input modulation waveform which is contaminated with noise is shown in Fig. 5.5. The distorted output square wave signal was fed into a 'Zero-order hold' block with an 'Ideal Rectangular Pulse Filter' block in Simulink to obtain the filtered response as shown in Fig. 5.5. The filter details could be found in Simulink help directory.

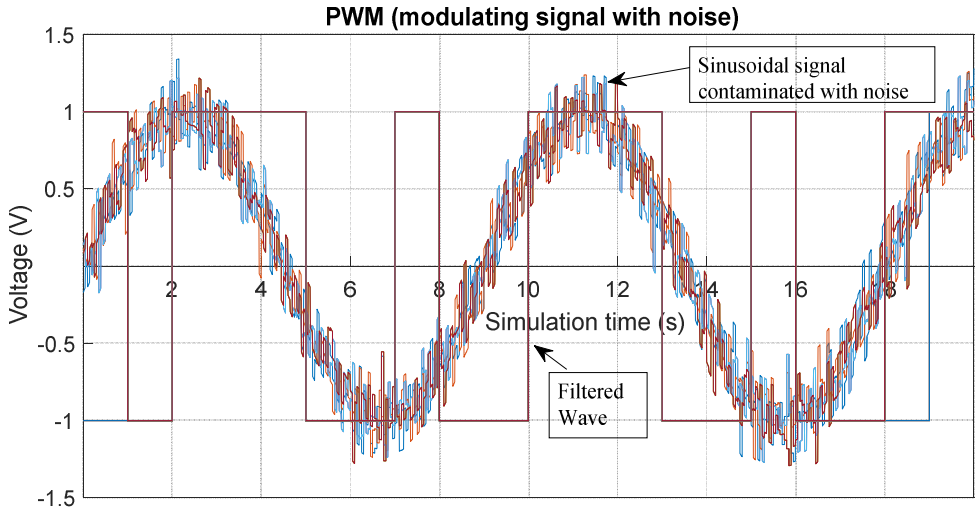

Figure 5.5: Input modulation WF is contaminated with noise and the output square wave is rectified with a 'Zero-Order Hold' and an 'Ideal Rectangular Pulse Filter' in Simulink.

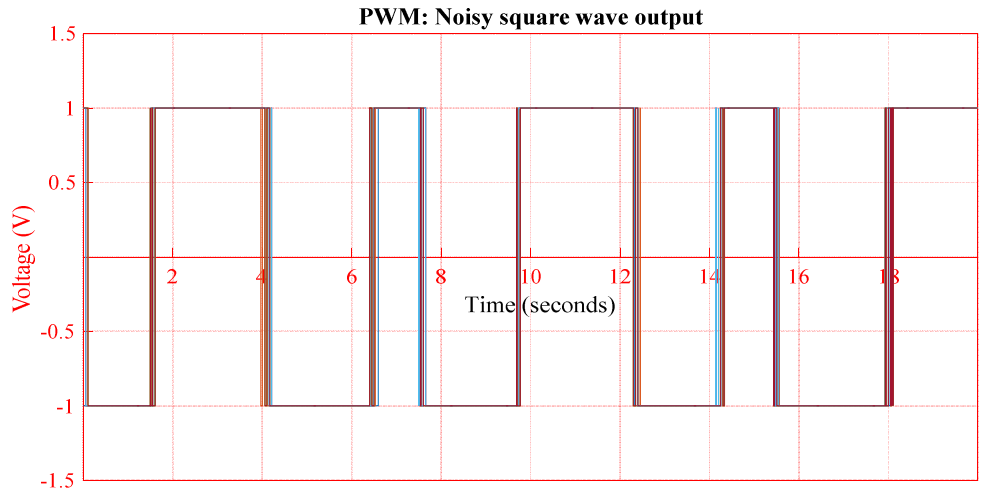

Figure 5.6: Square wave output signal with noise due to input modulating signal.

Fig. 5.6 shows the noisy square wave output signal after PWM. The Simulink block diagram shown in Fig. 5.7 (see the bottom right hand corner) includes additional 'Zero-Order-Hold block' and an 'Ideal Rectangular Pulse Filter' for filtering the noise in the square wave signal.

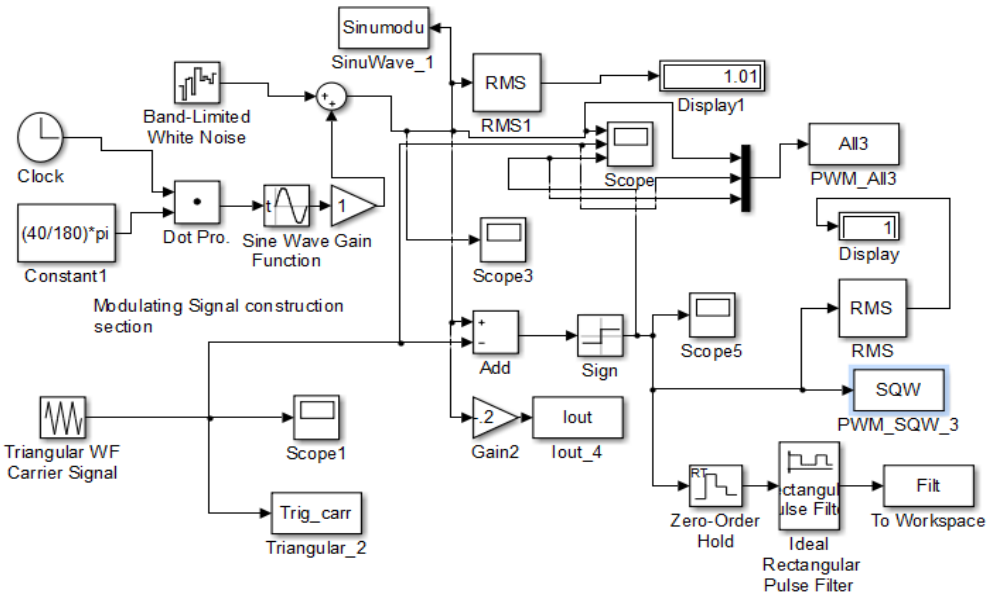

Figure 5.7: Simulink block diagram for the filtered square wave output by Ideal Rectangular Pulse Filter.

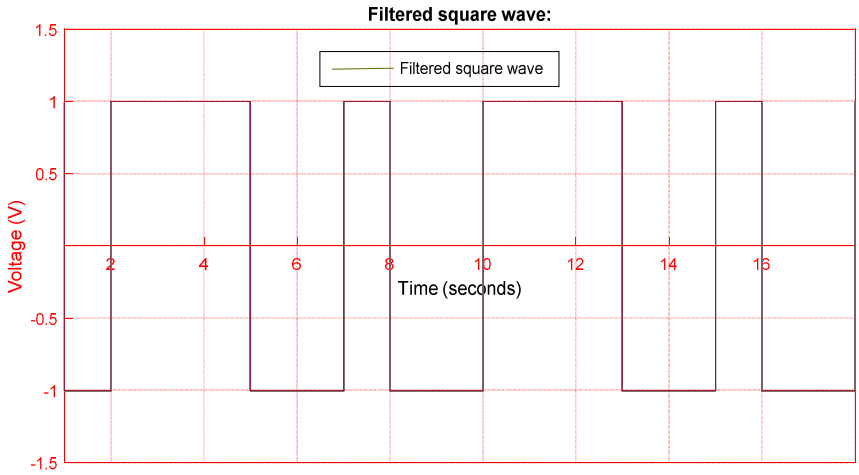

Figure 5.8: Square wave output signal is filtered by Ideal Rectangular Pulse Filter and a Zero-Order Hold blocks

5.2. Grid-Side Converter Modelling

The grid-side converters are generally bi-directional. The AC/DC converter is there to accommodate the rectifier action and the DC/AC inverter action is for the DFIG to connect into the grid. This section will describe the mathematical modelling of the converter. Applying Kirchhoff's law to the circuit diagram shown in Fig. 5.1 we can write the following equations:

$$C\frac{dv_{dc}}{dt} = i_{dc} - i_L = S_a i_a + S_b i_b + S_c i_c - i_L \tag{5.1}$$

The voltage balance across the inductors Chen and Chen P-H, (2014),

$$\begin{bmatrix} v_a \\ v_b \\ v_c \end{bmatrix} = R\begin{bmatrix} i_a \\ i_b \\ i_b \end{bmatrix} + L\frac{d}{dt}\begin{bmatrix} i_a \\ i_b \\ i_c \end{bmatrix} + \begin{bmatrix} S_a \\ S_b \\ S_c \end{bmatrix} V_{dc} + \begin{bmatrix} u_n \\ u_n \\ u_n \end{bmatrix} \tag{5.2}$$

where, u_n is defined by the Equation (5.3).

where,

(The symbols defined here can appear in other chapters and in the nomenclature with different definitions)

S_a, S_b, S_c : represents three-phase bridge arm switching function.

$S = 1$: the top switch is on and the bottom switch is close

$S = 0$: the bottom switch is on and the top switch is close

i_{dc} : DC-link output current

i_L : DC-link load current

v_{dc} : DC-link output voltage

C : filter capacitor

L : inductance of grid-side

R : resistance of grid-side

v_a, v_b, v_c : phase voltages

i_a, i_b, i_c : phase currents.

Due to the summation of the three-phase currents of the system without a neutral line is zero, hence, $i_a + i_b + i_c = 0$.

With algebraic manipulation, we can get Chen and Chen, P-H (2014),

$$u_n = \frac{v_a + v_b + v_c}{3} - \frac{1}{3}(S_a + S_b + S_c)v_{dc} \tag{5.3}$$

Transforming the above equations into a $d-q$ axis synchronously rotating frame ($\omega_1 =$ is the synchronous angular frequency),

$$u_d = -L\frac{di_d}{dt} - Ri_d + \omega_1 Li_q + v_d \tag{5.4}$$

$$u_q = -L\frac{di_q}{dt} - Ri_q - \omega_1 Li_d + v_q \tag{5.5}$$

$$C\frac{d}{dt}v_{dc} = i_{dc} - i_L \tag{5.6}$$

where,

u_d, u_q : the $d-q$ components of bridge arm output voltage

v_d, v_q : the $d-q$ components of grid voltage

i_d, i_q : the $d-q$ components of input currents

Under the assumption of the synchronously rotating frame, by taking the d axis aligns with the grid voltage. The grid voltage components are,

$$v_d = \text{constant} \tag{5.7}$$

$$v_q = 0 \tag{5.8}$$

Neglecting the harmonics by maintaining the switching action of the converter less than 100Hz, we can neglect the converter losses,

$$P_r = v_{dc}i_{dc} = \frac{3}{2}(v_d i_d + v_q i_q) = \frac{3}{2}v_d i_d \tag{5.9}$$

When $P_r > 0$ implies the GSC works in a rectifier state and absorbs energy from the grid. When $P_r < 0$ (is less than zero) represents the GSC works in inverter state and delivers energy to the grid from the DC side. If m_1 is the modulation index (the ratio of v_m / v_c; where v_m, v_c are the modulating signal and the triangular carrier signal respectively) which is a known value and is generally taken as 0.75 (a value less than 1)),

$$v_d = \frac{m_1}{2\sqrt{2}} v_{dc} \tag{5.10}$$

Using Equations (5.9) and (5.10), the DC-link output current and voltage can be derived as,

$$i_{dc} = \frac{3m_1 i_d}{4\sqrt{2}} \tag{5.11}$$

and

$$C\frac{dv_{dc}}{dt} = i_{dc} - i_L = \frac{3m_1 i_d}{4\sqrt{2}} - i_L \tag{5.12}$$

From Equation (5.12) it can be seen that the DC link voltage v_{dc} can be controlled through i_d. The reactive power Q_r from or to the source can be written as,

$$Q_r = \frac{3}{2}\left(v_d i_d - v_q i_d\right) = \frac{3}{2} v_d i_q \tag{5.13}$$

According to the Equation (5.13), the reactive power from or to the grid can be controlled through i_q. If we assume that unity power factor for the grid-side, then the i_q value also become zero. Then the final result is not realistic. Hence, assuming that i_q and i_d are not equal to zero we proceed to seek a feasible solution,

Assuming new voltages are,

$$u_{d1} = Ri_d + L\frac{di_d}{dt} \tag{5.14}$$

$$u_{q1} = Ri_q + L\frac{di_q}{dt} \tag{5.15}$$

Equations (5.4) and (5.5) given earlier could be arranged to substitute u_{d1} and u_{q1},

$$u_d = -\left(L\frac{di_d}{dt} + Ri_d \right) + \omega_1 L i_q + v_d$$

$$u_q = -\left(L\frac{di_q}{dt} + Ri_q \right) - \omega_1 L i_d + v_q$$

Now we can write,

$$u_d^* = -u_{d1} + \left(\omega_1 L i_q + v_d \right) \tag{5.16}$$

$$u_q^* = -u_{q1} - \left(\omega_1 L i_d \right) \tag{5.17}$$

It should be noted that by adding the compensation terms, Equations (5.16) and (5.17) have eliminated the input AC current. Also, it should be noted that by adding the feedforward compensation of the grid voltage, we can find the reference voltages u_d^* and u^*_q for control purposes.

5.3. Rotor-Side Converter (RSC) modelling

Rotor-side modelling could be carried out in a similar manner as in the previous section on grid side modelling. We can neglect the generator stator winding resistance as it is negligible. The phase difference between stator flux and the stator voltage vector is 90°. Hence, by utilising the stator-flux-oriented to align the stator flux vector position with *d*-axis, the flux equation is,

$$\psi_{ds} = \psi_s \tag{5.18}$$

$$\psi_{qs} = 0 \tag{5.19}$$

To keep the stator flux ψ_s constant, the voltage equations can be expressed as,

$$v_{ds} \approx \frac{d}{dt}\psi_s = 0 \tag{5.20}$$

$$v_{qs} \approx \omega_1 \psi_s = V_s \tag{5.21}$$

where, V_s is the space vector amplitude of stator voltage. The active and reactive powers can be written as,

$$P_s = \frac{3}{2}\left(v_{ds} i_{ds} + v_{qs} i_{qs}\right) \approx \frac{3}{2} V_s i_{qs} \tag{5.22}$$

$$Q_s = \frac{3}{2}\left(v_{qs} i_{ds} - v_{ds} i_{qs}\right) \approx \frac{3}{2} V_s i_{ds} \tag{5.23}$$

According to the Equation (5.23), while DFIG is connected to an infinite grid, the stator voltage is considered a constant. The stator current is the only controlled quantity. Therefore, the DFIG output power to the grid can be controlled by stator current, which is achieved by the goal of independent control of active and reactive power output.

Another assumption we make is due to the stator windings are directly connected to the power systems and the effect of the stator resistance is very small, the equivalent stator magnetising current can be considered a constant, i.e.:

$$i_{ms} = \frac{\psi_s}{L_m} \approx \frac{V_s}{L_m \omega_1} \tag{5.24}$$

Substituting Equation (5.24) in the flux Equations (5.25) to Equation (5.28), the *d-q* axis stator current can be calculated as given by the Equations (5.29 and (5.30),

The flux equations are,

$$\psi_{ds} = -L_s i_{ds} + L_m i_{dr} \tag{5.25}$$

$$\psi_{qs} = -L_s i_{qs} + L_m i_{qr} \tag{5.26}$$

$$\psi_{dr} = -L_r i_{dr} + L_m i_{ds} \tag{5.27}$$

$$\psi_{qr} = -L_r i_{qr} + L_m i_{ds} \tag{5.28}$$

hence,

$$i_{ds} = \frac{L_m i_{dr} - \psi_{ds}}{L_s} = \frac{L_m (i_{dr} - i_{ms})}{L_s} \tag{5.29}$$

$$i_{qs} = \frac{L_m}{L_s} i_{qr} \tag{5.30}$$

Substituting Equation (5.29) and (5.30) into Equations (5.31) to (5.34),

$$v_{ds} = -i_{ds}R_s + \frac{d\psi_{ds}}{dt} - \omega_1\psi_{qs} \tag{5.31}$$

$$v_{qs} = -i_{qs}R_s + \frac{d\psi_{qs}}{dt} + \omega_1\psi_{ds} \tag{5.32}$$

$$v_{dr} = i_{dr}R_r + \frac{d\psi_{dr}}{dt} - \omega_s\psi_{qr} \tag{5.33}$$

$$v_{qr} = i_{qr}R_r + \frac{d\psi_{qr}}{dt} + \omega_s\psi_{dr} \tag{5.34}$$

the following equations are obtained,

$$v_{dr} = i_{dr}R_r + \sigma L_r \frac{di_{dr}}{dt} - \omega_s\sigma L_r i_{qr} \tag{5.35}$$

$$v_{qr} = i_{qr}R_r + \sigma L_r \frac{di_{qr}}{dt} + \omega_s\left(\sigma L_r i_{dr} + \frac{L_m^2}{L_s} i_{ms}\right) \tag{5.36}$$

where, $\sigma = 1 - \frac{L^2{}_m}{L_s L_r}$ is the leakage factor.

The control variables v_{dr} and v_{qr} of the rotor voltage can be obtained from Equations (5.35) and (5.36). The influence of the cross-coupling between the *d-q* axis components of rotor current on system performance is small, which can be eliminated by adopting some control law.

5.4. Dynamic Modelling of Synchronous Buck Converter (SBC).

Having described the mathematical derivations for the GSC and the RSC in this section we will model the SBC which is frequently used in power electronics and for generating power with WTs. Though, a detailed description is not given here one should note that any basic converter or switched power supply consists of five standard components: a pulse-width modulating controller; transistor switch (active switch); an inductor; a capacitor; a diode (switch). The switch can be MOSFET, IGBT, JFET or a BJT. We choose the IGBT as there

are some distinct advantages and due to high efficiency (around 98%). IGBT acts as a switch since the requirement is for fast switching action. The capacitor generally provides the filtering action by providing a path for the harmonic currents away from the load. The output capacitance (across the load with capacitance *C* in our Simulink block diagram) is required to minimise the voltage overshoot and ripples present at the output of a step-down converter. The capacitor is large enough so that its voltage does not have any noticeable change during the time the switch is off (Karunaratne, 1999). Large overshoots are caused by insufficient output capacitance, and large voltage ripple is caused by insufficient capacitance as well as a high equivalent-series-resistance (ESR) in the output capacitor. Thus, to meet the ripple specification for a step-down converter circuit, we must include an output capacitor with sufficient capacitance and low ESR (Karunaratne, 1999). Sometimes ESR is identified as the effective series resistance with the capacitor and it should be low enough to compensate the phenomena.

The MATLAB/Simulink SBC main model is shown in Fig. 5.9. and its EEC diagram is shown in Fig. 5.10. The simplified state-space model equations for the SBC is given by the set of equations shown in Equation (5.37).

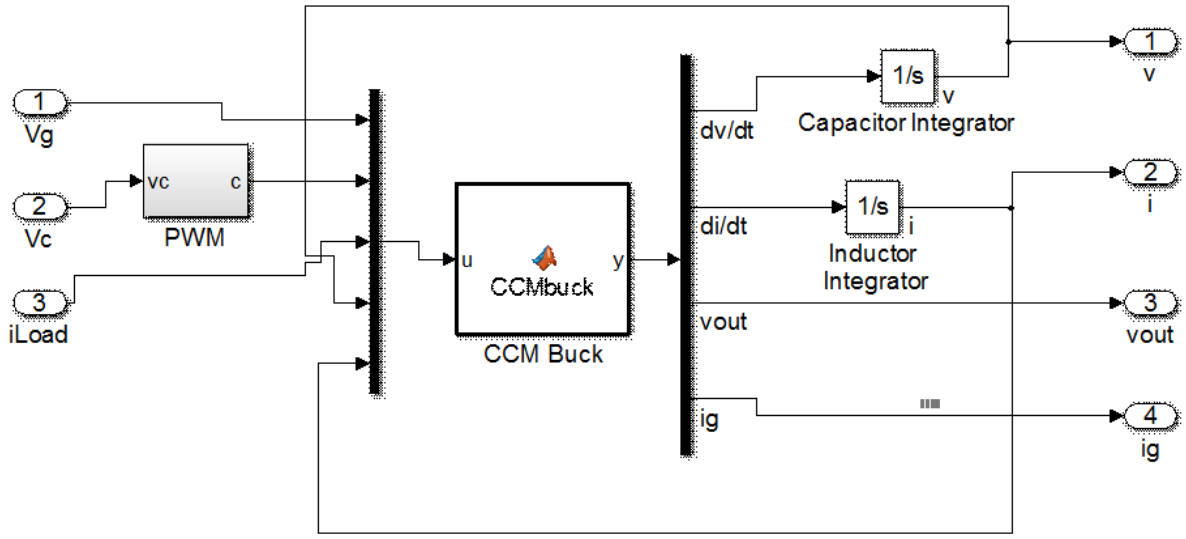

Figure 5.9: Simulink block diagram for the synchronous buck converter.

$$
\left.
\begin{aligned}
&V_{out} = v + R_{esr}\left(i - i_{Load}\right) \\
&i_g = \begin{cases} i & (c=1) \\ 0 & (c=0) \end{cases} \\
&i_C = C\frac{dv}{dt} = i - i_{Load} \\
&v_L = L\frac{di}{dt} = \begin{cases} V_g & -\left(R_{on1} + R_L\right)i \quad -V_{out} \quad (c=1) \\ -\left(R_{on2} + R_L\right)i & -V_{out} \quad (c=0) \end{cases}
\end{aligned}
\right\} \qquad (5.37)
$$

Equation (5.37) is embedded into the MATLAB function for the bidirectional converter programme. Where, V_g is the 3 phase input voltage per phase. The parameter v is the voltage across the capacitor with capacitance C.

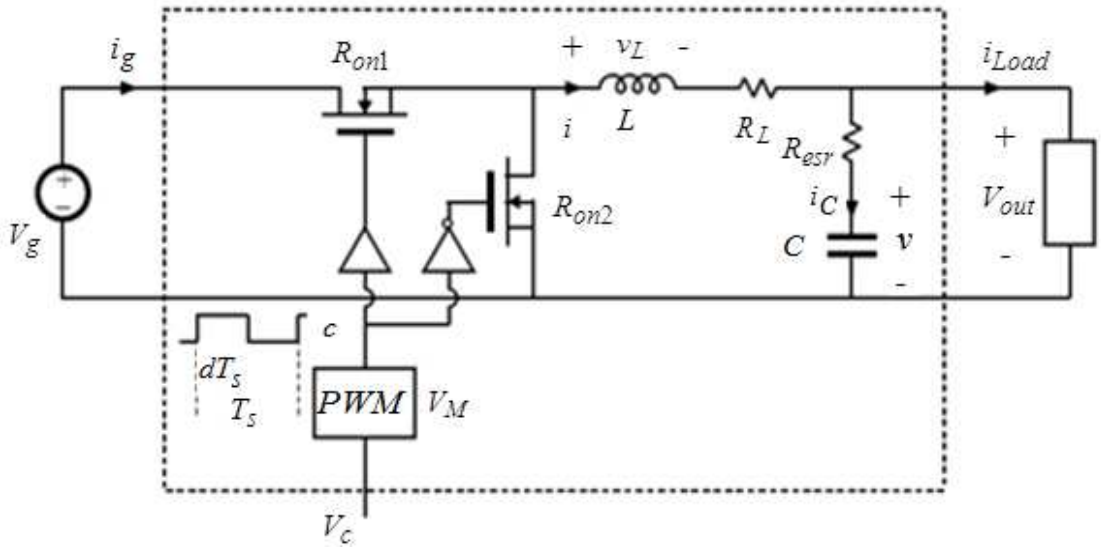

Figure 5.10: Synchronous buck converter circuit diagram.

In Fig. 5.10, R_{on1} and R_{on2} represents the active switch and the passive switch respectively. The active switch is the one which is controllable and the passive switch has diode with it. Generally, the input voltage is higher than the output voltage for buck converters. All other components shown there in the diagram are standard circuit elements in a buck converter.

The inductor, L shown in Fig 5.10, is defined in the Simulink 'Function Block Parameters: 'SyncBuck', which is not visible in Fig. 5.9. as it is in a subsystem called 'SyncBuck'. The parameter values for the simulation were entered into the Simulink block diagram by double clicking the 'SyncBuck' block. The numerical value specified there for the inductor, L is 1×10^{-6} (H). The capacitor numerical value, C is 200×10^{-6} (F). The other numerical values

defined in the 'Function block': the switching frequency = 1×10^{6} (Hz). Transistor switch $R_{on1} = 20\times10^{-3}$ (Hz); $R_{on2} = 20\times10^{-3}$ (Hz); inductor resistance $R_L = 10\times10^{-3}(\Omega)$, Vg=5V, (Erickson Byeon, (2016). These numerical values are real values applicable for this type of power converter. Hence, the 'x-axis' in the characteristic graphs are shown in $\times10^{-4}$ scale. The MATLAB iterative algorithmic program for the Equation 5.37 can be written as given next,

```
function y = CCMbuck (u, L, RL, Ron1, Ron2, Resr)
vg=u (1) ;   % Vg is the modulating signal which is equal
             % to input voltage of the 3 phase/per phase
d= u (2);
iLoad=u(3) ;
v= u(4) ;
i = u(5);
vout=v+Resr*(i-iLoad);
ig=d*i;
iC=i-iLoad;
vL=d*(vg-(Ron1+RL)*i-vout)+(1-d)*(-(Ron2+RL)*i-vout);
y = [iC/C   vL/L  vout  ig];
```

The function y = CCMbuck (u, L, C, RL, Ron1, Ron2, Resr) is embedded into the 'CCMbuck' function block. The PWM switching frequency is modelled by 'Repeating Sequence block' and a 'Relay block' in the 'Discontinuities' library in Simulink. In the PWM ramp block in Fig. 5.11. the time value has been used to specify the switching period (e.g. [0 1e-6]) which corresponds to 1 MHz switching frequency, which represents actually a real time scenario. To describe further, on PWM ramp block, the block required to model is the 'Repeating Sequence block', which could be found in the Sources library. When you double click the Repeating Sequence Block (RSB), Repeating mask table could be found there. In this block the 'Time Values' are related to the x-axis and the output values shown in the block are related to the y-axis. They are related to the Input modulating sinusoidal signal and the carrier wave signal. These two arrays are specified in terms of variables [0 1/fs], (1/fs is a variable which is used here to signify the time up to the peak value of the triangular wave). In the other array (y-axis) necessary to specify the amplitude or rather the peak amplitude is the variable 'VM' which is presented in this manner, so that these signals can be altered as necessary to suit duty ratio or

frequency ratio. Hence, these values have been entered as [0 1/fs] so that fs is specified externally as a parameter. Output values are entered as [0 VM] that will allow us to externally specify the PWM ramp.

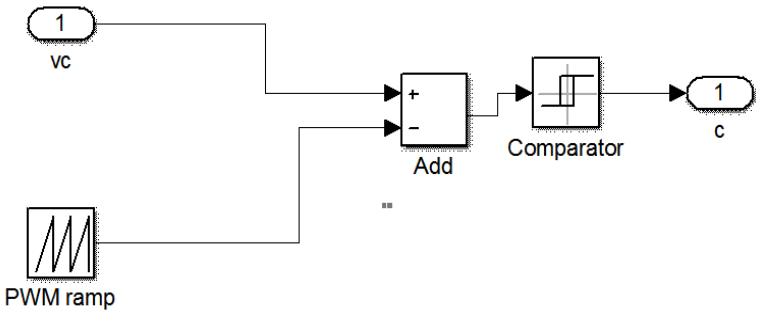

Figure 5.11: PWM switching frequency model.

The method to obtain a triangular WF from 'Repeating Sequence Block' and how to generate a 'Sinusoidal wave form' is not addressed here as it is available in the help directory in Simulink. The simulation results are shown in Fig. 5.12. to 5.16. The capacitor voltage on the load side versus simulation time is shown in Fig. 5.12. The input current versus simulation time is given in Fig. 5.13. The current shown in this figure is sampled at time intervals for PWM. The sampling scenario is visible from the inductor current versus time shown in Fig. 5.14. In Fig. 5.15 the parameter v_{out} represents the output voltage variation through the load. As expected the output voltage characteristics through the capacitor C versus simulation time (Fig. 5.11) are similar to the load voltage characteristics shown in Fig. 5.15. Function of the capacitor on the load side retains the output voltage at a constant level when the load voltage goes up and down during the switching time (on-off) of the converter.

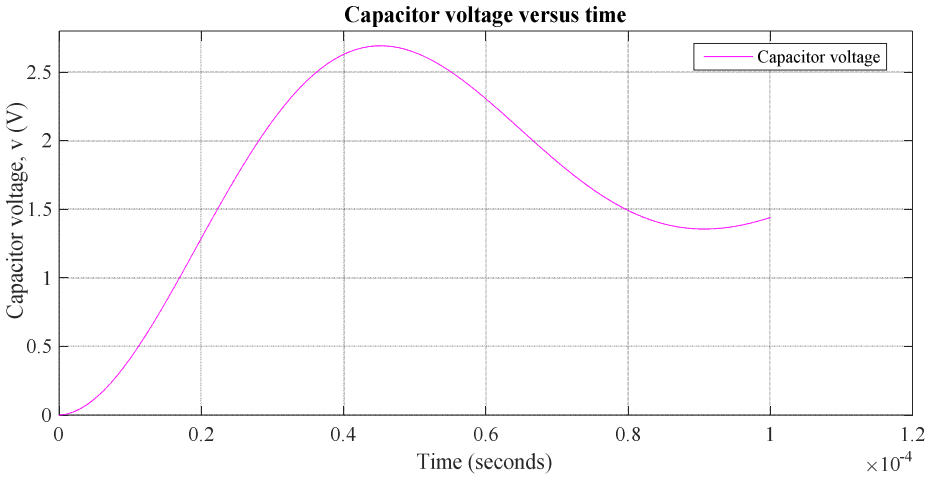

Figure 5.12: Capacitor voltage versus simulation time (s) in real time.

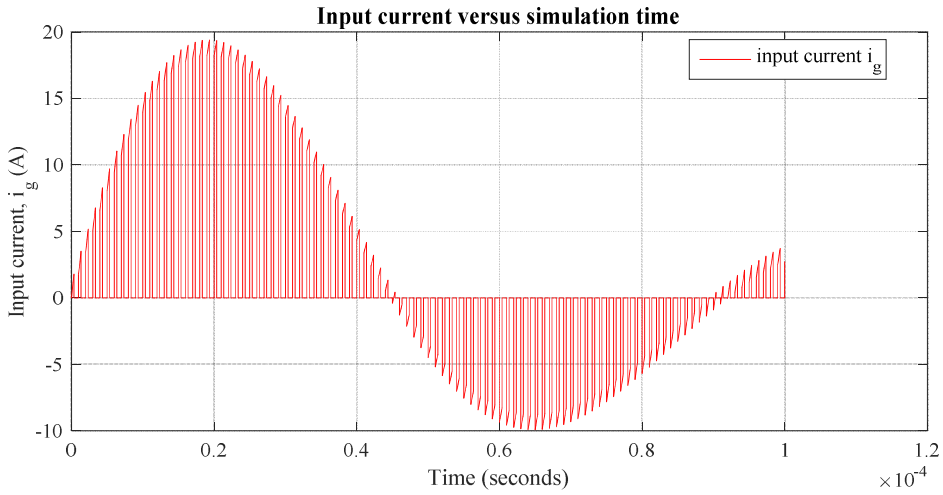

Figure 5.13: Input current versus simulation time (s) in real time.

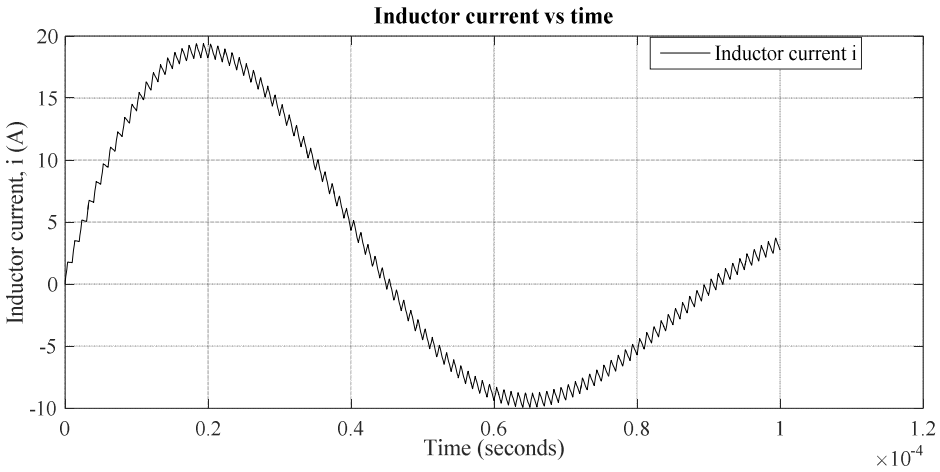

Figure 5.14: Inductor current versus simulation time (s) in real time.

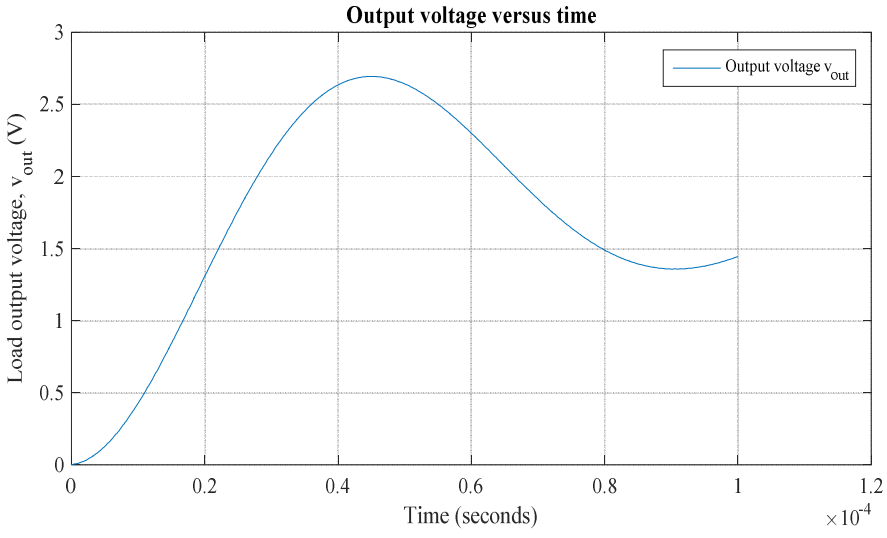

Figure 5.15: Output voltage variation through the load versus simulation time (s) in real time.

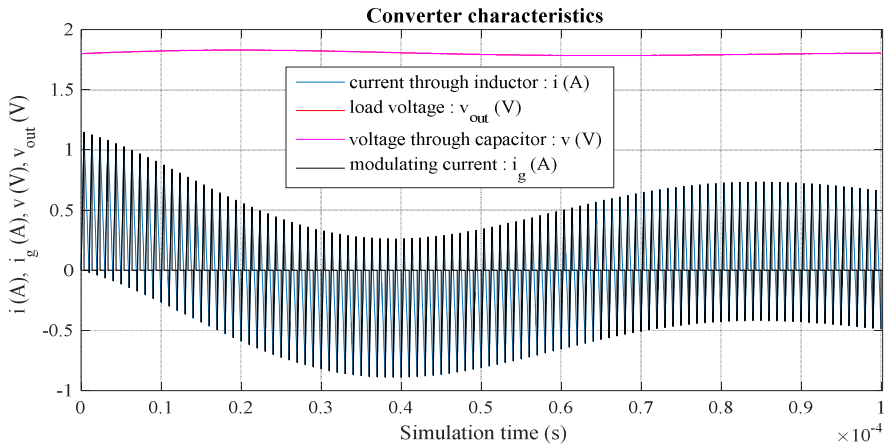

Figure 5.16. (a): Capacitor integrator and inductor integrator with initial conditions.

Converter dynamic simulation characteristics are shown in Fig. 5.16. (a) with the same x-axis scale similar to previous plots. As the present x-axis scale is too small to identify the signals separately enlarged x-axis figure is shown in Fig. 5.16. (b).

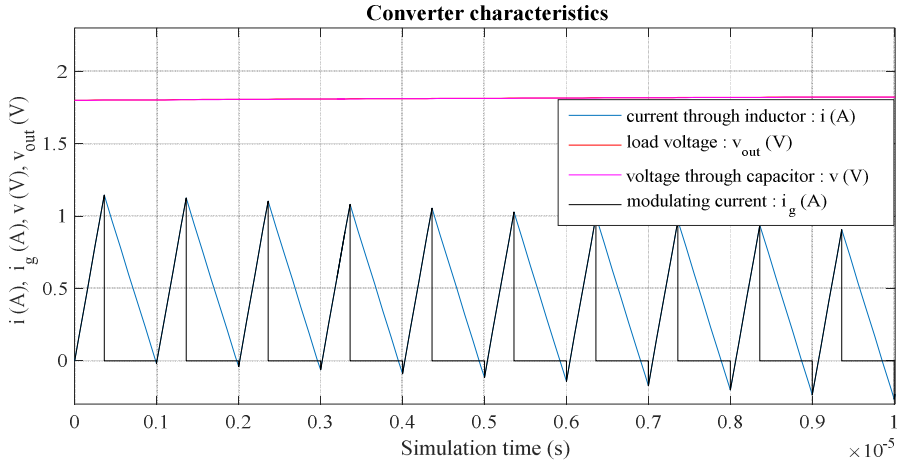

Figure 5.16. (b): Capacitor integrator and inductor integrator with initial conditions (enlarged figure).

Switched control signal model can be replaced with an averaged duty cycle waveform as given in the Simulink block diagram shown in Fig. 5.17. The model developed has included a switch to transform it to an averaged model from the switching model. The SBC linearization method and the linearization related to signal modelling is not addressed here as it is beyond the limits and the boundaries marked for this research programme at the inception.

The control signal path V_c is now modified with a Switch block and with a PWM Gain block. The Switch threshold is entered as 0.5 and the constant block is labelled as SW. The constant SW is set for zero for the averaged model in which the PWM is modelled as 1/VM gain to generate duty cycle d. The constant SW is set to 1 for controlled signal model. The switching

model in which the actual PWM is used to generate the pulsating switch control is with the variable $c(t)$ (see Equation 5.37: c =1 and c =0). The simulation results of the switched control averaged signal model presented by the Simulink block diagram shown in Fig. 5.17 is described next.

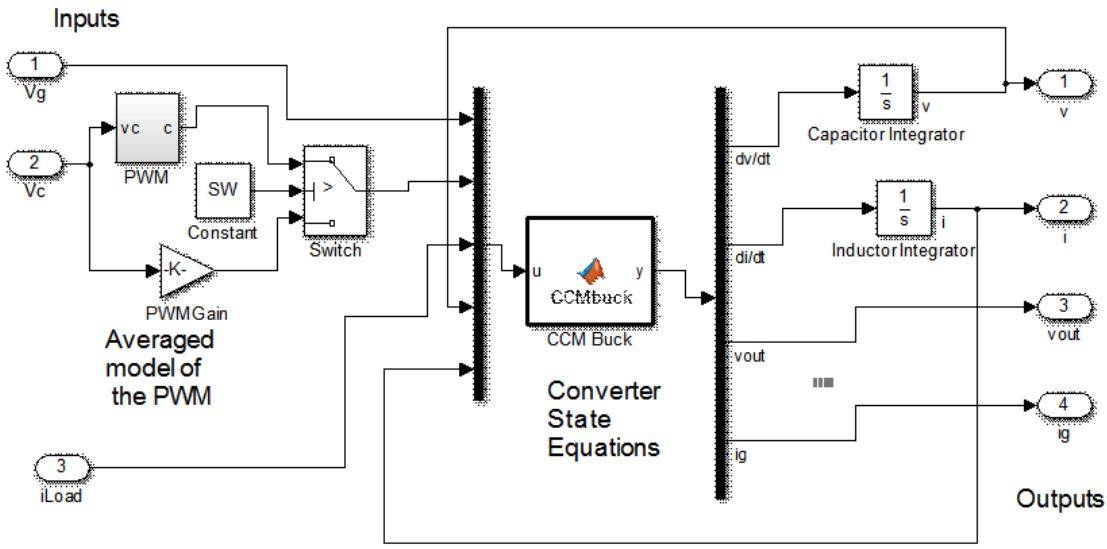

Figure 5.17: Averaged model of the of the Converter.

Bode plot from the SBC Simulink model is shown in Fig. 5.18. Bode plot here represents the graph of magnitude and phase of the SBC transfer function. Magnitude is plotted in decibels and the phase is in degrees, while the frequency is shown on a logarithmic scale. The crossover frequency normally identifies as f_C is the frequency where the control loop gain is unity and in other words 0 dB. The crossover frequency for this case is 2.65×10^4 Hz. The other point of interest in this graph is the phase lag reaches the 180º which is not concurrently happening in this plot. Hence, there is no gain margin (GM) which is correct as it is a buck converter where the output voltage is generally lower than the input voltage. Other condition required to check for the stability is the phase lag less than -180º (degrees). This condition is satisfied here as there is no phase lag. At other frequencies, the phase lag can exceed 180 degrees and control loop will still remain stable. Therefore, the SBC system is stable from the observation of the Bode Plot.

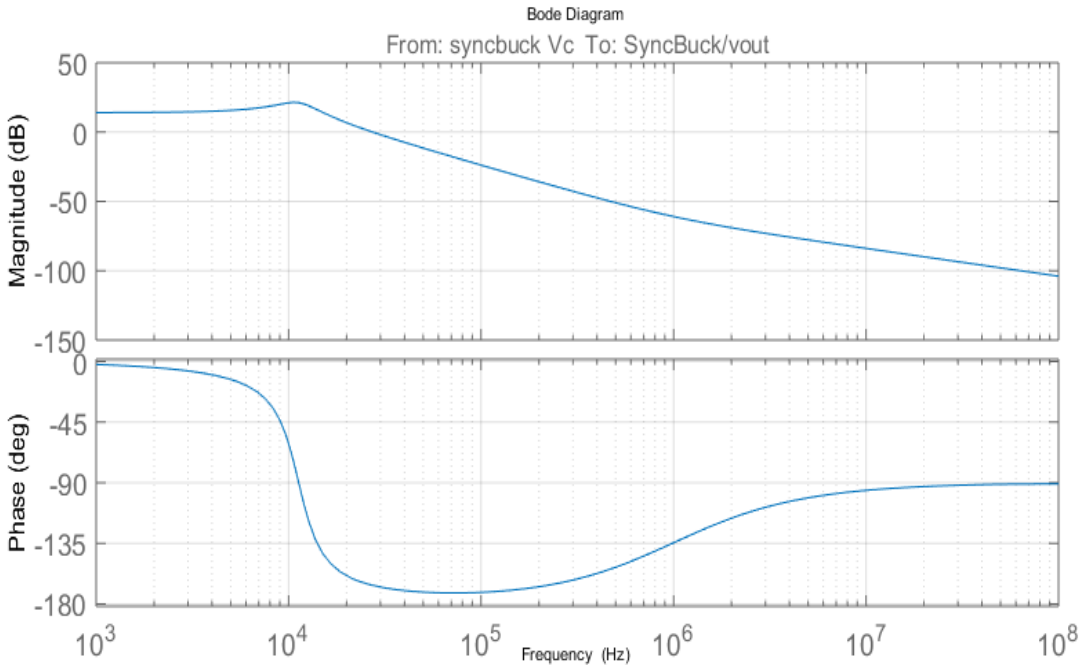

Figure 5.18: Buck converter open-loop control to output magnitude and Phase response.

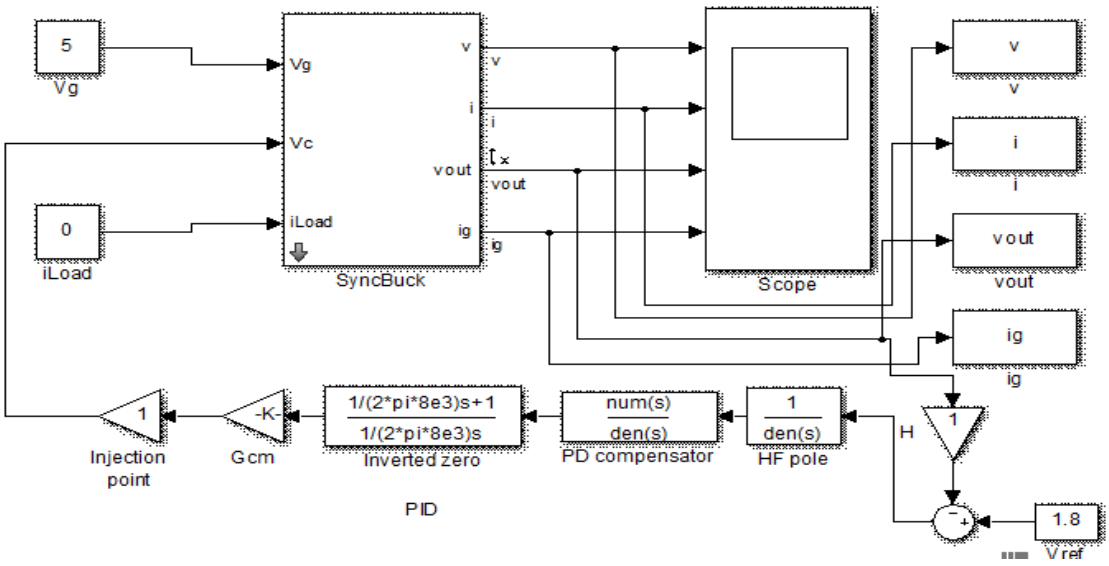

Figure 5.19.: Buck converter closed-loop control with a PID controller.

The detailed description of the 'SyncBuck' subsystem block shown in Fig. 5.19. is illustrated in Fig. 5.20. The inputs are in the left hand side of the figure and the outputs are in the right hand side. The converter state space equations are included in the 'CCM Buck' function block.

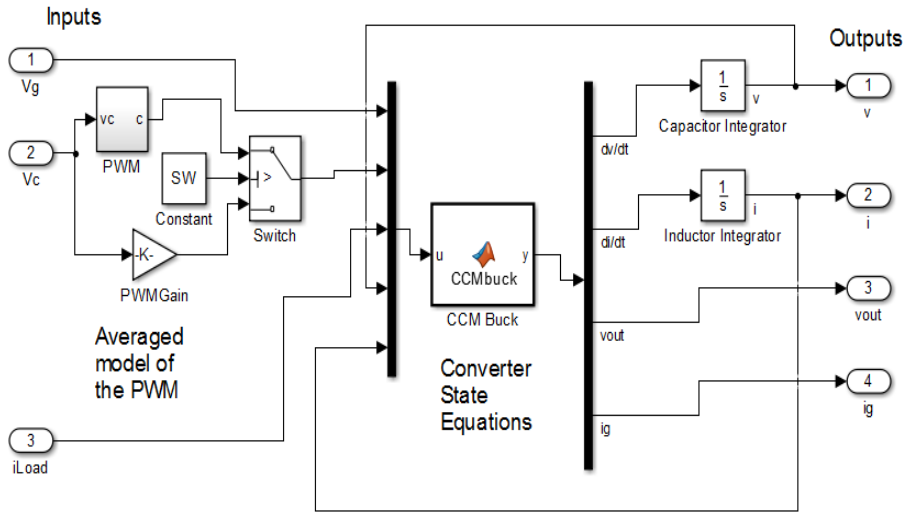

Figure 5.20: Simulink 'SyncBuck' subsystem block.

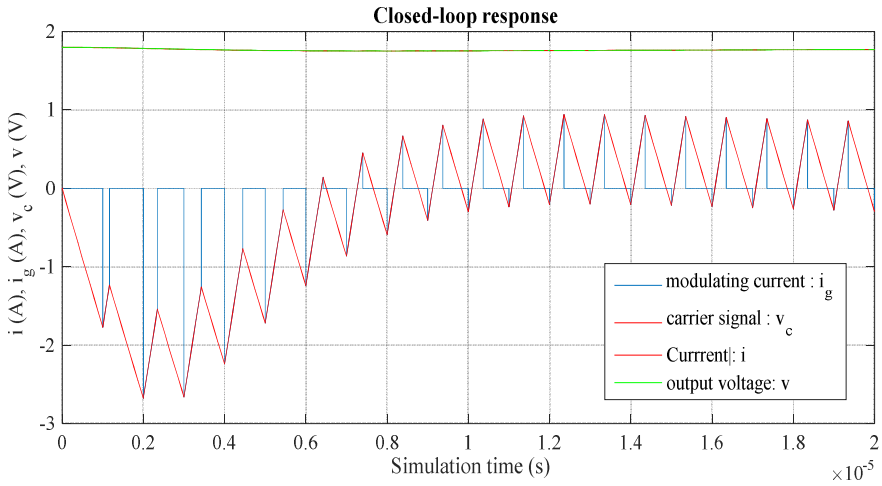

Figure 5.21: Closed-loop response of the 'Syncbuck' converter.

SBC active switch can be controlled for switching frequency and the duty ratio for stability. The SBC block diagram shown in Fig. 5.19. is deployed with a PID controller to control the carrier signal, for unexpected fluctuations of the modulating signal. The closed loop response of the SBC is shown in Fig. 5.21. As it can be seen from the Fig. 5.21, the current through the inductor i, and the modulating current i_g (pulse-signals) are settling to a steady state value with the time and the parameter v is reaching to the reference voltage of 1.8 V (DC). Fig. 5.22 shown here, illustrates the topology of the transfer function arrangement in block diagram format. The difference here to the previous state-space representation is that all blocks are

presented in Laplace domain. Detailed description on voltage mode regulation can also be found in Rahman (2016).

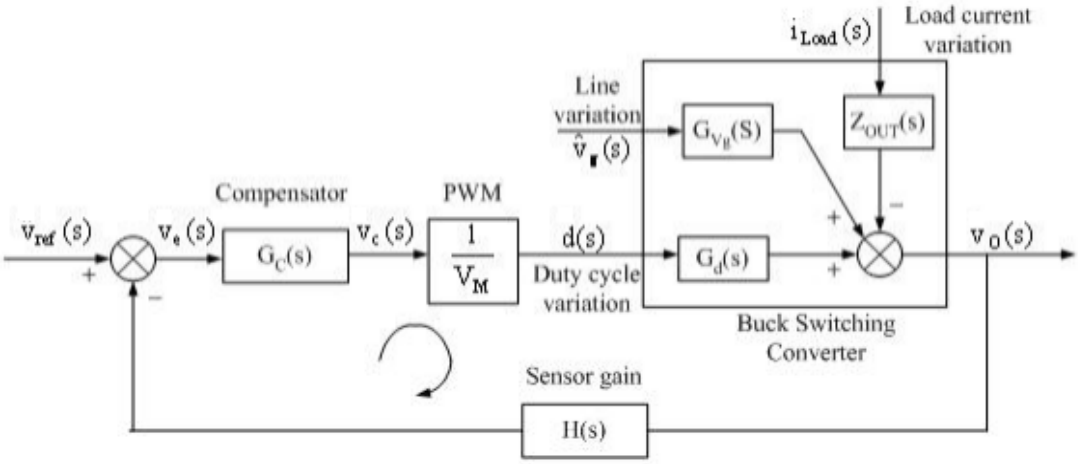

Figure 5.22: Synchronous buck converter: voltage mode regulation in Laplace domain.

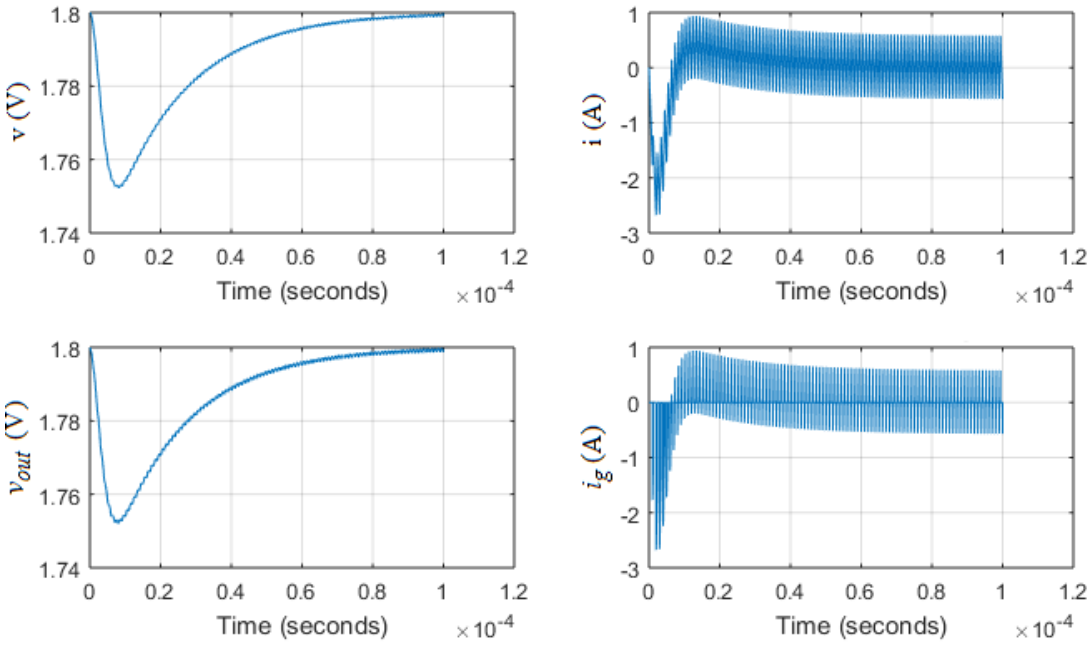

Figure 5.23: Synchronous buck converter characteristics.

Fig. 5.23. shows the characteristic of all outputs as subplots. The output voltage and the DC current outputs are reaching steady state values after implementation of the controller.

5.5. Power Converter Applications in Hybrid Energy Power Generation systems.

Due to complementary nature of the wind and solar energy, it is now customary to use both systems together for electricity generation. However, when both sources cannot provide

sufficient power when the customer demand is high, alternative backup sources like battery storage systems or capacitor banks provide energy for short durations until the wind and solar systems come back to normal operating conditions. Fig. 5.24. shows a typical block diagram representation of a generic hybrid power supply system with more than two renewable energy sources. The green colour blocks represent the fuel cell (FC), ultra-capacitor (UC), WT and BS systems. The next level down, the orange colour blocks represents all power converters connected. As it can be seen from this diagram that power converters are connected into many electrical power systems. They can be either AC/DC or DC/AC or even DC/DC transformations.

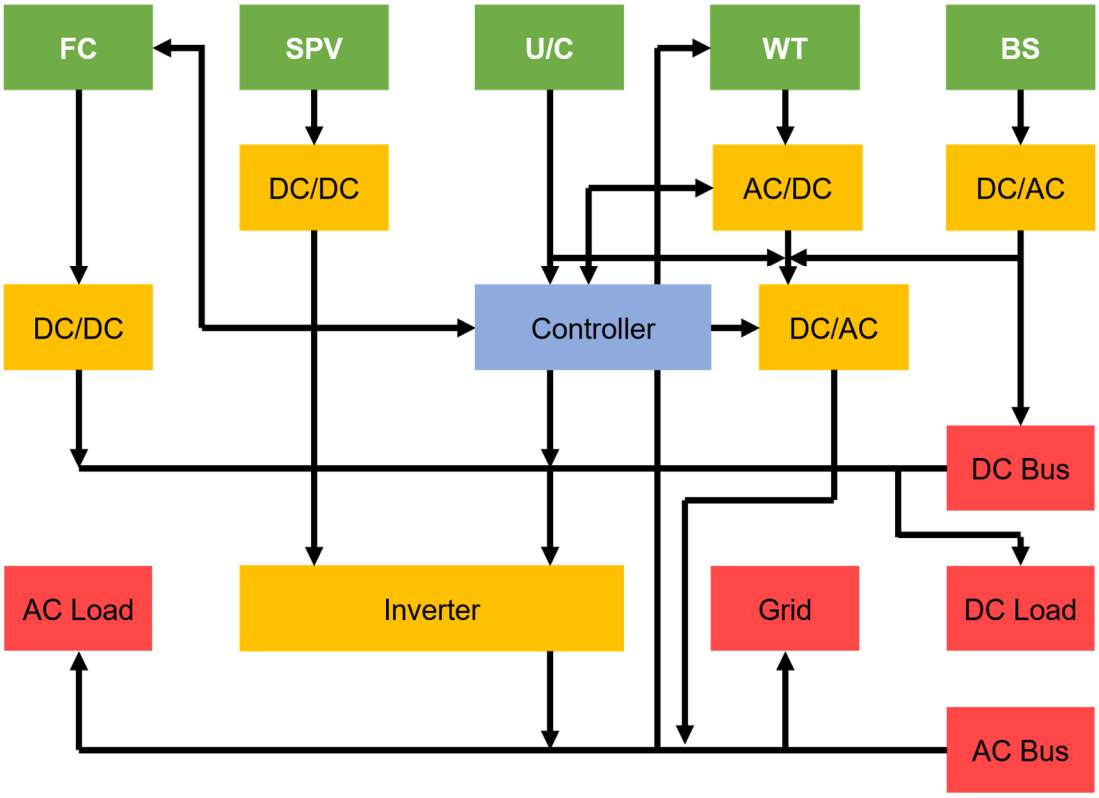

Figure 5.24: Power converters are used for DC/DC, AC/DC, DC/AC convertion.

In the block diagram, it is shown that the AC power is directly connected to the WT generator which provides the necessary power for the excitation in a form of a synchronous electric flux. The WT with DFIG rotor which will rotate at a speed greater than the synchronously induced flux speed from the grid to augment the generator to act as a generator. A continuous arrow from the AC bus to the WT is shown by this implementation. Variable wind speed is controlled by converting the electrical power initially to DC by power using converters and transformed

back into AC power with power inverters. The function of the controller is to control every sub-system in the hybrid energy system.

Summary

Comprehensive description to the PWM technique was provided with the wave form (WF) analysis. Dynamic Simulink model which offers repeatable results can be used for the other WF analysis combined with WTs can be stated as a contribution in this chapter as it was a concise presentation. When the input modulating WF is contaminated with noise, the filtering process was explained with the use of a rectangular pulse filter is another contribution in this section. Dynamic Simulink model for the SBC was presented with the mathematical formulations. Mathematical model given there for the SBC was transformed into an iterative algorithm in MATLAB and then it was embedded into a function block in the converter model. Stability analysis of the SBC was presented in relation to the Bode plot. Grid side and the RSC mathematical models which could be used for DFIG or PMIG modelling was described with special reference to bidirectional power converter. Application of power converters in hybrid energy power supply systems was described at the end of the chapter.

Chapter 6: Dynamic Modelling of Solar Photovoltaic Arrays

Outline

Mathematical modelling and simulation of solar photovoltaic (SPV) arrays is described in this chapter. The simulation results from the developed dynamic model is analysed to extract the maximum power from the sunlight at any irradiance and at given ambient temperature. Materials used for manufacturing SPV cells and the efficiency of a SPV cells are also briefly described in this section. Simulation results have been compared with a SOLKAR brand PV module.

6.0. Introduction

Solar photovoltaic cells convert sunlight into electricity. PV electricity generated from the cells can either be fed into the grid or can be stored as backup power sources to be used in the night or when necessary at times where the Sun is obscured. The electricity generated through the PV cell is environmentally friendly and helps the planet to reduce the greenhouse gas emissions while reducing the carbon footprint.

The generated current, voltage and its resistance characteristics will vary depending on the radiant light and the ambient temperature. Photovoltaic cells are made up of semiconductor materials like silicon, gallium arsenide, copper indium gallium di-selenide (CIGDS), cadmium telluride (CdTe) and amorphous silicon (a-Si) (Sengupta et al., 2016; Clement and Prasanth, 2016).

When making PV cells purified material is cut into very thin layers (wafers) of 180 -240 micrometres thick and in between, organic dyes and organic polymers are deposited to support the substrate. Polycrystalline silicon or multi-crystalline silicon is widely used as it is less expensive to produce, though, it is slightly less efficient (Clement and Prasanth, 2016). Monocrystalline silicon solar cells are expensive than the Polycrystalline as Monocrystalline cells (c-Si) have Single-crystal wafer cells. Boron or phosphorous dopant impurity atoms are added to molten silicon to get the n-type or p-type charging effect (Breeze, 2008). The majority of PV cells available in the market today are made out of monocrystalline silicon, polycrystalline silicon, amorphous silicon, cadmium telluride, and copper indium selenide/sulphide (Breeze, 2008).

When sunlight hits the semiconductor surface of a solar cell, photons with energy greater than the bandgap energy of the semiconductor creates some electron-hole pairs proportional to the incident irradiation. Then the electrons in the silicon material in the PV springs up and attracted towards the N-type semiconductor material. This will cause more negatives in the N-type and more positives in the P-type semiconductors generating a higher flow of electricity. This is known as the Photovoltaic effect. The amount of current generated by a PV cell depends on its efficiency (a type of PV cell) its size (surface area) and the intensity of sunlight striking the surface. A single solar cell can create a very little amount of power. To create a large amount of current or voltage many solar cells are either connected in series or parallel. Solar array or PV module is made up of many solar cells connected either in series or parallel. Typical cross section of a PV cell is shown in Fig. 6.1 (Meier et al., 2004).

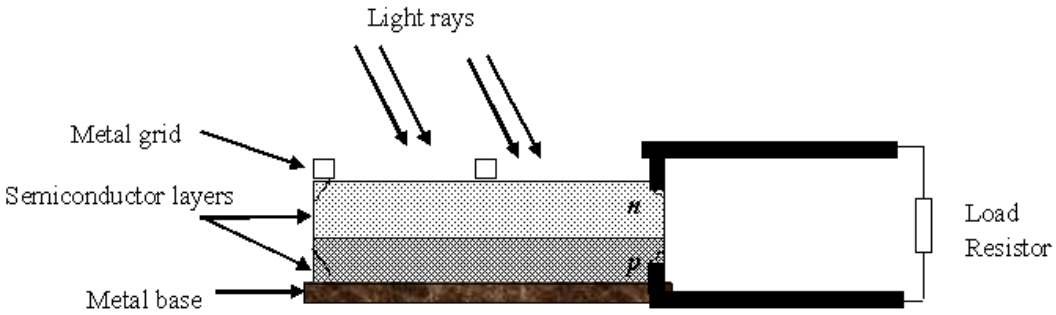

Figure 6.1: Physical structure of a PV cell (Cross section).

It is observed that a normal PV cell can generate a voltage around 0.5 to 0.8 volts depending on the type of semiconductor and the built-up technology (Breeze, 2008). Under peak sunlight conditions a typical commercial PV cell with a surface area of about 25 square inches (0.0161 m^2) can generate approximately about 2 watts at peak power (Clement and Prasanth, 2016). Since a single cell can produce only a very low current and voltage, PV cells connected in series can get a high voltage while keeping the same current. When PV cells are connected in parallel it can produce high current while keeping the voltage constant. Depending upon the requirement cells can be connected in series and parallel to make one module that gives high current and voltage.

The efficiency of a PV cell depends on their type. There are three main types of PV cells available in the market. They are monocrystalline, polycrystalline and thin film. The monocrystalline and polycrystalline PV cells are manufactured using microelectronic manufacturing technology. The efficiency of monocrystalline cells is in the range of 10%- 15%,

while polycrystalline (or multi-crystalline) PV cells are in the range of 9% -12%. For thin film cells, the efficiency is 10% for a-Si (amorphous Silicon), 12% for CuInSe2 and 9% for CdTe (Leea and Ebong, 2017). Technology in this area has been rapidly developing and it has found that different technologies can achieve efficiencies up to 20%. GaInP/GaInAs/Ge multi-junction solar cells can get the efficiency up to 40%. The highest efficiency so far recorded was by using multiple junction cells at high solar concentrations (43.5% using 418 x concentrations). They are still under the experimental stage. Thermodynamically it is understood that the maximum theoretically possible conversion efficiency for the sunlight is 86% according to the Carnot limit. All of these measurements were taken under standard conditions: measured under the global AM1.5 (1000 W/m^2) at 25°C (IEC 60904–3: 2008, ASTM G-173-03 global).

6.1. Dynamic Modelling of a SPV Cell

In literature single diode PV cell has been used by many researchers than two diode model as we discussed previously. (for example: Humada et al., 2016).

G : Irradiance

T : Temperature (Operating temperature)

The SPV cells used for modelling has a p-n semiconductor junction that directly converts light energy into electricity.

I_{ph} : Photogenerated current depending on irradiance (G) and temperature (T)

R_{sh} : Intrinsic shunt resistance of the cell

R_s : Series resistance

I_{rs} : PV cell reverse saturation current

$I_{ph,ref}$: Photocurrent (A) at STC.

μ_{Icc} : Coefficient; temperature coefficient at particular short circuit current (A/K)

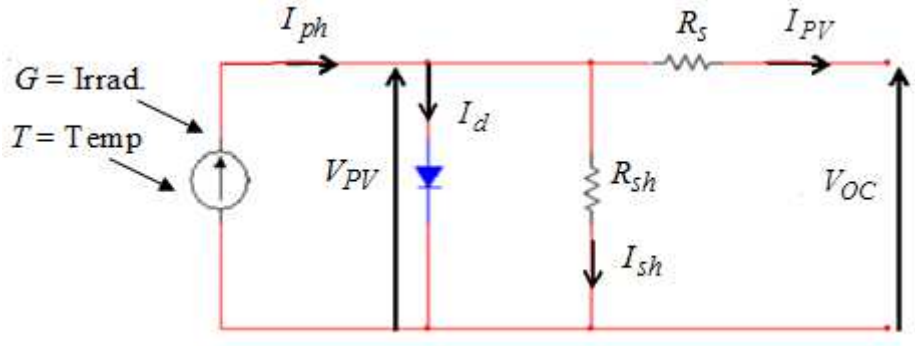

Figure 6.2: Single diode equivalent electrical circuit for a PV cell.

The mathematical model implemented in this paper was the model presented in Pandiarajan and Ranganath (2011). The parameter V_{PV} is equal to the PV cell open circuit voltage V_{OC}. Usually, R_{sh} is very large and R_s is very small compared to R_{sh}. Hence, R_s may be neglected to simplify the mathematical model. The output current *I* can be written as (from Kirchhoff's current law),

$$I_{PV} = I_{ph} - I_d - I_{sh} \tag{6.1}$$

The photogenerated current is related to the $I_{ph,ref}$ as given in Chouder and Silvestre (2013);

$$I_{ph} = \frac{G}{G_{ref}}(I_{ph,ref} + \mu_{Icc}(T - T_{ref})) \tag{6.2}$$

Generally, the parameter V_{OC} as illustrated in Fig. 6.2., is used to calculate the I_{rs} which is the module reverse saturation current. The parameter $I_{ph,ref}$ in Equation (6.2) is identified as I_{SCr} which is the short circuit current that is available from the manufacturers at the time of production or from technical data. (*G* and G_{ref} are the irradiance at operating temperature and at standard conditions. *G* at operating conditions is identified as λ and G_{ref} is taken as 1000; which is: irradiance at standard test conditions (STCs): 1000 W/m^2 and 25ºC or at (298ºK),

$$I_{ph} = \left[I_{SCr} + K_i(T_{op} - 298)\right] \times \lambda / 1000 \tag{6.3}$$

$$I_{rs} = I_{SCr} / \left[\exp(qV_{OC} / N_s KAT) - 1\right] \tag{6.4}$$

The parameter I_o is the PV cell saturation current (A) which is related to the diode properties. The saturation current I_o is given by the mathematical relationship,

$$I_o = I_{rs}\left[\frac{T_{op}}{T_{ref}}\right]^3 \exp\left[\frac{qE_{go}}{BK}\left\{\frac{1}{T_{ref}} - \frac{1}{T_{op}}\right\}\right] \tag{6.5}$$

Where, I_{rs} is the reverse saturation current of the PV cell.

E_{go} : is the band gap for silicon =1.1eV

K : is Boltzmann constant = 1.3805e-23Nm/º K

q : is Electron charge =1.6e-19 Coulomb

$A = B$: is an ideality factor and is taken to be equal to 1.6

N_s , N_p : is the number of modules connected in series, and parallel respectively

K_i : is the short-circuit current temperature co-efficient at I_{SCr} = 0.0017A / ºC

$$I_{PV} = N_p \times I_{ph} - N_p \times I_o \left[\exp\left\{ \frac{q(V_{PV} + I_{PV} R_s)}{N_s KAT_{op}} \right\} - 1 \right] \quad (6.6)$$

The following parameter values were extracted from reference Pandiarajan and Ranganath, (2011) for this simulation studies and these values are related to the SOLKAR brand SPV module of 36 W: N_p=1, N_s =36, I_{SCr} = 2.55 A, V_{OC}=21.24 V, I_{mp}= 2.25, V_{OC} at maximum power = 16.56 (V). The voltage at maximum power can be different from the open circuit voltage. In this SPV array 36 solar cells are connected in series and the open circuit voltage delivered when operating at maximum power with specified conditions is 16.66 V. The electrical specifications were conducted at test conditions and the irradiance of 1 kW/m^2, spectrum of 1.5 air mass and the cell temperature at 25˚C. (see Pandiarajan and Ranganath (2011) for more details).

6.2. Simulation Results of the Dynamic PV Cell Model

Irradiance and the insolation

For the measurement of irradiance, the Sunlight falling into the PV panel must be vertical or the panel must be perpendicular to the rays. The units of irradiance are watts per square metre. Insolation is also an energy measurement of the sunlight but, taken as an average over a period of time. Unit of measurement for insolation is given either in kW per second or hour. In this instance, we assume that both measurements are taken per second and also the insolation varies with time.

The PV module is represented by the Equations (6.1), (6.3), (6.4), (6.5) and (6.6). The Equations represented by (6.2) and (6.3) are the same but with different symbols for convenience to use in MATLAB. The variation of V_{PV} versus I_{PV} at constant Insolation/Irradiance of G/1000= 1 units is given in Fig. 6.3. The Simulink model and the relevant MATLAB script files are given in Appendix: B.

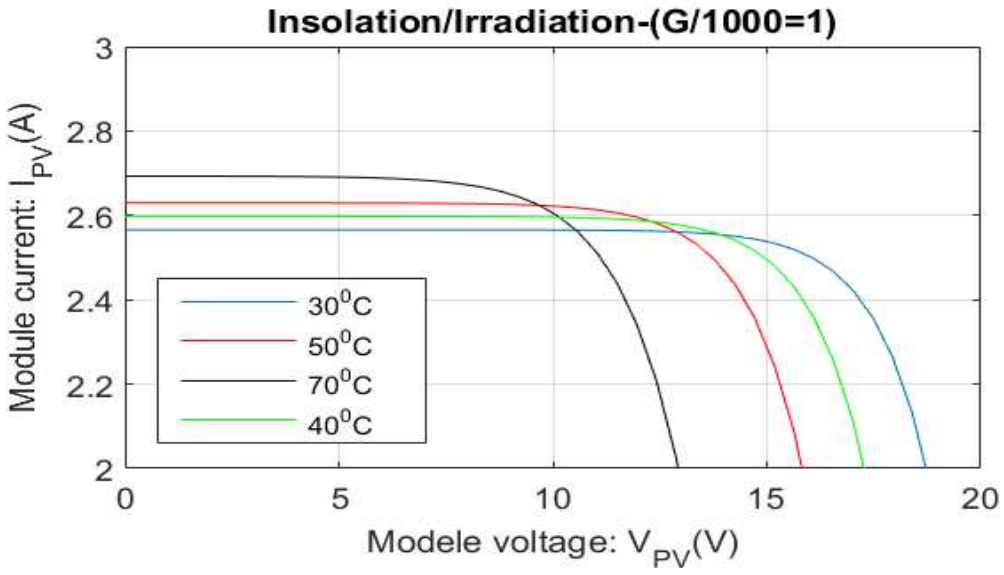

Figure 6.3: the variation of V_{PV} versus I_{PV} at constant Irradiance of G = 1kW/m^2 irradiance

The output characteristics of V_{PV} versus I_{PV} at constant ambient temperature while changing the irradiance is given in Fig. 6.4.

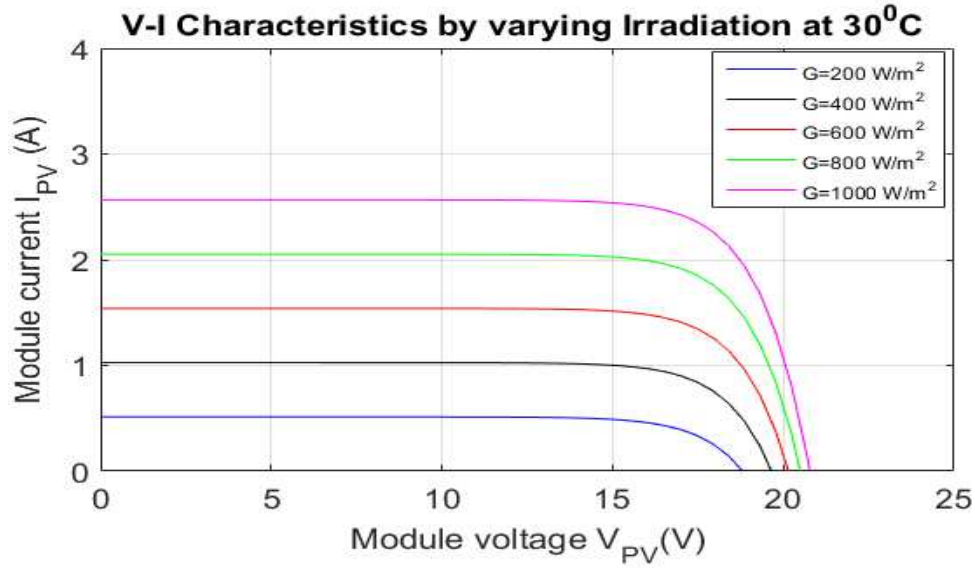

Figure 6.4: V_{PV} versus I_{PV} at constant ambient temperature (at 30ºC) while changing the irradiance.

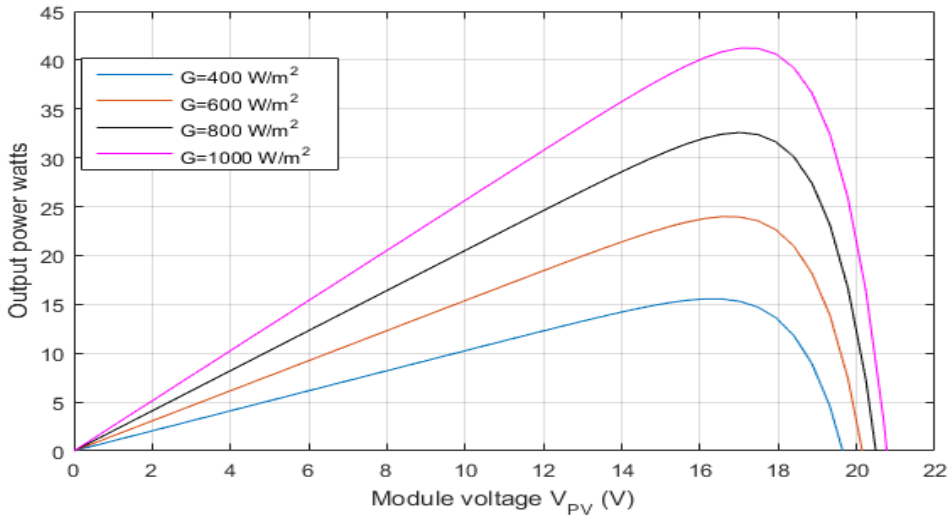

Figure 6.5: Plot of power curves at a constant temperature with varying irradiances.

Fig. 6.5 shows the output power variation of the module at varying irradiances. As it can be seen in Fig. 6.5. for a constant irradiance curve, there exists a maximum power point. By varying the module current I_{PV} or by varying the module voltage V_{PV} it is possible to extract maximum power from the PV module for certain irradiance. In literature, there have been many maximum power point tracking algorithms reported.

At constant irradiance of 1 kW/m^2 with varying ambient temperature the module voltage versus extracted power is given by Fig. 6.6.

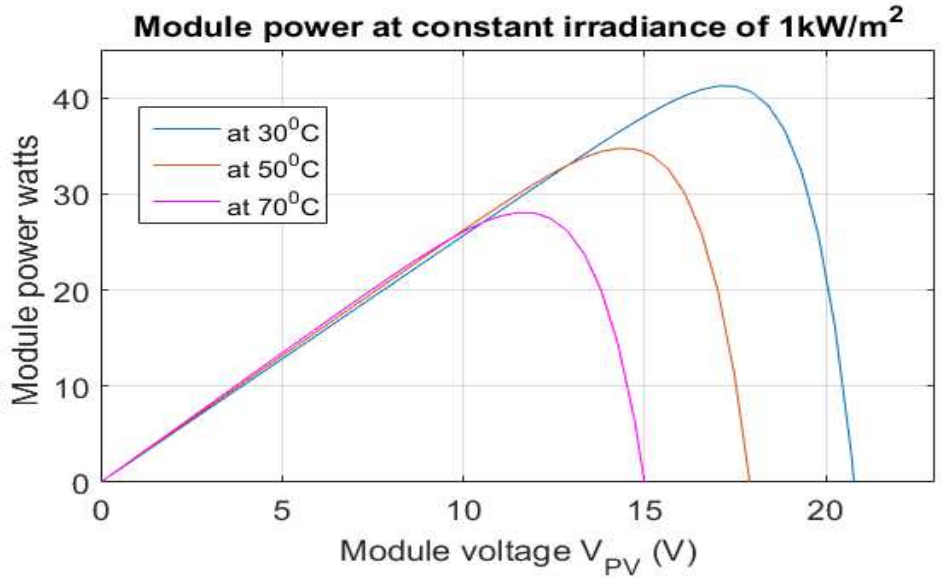

Figure 6.6: Module voltage V_{PV} versus extracted power at different temperatures keeping irradiance constant.

6.3. Maximum Power Point Tracking for a SPV Module

Perturb and Observe (P&O) is one of the commonly used tracking methods for searching the maximum power from solar arrays. It is an algorithm operates by perturbation (slight increase or decrease) of power with respect to current or voltage in the module. By using this algorithm, the program can track the maximum power point by increasing or decreasing the current or voltage by observing the earlier power in the array. P&O algorithm is known as a hill climbing method as it employs the method of increase decrease strategy to search the maximum point at the local maximum.

Incremental conductance (IC) method is an another method which is reported in the literature. In this method, a controller measures incremental changes in the current and voltage of the array to predict the effect of a voltage change. Though this method requires more computational time in the controller, it can track changing conditions more rapidly than the P&O method. Similar to the P&O algorithm, incremental conductance method also uses the oscillations near the maximum power point. This method utilises the incremental conductance (dI/dV) of the photovoltaic array to compute the sign of the change in power with respect to voltage, dP/dV (Bellia, et al., 2014). The incremental conductance method computes the maximum power point by comparison of the incremental conductance (I_Δ / V_Δ) to the array conductance (I / V). When these two are the same ($I / V = I_\Delta / V_\Delta$), the output voltage is the MPP voltage. The controller maintains this voltage until the irradiation changes and the process are repeated (Bellia et al., 2014) (note: I_Δ and V_Δ denotes the fractional changes of I and V). Other methods used for tracking the MPP are the current sweep and constant voltage methods, Short-Current Pulse Method, Temperature method etc. In literature, it is indicated that the P&O and IC algorithms are in general the most efficient of the analysed MPPT techniques (Faranda and Leva, 2008). Flow charts for both P&O and IC algorithms can be found in reference: Ishaque, et al., (2014).

The maximum power point tracking (MPPT) points for varying irradiances of 1000 W/m^2, 800W/m^2 and 400 W/m^2 in the same plot of module voltage V_{PV} versus I_{PV} are shown in Fig. 6.9. The MATLAB source code for the plot is given in Appendix B.

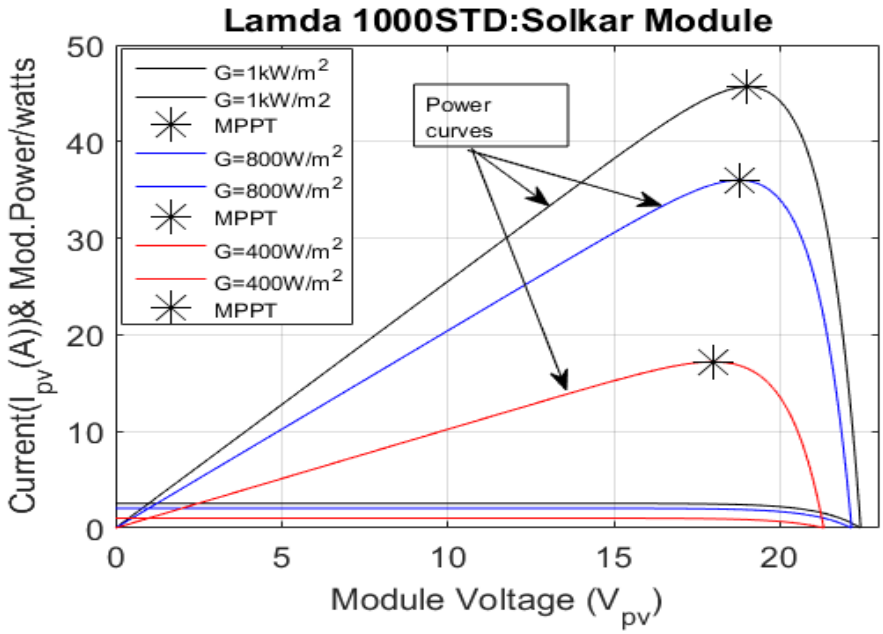

Figure 6.9: Maximum power point tracking (MPPT) points for varying irradiances.

The dynamic single PV cell model developed can be extended into a large PV array depending on the design requirements. The procedure is similar to the BP modelling method which was covered in Chapter 2. For high voltage requirements, the PV cells should be connected in series while the parallel connection is there for the high current requirement.

Summary

Introduction to the chemistry of complex raw materials used for SPV cell manufacturing was covered with special reference to polycrystalline and multicrystalline silicon. Photon energy in the sunlight was described relating to electron-hole pairs, N-type and P-type semiconductor materials in SPV arrays. Dynamic model for a single diode array was presented with its simulation characteristics. Maximum power point search algorithm was generated to search the MPP tracking system with the power versus module current characteristic plots. The dynamic model of the SPV array presented was very suitable to combine with the battery storage systems and with WTs to provide continuous power supply.

Chapter 7

Conclusion and suggestion for future work:

7.0. Conclusions

Modelling and control of renewable energy power conversion systems with battery storage units is a challenge for control engineers due to nonlinear nature of many parameters involved in every dynamic system. Dynamic models that represent PV, WT and BS systems are necessary for system analysis, controller development and testing prior to prototype construction.

An accurate, comprehensive, new dynamic Li-ion battery model has been developed. As Randle-Warburg circuit model was not sufficient to capture the nonlinearity of the battery cell chemistry and thus a modified nonlinear Randle-Warburg circuit model was developed. The model developed captures the entire dynamic characteristics of a battery for a wider range of non-linear open circuit voltage than the existing battery models found in literature. Simulation results of the model has shown that the battery open circuit voltage is at its highest value when the *SOC* is equal to 100%, which could discharge gradually down to zero voltage with simulation time or with the battery capacity. One such example can be shown by comparing the V_{bat} versus battery capacity shown in Fig. 2.2 in this thesis.

The cell model can be implemented with different capacities and parameters. The thermal model developed is an extension of the model developed in this thesis (research). which accommodates the reversible and irreversible heat effect within the battery cell and the ambient temperature changes. The following aspects of heat generation and effects have been included in the developed thermal model: activation energy (interfacial kinetics), concentration (species transport), and ohmic losses (Joule heating from movement of charged particles) to feedback data for simulation to the equivalent electrical circuit with a feedback iteration loop. The proposed model is capable of simulating the concentration polarisation and electrochemical polarisation separately. The temperature effect on activation, diffusion polarisation and due to different electrolyte chemistries is also included in the model with a new polynomial equation. The temperature effect on activation, diffusion polarization and due to different electrolyte

chemistries is modelled by the parameter $\Delta V_{Che}(T)$ which is a function of the temperature. The new polynomial Equation (2.19) given there presents the accurate variation of battery output voltage variation due to the effects of activation and diffusion polarisation due to different electrolyte chemistries than the existing battery models in the literature. The other new polynomial Equation (2.20) represents battery output voltage variation due to the amount of active material available in the electrodes which enriches additional accuracy to the model due to the unexpected accumulation of ions.

The accuracy and the validity of the model was tested with known experimental results and by comparing the data published in literature. The validity of the simulation model was confirmed not only for Li-ion batteries but also for Lead-acid, NIMH, Nickel-Cadmium and $LiMn_2O_4$ batteries.

The BP model developed in this thesis was a new model built from battery cell equivalent electrical circuit. Depending on the voltage/current requirement the number of cells connected in series/parallel could be calculated from the derived formula. The new mathematical formulation for the current and voltage division to each cell to form either series or parallel BPs for the simulation models has been presented with correct mathematical proof. The developed model was validated by simulating several multi-cell BP configurations in Simulink. The model is suitable for a range of series-parallel combinations of dissimilar individual cells with differing voltage outputs, due to a variety of physical reasons (Temperature, internal impedances, the initial state of charge of battery cells etc.). Novel application to SOC estimation was achieved by using the Kalman Filter application.

The six state input, state-space model of a HAWT comprising two-mass model of the gear changing mechanism, a hydraulic actuator, non-linear model of wind speed, doubly fed induction generator (DFIG) was given and analysed by transforming into linearized models where applicable.

7.1. Suggestions for Future Work

The dynamic electrochemical and thermal characteristics are different from the battery cell to a battery pack (BP). Cell level random variations of ageing and plating can substantially reduce the lifetime of the whole pack. The use of MPC and the novel use of wireless sensing and remote battery health monitoring systems have been considered as some of the solutions to

suppress the ageing and plating mechanisms of individual cells. This approach has been considered very effective to reconfigure the status of battery packs for urban running electric/hybrid electric vehicles. In this context, an accurate dynamic cell level battery model, as well as a complete BP model, is necessary for simulation research that involves designing battery management and monitoring systems. The same scenario is applicable to PV arrays for the stable output voltage. The major difficulty is the highly nonlinear characteristics of both battery parameters and PV parameters. Application of MPC is suggested for voltage balancing of BP and PV arrays. The model developed in this thesis considered the ageing partially as a capacity fading factor and for cycling, an empirical formula published in the literature was used. Although the cycling resistance can include ageing effects, the ageing effect due to repeated cycling and that due to the storage have not been considered separately as it would involve the study of organic electrolytes, insoluble protective films and progressive clogging of the micropores of the negative electrode by the passivation layer growth. Then the general energy balance equations used by Bernardi, Pawlikowski, and Newman applied earlier in this thesis to establish the battery cell temperature has to be modified, as the active surface area and the current density coefficients vary with time or cyclic time. In this scenario, the overall cell resistance increases with cycling, the lithium deposits on the anode like a plate and can rapidly increase the capacity decay. Future research is open in this context to develop a battery equivalent electrical circuit with sufficient experimental results. Literature review reveals that sizing and cost optimisation of hybrid WT/SPB/BS systems is a prospective area for research and development.

The life-cycle prediction life cycle analysis related to carbon footprint of battery manufacturing is another challenging task as the experimental work takes many years to complete. The chemical analysis is complicated as batteries have to undergo so many cycles under certain test procedures. Usually, in addition to non-destructive analysis manufactures use destructive analysis to investigate the chemistry of batteries. Careful disassembly is necessary to observe and analyse the internal battery materials.

Battery storage systems

Grand challenges ahead of battery storage systems or battery cells are to design battery cells capable of working at temperature ranges of -50ºC to 150ºC or even wider extents. Zebra batteries can work at temperatures over 270ºC as they use Sodium Nickel Chloride (NaNiCl). The cycle time of these batteries extends up to 4500 cycles at 80% depth of discharge. Zebra

batteries use plain salt and nickel as the raw materials for their electrodes. For the electrolyte, they use a combination of ceramic electrolyte and a molten salt Dustmann (2004). Operating temperature for molten salt should be greater than 160ºC for sodium ion to be conductive. The lowest temperature they have specified has been -40ºC (Kim et al., 2015) which is good up to certain extent for the applications closer to the North Pole and the South Pole. Different chemistries have been applied in the design and manufacture of Zebra batteries in Switzerland. Battery technology and the chemistry are challenging areas for the scientists to develop cost effective batteries which are suitable to operate at temperatures -150º to 150ºC which is an essential requirement for human settlement on the planet Mars.

Solar Panel Efficiency

Increasing the efficiency of PV cell is another challenge that design engineers and scientists face with. The average commonly available PV panels has the efficiency up to 15%. Special purpose expensive panels are there with the efficiency in the range of 40% -45%. An alternative approach is to design concentrated solar power technology (CSP) with multi-junction solar cells. The CSP plants have been operating in the US for more than 15 years without any fault and Australia, China, India are the other countries investing heavily in this area (CSP plants, 2016). Cost optimisation and effective design of such systems is another emerging area for researchers to investigate (Understand Solar, 2016).

Wind turbine control

Control systems design and power generation from floating offshore wind turbines is a promising area for research. Stability challenges are there for floating structures which provide sufficient buoyancy to support the weight of the turbine and to restrain pitch, roll, tilt and heave motions within acceptable limits.

Wind turbine manufacturers are currently focussed in the areas of changing aerodynamic properties to maximise the efficiency of the turbine blades using hydraulic actuators other than the traditional pitch motor. For example, micro-tabs and tiny valves to allow pressurized air to flow out of the blade may change the flow of the air across the blade, thus affecting the lift and drag coefficients and providing another possibility for control (Pao and Johnson, 2009).

Controller design for vibrating blades and limit the low-frequency motions of the tower is also considered at the development stage. Literature indicates that MPC controllers with fuzzy switching algorithms are well suited for all wind speed operating regions.

Results of MPC controller can be compared with the application of H_∞ controller and the standard PID controller to confirm the preferred results (which is already in this thesis but, exhaustive simulation tests are recommended for future research). Design and implementation of offshore floating oil rigs have proved the success of the technical challenges. However, the question remains unanswered regarding the economic viability of offshore floating wind turbines.

Appendix A

The Output Measurement Noise and the Augmented Model

This section briefly describes the formulation of A_m, B_m and the C_m matrices which is necessary for Chapter 3 and Chapter 4.

When designing MPC controllers, it is always necessary to measure one or more outputs at each computer iteration to manipulate the input signals or measurements. When measuring the output, it is impossible to avoid the noise. with the measurements and hence, there should be tolerances for the measurement noise. Though, our WT state space model described in Chapter 4, did not incorporate the noise term, it can be included in the system by converting the model into an *augmented system.* This disturbance noise in general, incorporated into MPC by adding a step input which enters the linear model through the state equation resulting in the augmented model leading to a higher order system. This technique is similar to reduce the noise by adding an integrator to a State-feedback control system.

Consider the total wind turbine plant that we have derived in Chapter 3,

$$A_m = \begin{bmatrix} 0 & 0.0010 & 0 & 0 & 0 & 0 \\ -3.1131 & -0.1004 & 0 & 0 & 0 & 0 \\ 0 & 0 & -0.0100 & 0 & 0 & 0 \\ 0.1440 & 0 & 0 & -0.0001 & 0.0000 & -0.0119 \\ 0 & 0 & -0.0001 & 0.0815 & -0.0010 & 8.1490 \\ 0 & 0 & 0 & 0.0010 & -0.0000 & 0 \end{bmatrix} *1.0e+03$$

$$B_m = \begin{bmatrix} 0 & 0 & 0 \\ 0 & 1 & 0 \\ 0 & 0 & 1 \\ 0.32 & 0 & 0 \\ 0 & 0 & 0 \\ 0 & 0 & 0 \end{bmatrix}$$

$$\text{and } C_m = \begin{bmatrix} 0 & 0 & 0 & 1 & 0 & 0 \\ 0 & 0 & 0 & 0 & 1 & 0 \\ 0 & 0 & 1/.1 & 0 & 1/.1 & 0 \\ 0 & 0 & 0 & 0 & 0 & 1 \end{bmatrix}$$

For a MIMO system, the state-space model with noise can be written as given next,

$$x_m(k+1) = A_m x_m(k) + B_m u(k) + B_d \omega(k) \tag{A.4.1}$$

$$y(k) = C_m x_m(k) \tag{A.4.2}$$

Where, $\omega(k)$ is an input disturbance assumed to be a sequence of integrated white noise and hence, the input noise is assumed to be with zero-mean white noise sequence represented by the equation,

$$\omega(k) - \omega(k-1) = \varepsilon(k) \tag{A.4.3}$$

The augmented model for the above total WT model can be written as given in Wand (2009),

$$\begin{matrix}\Delta x_m(k+1) \\ y(k+1)\end{matrix} = \begin{bmatrix} A_m & o_m^T \\ C_m * A_m & I_{q\times q}\end{bmatrix}\begin{bmatrix}\Delta x_m(k) \\ y(k)\end{bmatrix} + \begin{bmatrix} B_m \\ C_m B_m\end{bmatrix}\Delta u(k) + \begin{bmatrix} B_d \\ C_m B_d\end{bmatrix}\varepsilon(k) \tag{A.4.4}$$

$$y(k) = \begin{bmatrix} o_m & I_{q\times q}\end{bmatrix}\begin{bmatrix}\Delta x_m(k) \\ y(k)\end{bmatrix} \tag{A.4.5}$$

o_m matrix has the dimensions $= n_1 \times q$

q is the number of outputs and n_1 is defined as the number of states.

Output matrix has the dimensions of [$o_m^{'}$, eye(4)] = 4x10 (four rows and 10 columns)]

The augmented system matrices for the total WT model that was designed in Chapter 3 can be written as given below (n_1=6; q=4, o_m= zeros(6,4), $I_{q\times q}$ =eye(4,4)):

$$A = \begin{bmatrix} A_m & o_m^T \\ C_m A_m & I_{q\times q}\end{bmatrix}; B = \begin{bmatrix} B_m \\ C_m B_m\end{bmatrix}; \; C = \begin{bmatrix} o_m & I_{q\times q}\end{bmatrix} \tag{A.4.6}$$

C= [$o_m^{'}$ eye(4)]

ans = [0 0 0 0 0 0 1 0 0 0; 0 0 0 0 0 0 0 1 0 0; …

0 0 0 0 0 0 0 0 1 0; 0 0 0 0 0 0 0 0 0 1]

```
A=


  1.0e+04 *

         0    0.0001         0         0         0         0         0         0         0         0
   -0.3113   -0.0100         0         0         0         0         0         0         0         0
         0         0   -0.0010         0         0         0         0         0         0         0
    0.0144         0         0   -0.0000    0.0000   -0.0012         0         0         0         0
         0         0   -0.0000    0.0081   -0.0001    0.8149         0         0         0         0
         0         0         0    0.0001   -0.0000         0         0         0         0         0
    0.0144         0         0   -0.0000    0.0000   -0.0012    0.0001         0         0         0
         0         0   -0.0000    0.0081   -0.0001    0.8149         0    0.0001         0         0
         0         0   -0.0101    0.0815   -0.0010    8.1490         0         0    0.0001         0
         0         0         0    0.0001   -0.0000         0         0         0         0    0.0001
```

```
B=

ans=

    [ 0     0     0;    0   1.0000    0;   0     0   1.0000;  0.3200    0     0; . . .
      0     0     0;    0     0     0;   0.3200   0     0;      0     0     0; . . .
            0     0  10.0000;   0     0     0];
```

In the MATLAB script file given here $m1$ is defined as the size of q which is the number of state-space outputs and $n1$ is defined as the size of the state-space vector. MATLAB
The MATLAB program code given below will compute the same result for the augmented model.

MATLAB Script file to compute augmented matrices:

The Ad, Bd, Cd and Dd shown in the script file are discrete matrices and the A_e, B_e, and C_e are augmented matrices.

```
Am_4=-0.0734;
Ad=[0 1 0 0 0 0; -3.1131e+03 -2*55.794*0.9 0 0 0 0; 0 0 -1/0.1 0 0 0;...
   144  0   0  Am_4 1.4050e-05 -11.94;...
   0  0  -0.066  81.49  -.95   8.1490*10^3;0   0   0   1   -1/85 0];     % 8.1490e+03
Bd=[0   0   0;0  1  0;0 0 1; 0.32 0 0;0 0 0; 0 0 0];
Cd=[0   0   0   1   0   0; 0   0   0   0   1   0;0  0  1/.1  0 1/.1  0;... 0   0   0   0   0   1];
Dd=[zeros(4,3)]; n1=6; m1=4;% n1= number of states; m1=q;
[m1,n1]=size(Cd)
[n1,n_in]=size(Bd); A_e=eye(n1+m1,n1+m1)
A_e(1:n1,1:n1)=Ad; A_e(n1+1:n1+m1,1:n1)=Cd*Ad;
B_e=zeros(n1+m1,n_in)
B_e(1:n1,:)=Bd; B_e(n1+1:n1+m1,:)=Cd*Bd; C_e=zeros(m1,n1+m1);

C_e(:,n1+1:n1+m1)=eye(m1,m1)
```

MATLAB Script for the Cp_max and the b-optimum is given next:

```
clf
clear all
b=0:.01:1;
for j=1:length(b)
Cp(j)=0.5*(1-b(j).^2).*(1+b(j))
end
plot(b,Cp,'k')
[Cp_max,I]=max(Cp)
b(I)
xlabel('Interference parameter, b')
ylabel('Power coefficient, Cp)')
title('Plot of Cp versus b', 'Fontsize',12)
p=b(I); q=Cp_max
line([p p],[0 q],'marker','.','LineStyle','--')
line([0,p],[q q],'marker','.','LineStyle','--','Color','r')
text(p+.05,q+.05,'(b-optimum, Cp_max)')
%line([0,Cp_max],[b(I),Cp_max],'b','LineStyle','--')
```

MATLAB script file for a plot:

```
clf
plotyy(lamda_b0,cp_0,lamda_b0,Ct_beta_0);
[AX,H1,H2]=plotyy(lamda_b0,cp_0,lamda_b0,Ct_beta_0)
set(get(AX(1),'Ylabel'),'String','C_p values')
set(get(AX(2),'Ylabel'),'String','C_t values(torque coefficient)')
set(H1,'LineStyle','-')
set(H2,'LineStyle',':')
grid(gca,'minor')
```

MATLAB functions and the main program for the Stall control of WT and MPC controller

1

```
----------------------------------------------------
function [Cd, Cl]=Blade_CdCl(AR, Cdstall, Clstall, alphas, alpha_st)
Cd_max= 1.11+ 0.018*AR;
B1=Cd_max;
A1=B1/2;
d2r=pi/180;
alpha_stall=d2r*alpha_st;
alpha=d2r*alphas;
B2=(Cdstall-Cd_max*(sin(alpha_stall)^2))/cos(alpha_stall);
%na=length(alpha);
Cd= B1*sin(alpha).^2+ B2*cos(alpha);% (alpha=15 to 90)
A2=(Clstall-Cd_max*sin(alpha_stall)*cos(alpha_stall))*sin(alpha_stall)…
/(cos(alpha_stall)^2);
Cl=A1.*sin(2*alpha)+A2.*(cos(alpha).^2)./sin(alpha); % alpha 15 to90
```

2

```
%----------------------------------------------------
function bopt=control_demand(theta0, vw, ksidot, wr, R, model, Pd)
%theta=theta0;
options = optimset('Display','off','MaxFunEvals',50000,'MaxIter',50000);
theta_fit=fmincon(@(theta) PTCostFunction(theta,vw, ksidot, wr, R, model,
Pd),theta0,[],[], [], [],0,18,[],options);
bopt=theta_fit;
```

```
                              3
-------------------------------------------------
function [Phi_Phi,Phi_F,K]=mpcgmo(A,B,C,Nc,Np)
AB=B;
CA=C*A;
F=CA;
nc=size(B,2);
row=B;
   for j=2:Nc
      row=[row 0*B];
   end
   phi=C*row;
   for i=2:Np
      AB=A*AB;
      row=[AB row(:,1:nc*Nc-nc)];
      phi=[phi;C*row];
      F=[F;CA*A];
   end
   %A
   %B
   %C
   %tem=[C*B 0*C*B 0*C*B;
   %   C*B C*A*B 0*C*B;
   %   C*B C*A*B C*A*A*B]
   %phi
  Phi_Phi= phi'*phi;
  Phi_F= phi'*F;
K=Phi_Phi\Phi_F;
```

4.

```
---------------------------------------------------------
function cost=PTCostFunction(theta,vw, ksidot, wr, R, model, Pd)
Prr =turbine_power(theta, vw, ksidot, wr, R, model);

%if Prr<Pd
cost=0;
%else
err=(Prr-Pd);
if Pd>0
cost=abs(err)/Pd;
else
cost=abs(err);
end
cost=cost*cost;
%end
```

```
                                5
-------------------------------------------------
function Cp=Stalled_blade_cp(eps, iter, N, R, cr, ltsr, Vf, pitch, astall, CD0, Clstall, Cdstall)
pi=3.141592653589;
rads=pi/180;
TipicalR=20.3;
root=4.5;
sc=R/TipicalR;
cbar=cr*R;
rr=[root*sc:sc:R];% radius of element
rr=[rr R];
nr=size(rr,2);
for i=1:nr
r(i)=rr(nr-i+1);
end
cn=sc*[0.265 0.545 0.705 0.806 0.881 0.955 1.026 1.095 1.163 1.229 1.294…
 1.356 1.42 1.481 1.54 1.597 1.63]/cbar;% chord of element
nc=size(cn,2);
gamma=[0.02 0.05 0.14 0.33 0.77 1.36 2.02 2.6 3.15 4 4.85 5.85 7.45…
 10.05 13 16.3 20]-4;% check 3.15 % aerofoil inlet angle
ng=size(gamma,2);
%nr=size(r,2)
rn=r/R;
%Cp=wtbdcp(N, R, CD0, cbar, ltsr, Vf, rn, cn, iter, eps);
Cp=wtbdan(N, R, CD0, cbar, ltsr, Vf, rn, Cdstall, Clstall, pitch,gamma,…
 astall, cn, iter, eps);
```

6

```
function Prr =turbine_power(theta, vw, ksidot, wr, R, model)
pi=4*atan(1.);% pi=3.14159265358979323846264 3;
d2r=pi/180;
H=90;   % Tower Heightpitch=0;
astall=18;    % in degrees
Clstall=1.06;Cdstall=.1;  CD0=0.007;eps=0.002;iter=200; % Blade data N, nelem,
% R, cr,  ltsr, VF, % rn, cn, gamma
N=3;  nelem=17;    % no of blades %R=65; % blade radius
cr=0.0803;  tsr=8;% lambda - tip speed ratio=Omega*R/Vi
Vf=7; %inflow velocity in m/s
rho=1.225-H*1.194e-04; %kg/m3 density of air
Lambda=vw/(wr*R); % ETH definition
Lambda=1/Lambda; % Our Lambda %Lambda=8.5;
beta=theta; %if beta>0.1920 beta=0.1920; end %if beta<0 beta=0;
end%c1=0.5;c2=116;c3=0.4;c4=0;c5=5;c6=21;c7=0.08;c8=0.035;
if model>-1
if model==0
coefs=[0.5;116;0.4;0;5;21;0.08;0.035];
end
c1=coefs(1);c2=coefs(2);c3=coefs(3);c4=coefs(4);c5=coefs(5);c6=coefs(6);c7=coefs(7);…
c8=coefs(8);
gami=(1/(Lambda+c7*beta))-c8/(1+beta*beta*beta);
gama=1/gami;   %if beta<astall
Cp=c1*(c2*gami-c3*beta-c5)*exp(-c6*gami); %end
else
Cp=Stalled_blade_cp(eps, iter, N, R, cr, ltsr, Vf, beta, astall, CD0, Clstall, Cdstall) ;
end    %Cp=0.38; % Ft=0.5*rho*pi*R*R*Ct*vw^2;
% Pr=0.5*rho*pi*R*R*Cp*vw^3;
vwr=vw-ksidot; Prr=0.5*rho*pi*R*R*Cp*vwr^3;
%g=-(c7/(Lambda+0.08*beta)^2)+3*c8*beta*beta/((1+beta*beta*beta)^2);
%dCp=c1*(c2*g*(1-c6*gami)-c3*(1-c6*beta*g)+c6*c5*g)*exp(-c6*gami);
%dPrr=0.5*rho*pi*R*R*dCp*vwr^3;
```

```
close all
pi=4*atan(1.);% pi=3.14159265358979323846264 3;
nclp=1;
rads=pi/180; N=10000; dt=0.002; ns=8;%????
R=63;vw=8;% 8-18
Jr=5.9154e7;% kgm^2
Jg=500;%kgm^2
mtow=4.2278e05;%Kg
ktow=1.6547e6;% Nm/rad
dtow=2.0213e3; % kgm^2/rad/s
wntow=sqrt(ktow/mtow); %??????
zetas=dtow/(2*mtow*wntow); %??????
wn=0.88; % rads/s,
zeta=0.9;Ng=97;Ds=8.3478e07;% kgm^2/rad/s
Ks=8.7354e08;% Nm/rad;
Ttou=0.1;%sec
Pe_nom=5e06;
wg_nom=122.91;% rads/sec
wg_min=70.16;
wr_nom=1.26;
theta_min=0;
theta_max=.4365;% Earlier it was degrees 25=.4365 rad
thetadot_min=-.1396;% I changed it to radians degs/s = -.1396
thetadot_max=.1396;
% theta_max=25;% degrees 25=.4365 rad
% thetadot_min=-8;% degs/s = -.1396
% thetadot_max=8;%degs/s  degrees 8=.1396
thetaref=0;
region=3;
x0=[wr_nom wg_nom 0 0 0 0.05 0 0];
Xf=[];time=[];
for k=1:N
  kstar=k-100*floor(k/100) ;
  if kstar==0
      k;
  end
```

```
tspan=[(k-1)*dt k*dt];
  options = odeset('RelTol',1e-4,'AbsTol',1e-5);
  if k>300
     options = odeset('RelTol',1e-01,'AbsTol',1e-3);
  end
    % ode23, ode45, ode113, ode15s, ode23s, ode23t, ode23tb
    %[A Bfbk Bdis Bgen]=vs_hawt_linear_eqns(xe, R, vw, Jr, Jg,…
 wntow, wn, zetas, zeta, mtow, Ng, Ds, Ks, Ttou)
    % this from
  [tf, xf]=ode45(@(t,x)vs_hawt_eqns(t,x, R, vw,Jr,Jg,wntow,wn,…
zetas,zeta, mtow,Ng,Ds, Ks, Ttou, Pe_nom,region,thetaref, 0*x',0*x),tspan,x0);
  [nt nj]=size(xf);
  x0=xf(nt,:);
  x0=x0';
  time=[time tf(nt)];
  Xf=[Xf x0];
end
% xe(1)=0;
% xe(2)=0;xe(3)=0;xe(4)=0;
% xe(5)=0;xe(6)=0;
% xe(7)=0;xe(8)=0;
xe=x0;
[Awt Bfbk Bdis Bgen Ar Bfbkr]=vs_hawt_linear_eqns(xe, R, vw, Jr, Jg,…
 wntow, wn, zetas, zeta, mtow, Ng, Ds, Ks, Ttou);
% Use A, Bffbk in your mpcg programme
awt=Ar;
atwt=Ar';
ranb=rank(ctrb(awt,Bfbkr))
Cwt=[1 0 0 0 0 0 0 0;
    0 0 0 0 1 0 0 0;
    0 0 0 0 0 0 1 0;
    0 0 0 0 0 0 0 1];
ranc=rank(ctrb(atwt, eye(3)))
Ard=eye(3)+Ar*dt;
[Phi_Phi,Phi_F,K]=mpcgmo(Ard,Bfbkr,eye(3),20,20);
Kmpc=K(1,:)
awt=Awt;
```

```
atwt=Awt';
Bfb=[Bdis Bfbk Bgen];
nc=size(Bfb, 2);
ranb=rank(ctrb(awt,Bfb))
ranc=rank(ctrb(atwt,Cwt'))
Awtd=eye(8)+Awt*dt;
[Phi_Phi,Phi_F,Kf]=mpcgmo(Awtd,Bfb,Cwt,20,20);
Kmpcf=Kf(1:nc,:)
figure(1)
plot(time,Ng*Xf(1,:),'m-', 'LineWidth',0.5,'MarkerSize',2)
   hold on
plot(time,Xf(2,:),'b-.', 'LineWidth',0.5,'MarkerSize',2)
figure(2)
plot(time,Xf(8,:),'m-', 'LineWidth',0.5,'MarkerSize',2)
   hold on
figure(3)
plot(time,Xf(1,:)-Xf(2,:)/Ng,'m-', 'LineWidth',0.5,'MarkerSize',2)
hold on
thetaref=0;
region=3;
Kfbk=Kmpcf(2,:);
Kfbk(1,1:7)=Kmpcf(2,1:7);
xin=xe;
if nclp~=0
x0=[wr_nom wg_nom 0 0 0 0.05 0 0];
Xf=[];time=[]; betad=[];theta0=0.0;Prrclp=[];Prrop=[];
for k=1:N
   x0i=x0;
   x0i(6)=theta0;
 kstar=k-2000*floor(k/2000) ;
 if kstar==0
    k
 end
```

```
tspan=[(k-1)*dt k*dt];
  options = odeset('RelTol',1e-4,'AbsTol',1e-5);
  if k>300
     options = odeset('RelTol',1e-01,'AbsTol',1e-3);
  end
    % ode23, ode45, ode113, ode15s, ode23s, ode23t, ode23tb
    %[A Bfbk Bdis Bgen]=vs_hawt_linear_eqns(xe, R, vw, Jr, Jg, wntow, wn, zetas, zeta, mtow,
Ng, Ds, Ks, Ttou)
    % this from
  [tf, xf]=ode45(@(t,x)vs_hawt_eqns(t,x, R, vw,Jr,Jg,wntow,wn,zetas,. . .
   zeta, mtow,Ng,Ds, Ks, Ttou, Pe_nom,region,thetaref,Kfbk,xin),tspan,x0i);
  [nt nj]=size(xf);
  x0=xf(nt,:);
  x0=x0';
  time=[time tf(nt)];
  Xf=[Xf x0];
  model=-1; %=-1 for stall control; 0, 1, 2 for other Cp models
  %model=0;
  P_limit=  0.0e+06;
  bopt=control_demand(theta0, vw,x0(5), x0(1), R, model, P_limit);
  %theta0=bopt;
  betad=[betad bopt];
  prrc =turbine_power(0, vw, x0(5), x0(1), R, model);
  Prrop=[Prrop prrc];
  prrc =turbine_power(bopt, vw, x0(5), x0(1), R, model);
  Prrclp=[Prrclp prrc];
end
end
```

```
figure(1)
plot(time,Ng*Xf(1,:),'r--', 'LineWidth',0.5,'MarkerSize',2)

plot(time,Xf(2,:),'k-.', 'LineWidth',0.5,'MarkerSize',2)
   grid on
legend('Ng*wr-open loop','wg-open loop', 'Ng*wr-closed loop','wg-closed loop')
ylabel('w')
xlabel('Time')
title('HAWT (Wind Turbine) Response Speeds')
figure(2)
plot(time,Xf(8,:),'r-', 'LineWidth',0.5,'MarkerSize',2)
   grid on
legend('Open loop', 'Closed loop')
ylabel('Tg')
xlabel('Time')
title('HAWT (Wind Turbine) Response Torque')
figure(3)
plot(time,Xf(1,:)-Xf(2,:)/Ng,'r-', 'LineWidth',0.5,'MarkerSize',2)
grid on
legend('Open loop', 'Closed loop')
ylabel('Twist rate')
xlabel('Time')
title('Wind Turbine Rotor Twist Rate')
figure(4)
plot(time,betad,'m-', 'LineWidth',0.5,'MarkerSize',2)
   grid on

ylabel('Theta in degrees')
xlabel('Time')
title('Demanded Blade Angle')
```

```
figure(5)
plot(time,Prrop,'b-', 'LineWidth',0.5,'MarkerSize',2)
hold on
plot(time,Prrclp,'m-', 'LineWidth',0.5,'MarkerSize',2)
   grid on
legend('with Blade fixed', 'with Blade feedback')
ylabel('Power Output')
xlabel('Time')
title('Closed Loop Power Output')
```

```
                                    7
function xdot=vs_hawt_eqns(t,x, R, vw, Jr, Jg, wntow, wn, zetas, zeta, mtow, . . .
Ng, Ds, Ks, Ttou, Pe_nom, region,thetaref, Kfbk,xin)
pi=4*atan(1.);% pi=3.14159265358979323846264 3;
wr=x(1);wg=x(2);delta=x(3);ksi=x(4);ksidot=x(5);theta=x(6);thetadot=x(7);Tg=x(8);
wg_min=70.16;  wr_nom=1.26;
H=90;% Tower Height
rho=1.225-H*1.194e-04; %kg/m3 density of air
Lambda=vw/(wr*R); % ETH definition
Lambda=1/Lambda; % Our Lambda
%Lambda=8.5;
beta=theta*180/pi; model=0;
if model==0
coefs=[0.5;116;0.4;0;5;21;0.08;0.035];
end
c1=coefs(1);c2=coefs(2);c3=coefs(3);c4=coefs(4);c5=coefs(5);c6=coefs(6);
c7=coefs(7);c8=coefs(8);
gami=(1/(Lambda+c7*beta))-c8/(1+beta*beta*beta);
gama=1/gami;
%if beta<astall
Cp=c1*(c2*gami-c3*beta-c5)*exp(-c6*gami);
```

```
%Cp=0.38;
Ct=0.5;
% Ft=0.5*rho*pi*R*R*Ct*vw^2;
% Pr=0.5*rho*pi*R*R*Cp*vw^3;
vwr=vw-ksidot;
Ftr=0.5*rho*pi*R*R*Ct*vwr^2;
Prr=0.5*rho*pi*R*R*Cp*vwr^3;
Tg_nom=Prr/(Ng*wr_nom);
if wr>0 Tg_nom=Prr/(Ng*wr);end
Pg_nom=Prr;
if Pg_nom>Pe_nom
if wr>0    Tg_nom=Pe_nom/(Ng*wr);end
   Pg_nom=Pe_nom;
End
if region<3
   Tgref=Tg_nom;
elseif wg>wg_min
   Tgref=Pg_nom/wg;
elseif wg>0
   Tgref=Pe_nom/wg_min;
else
   Tgref=Tg_nom;
end
%states=[wr wg delta(shaft twist) towe-disp
% Closed loop case
thetaref=thetaref-Kfbk*(x-xin);
xdot1=((Prr/wr)-Ds*(wr-wg/Ng)-delta*Ks)/Jr; %eq.1
xdot2=0;
if wg>wg_min
xdot2=( wr*Ds/(Ng)- wg*Ds/(Ng^2)+delta*Ks/Ng-Tg)/Jg  ;  %eq.2
end
xdot3=wr-wg/Ng;
xdot4=ksidot;
Dt=2*zetas*wntow;Ktow=mtow*wntow*wntow;
xdot5=-(Ktow*ksi+Dt*ksidot-Ftr)/mtow;     % ksi equaton
xdot6= thetadot;
```

```
xdot7= -(wn*wn)*(theta-thetaref)-2*zeta*wn*thetadot ;% theta Equation
xdot8=-(1/Ttou)*(Tg-Tgref);
xdot=[xdot1 xdot2 xdot3 xdot4 xdot5 xdot6 xdot7 xdot8]';
```

8

```
function Cp=wtbdan(N, R, CD0, cbar, ltsr, Vf, rn, Cdstall, Clstall, pitch, . . .
gamma, astall, cn,iter, eps )
Omega=ltsr*Vf/R;
nr=length(rn);
nar=floor(0.5*nr);
r=rn*R;
c=cn*cbar;
sigmab=N*c./(2*pi*r);% solidity ratio
lar=Omega*r/Vf;
ti=atan(1./lar);
beta=2*ti/3;
a=0;
ad=0;
d2r=pi/180;
for jj=1:iter
inci=beta-gamma*d2r-pitch*d2r;
if inci<astall
CL=2*pi*sin(inci);
%CL=2*pi*inci;
%sb=sin(beta); cb=cos(beta);
%CL=4.*sb.*(cb-lar.*sb)./(sigmab.*(sb+lar.*cb));
CD=CD0;
else
   % stalled
   [CD, CL]=Blade_CdCl(rn(nar), Cdstall, Clstall, inci, astall);
   %CL=2*pi*sin(inci);
   %CD=CD0;
end
```

```
sb2=4*sin(beta).^2;
Cn=sigmab.*(CL.*cos(beta)+CD.*sin(beta));
Ct=sigmab.*(CL.*sin(beta)-CD.*cos(beta));
%sbcb=4*sin(beta).*cos(beta);
%cbcb=4*cos(beta).*cos(beta);
sbcb=4*sin(beta).*cos(beta);
a0=a; ad0=ad; a=1./(1+(sb2./Cn));
ad=1./((sbcb./Ct)-1);
%ti=atan(1./lar);
beta=atan((1-a)./((1+ad).*lar));
norma=norm(a-a0)+norm(ad-ad0);
if norma<eps break;end
end
nr=size(r,2);
ltip=lar(1);%lroot=lar(nr);
Cp=0;
for i=1:nr-1
dla=lar(i)-lar(i+1);
sigav=(sigmab(i)+sigmab(i+1))/2;
CLav=(CL(i)+CL(i+1))/2;
aav=0.5*(a(i)+a(i+1));
bav=0.5*(beta(i)+beta(i+1));
cdr=0.5*(CD/CL(i)+CD/CL(i+1));
larav=0.5*(lar(i)+lar(i+1));
Cp=Cp+(2/(ltip*ltip))*sigav*CLav*((1-aav)^2)*(1/sin(bav))*(1-
cdr*cot(bav))*larav*larav*dla;
end
```

```
9

function [A Bfbk Bdis Bgen Ar Bfbkr]=vs_hawt_linear_eqns(xe,. . .
 R, vw, Jr, Jg, wntow, wn, zetas, zeta, mtow, Ng, Ds, Ks, Ttou)
%wg= gene shaft speed, wr= rotor speed, gear ratio= Ng , ..
%wn= natural
%frequency of actuator, teta is the actual pitch angle tetaref=
%demandedpitch angle
%
pi=4*atan(1.);% pi=3.14159265358979323846264 3;
% x(1)=8.5;x(2)=122; x(3)=-100; x(4)=.9;x(5)=.2;x(6)=.2
% x(7)=.2;x(8)=12000;
% wr=8.5;
wr=xe(1);
wg=xe(2);delta=xe(3);ksi=xe(4);
ksidot=xe(5);theta=xe(6);
thetadot=xe(7);Tg=xe(8);
H=90;% Tower Height
rho=1.225-H*1.194e-04; %kg/m3 density of air
Lambda=vw/(wr*R); % ETH definition
Lambda=1/Lambda; % Our Lambda
%Lambda=8.5;
beta=theta*180/pi;
model=0;
if model==0
coefs=[0.5;116;0.4;0;5;21;0.08;0.035];
end
c1=coefs(1);c2=coefs(2);c3=coefs(3);c4=coefs(4);c5=coefs(5);
c6=coefs(6);c7=coefs(7);c8=coefs(8);
gami=(1/(Lambda+c7*beta))-c8/(1+beta*beta*beta);
gama=1/gami;
%if beta<astall
Cp=c1*(c2*gami-c3*beta-c5)*exp(-c6*gami);
%c1=0.5;c2=116;c3=0.4;c4=0;c5=5;c6=21;c7=0.08;c8=0.035;
```

```
%Cp=0.38;
g=-(c7/(Lambda+c7*beta)^2)+3*c8*beta*beta/((1+beta*...
beta*beta)^2);
dCp=c1*(c2*g*(1-c6*gami)-c3*(1-c6*beta*g)+c6*c5*g)*exp(-c6*gami)
Ct=0.5;
% Ft=0.5*rho*pi*R*R*Ct*vw^2;
% Pr=0.5*rho*pi*R*R*Cp*vw^3;
vwr=vw-ksidot;
%Ftr=0.5*rho*pi*R*R*Ct*vwr^2;
Prr=0.5*rho*pi*R*R*Cp*vwr^3;
dPrr=0.5*rho*pi*R*R*dCp*vwr^3;
%xdot1=((Prr/wr)-Ds*(wr-wg/Ng)-delta*Ks)/Jr; %eq.1
%xdot2=( wr*Ds/(Ng)- wg*Ds/(Ng^2)+delta*Ks/Ng-Tg)/Jg ; %eq.2
%xdot3=wr-wg/Ng;
%xdot4=ksidot;
Dt=2*zetas*wntow;
Ktow=mtow*wntow*wntow;
%xdot5=-(Ktow*ksi+Dt*ksidot-Ftr)/mtow; % ksi equaton
%xdot6= thetadot;
%xdot7= -(wn*wn)*(theta-thetaref)-2*zeta*wn*thetadot ;%theta
%xdot8=-(1/Ttou)*(Tg-Tgref);
% xdot=[xdot1 xdot2 xdot3 xdot4 xdot5 xdot6 xdot7 xdot8]';
if wr~=0
a11=-(Prr/((wr^2)*Jr))-(Ds/Jr);
a16=(dPrr/(wr*Jr));
else
a11=-(Ds/Jr);
a16=0;
end
%states=[wr wg delta tower_disp tower_vel theta theta_dot Tg]
A=[a11 Ds/(Ng*Jr) -Ks/Jr 0 0 a16 0 0;
Ds/(Ng*Jg) -Ds/(Ng^2)/Jg Ks/(Ng*Jg) 0 0 0 0 -1/Jg;
1 -1/Ng 0 0 0 0 0 0;...
```

```
0 0 0 0 1 0 0 0;
0 0 0 -Ktow/mtow -Dt/mtow 0 0 0;
0 0 0 0 0 0 1 0;
0 0 0 0 0 -wn*wn -2*zeta*wn 0;
0 0 0 0 0 0 0 -(1/Ttou)];

B=[zeros(4,3);[Ktow/mtow 0 0;0 0 0; 0 wn*wn 0; 0 0 -(1/Ttou)]];
Bfbk=B(:,2);
Bdis=B(:,1);
Bgen=B(:,3);
Ar=[a11 a16 0;
   0    0   1
   0 -wn*wn -2*zeta*wn];
Bfbkr=[0;0;wn*wn];
```

Appendix B

Computing Toeplitz Matrix ϕ from a MATLAB Function:

The following program code calculates the Toeplitz matrix ϕ and the $\phi^T\phi$ matrix:

```
function [Phi_Phi,Phi_F,K]=MPC_Attempt07_06(A,B,C,Nc,Np)
AB=B;
CA=C*A;
F=CA;
nc=size(B,2)
row=B;
   for j=2:Nc  %
      row=[row 0*B];
   end
   phi=C*row;
   for i=2:Np-1 % earlier Np
      AB=A*AB;
      row=[AB row(:,1:nc*Nc-nc)];
      phi=[phi;C*row];
      F=[F;CA*A];
   end
  Phi_Phi= phi'*phi;
  Phi_F= phi'*F;
%K=Phi_Phi\Phi_F; Earlier
K=(inv(Phi_Phi)+1)*Phi_F
```

From the function MPC_Attempt07_06(A,B,C,Nc,Np), K_{mpc} is evaluated and the results have been used to obtain the closed-loop responses.

The following MATLAB Script can activate the Bode Plot:

```
model = 'syncbuck_OL_2FigMatFunct'
io=getlinio(model)
op=operspec(model)
op=findop(model, op)
ssm= linearize(model, op, io)
ltiview('bode', ssm)
```

MATLAB Script files for PV Cells and Arrays. MATLAB script that can be used to plot the output voltage against the output current under varying temperature.

```
clear all;
clc
rs=0.1;            %Rs is the series resistance of a PV module
np=1;              %Np is the number of cells connected in parallel
ns=36;             %Ns is the number of cells connected in series
voc=21.24;         %vpv=voc
iscr=2.55;         %ISCr is the PV module short-circuit current at 25 C
                   %and 1000 W/m2 = 2.55A
Tr=298;            %Tr is the reference temperature = 298 K
a=1.6;b=1.6;       %A = B is an ideality factor = 1.6
k=1.3805e-23;      %k is Boltzman constant = 1.3805 × 10-23 J/K
q=1.6e-19;         %q is Electron charge = 1.6 × 10-19 C
ki=0.0017;         %Ki is the short-circuit current temperature
                   %co-efficient at ISCr = 0.0017A /0C
lamda=1000;        %is the PV module illumination (W/m2) = 1000W/m2
ego=1.1;           %Ego is the band gap for silicon = 1.1 eV
 Top=300;          %Top is the module operating temperature in Kelvin
iph=(iscr+ki*(Top-298))*lamda/1000; %Iph is the light generated current in
                          %a PV module (A): The current source
                          %Iph represents the cell photocurrent
```

```
m=(q*voc)/(ns*a*k*Top);
irs=iscr/(exp(m)-1);     %Module reverse saturation current
io=irs*((Top/Tr)^3)*exp((q*ego/b*k)*(1/Tr-1/Top)); %Io is the PV module
                                    %saturation current (A)
ipv=2.5;           %Ipv is output current of a PV module (A)
vpv=0:1:23;      %Vpv is output voltage of a PV module (V)
ipv=zeros(size(vpv));
for i=1:length(vpv)
  ipv(i)=np*iph-np*io*(exp(((q*(vpv(i)+ipv(i)*rs)/(ns*k*a*Top)))-1));
end
figure(1)
set(gcf,'Color', 'w')
plot(vpv,ipv)
xlim([0 25])
ylim([0 3])
xlabel('Module Voltage (Vpv)')
ylabel('Module Current (Ipv)')
title('Power curve from Matlab at Lamda =1000:Solkar Module')
```

MATLAB source code for the MPPT is given below:

```
% Matlab code used to plot the output voltage against the output current
% under varying temperature conditions.
clear all
imp=7.61;       % array current at maximum power point;it is a constant
vmp=26.3;       %array voltage @ MPP. taken as const temporarily
pmax_e=vmp*imp;  % max experimental power; factory defined max. power
rs=0.1;            %Rs is the series resistance of a PV module
np=1;              %Np is the number of cells connected in parallel
ns=36;             %Ns is the number of cells connected in series
voc=21.24;          %vpv=voc
iscr=2.55;         %ISCr is the PV module short-circuit current at 25 C
                %and 1000W/m2 = 2.55A
Tr=298;            %Tr is the reference temperature = 298 K
a=1.3;b=1.3;       %A = B is an ideality factor = 1.6
k=1.3805e-23;       %k is Boltzman constant = 1.3805 × 10-23 J/K
```

```
q=1.6e-19;          %q is Electron charge = 1.6 × 10-19 C
ki=0.0017;          %Ki is the short-circuit current temperature
            %co-efficient at ISCr = 0.0017A /0C
            %lamda=1000;%is the PV module illumination
            %(W/m2) = 1000W/m2
lamda=400;
ego=1.1;            %Ego is the band gap for silicon = 1.1 eV
Top=300;            %Top is the module operating temperature in Kelvin
iph=(iscr+ki*(Top-298))*lamda/1000; %Iph is the light generated current in
                            %a PV module (A): The current source
                            %Iph represents the cell photocurrent
m=(q*voc)/(ns*a*k*Top);
irs=iscr/(exp(m)-1);            %Module reverse saturation current
io=irs*((Top/Tr)^3)*exp((q*ego/b*k)*(1/Tr-1/Top)); %Io is the PV module
                                    %saturation current (A)
ipv=0;%2.5;           %Ipv is output current of a PV module (A)
vpv=0:.1:23;        %Vpv is output voltage of a PV module (V)
ipv=zeros(size(vpv));
index=0;% initialize index
p=zeros(size(vpv));
for i=1:length(vpv)
  ipv(i)= np*iph-np*io*(exp(((q*(vpv(i)+ipv(i)*rs)/(ns*k*a*Top)))-1));
  p(i)=ipv(i)*vpv(i)
  [pmax_m,index]= max(p) % find the maximum power and index of the array
  error=abs((pmax_m-pmax_e)); % finds the error between exp and model
  v_atmaxp=vpv(index)
  i_at_max=ipv(index)
end
figure(1)
set(gca,'fontsize',14)
set(gcf,'Color', 'w')
plot(vpv,ipv,'r')
hold on
```

```
xlim([0 23])
ylim([0 50])
grid on
xlabel('Module Voltage (V_p_v)','fontsize',14)
ylabel('Current(I_p_v(A))& Mod.Power/watts','fontsize',14)
title('Lamda 1000STD:Solkar Module')
plot(vpv,p,'r')
plot(vpv(index),pmax_m,'k*','MarkerSize',16)
hold on
```

Simulink model for the dynamic PV cell model is shown in Fig. B.1: Simulation results were tested for SOLKAR 36W PV model.

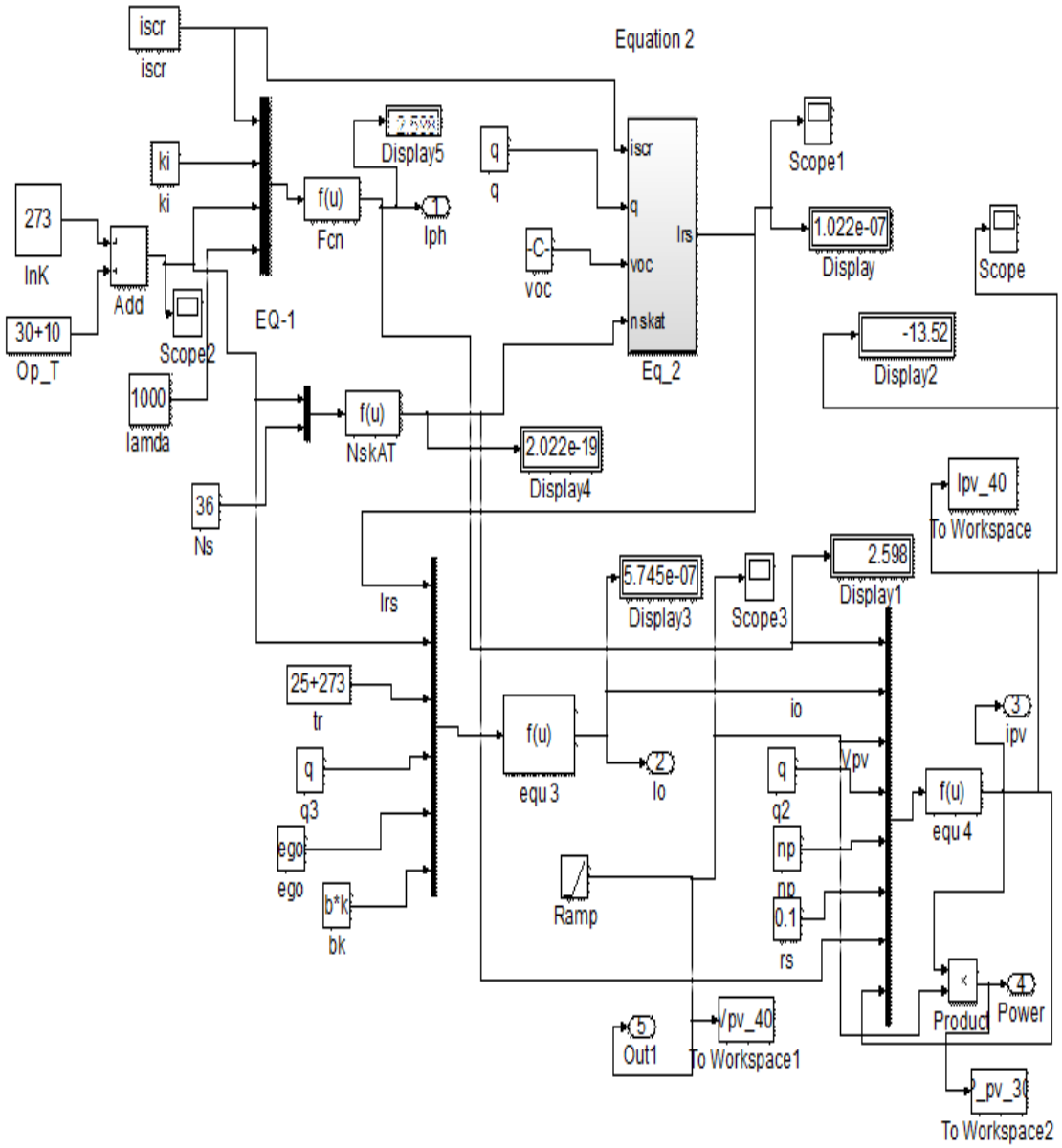

Figure B.1: Simulink block diagram of the PV module (SOLKAR 36W PV Module).

Appendix C

Discretization of continuous time state space models

Continuous time state space models can be discretized by using Euler forward method (equation 2.40) or by using Euler backward method (equation 2.38).

Euler forward method:

$$\dot{x} = \frac{x(k+1) - x(k)}{T_s} \tag{2.38}$$

Euler backward method:

$$\dot{x} = \frac{x(k) - x(k-1)}{T_s} \tag{2.39}$$

Where, T_s is the sampling time.

For state space system:

$$\begin{aligned} \dot{x} &= Ax + Bu \\ y &= Cx + Du \end{aligned} \tag{2.40}$$

Using equation 2.40 we can write:

$$\begin{aligned} \frac{x_{k+1} - x_k}{T_s} &= Ax_k + Bu_k \\ y_k &= Cx_k + Du_k \end{aligned} \tag{2.41}$$

From equation (2.41) we can write:

$$\begin{aligned} x_{k+1} &= \underbrace{(I + T_s A)}_{A_d} x_k + \underbrace{T_s B}_{B_d} u_k \\ y_k &= \underbrace{C}_{C_d} x_k + \underbrace{D}_{D_d} u_k \end{aligned} \tag{2.42}$$

Where, I is the identity matrix.

Using MATLAB we can write the script file in 3 short lines: $I = eye(2); A_d = I + T_s * A;$ $B_d = T_s * B;$ Where, T_s is the sampling time.

Kalman Filter:

A Kalman filter (KF) is popular in space applications and in circumstances where we cannot take direct measurements. It gives accurate measurements for uncertain observations. The KF is an optimal estimator and is recursive and therefore the new measurements can be processed as they arrive. Optimality is arrived by assuming if all noise present is *Gaussian* then the KF minimises the mean square error of the estimated parameters.

Given the mean and standard deviation of the noise, the Kalman filter is the best linear estimator. It can be applied to nonlinear situations and the estimators still can give you better results.

Generally, the *Normal distribution* is called *Gaussian* distribution (Named after Guss 1777-1855). Gaussian distribution is a mathematical model which represents a typical curve that describes approximately the shape of many relative frequency distributions. For a random variable x with mean μ and standard deviation σ, the normal distribution curve is,

$$f(x) = \frac{1}{\sqrt{\left(2\pi\sigma^2\right)}} \exp\left\{ -\frac{(x-\mu)^2}{2\sigma^2} \right\} \qquad \text{(C.1)}$$

The curve is symmetrical about $x = \mu$ vertical line; it has one maximum at $x = \mu$; the area under the curve is 1; when $x \to \pm\infty, f(x) \to 0.$ A convenient way to denote *X* is normally distributed with mean μ and variance σ^2 is: $X = N\left(\mu, \sigma^2\right)$: The following MATLAB command gives the plot of the Function given in Fig. C.1.

The graph is shown in Fig. C.2, which is the normal distribution curve depends on two factors: the mean and the standard deviation. The mean μ determines the location of the centre and the standard deviation determines the height and width. When the standard deviation is large the curve shown will be short and wide, and the small standard deviation resembles the tall and narrow curve. It is also noted that the area under the curve is equal to one and the standard deviation is the square root of the variance.

The mean is the average of all elements: $\mu = \frac{\sum_{i=1}^{N} x_i}{N}$; The population variance is given by,

$$\sigma^2 = \frac{\sum_{i=1}^{N} (x_i - \mu)^2}{N} \tag{C.2}$$

Probability of an event can be expressed mathematically: the number of expected occurrences of an event divided by the number of expected occurrences plus the number of failures of occurrences (this adds up to the total of possible outcomes), (a and b are events),

$$p(a) = p(a)/[p(a) + p(b)] \tag{C.3}$$

It should be noted that probability equal to 1 means that it is almost sure that incident will occur and zero means that there will be no possibility that event will occur.

```
x = [-3:.1:6]; % μ equal to 0 and σ equal to 1
norm = normpdf(x,0,1);
figure;
plot(x,norm)
```

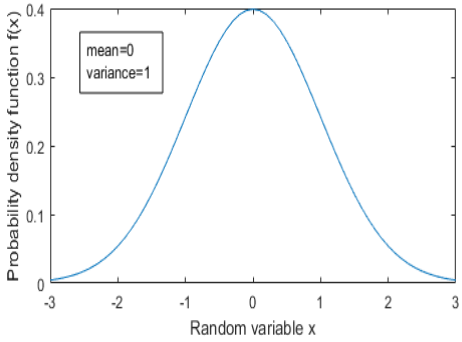

Figure C.1: Gaussian distribution μ equal to 0 and σ equal to 1.

The same MATLAB in built function can be written from first principles as given below: for different μ equal to 0 and σ equal to 1(legend: blue), μ equal to 0.5 and σ equal to 1.5 (legend: red):

```
clear all
clf
x= [-3:.1:6];
u=0; sig=1;
```

```
y=(1/(sqrt(2*pi*sig^2))).*exp(-((x-u).^2)/(2*sig^2))
plot(x,y)
hold on
u=.5; sig=1.5
y=(1/(sqrt(2*pi*sig^2))).*exp(-((x-u).^2)/(2*sig^2))
plot(x,y,'r')
```

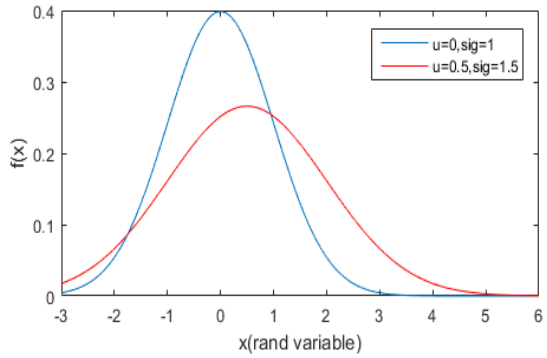

Figure C.2: Gaussian distribution: μ equal to 0 and σ equal to 1, μ equal to 0.5 and σ equal to 1.5

In Statistics covariance presents an indication on how much two random variables change together. It necessary to understand the term *Correlation* also as links to *covariance*. Correlation is a scaled version of covariance that takes on values in [−1, 1] with a correlation of ±1indicates a perfect linear association and 0 indicates no linear relationship between the variables. The following simple example clarifies the difference:

Generally, the Covariance doesn't really indicate about the strength of the relationship between the two variables, while correlation does. For example:

For two random variable vectors X and Y, the covariance is defined as,

cov(X, Y)= E[(X- E[X])(Y - E[Y])], E[X] is the expected value of X is also the mean value of X.

$$\begin{aligned} \text{cov}(X, Y) &= E[(X- E[X])(Y - E[Y])], \\ &= E[XY- XE[Y]- E[X]Y +E[X]E[Y]] \\ &= E[XY]- E[X\}E[Y]-E[X]E[Y] + E[X]E[Y] \\ &= E[XY]-E[X]E[Y] \end{aligned} \quad \text{(C.4)}$$

Variance is a special case of covariance when the two variables are identical [138].

$$\text{cov}(X, X) = \text{Var}(X) = \sigma^2(X) \quad \text{(C.5)}$$

Covariance Matric:

If X and Y are two random variable vectors, then another convenient way to define the

$$\begin{bmatrix} x_1 & x_2 & \cdots & x_n \\ y_1 & y_2 & \cdots & y_n \end{bmatrix}$$; sampled n times

Assuming: $X = [x_1 \quad x_2 \quad x_3 \quad \cdots \quad x_n]$; and

$$Y = [y_1 \quad y_2 \quad y_3 \quad \cdots \quad y_n];$$

$$\text{cov}(X,Y) = \frac{1}{n}\sum_{i=1}^{n} (x_i - \mu_X)(y_i - \mu_Y), \text{“sample covariance”} \tag{C.6}$$

$$\text{cov}(X,Y) = \frac{1}{n}[x_1 - \mu_X \quad x_2 - \mu_X \quad \cdots \quad x_n - \mu_X]\begin{bmatrix} y_1 - \mu_Y \\ y_2 - \mu_Y \\ \vdots \\ y_n - \mu_Y \end{bmatrix} \tag{C.7}$$

where μ_X is the mean of *X*, μ_Y is the mean of *Y:*

Example:
```
clear all
n=4
x= [2.1, 2.5, 3.6, 4.0];
m_x=mean(x) %(mean = 3.1)
y= [8, 10, 12, 14];
m_y=mean(y) %(mean = 11)
cov(x,y)
p=var(x)
q=var(y)
```

```
ans =
   0.8033    2.2667
   2.2667    6.6667
p =
   0.8033
q =
```

6.6667

Diagonals represents the var(x) and var(y); cov(X,Y)=cov(Y,X)=2.2667;

The *covariance matrix* of two random variables is the matrix of pair-wise covariance calculations between each variable:

$$C = \begin{pmatrix} \mathrm{cov}(X,X) & \mathrm{cov}(X,Y) \\ \mathrm{cov}(Y,X) & \mathrm{cov}(Y,Y) \end{pmatrix}$$

$E[x_1]$ is defined as the expected value of x_1 or mean value of x_1 and it is generally denoted by $\bar{x}_1$;where p is the joint probability density function of x_1 and x_2.

The correlation coefficient is the normalised quantity,

$$\rho_{12} \equiv \frac{\sigma^2_{x_1 x_2}}{\sigma_{x_1}\sigma_{x_2}}, \quad -1 \le \rho_{12} \le +1 \tag{C.8}$$

Weibull Wind Model,

$$f(v) = \frac{k}{A}\left(\frac{v}{A}\right)^{k-1} Exp\left(-\left(\frac{v}{A}\right)^{k}\right) \tag{C.9}$$

A is a Weibull Scale Parameter in m/s. The parameter *A* indicates the characteristics of wind speed distribution and generally, *A* is proportional to mean wind speed. The parameter *k* is generally identified as the Weibull form parameter. It generally specifies the shape of the Weibull distribution and the values are taken in between 1 and 3. The mean wind speed of v = 5.32 m/s Weibull A = 6.00 and k =2.0 the Simulink block diagram (Fig. C.3. and Fig C.4.) and the characteristics of wind distribution are shown below:

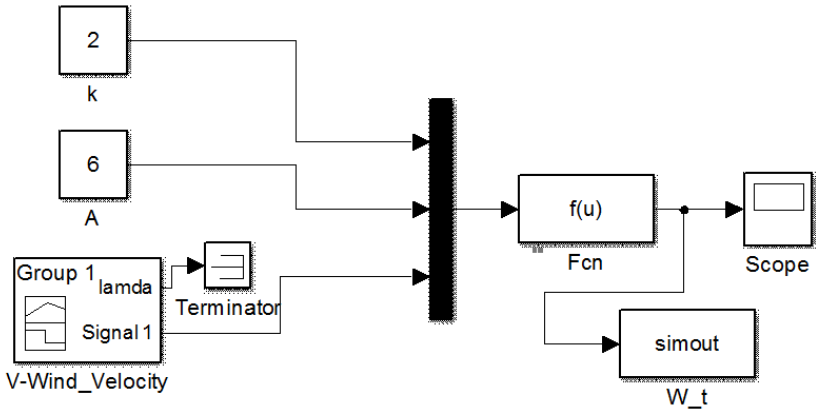

Figure C.3: Simulink block diagram for Weibull wind distribution.

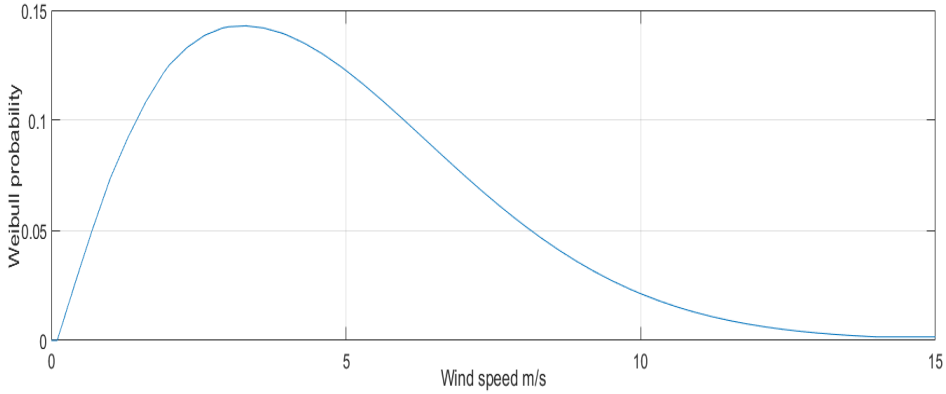

Figure C.4: Weibull wind distribution.

Appendix D

Introduction to Linearization via Taylor series expansion:

Taylor Series expansion in mathematics can be used to linearize nonlinear functions with good accuracy. When linearizing generally we use an optimum point or equilibrium point in the curve to linearize the function at that point. The idea is suitable up to a suitable range to the left and the right of the curve. If x is a function of $f(x)$ and if the equilibrium point on the curve is $\bar{x}$ then the Taylor series expansion can be given as given below,

$$f(x) = f(\bar{x}) + \left.\frac{df}{dx}\right|_{x=\bar{x}} (x-\bar{x}) + \frac{1}{2}\left.\frac{d^2 f}{dx^2}\right|_{x=\bar{x}} (x-\bar{x})^2 + HOT \tag{D.1}$$

where, *HOT* implies the higher order terms.

When x is sufficiently close to $\bar{x}$ we can ignore the higher order terms as they are very close to zero.

Neglecting the quadratic and higher order terms,

$$f(x) = f(\bar{x}) + \left.\frac{df}{dx}\right|_{x=\bar{x}} (x-\bar{x}) \tag{D.2}$$

At steady state we can take $\frac{d\bar{x}}{dt} = f(\bar{x}) = 0$; hence we can write,

$$f(x) \approx \left.\frac{df}{dx}\right|_{x=\bar{x}} (x-\bar{x}) \tag{D.3}$$

Now consider a function with one State variable and one input variable,

$$\dot{x} = \frac{dx}{dt} = f(x,u) \tag{D.4}$$

Applying Taylor series expansion to Equation (D.4), we can write,

$$\dot{x} = f(\bar{x},\bar{u}) + \left.\frac{\partial f}{\partial x}\right|_{\bar{x},\bar{u}} (x-\bar{x}) + \left.\frac{\partial f}{\partial u}\right|_{\bar{x},\bar{u}} (u-\bar{u}) + HOT \tag{D.5}$$

At the equilibrium point or at steady state we can take $f(\bar{x},\bar{u})$ is equal to zero. Hence we can write the Equation (D.6) as given below,

$$\frac{d(x-\bar{x})}{dt} \approx \left.\frac{\partial f}{\partial x}\right|_{\bar{x},\bar{u}} (x-\bar{x}) + \left.\frac{\partial f}{\partial u}\right|_{\bar{x},\bar{u}} (u-\bar{u}) \qquad \text{(D.6)}$$

Taking $\Delta x = x - \bar{x}$ *and* $\Delta u = u - \bar{u}$ we can write the state-space representation,

$$\frac{d\Delta x}{dt} = a\Delta x + b\Delta u \qquad \text{(D.7)}$$

Where, $a = \left.\frac{\partial f}{\partial x}\right|_{\bar{x},\bar{u}}$ and $b = \left.\frac{\partial f}{\partial u}\right|_{\bar{x},\bar{u}}$.

MATLAB script file which had no solution for the β search.

```
% β is the pitch angle here.
clc;
clear all
lamda=5;
c1=.5176;c2=116;c3=0.4;c4=5;c5=21;c6=0.0068;
syms beta;
g=1/(lamda+0.08*beta)-0.035/(1+beta^3)
cp=c6*lamda+ c1*(exp(-c5*g))*(c2*g-c3*beta-c4)
dg=-0.08/(lamda+0.08*beta)^2 + (0.105*beta^2)/(1+beta^3)^2
dcp=c1*(exp(-c5*(1/(lamda+0.08*beta)-0.035/(1+beta^3)))*(c2*(-0.08/(lamda+0.08*beta)^2 +
(0.105*beta^2)/(1+beta^3)^2)-c3)-...
   c1*c5*(c2*(1/(lamda+0.08*beta)-0.035/(1+beta^3))-c3*beta-c4)*...
   (exp(-c5*(1/(lamda+0.08*beta)-0.035/(1+beta^3))))*(-0.08/(lamda+0.08*beta)^2 +
(0.105*beta^2)/(1+beta^3)^2))
fun=@(beta) dcp
[beta,fval]=fminsearch(fun,beta); %initial guess = 3
beta_op=beta
g=1/(lamda+0.08*beta_op)-0.035/(1+beta_op^3)
cp_op=c6*lamda+ c1*(exp(-c5*g))*(c2*g-c3*beta_op-c4)
```

Program code for optimum pitch angle β and then to find the maximum C_P is given below (MPPT):

```
clear all
i=1; j=1;
for lamda=1:8
   fun=@(beta) ((0.44 -0.0167*beta)/(15-0.3*beta)^2)*cos((180/pi))*(pi*(lamda-3)/(15-
0.3*beta))...
    -0.0167*sin ((180/pi)*pi*(lamda-3)/(15-0.3*beta))-0.00184*(lamda-3)
beta=[2]
options=optimset('display','iter'); % show iterations
[beta]=fzero(fun,beta)
beta
i=i
cp(i)=(0.44-0.0167*beta)*sin(pi*(lamda-3)/(15-0.3*beta))-0.00184*(lamda-3)*beta
j=j
beta(j)=beta
end
```

MATLAB script for searching optimum lamda (λ)and reference turbine speed ω_{ref}

```
clear all;
clc; teta=3;c1=0.5176;R=20;c2=116;c3=0.4;c4=5;c5=21;c6=0.0068; %This program search for
optimum Lamda
lamda=fzero(@(lamda)c2-c5*(c2*(1/(lamda+0.08*teta)-0.035/(1+teta^3))-...
   c3*teta-c4)+c6,6)
```

```
v_w=10;
a=1/(lamda+0.08*teta)-0.035/((teta^3)+1);
cp=c1*(c2*a-c3*teta-c4)*exp(-c5*a)+c6*lamda
p=0.5*1.225*cp*(pi)*(R^2)*(v_w)^3
omega_ref=v_w*lamda/20
```

Appendix E

Permission letters

Re: Active and Reactive Power control of DFIG

H

陳鴻誠 hcchen <hcchen@ncut.edu.tw>

Reply|

Today 09:02

Singappuli Mudiyanselage Wijewardana

Inbox

Dear Singappuli,

I am very delighted to permit of quoting some parts of my paper into your thesis.

Best regards,

H.C.Chen

Dear Prof Chen

I am a PhD student at Queen Mary University of London currently in the write-up stage of my PhD degree in renewable energy sources modelling and control.

I read your above paper, which was published in A.M.I.Sci.8 No11 Journal and I believe it is an excellent paper which clearly explains the mechanism of GSC and the RSCs.

I would be very pleased if you could kindly grant me your permission to include the mathematical derivation parts of section 2.2 and 2.3 into my PhD thesis. I am willing to include your permission email to my thesis as well as I will quote your paper as an important reference into my Thesis. Thanking you and best regards

Singappuli
PhD student QMUL

LW

Liuping Wang <liuping.wang@rmit.edu.au>

Today 09:51

Singappuli Mudiyanselage Wijewardana

Reply

You replied on 06/06/2016 10:06.

Action Items

Thanks for the kind message. Yes, please go ahead to use them. I am glad that it is useful.
Good luck with your PhD thesis.

Best wishes
Liuping

SW

Singappuli Mudiyanselage Wijewardana

Dear Professor Wang Thanks for the reply. Currently I am writing my PhD thesis in Modelling and Control of R... Mon 06/06/2016 09:11

LW

Liuping Wang <liuping.wang@rmit.edu.au>

Thanks for the question-- q^{-1} is the backward shift operator for discrete-time system. Maybe, I used it for th... Sun 05/06/2016 22:37

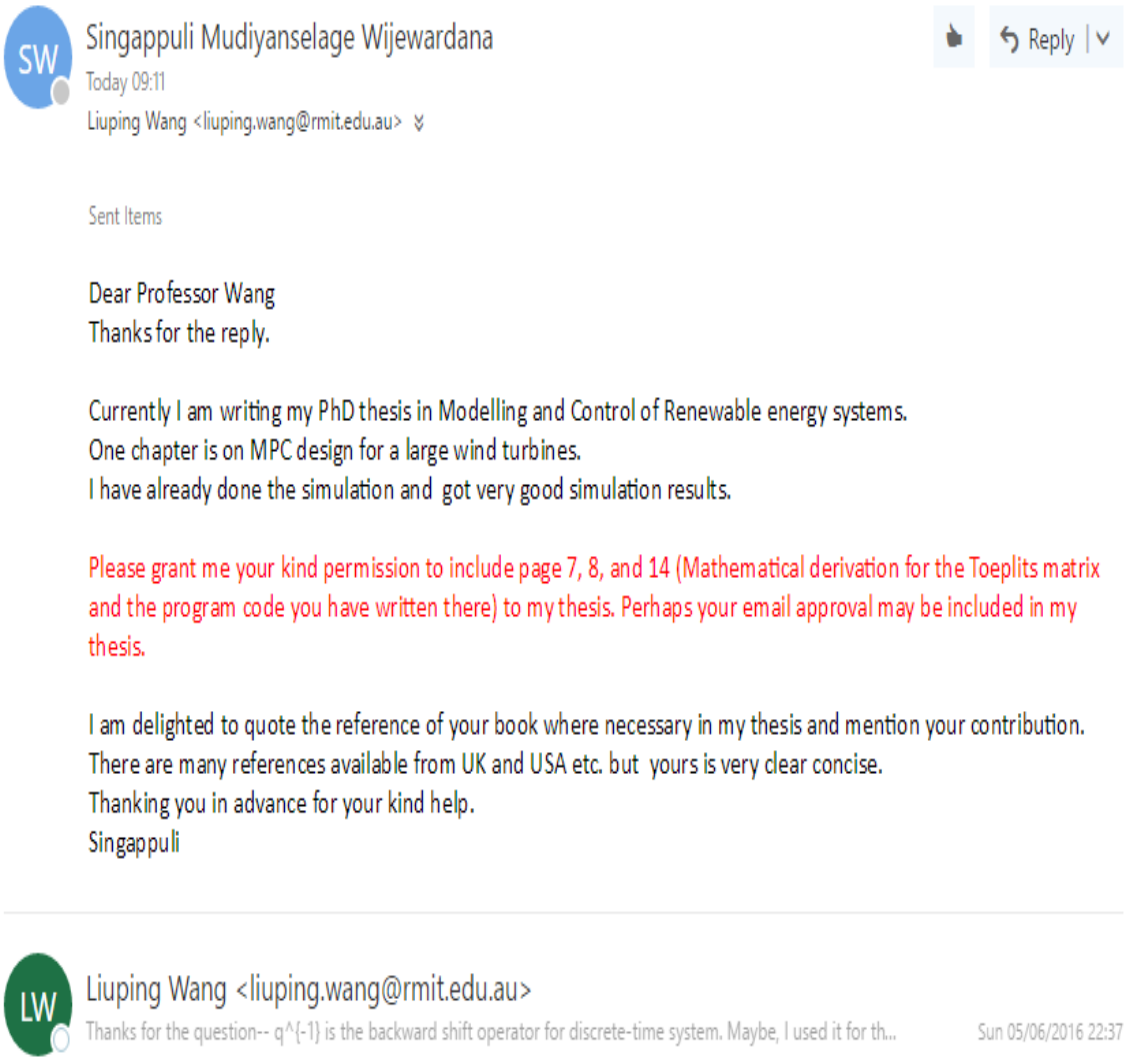

Singappuli Mudiyanselage Wijewardana
Today 09:11
Liuping Wang <liuping.wang@rmit.edu.au>

Reply

Sent Items

Dear Professor Wang
Thanks for the reply.

Currently I am writing my PhD thesis in Modelling and Control of Renewable energy systems.
One chapter is on MPC design for a large wind turbines.
I have already done the simulation and got very good simulation results.

Please grant me your kind permission to include page 7, 8, and 14 (Mathematical derivation for the Toeplits matrix and the program code you have written there) to my thesis. Perhaps your email approval may be included in my thesis.

I am delighted to quote the reference of your book where necessary in my thesis and mention your contribution.
There are many references available from UK and USA etc. but yours is very clear concise.
Thanking you in advance for your kind help.
Singappuli

Liuping Wang <liuping.wang@rmit.edu.au>
Thanks for the question-- q^{-1} is the backward shift operator for discrete-time system. Maybe, I used it for th...
Sun 05/06/2016 22:37

Permission Email and Approval from

Professor Robert W Erickson

Professor Electrical and Computer Engineering

- ECOT 356 (Engineering Centre, Office Tower, third floor)
- Telephone: (303) 492-7003
- Department fax: (303) 492-2758

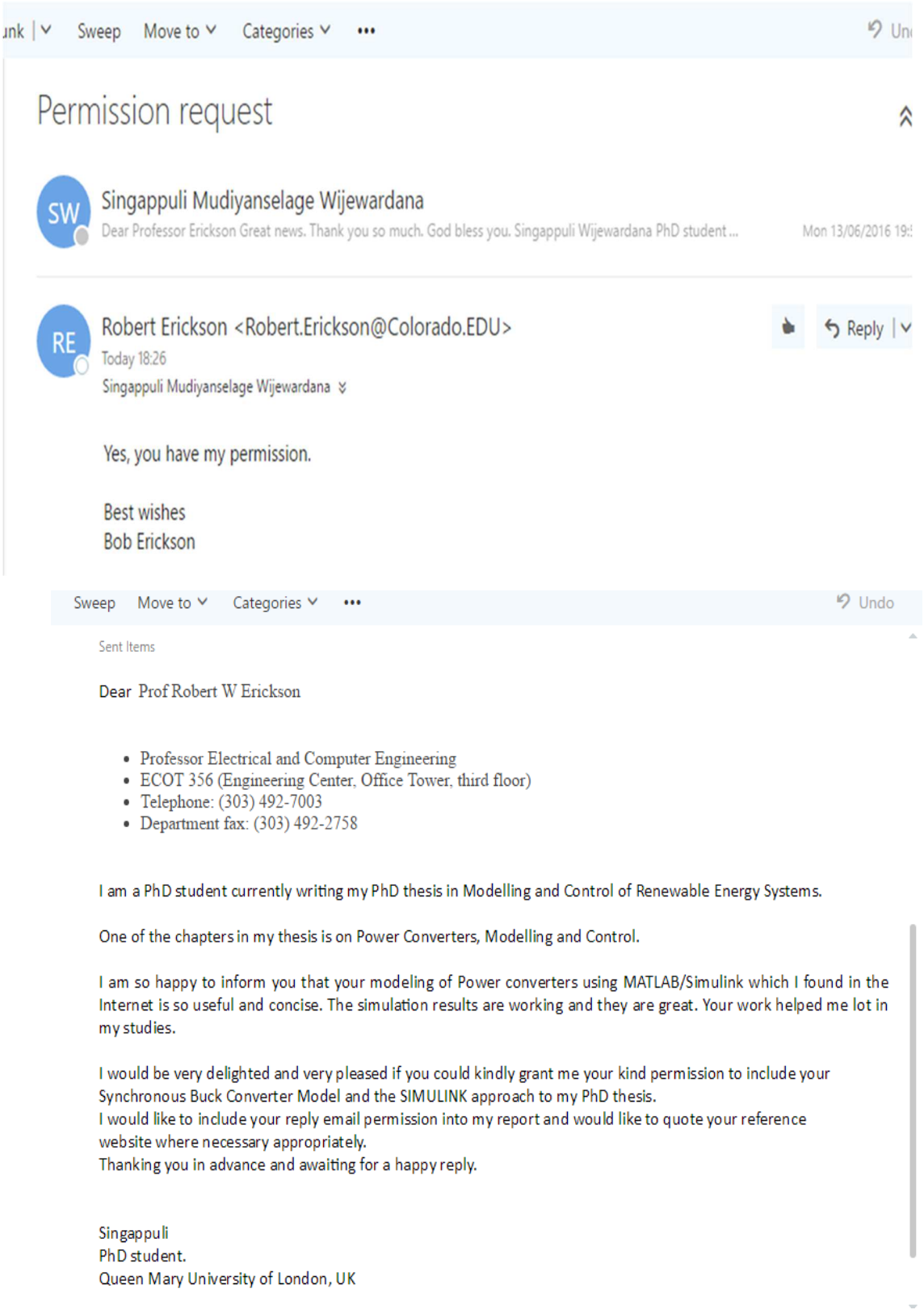

ınk | Sweep Move to Categories ••• Un

Permission request

SW

Singappuli Mudiyanselage Wijewardana

Dear Professor Erickson Great news. Thank you so much. God bless you. Singappuli Wijewardana PhD student ... Mon 13/06/2016 19:

RE

Robert Erickson <Robert.Erickson@Colorado.EDU>

Reply

Today 18:26

Singappuli Mudiyanselage Wijewardana

Yes, you have my permission.

Best wishes
Bob Erickson

Sweep Move to Categories ••• Undo

Sent Items

Dear Prof Robert W Erickson

- Professor Electrical and Computer Engineering
- ECOT 356 (Engineering Center, Office Tower, third floor)
- Telephone: (303) 492-7003
- Department fax: (303) 492-2758

I am a PhD student currently writing my PhD thesis in Modelling and Control of Renewable Energy Systems.

One of the chapters in my thesis is on Power Converters, Modelling and Control.

I am so happy to inform you that your modeling of Power converters using MATLAB/Simulink which I found in the Internet is so useful and concise. The simulation results are working and they are great. Your work helped me lot in my studies.

I would be very delighted and very pleased if you could kindly grant me your kind permission to include your Synchronous Buck Converter Model and the SIMULINK approach to my PhD thesis.
I would like to include your reply email permission into my report and would like to quote your reference website where necessary appropriately.
Thanking you in advance and awaiting for a happy reply.

Singappuli
PhD student.
Queen Mary University of London, UK

References

[1] Abbas, F. A. R. and Abdulsada, M. A. (2010). Simulation of Wind-Turbine Speed Control by MATLAB, International Journal of Computer and Electrical Engineering, (2), No. 5, October, pp.1793-8163

[2] Ackermann, T. (2005). Wind power I power systems, John Wiley & Sons, Ltd, The Atrium, Southern Gate, Chichester, West Sussex PO19 8SQ, England, 2005.

[3] Ahmed, N. A. and Al-Othman, A.K. (2011). Development of an efficient utility interactive combined wind/photovoltaic/fuel cell power system with MPPT and DC bus voltage regulation. Electric Power Systems Research. (81), No. 5, pp. 1096-1106.

[4] Aho, J., Buckspan, A., Laks, J., Fleming, P., Jeong, Y., Dunne, F., Churchfield, M., Pao, L. and Johnson, K. (2012). Tutorial of Wind Turbine Control for Supporting Grid Frequency through Active Power Control, 2012-American Control Conference Montreal, Canada June 27-29, pp. 1-12.

[5] Amusat, O. O., Shearing, P.R. and Fraga, E. S. (2016). Optimal integrated energy systems design incorporating variable renewable energy sources. Computers and Chemical Engineering, (95), pp. 21–37.

[6] Anderson, J.P. (2009), State-space modelling, system identification and control of a 4th order rotational mechanical system, M.Sc thesis submitted, naval postgraduate school Monterey, California, 2009.

[7] Arsalan, M. J. and Khan, J. (2016), Solar power technologies for sustainable electricity generation-A review, Renewable and Sustainable Energy Reviews (55) pp. 414-425.

[8] Babaei, E., Esmaeel, M. and Mahmoodieh, S. (2014). Systematically method of designing the elements of the Cuk converter Electrical Power and Energy Systems (55), pp. 351–361.

[9] Badawe, M., Iqbal, T. and Mann, G. K. I. (2012). Optimization and modelling of stand-alone Wind/PV Hybrid energy system. (2012), 25th Canadian Conference on Electrical and Comp. Eng. (CCECE) IEEE, 2012.

[10] Bandhauer, T. M., Garimella, S. and Fuller, T. F. (2011). A Critical Review of Thermal Issues in Lithium-ion Batteries. (153) 3, pp. R1-R25.

[11] Bao, K. (2012). Battery charge and discharge control for energy management in EDV and utility integration, M.Sc. Thesis submitted to the Department of Electrical and Computer Engineering in the Graduate School of the University of Alabama. pp. 14-36.

[12] Barelli, L., Bidini, G. and Bonucci, F. (2016). A micro-grid operation analysis for cost-effective battery energy storage and RES plants integration, Journal of Power Sources, Energy, (113), pp. 831-844.

[13] Belgium inaugurates wind farm with largest wind turbines, [online], Available at http://www.renewableenergyfocus.com/view/5588/belgium-inaugurates-wind-farm-with-largest-wind-turbines/, Accessed on 28 April 2016.

[14] Belhaouas, N., Cheikh, M. S. A., Malek, A. and C. Larbes, C. (2016). MATLAB-Simulink of Photovoltaic system based on a two-diode simulator with shaded solar cells, Revue des Energies Renouvelables. (16) No.1, pp. 65-73.

[15] Bellia, H., Youcef, R. and Fatima, M. (2014), a detailed modelling of photovoltaic module using MATLAB, NRIAG Journal of Astronomy and Geophysics3 (2014) pp. 53–61.

[16] Bemporad, A. (2006). Model Predictive Control Design: New Trends and Tools. Proceedings of the 45th IEEE Conference on Decision & Control Manchester Grand Hyatt Hotel San Diego, CA, USA, December 13-15, 2006.

[17] Bernardi, D., Pawlikowski, E. and Newman, J. (1985). A General Energy Balance for Battery Systems, J. Electrochemical Society. (132)-No.1, pp. 5-12.

[18] Bhatnagar, P. and Nema, R. K. (2013). Maximum power point tracking control techniques: State-of-the-art in photovoltaic applications, Renewable and Sustainable Energy Reviews (23), pp. 224–241.

[19] Bhide, S. and Shim, T. (2009). Development of Improved Lithium-ion Battery Model Incorporating Thermal and Rate Factor Effects, University of Michigan USA, 978-1-4244-2601 IEEE.

[20] Bianchi, F.C., Mantz, R.J. and Christiansen, C. F. (2005). Gain scheduling control of variable-speed wind energy conversion systems using quasi-LPV models, Control Engineering Practise (13), pp. 247-255.

[21] Blaabjerg, F. and Ma, K. (2013), Future on Power Electronics for Wind Turbine Systems, IEEE Journal of emerging and selected topics in power electronics, (1), no. 3, pp. 139-152.

[22] Bo, L., Xueqing, Y. and Lin, Z. (2015), Li-ion SOC Estimation Based on EKF Algorithm. The 5th Annual IEEE International Conference on Cyber Technology in Automation, Control and Intelligent Systems June 8-12, 2015, Shenyang, China.

[23] Bose, B.K. (2014). Modern Power Electronics and AC Drives, PHI Learning Pvt. Ltd. Delhi-110092, 2014.

[24] Breeze, A. J. (2008), Next generation thin-film solar cells, IEEE, CFP08RPS-CDR 46th Annual International Reliability, Physics Symposium, Phoenix, 2008.

[25] Breyer, C., Koskinen, O. and Blechinger, P. (2015). Profitable climate change mitigation: The case of greenhouse gas emission reduction benefits enabled by solar photovoltaic systems, Renewable and Sustainable Energy Reviews. (49), pp. 610-628

[26] Bruen, T. and Marco, J. (2016). Modelling and experimental evaluation of parallel connected lithium ion cells for an electric vehicle battery system, Journal of Power Sources (310), pp. 91-101.

[27] Byeon, G., Park, I. K. and Jang, G. (2010), Modelling and control of a Doubly-Fed Induction Generator (DFIG) wind power generation system for Real-time simulations, Journal of Electrical Engineering & Technology, Vol. 5, No. 1, pp 61-69, (2010).

[28] Călugăru, G. and Dăniúor, E-A. (2016). Improved Aircraft Attitude Control Using Generalized Predictive Control Method, IEEE, pp. 101-106.

[29] Cao, Y. (2014), ENGR487 Lecture22 Discrete Kalman Filter Implementation using Simulink (Part-I) [Online] available at: https://www.youtube.com/watch?v= aPFZ Sg43Vmc, Accessed on 24th April, 2016.

[30] Chang, Wen-Yeau (2013). The State of Charge Estimating Methods for Battery: A Review. Hindawi Publishing Corporation ISRN Applied Mathematics Volume -2013, Article ID: 953792,7-pages http://dx.doi.org/10.1155/2013/953792.

[31] Chen, H-C and Chen, P-H. (2014). Active and reactive power control of doubly fed induction generator, Appl. Math. Inf. Sci. (8) No.11, pp. 117-124.

[32] Chen, M. and Rincon-Mora, G. A. (2006). Accurate Electrical Battery Model Capable of Predicting Runtime and I–V Performance, IEEE Transactions on Energy Conversion. (21)-2, pp. 504-511.

[33] Chen, Z., Fu, Y. and Chris, C. (2013), State of charge estimation of Li-ion batteries in electric drive vehicles using Extended Kalman Filtering, IEEE Transactions on vehicular technology, (62) 3, pp. 1020-1030.

[34] Cherfia, N., Kerdoun, D. and Boumassata, A. (2013). Sliding mode control indirect strategy of the active and reactive power for the wind turbine DFIG., Conference Internationale des Energies Renouvelables, Sousse, Tunisie.

[35] Cho, G. Y., Choi, J.W., Park, J.H. and Cha, S.W. (2014). Transient modelling and validation of Lithium ion battery pack with air cooled thermal management system for electric vehicles, International Journal of Automobile Technology. (15) No.5, pp. 795-803.

[36] Chouder, A. and Silvestre, S. (2013). Monitoring, modelling and simulation of PV systems using LabVIEW, Solar Energy, (91), pp. 337-34.

[37] Ciobotaru, M., Kerekes, T., Teodorescu, R. and Bouscayrol, A. (2006), PV inverter simulation using Matlab/Simulink graphical environment and PLECS blockset, IEEE, pp. 5313-5338.

[38] Clement R. C. and Prasanth, R. (2016), A critical review of recent developments in nanomaterials for photoelectrodes in dye sensitized solar cells, Journal of Power Sources (317), pp.120-132.

[39] Commin, A. N., McClatchey, J., Davidson, M. W. H. and Gibb, S. W. (2017). Close-proximity tidal phasing for 'firm' electricity supply, Renewable Energy. (102), pp. 380-389.

[40] Cuesta, A. B., Gomez-Gil, F. J., Fraile, J. V. M., Rodríguez, J. A., Calvo, J. R. and Vara, J. P. (2013), Feasibility of a Simple Small Wind Turbine with Variable-Speed Regulation Made of Commercial Components Energies (6), pp. 3373-3391; doi:10.3390/en6073373.

[41] Dali M., Belhadj, J. and Roboam, X. (2010). Hybrid solar-wind system with battery storage operating in grid–connected and standalone mode: Control and energy management, Experimental investigation, Energy (35), pp. 2587-2595.

[42] DC motor model, (2016). Available on: http://ctms.engin.umich.edu/CTMS/index.php?example =MotorSpeed&section=SimulinkModeling, Accessed on 30 April 2016.

[43] Delimustafic, D., Islambegovic, J., Akasamovic, A. and Masic, S. (2011). Model of Hybrid Renewable Energy System: Control, Supervision and Energy Distribution, (2011), IEEE.

[44] Deori, L., Garatti, S. and Prandini, M. (2015). A model predictive control approach to aircraft motion control2015 American Control Conference Palmer House Hilton July 1-3, 2015. Chicago, IL, USA, IEEEXplore.

[45] Ding, F., Loparo, K. A. and Wang, C. (2012). Modelling and simulation of Grid-connected hybrid AC/DCMicrogrid. [Online] Available: http://ieeexplore.ieee.org /stamp/stamp.jsp?arnumber=06343969, e-mail: fei.ding@case.edu. IEEE.

[46] Dolan, B. (2010), Wind turbine modelling, control and fault detection, PhD thesis submitted to the Department of Informatics and Mathematical Modelling, Technical University of Denmark, Kongens, Lyngby, 2010.

[47] Dubarry, M., Vuillaume, N. and Bor Liaw, B.Y. (2009). From single cell model to battery pack simulation for Li-ion batteries, Journal of Power Sources, (186), pp. 500-507.

[48] Ekanayake, J. B., Holdsworth, L, Wu, X-G. and Jenkins, N. (2003), Dynamic Modeling of Doubly Fed Induction Generator Wind Turbines, IEEE transactions on power systems, (18), No. 2 May 2003.

[49] Electrical Machines – Generators (Description and Applications), (2016). [Online] Available at: http://www.mpoweruk.com/generators.htm Accessed on 08 June 2016.

[50] Elmetennani, S., Laleg-Kirati, T. M., Djemai, M. and M. Tadjinec, M. (2016). New MPPT algorithm for PV applications based on hybrid dynamical approach, Journal of Process Control. (48), pp. 14–24.

[51] Eltiganin, D. and Masri, S. (2015). Challenges of integrating renewable energy sources to smart grids: A review, Renewable and Sustainable Energy Reviews, (52), pp. 770–780.

[52] Erdinc, O., Vural, B., and Uzunoglu, M., (2009), A dynamic Lithium-ion battery model considering the effects of temperature and capacity Fading, Clean Electrical Power, 2009-International Conference, Capri, IEEE, pp. 383-386.

[53] Erickson, R. and Maksimovic, D. (2016), Fundamentals of Power Electronics second edition Modeling of Power Converters using MATLAB and Simulink, [Online] available on http://slideplayer.com/slide/9054248/, Accessed on 12 June 2016

[54] EU PARLIAMENT DIRECTIVE 2009/28/EC, THE EUROPEAN PARLIAMENT AND OF THE COUNCIL, On the promotion of the use of energy from renewable sources and amending and subsequently repealing Directives 2001/77/EC and 2003/30/EC B. Online, Available on: http://eur-lex.europa.eu/legal-content/ EN/ALL /?uri= CELEX%3A32009L0028, Accessed on 23 Nov. 2016.

[55] Faranda, R. and Leva, S. (2008), Energy comparison of MPPT techniques for PV Systems, WSEAS Transactions on Power Systems. (3), Issue-6, June 2008.

[56] Fletcher, J. and Yang, J. (2016), Introduction to Doubly-Fed Induction Generator for Wind Power Applications, University of Strathclyde, Glasgow United Kingdom, [Online] Available at http://cdn.intechopen.com/pdfs/12519.pdf, Accessed on 09 June 2016.

[57] Gallo, D., Landi, C., Luiso, M. and Morello, R., (2013), Optimisation of Experimental Model Parameter Identification for Energy Storage Systems, *Energies*. ISSN 1996-1073.

[58] Ganesan, N., Basu, S., Hariharan, K. S., Kolake, M. S., Song, T., Yeo, T., Dong Kee Sohn, D. K. and Doo, S. (2016), Physics based modeling of a series parallel battery pack for asymmetry analysis, predictive control and life extension, Journal of Power Sources, (322) pp. 57-67.

[59] Gao, L., S. Liu, S. and Dougal, A. (2002), Dynamic Lithium-Ion Battery Model for System Simulation, IEEE Transactions on components and packaging technologies, (25), NO. 3.

[60] Gosk, A. (2011). Model Predictive Control of a Wind Turbine", M.Sc. thesis in Engineering, Informatics and Mathematical Modelling Department, Technical University of Denmark, 2011.

[61] Han, J., Kim, D. and Sunwoo, M. (2009). State-of-charge estimation of lead-acid batteries using an adaptive extended Kalman filter, Journal of Power Sources. (188), pp. 606–612.

[62] Hand, M. M. (1999). Variable-Speed Wind Turbine Controller Systematic Design Methodology a Comparison of Non-Linear and Linear Model Based Designs, National Renewable Energy Laboratory 1617 Cole Boulevard Golden, Colorado 80401-3393, July 1999.

[63] He, H., Xiong, R. and Fan, J. (2011). Evaluation of Lithium-Ion Battery Equivalent Circuit Models for State of Charge Estimation by an Experimental Approach, Energies (4), pp. 582-598; doi:10.3390/en4040582.

[64] He, Z., M. Gao, M., Wang, C., Wang, L. and Liu, Y., (2013). Adaptive State of Charge Estimation for Li-Ion Batteries Based on an Unscented Kalman Filter with an Enhanced Battery Model, Energies. (6), 4134-4151.

[65] Henriksen, L.C. (2007). Model Predictive Control of a Wind Turbine, M.Sc Thesis in Engineering, Informatics Mathematical Modelling, the Technical University of Denmark 2007.

[66] Heriche, H., Rouabah, Z. and Bouarissa, N. (2016), High-efficiency CIGS solar cells with optimization of layers' thickness and doping, Optik (127), pp. 11751-11757.

[67] Hess, H. L., Melek, N.A.A. and Muljad, E. (2000). Power Converter for Wind Turbine Application, (2000) IEEE, pp. 1275-1276.

[68] Hocaoglu, F. O., Gerek, O. N. and Kurban, M. (2009). The effect of model generated solar radiation data usage in hybrid (Wind-PV) sizing studies, Energy Conversion and Management (50), pp. 2956-2963.

[69] Horkheimer, D.P. (2012). Gain Scheduling of an Extended Kalman Filter for Use in an Attitude/Heading Estimation System, A thesis submitted to the faculty of the graduate school of the University of Minnesota.

[70] Humada, A. M., Hojabri, M., Mekhilef, S. and Hamada, H. M. (2016), Solar cell parameters extraction based on single and double-diode models: A review Renewable and Sustainable Energy Reviews, (56) pp, 494-509.

[71] Hure, N. (2016). Model Predictive Control of a Wind Turbine, Department of Control and Computer Engineering Faculty of Electrical Engineering and Computing of University of Zagreb. [Online] Available on: https://www.fer.unizg.hr /download /repository/ KDI_Nik ola_Hure.pdf, Accessed on: 10 April 2016.

[72] Huria, T. (2012), Rechargeable lithium battery energy storage systems for vehicular applications -Land Vehicles and Transport Systems, PhD Dissertation, Submitted at Universita Di PISA Engineering School.

[73] Hypiusová, M. and Vesely, V. (2015), Robust MPC controller design: Infinite prediction horizon controller design: IFAC paper Online 48-14, pp 332-340.

[74] Ilka, A. (2015). Gain-Scheduled Controller Design, PhD Thesis submitted to the Institute of Robotics and Cybernetics, Faculty of Electrical Engineering and Information Technology, Ilkoviˇcova 3, 812 19 Bratislava.

[75] Ishaque, K., Salam, Z. and Lauss, G. (2014), The performance of perturb and observe and incremental conductance maximum power point tracking method under dynamic weather conditions, Applied Energy, (119), pp. 228-236.

[76] Ishaque, K., Salam, Z. and Taheri, H. (2011). Accurate MATLAB Simulink PV system simulator based on Two-diode model, Journal of Power Electronics. (11), No 2, pp. 179-187.

[77] Iskandarani, M., Givigi, S. N., Rabbath, C. A. and Beaulieu, A. (2013). Linear Model Predictive Control for the Encirclement of a Target Using a Quadrotor Aircraft 21st Mediterranean Conference on Control & Automation (MED) Platanias-Chania, Crete, Greece, June 25-28, 2013.

[78] Islam, M. R., Guo, Y., and Zhu, J. (2013), Power converters for wind turbines: Current and future development, Materials and processes for energy: communicating current research and technological developments (A. Méndez-Vilas, Ed.), pp. 559-571.

[79] Jaguemont, J., Boulon, L. and Dube, Y. (2016). A comprehensive review of lithium-ion batteries used in hybrid and electric vehicles at cold temperatures. Applied Energy (164), pp. 99-114.

[80] Jain, A., Schildbach, G., Fagiano, L. and Morari, M. (2015), On the design and tuning of linear model predictive control for wind turbines, Renewable Energy (80), pp. 664-673.

[81] Jeong, H-G., Kim, W-S., Lee, K-B., Jeong, B-C. and Song, S-H. (2008). A sliding mode approach to control the active and reactive powers for a DFIG in wind turbines, IEEE., pp. 120-125.

[82] Jitendra, K., Ankit, C. and Kumar, J. M. (2012). Modelling and Simulation of Wind-PV Hybrid Power System using Matlab/Simulink, IEEE Students' Conference on Electrical, Electronics and Computer Science. 2012.

[83] Kabalci, K. (2013). Design and analysis of hybrid renewable energy plant with solar and wind power. Energy Conversion and Management. (72), pp. 51-59.

[84] Kalantar, M. and Mousavi S.M.G., (2010). Dynamic behaviour of a stand-alone hybrid power generation system of wind turbine, microturbine, solar array and battery storage, Applied Energy, (87), pp. 3051-3064.

[85] Kamarzaman, N. A. and Tan, C. W. (2014). A comprehensive review of maximum power point tracking algorithms for photovoltaic systems, Renewable and Sustainable Energy Reviews. (37), pp. 585-598.

[86] Karunaratne, S. (1999), Power Systems, Lecture Notes, Electrical Engineering and Power Systems, Faculty of Engineering, University of Moratuwa, Katubedda, Moratuwa, Sri Lanka.1999.

[87] Kaviani, A. K., Riahy, G.H. and Kouhsari, S. (2009). Optimal design of reliable hydrogen-based standalone Wind/PV generating system, considering components outages. Elsevier Renewable Energy. (34). pp. 2380- 2390.

[88] Khan, R., Williams, P., Hill, R. and Bil, C. (2011). Fault Tolerant Flight Control System Design for UAV's Using Nonlinear Model Predictive Control, Australian Control Conference 10-11 November 2011, Melbourne, Australia.

[89] Krause, P. C., Wasynczuk, O. and Sudhoff, S. D. (1998), Analysis of electric machinery and drive systems, IEEE press, 445 Hoes lane, PO Box 1331. NJ, US.,pp. 53-59; pp. 147-161.

[90] Kroeze, R. C. and Krein, P.T. (2008), Electrical Battery Model for Use in Dynamic Electric Vehicle Simulations, Power Electronics Specialists Conference, 2008. PE University of Illinois at Urbana-Champaign Dept. of Electrical and Computer Engineering, Urbana, IL 61801, IEEE, pp. 1336-1342.

[91] Kumar, L. and Jain, S. (2013). A multiple source DC/DC converter topology, Electrical Power and Energy Systems (51), pp. 278-291.

[92] Kumar, T. P., Subrahmanyam, N. and Sydulu, M. (2014). Fuzzy Controlled Power Management Strategies for a Grid Connected Hybrid Energy System, 978-1-4799-2014 IEEE Xplore.

[93] Kusiak, A., Li, W. and Song, Z. (2010). Dynamic control of wind turbines. Renewable Energy (35), pp. 456–463.

[94] Lagarias, J. C., Reeds, J.A., Wright, M. and Wright, H.P.E. (1998) Convergence properties of the Nelder–mead simplex method in low dimensions, SIAM J. OPTIM, 1998 Society for Industrial and Applied Mathematics (9), No. 1, pp. 112-147.

[95] Larsen, A.J. and Mogensen, T.S. (2006) Individual pitchregulering af vindmølle, M.Sc. Thesis submitted to the Technical University of Denmark Informatics and Mathematical Modelling Building 321, DK-2800 Denmark, Kongens.

[96] Lau, S. and Archer, L.A. (2016), Nucleation and Growth of Lithium Peroxide in the Li−O2 battery, Nano Letters, pubs.acs.org/NanoLett, Cornell University, Ithaca, New York 14850, United States, Accessed on: 04 October 2016.

[97] Lee, J., Nam, O. and Cho, B. H. (2007), Li-ion battery *SOC* estimation method based on the reduced order extended Kalman filtering, Journal of Power Sources, (174), pp. 9–15.

[98] Leea, T. D. and Ebong, A. U. (2017), A review of thin film solar cell technologies and challenges, Renewable and Sustainable Energy Reviews, (Article in press) Corresponding author. E-mail addresses: taesoodaniellee@gmail.com (T.D. Lee), Aebong1@uncc.edu (A.U. Ebong).

[99] Leith, D. J and Leithead, W. E. (2002). Application of Nonlinear Control to a HAWT. Department of Electronic & Electrical Engineering, University of Strathclyde GLASGOW G1 lQE, U.K., **IEEE *Xplore*:** 06 August 2002**.**

[100] Leith, D. J. and Leithead, W. E. (2000), Appropriate realisation of gain-scheduled controllers with application to wind turbine regulation, Department of Electronic & Electrical Engineering, University of Strathclyde, GLASGOW G1 1QE, U.K.

[101] Leith, D. J., Tsourdosb, A., Whiteb, B.A. and Leithead, W. A. (2001). Application of velocity-based gain-scheduling to lateral auto-pilot design for an agile missile, Control Engineering Practice (9), pp.1079–1093.

[102] Leith, D.J. and Leithead, W. E. (1998). Implementation of wind turbine controllers, Department of Electronic & Electrical Engineering, University of Strathclyde, Glasgow G1 1QE, U.K.

[103] Li, J., and Mazzola, M. S. (2013). Accurate battery pack modelling for automotive applications, Journal of Power Sources, (237), pp. 215-228.

[104] Lithium-ion Batteries (Panasonic) Technical Handbook' 99. [Online] available at: http://www.master-instruments.com.au/ files/data_sheets /Lithium/ Panasonic %20-Lithium%20Ion%20Hanbook.pdf. Accessed: 22 June (2015) 14-25.

[105] Long, X., Junping, W. and Quanshi, C. (2012). Kalman filtering state of charge estimation for battery management system based on a stochastic fuzzy neural network battery model, Energy Conversion and Management. (53), pp. 33-39.

[106] Maciejowski, J.M. (2002). Predictive control with constraints, Prentice Hall, ISBN: 978-0-2013-9823-6, 2002.

[107] Maheshn, A. and Sandhu, S.K. (2015). Hybrid wind/photovoltaic energy system developments: Critical review and findings. Renewable and Sustainable Energy Reviews, (52), pp. 1135–1147.

[108] Makinejad, K., Arunachala, R., Arnold, S., Ennifar, H., Zhou, H., Jossen, A. and Changyun, W. (2015). A lumped Electro-Thermal Model for Li-ion Cells in Electric Vehicle Application, EVS28 KINTEX, Korea.

[109] Martinez, J. (2007). Modelling and Control of Wind Turbines, M.Sc thesis submitted to Imperial College London in partial fulfilment of the requirements for the degree of Master of Science in Process Systems Engineering and for the Diploma of Imperial College. pp. 8-10

[110] Martinez, J. and Medina, A. (2010), A state space model for the dynamic operation representation of small scale Wind Photovoltaic hybrid systems. Renewable Energy. (35), pp. 1159–1168.

[111] Meenakshi, S., Rajambal, K., Chellamuthu, C. and Elangovan, S. (2006). Intelligent controller for a stand- alone hybrid generation system. IEEE, 2006.

[112] Meier, J., Spitznage, J., Kroll, U., Bucher, C., Fay, S., Moriarty, T. and Shah, A. (2004), Potential of amorphous and microcrystalline silicon solar cells, Thin Solid Films, Vol. (451-452), No.22, pp. 518-524.

[113] Melício R., Mendes, V. M. F. and Catalão, J. P. S. (2010), Power converter topologies for wind energy conversion systems: Integrated modeling, control strategy and performance simulation, Renewable Energy, (35), pp. 2165-2174

[114] Mirzaei, M., Poulsen, N. K. and Niemann, H. H. (2012). Robust Model Predictive Control of a Wind Turbine Published in 2012 American Control Conference Fairmont Queen Elizabeth, Montréal, Canada June 27-June 29, 2012.

[115] Mirzaei, M., Soltani, M., Poulsen, N. K and Niemann, H. H. (2013), Model Predictive Control of Wind Turbines using Uncertain LIDAR Measurements, American Control Conference (ACC), Washington, DC, USA, June 17-19, 2013

[116] Mohammadi, M., Hosseiniah, S. H. and Gharehpetian, G.B. (2012). Optimisation of hybrid solar energy sources/wind turbine systems integrated to utility grids as microgrid (MG) under pool/bilateral/hybrid electricity market using PSO. Solar Energy, (86), pp.112-125

[117] Morari, M. and Lee, J. H. (1999) Model predictive control: past, present and future, Computers and Chemical Engineering 23 (1999), pp. 667-682.

[118] Nasiri, M., Milimonfared, J. and Fathi, S. H. (2014), Modelling, analysis and comparison of TSR and OTC methods for MPPT and power smoothing in permanent magnet synchronous generator-based wind turbines, Energy Conversion and Management (86), pp. 892-900

[119] Nejad, S., Gladwin, D. T. and Stone, D. A. (2016). A systematic review of lumped-parameter equivalent circuit models for real-time estimation of lithium-ion battery states, Journal of Power Source, (316), pp, 183-196

[120] Njiri, J. G. and Dirk Söffker, D. (2016). State-of-the-art in wind turbine control: Trends and challenges, Renewable and Sustainable Energy Reviews. (60), pp. 377-393.

[121] Novak, J. and Chalupa, P. (2013). Wind Turbine Control with Multiple Model Predictive Control, Recent Advances in Automatic Control, Information and Communications, ISBN: 978-960-474-316-2.

[122] Npower, (2017). Wind Turbine Power Calculations RWE npower renewables Mechanical and Electrical Engineering Power Industry, [Online], Available at: http://www.raeng. org.uk/publications/other/23-wind-turbine, Accessed on: 07 Jan 2017.

[123] Okoro, O. I. (2003), MATLAB Simulation of Induction Machine with Saturable Leakage and Magnetizing Inductances The Pacific Journal of Science and Technology, (5) available on: http://www.akamaiuniversity.us/PJST.htm.

[124] Onar, O., Uzunoglu, and M.S. Alam, M. S. (2006). Dynamic modelling of, design and simulation of a wind/fuel cell/ultra-capacitor-based hybrid power generation system, Journal of Power, (161), pp. 707-722.

[125] Opitza, A., Badamia, P., Shena, L., Vignaroobana, K. and Kannan, A.M. (2017). Can Li-Ion batteries be the panacea for automotive applications? Renewable and Sustainable Energy Reviews. (68), Part 1, pp. 685–692

[126] Pandey, A. and Bansal, H. O. (2013), Temperature dependent circuit-based modelling of high power Li-Ion battery for plug-in hybrid electrical vehicles" *ICATE 2013 IEEE* Paper Identification Number-85.

[127] Pandey, A. K., Tyagi, V. V., Jeyraj, A., Selvaraj, L., Rahim, N. A. and Tyagi, S. K. (2016). Recent advances in solar photovoltaic systems for emerging trends and advanced applications, Renewable and Sustainable Energy Reviews. (53), pp. 859–884.

[128] Pandiarajan, N. and Ranganath, M. (2011). Mathematical modelling of a photovoltaic module with MATLAB/Simulink, International Conference on Electrical Energy Systems (ICEES-2011), 3-5 Jan 2011, pp.314-319.

[129] Pao, L.Y. and Johnson, K. E. (2009). A Tutorial on the Dynamics and Control of Wind Turbines and Wind Farms, American Control Conference Hyatt Regency Riverfront, St. Louis, MO, USA June 10-12, 2009.

[130] Papachristos, C., Alexis, K., Nikolakopoulos, G. and Tzes, A. (2011). Model Predictive Attitude Control of an unmanned Tilt–Rotor aircraft, IEEE, pp. 922-927.

[131] Pérez, G., Garmendia, M., Reynaud, J. F., Crego, J. and Viscarret, U. (2015). Enhanced closed loop State of Charge estimator for lithium-ion batteries based on Extended Kalman Filter, Applied Energy (155), pp. 834–845.

[132] Plett, G.L. (2004), Extended Kalman filtering for battery management systems of Lipb-based HEV battery packs—Part 2. Modeling and identification. J. Power Sources, (134), pp. 262-276.

[133] Plett, G.L. (2004), Sigma-point Kalman filtering for battery management systems of LiPB-based HEV battery packs: Part 1: Introduction and state Estimation-Part 1., J. Power Sources 2004, 161), 1356–21368.

[134] Power electronic converters, [Online], Available at: https://www.elprocus.com/power-electronic-converters/, Accessed on 10 April 2016.

[135] Qin, L. and Lu, X. (2012). MATLAB/Simulink-Based Research on Maximum Power Point Tracking of Photovoltaic Generation, 2012-International Conference on Applied Physics and Industrial Engineering, Physics Procedia, (24), pp. 10-18.

[136] Ragheb, M. and Ragheb, A. M. (2015). Wind Turbines Theory- The Betz Equation and Optimal Tip Speed Ratio," Department of Nuclear, Plasma and Radiological Engineering, USA. Available at www.intechopen.com, accessed on 16 Oct. 2015.

[137] Rahimi-Eichi, H. and Chow, Mo-Yuen. (2012), Adaptive Parameter Identification and State-of-charge estimation of Li-ion batteries, 38th IEEE conference in Industrial Electronics Society in Montreal, Canada.

[138] Rahman, M.S. (2016), Buck Converter Design Issues, Master thesis performed in the division of Electronic Devices, Linköping Institute of Technology, [Online] Available on:http://www.diva-portal.org/smash/get/diva2:24104/fulltext01, Accessed on 15 June 2016.

[139] Rao, Y.S. and Laxmi, A. J. (2012). Direct torque control of doubly fed induction generator based wind turbine under voltage dips", IJAET May 2012 ISSN:2231-1963, (3) Issue 2, pp. 711-720.

[140] Rassul Abbas, F. A. and Abdulsada, M.A. (2010). Simulation of Wind-Turbine Speed Control by MATLAB, International Journal of Computer and Electrical Engineering, (2), No. 5, October, (2010) 1793-8163.

[141] Ross, M.M.D. (2013), A simple but comprehensive Lead-Acid battery model for Hybrid System Simulation, 1471 Boul, Lionel- Bouled, Suite 26, Varennes, Quebec J3X 1P7. [Online]: Available: www. RERinfo.ca, Accessed on 18 Dec 2013.

[142] Rotondo, D. (2016). Advances in gain-scheduling and fault tolerant control techniques, PhD. Thesis submitted to the UNIVERSITAT POLITÈCNICA DE CATALUNYA.

[143] Saiju, R. and Heier, S. (2008) Performance Analysis of Lead Acid Battery Model for Hybrid Power System, 21-24 April, 2008, IEEE PES Transmission and Distribution Conference, Chicago, USA, IEEE.

[144] Sankarganesh, R. and Thangavel, S. (2012). Maximum power point tracking in PV system using intelligence based P & O technique and hybrid Cuk converter. International Conference on Emerging Trends in Science, Engineering and Technology, IEEE, pp. 429-436.

[145] Sarre, G., Blanchard, P. and Broussely, M. (2004). Aging of lithium-ion batteries, Journal of Power Sources, (127) pp. 65-71.

[146] Schlipf, D., Grau, P., Raach, S., Duraiski, R., Trierweiler, J. and Cheng, O. W. (2014). Comparison of linear and Nonlinear Model Predictive control of wind turbines using LIDAR, Proceedings of the American Control Conference, Portland, USA.

[147] Sengupta, D., Das, P., Mondal, B. and Mukherjee, K. (2016), Effects of doping, morphology and film-thickness of photo-anode materials for dye sensitized solar cell application – A review, Renewable and Sustainable Energy Reviews (60), pp. 356–376.

[148] Shahsavari, B., Maasoumy, M., Sangiovanni-Vincentelli, A. and Horowitz, R. Stochastic (2015), Model Predictive Control Design for Load Management System of Aircraft Electrical Power Distribution, 2015 American Control Conference Palmer House Hilton July 1-3, 2015. Chicago, IL, USA, IEEEXplore.

[149] Shamsi, M. H. (2016). Analysis of an electric Equivalent Circuit Model of a Li-Ion battery to develop algorithms for battery states estimation, M.Sc.ET. Thesis submitted to the Uppsala Universitet. Teknisk- Naturvetenskaplig Fakultet UTH-enheten. pp.52-62.

[150] Shivarama, K. K. and Kumar, S. (2015). A review on hybrid renewable energy systems, Renewable and Sustainable Energy Reviews, (52), pp. 907-916.

[151] Si, Y. and Karimi, H. R. (2014). Gain Scheduling H_2/H_∞ Structural Control of a Floating Wind Turbine, Proceedings of the 19th World Congress. The International Federation of Automatic Control Cape Town, South Africa. August 24-29, 2014.

[152] Simon, D. (2014), Model Predictive Control in Flight Control Design Stability and Reference Tracking, PhD thesis submitted to the Division of Automatic Control Department of Electrical Engineering Linköping University, SE-581 83 Linköping, Sweden.

[153] Slegers, N., Kyle, J. and Costello, M. (2006). Nonlinear Model Predictive Control Technique for Unmanned Air Vehicles, Journal of Guidance, Control, and Dynamics, (29). No.5, pp. 1179-1188.

[154] Smith, A. K. (2006). Electrochemical modelling, estimation and control of lithium-ion batteries, PhD. Thesis in Mechanical Engineering, Submitted at the Graduate School, The Pennsylvania State University, December.

[155] Solar Cell Efficiency, [Online] Available: http://en.wikipedia.org/wiki/Solar_cell _eff -iciency, Accessed: June 2013.

[156] Spera, D. A. (2008), Models of Lift and Drag Coefficients of Stalled and Unstalled Airfoils in Wind Turbines and Wind Tunnels, NASA/CR—2008-215434, National Aeronautics and Space Administration, Glenn Research Centre, Cleveland, Ohio, October, 2008.

[157] Takle, E. (2008). AgGM News Letter, Professor of Atmospheric science and professor of Agricultural Meteorology, Iowa St. University. gstakle@iastate.edu.

[158] Tan, Y. K., Mao, J.C. and Tseng, K.G. (2011) Modelling of Battery Temperature effect on Electrical Characteristic of Li-ion battery in Hybrid electric vehicles, *Power Electronics and Drive Systems Conference*, Singapore, IEEE, pp. 637-642.

[159] Tangler, J. L. and Kocurek, J. D. (2005), Wind Turbine Post-Stall Air Foil Performance Characteristics Guidelines for Blade-Element Momentum Methods, NREL/CP-500-36900, Presented at the 43rd AIAA Aerospace Sciences Meeting and Exhibit, Reno, Nevada, January 10–13, 2005.

[160] Tangler, J. L. and Ostowari, C. (1984), Horizontal Axis Wind Turbine Post Stall Air Foil Characteristics Synthetization, SERI/TP-257-4400, UC Category 261, DE91002198, Presented at the DOE/NASA Wind Turbine Technology Workshop, Cleveland, Ohio, May 1984.

[161] Thanangasundram, S., Arunachala, R., Makinejad, K. and Teutsch, T., (2012), A cell level model for battery simulation, *European Electric Vehicle Congress*, Brussels, Belgium, pp. 20-22.

[162] THE INSIDE OF A WIND TURBINE, US Department of Energy, [Online] Available at: https://energy.gov/eere/wind/inside-wind-turbine-0, Accessed on: 03_01_2017

[163] The MathWorks Inc, (2013) Generic Battery Model, [Online], Available at http://www.mathworks.co.uk, Accessed on 16 Dec 2013.

[164] Thomsen, S.C. (2006), Nonlinear Control of a Wind Turbines, M.Eng. in Electrical Engineering, thesis submitted at the Informatics and Mathematical Modelling Department, Technical University of Denmark, Building 321, Kongens Lyngby, DK-2800 Denmark, 2006.

[165] Tian, Y, Xia, B., Sun, W., Xu, Z. and Zheng, W. (2014), A modified model based state of charge estimation of power Lithium-ion batteries using unscented Kalman filter, J. Power Sources. (270), pp. 619-626.

[166] Tremblay, O. and Dessaint, L.A. (2009), Experimental Validation of a Battery Dynamic Model for EV Applications, *World Electric Vehicle Journal*, AVERE, (3), ISSN pp. 2032-6653, AVERE,

[167] Tsai, H-L, Tu, C-S. and Su, Y-J. (2008) Development of Generalized Photovoltaic Model Using MATLAB/SIMULINK, Proceedings of the World Congress on Engineering and Computer Science 2008WCECS 2008, San Francisco, USA.

[168] Tsang, K. M. & Chan, W. L. (2013). Model-based rapid maximum power point tracking for photovoltaic systems, Energy Conversion and Management (70), pp. 83-89.

[169] Tsang, K. M. and Chan, W. L. (2013). Three-level grid-connected photovoltaic inverter with maximum power point tracking, Energy Conversion and Management (65), pp. 221-227.

[170] Ugalde-Loo, C. E. and Ekanayake, J. B. (2010), State-Space Modelling of Variable-Speed Wind Turbines: A Systematic Approach, IEEE ICSET 2010 6-9 Dec 2010, Kandy, Sri Lanka.

[171] Ugalde-Loo, Ekanayake, J. B. and Jenkins, N. (2013), State-Space Modelling of Wind Turbine Generators for Power System Studies, IEEE TRANSACTIONS ON INDUSTRY APPLICATIONS, (49), NO. 1, JANUARY/FEBRUARY 2013.

[172] Uzunoglu, M., Onar, O. C. and Alam, M. S. (2009). Modeling, control and simulation of a PV/FC/UC based hybrid power generation system for stand-alone applications. Renewable Energy, (34), No. 3, pp. 509-520.

[173] Valerie, H., Johnson, A. and Pesaran, A.A. (2001). Temperature-Dependent Battery Models for High-Power Lithium-Ion Batteries, *National Renewable Energy Laboratory* (NREL), USA, 17th Electric Vehicle Symposium Montreal, Canada, 16-18, October 2000.

[174] Vepa, R. (2013), Dynamic Modelling Simulation and Control of Energy Generation, Chapter 4 on Wind Power Generation and Control, Lecture Notes in Energy Series No. 20, Springer Verlag, London.

[175] Viswanthan, V. V., Choi, D., Wang, D., Xu, W., Towne, S., Williford, E. R., Zhang, Ji-G., Liu, J. and Yang, Z. (2010). Effect of Entropy change of lithium intercalation in cathodes and anodes on Li-ion battery thermal management, J.O. Power sources, (195), pp. 3720-3729.

[176] Viterna, L.A. and Corrigan, R.D. (1981), Fixed Pitch Rotor Performance of Large Horizontal Axis Wind Turbines, DOE/NASA Workshop on Large Horizontal Axis Wind Turbines, Cleveland, Ohio, July 1981.

[177] Vodovozov, V. and Jansikene, R. (2016). Power electronic converters, [Online] Available on file:///C:/Thesis/Chapter-6_References/Converters%20good.pdf, Accessed on 14 June 2016.

[178] Vries, H. de., Nguyen, T.T., and Veld, B. O. het. (2015). Increasing the cycle life of lithium ion cells by partial state of charge cycling, Microelectronics Reliability (55) pp. 2247-2253.

[179] Wang, C. and Nehrir, M. H. (2008). Power management of stand-alone wind/photovoltaic/fuel cell energy system. IEEE transactions on energy conversion, (23). No.3, (2008) IEEE.

[180] Wang, F., Bai, L., Fletcher, J., Whiteford, J. and Cullen, D. (2007). The methodology for aerodynamic study on a small domestic wind turbine with scoop, Journal of Wind Engineering and Industrial Aerodynamics. (96), pp.1-24.

[181] Wang, L. (2009). Model predictive control design and implementation using MATLAB, 2009, ISBN: 978-1-84882-330-3, Springer –Verlag London Limited.

[182] Wei, G, Wang, Z., Li, W. and Ma, L. (2014). A Survey on Gain-Scheduled Control and Filtering for Parameter-Varying Systems, Reviews. Hindawi Publishing Corporation Discrete Dynamics in Nature and Society Volume 2014, Article ID 105815, 10 pages http://dx.doi.org/10.1155/2014/105815.

[183] Wu, F., Packard, A. and Balas, G. (2002). Systematic gain-scheduling control design: A missile autopilot example Asian Journal of Control, (4), No. 3, pp. 341-347.

[184] Wu, S. L., Chen P-C, Hsu, C-H. and Chang. K-Y, (2008). Gain schedule control of PVTOL aircraft dynamics with parameter-dependent disturbance. Journal of Franklin Institute, (345), pp 906-925.

[185] Xia, B., Chen, C., Tian, Y., Wang, M., Sun, W. and Xu, Z. (2015). State of charge estimation of lithium-ion batteries based on an improved parameter identification method, Energy (90), pp. 1426-1434.

[186] Xiao, M. and Choe, S-Y. (2013). Theoretical and experimental analysis of heat generations of a pouch type $LiMn_2O_4$/carbon high power Li-polymer battery, Journal of Power Sources, (241) pp.46-55.

[187] Xiong, R., He, H., Guo, H. and Ding, Y. (2011). Modelling for Lithium-Ion Battery used in Electric Vehicles, Procedia Engineering (15), pp. 2869-2874.

[188] Xue, D., Chen, Y. Q. and Atherton, D. P. (2007) Linear Feedback Control, The Society for Industrial and Applied Mathematics, Electronic version is for Chapter 6 only is available on at www.siam.org/catalog, pp. 84-235.

[189] Yu, Z., Huai, R. and Xiao, L. (2015), State-of-Charge Estimation for Lithium-Ion Batteries Using a Kalman Filter Based on Local Linearization, Energies (8), pp. 7854-7873.

[190] Yuxin, J., Qinglin, S., Zengqiang, C. and Sanpeng, D. (2015). Modelling and Simulation of an Electronic Oxygen Regulator Based on Generalized Predictive Control Algorithm, Proceedings of the 34th Chinese Control Conference July 28-30, 2015, Hangzhou, China.

[191] Zhang, C., Liu, J., Sharkh, S. M. and Zhang, Che. (2009). Identification of Dynamic Model Parameters for Lithium-Ion Batteries used in Hybrid Electric Vehicles, International Symposium on Electric Vehicles (ISEV), Beijing, China, Sep 2009. 11pp.

[192] Zhang, F., Shi, Q., Wang, Y. and Wang, F. (2007), Simulation Research on wind solar hybrid power system based on Fuzzy-PID control. Proceeding of International Conference on Electrical Machines and Systems, 2007, Oct. 8-11, Seoul Korea, pp. 338-342.

[193] Zoroofi, S. (2008), Modelling & simulation of vehicular power systems, MSc. Thesis submitted in partial fulfilment of requirements for the degree Master of Science, Department of Energy and Environment, Division of Power Engineering Chalmers University of Technology, Goteborg, Sweden.